Photoelectric Emission Properties of Photocathode Materials

BY

Tuo Li
M.S. in Statistics, University of Illinois at Chicago 2013
M.S. in Applied Math, University of Illinois at Chicago 2012
M.S. in Physics, University of Illinois at Chicago 2011

THESIS

Submitted in partial fulfillment of the requirements
for the degree of Doctor of Philosophy in Physics
in the Graduate College of the
University of Illinois at Chicago, 2015

Chicago, Illinois

Defense Committee:
W. Andreas Schroeder, Chair and Advisor
Juan Carlos Campuzano
Christoph Grein
Serdar Öğüt
Alan Nicholls, UIC Research Resources Center

To my parents,

Weiqi Li and Cunping Zhang

my baby and wife,

Chloe and Shuang.

ACKNOWLEDGMENTS

I thank my advisor Prof. W. Andreas Schroeder for his constructive advise and aspiring guidance during my time as a graduate student. Discussions with him strongly influenced the themes and topics explored in this thesis. Many thanks are also due to my more than wonderful group members over the past several years, John Hogan, Joel Berger and Stephanie Schieffer and Benjamin Rickman. Ben is owed special thanks, I truly appreciate his help in discussing our research related questions, nonetheless he is a particular generous person with his time. I also want to thank Rick DeJonghe, John Van Dyke, Bo Ling, Rui Yang, Bin Shi for their friendships and invaluable help with my research. Also, I would like to thank my committee members, Prof. Juan Carlos Campuzano, Prof. Christoph Grein, Prof. Serdar Öğüt, and Dr. Alan Nicholls, for their time, expertise and guidance at this exciting time in my PhD study; they also patiently explained many essential ideas which assisted in the progression of this thesis. I am indebted to them for many useful discussions regarding implementation of the theoretical methods. I would also like to thank Prof. Randall J. Meyer, Prof. Jing Wang, Prof. David Nicholls, Prof. Rafail Abramov, Prof. Mark Schlossman, Prof. Wai-Yee Keung, Prof. Arthur Licht and Dr. Dale Embers for their excellent teaching and theoretical expertise to my development as a PhD. Finally, thanks to my family for all their unconditional support and love.

TABLE OF CONTENTS

TABLE OF CONTENTS (Continued)

CHAPTER **PAGE**

LIST OF TABLES

LIST OF FIGURES

LIST OF FIGURES (Continued)

FIGURE **PAGE**

LIST OF FIGURES (Continued)

FIGURE **PAGE**

LIST OF FIGURES (Continued)

FIGURE **PAGE**

LIST OF FIGURES (Continued)

FIGURE **PAGE**

LIST OF FIGURES (Continued)

FIGURE **PAGE**

LIST OF FIGURES (Continued)

FIGURE **PAGE**

LIST OF ABBREVIATIONS

ARPES	Angle-Resolved Photoemission Spectroscopy
BZ	Brillouin Zone
BCC	Body-Centered Cubic
CBM	Conduction Band Minimium
DFT	The Density Functional Theory
DTEMs	Dynamic Transmission Electron Microscopy
dHvA	de Haas-van Alphen effect
ESTE	Excited-States Thermionic Emission
FCC	Face-Centered Cubic
GGA	Generalized Gradient Approximation
HCP	Hexagonal Close-Packed
HCI	Hollow Cone Illumination
LDA	Local Density Approximation
LDOS	Local Density of States
QE	Quantum Efficiency
RF	Radio Frequency
RMS	Root Mean Square

LIST OF ABBREVIATIONS (Continued)

RHEED	Reflection High-Energy Electron Diffraction
SBZ	Surface Brillouin Zone
UED	Ultrafast Electron Diffraction
UEM	Ultrafast Electron Microscope/Microscopy
UIC	University of Illinois at Chicago
UV	Ultraviolet
VBM	Valance Band Maximum
VCA	Virtual Crystal Approximation
XFELs	X-ray Free Electron Laser
YAG	Yttrium Aluminum Garnet

SUMMARY

In a bid to further improve the performance of photocathodes, and to identify excellent photocathodes, much research has been undertaken to understand the emission properties at a fundamental level. The quality of photocathode generated electron beam is fundamentally dependent upon the quality in both transverse and longitudinal (i.e., temporal) directions of the electron pulses produced by their front-end laser-driven electron gun. In the transverse spatial dimension, a high quality (high brightness) electron pulse requires a low normalized spatial transverse rms emittance. It is the aim of this thesis to facilitate and demonstrate a dramatic improvement in the performance of spatial-resolved research instruments by investigating selected robust photocathode materials exhibiting laser-driven emission with a low rms transverse momentum Δp_T.

In this thesis, I present my contributions to this cutting-edge research field by investigating high-brightness photocathodes, which could generate bright electron beam (high quantum efficiency and low spatial emittance). The field of photocathode analysis connects the root mean square transverse momentum of electrons from solid-state photocathodes to their electronic band structures, which thereby provides the consistent theoretical groundwork geared towards selecting high brightness photocathode materials for electron pulse generation.

CHAPTER 1

INTRODUCTION

Pulsed electron sources generated from laser-driven photoelectron guns are now key components in several of today's research instruments and facilities aimed at improving our understanding of materials, nanoscale systems, and molecular dynamics on fast timescales with high spatial resolution. Ultrafast and femtosecond electron diffraction (UED and FED) [1–7] have provided unprecedented temporal resolution at the atomic scale of laser-driven structural changes (e.g., phase-changes, including melting) of both bulk [3, 4, 8–13] and nano-scale [14] crystals, and in molecular reaction dynamics [15, 16]. Ultrashort (sub-picosecond) x-ray pulses generated using short electron pulses in x-ray free electron lasers (XFELs), such as at the Linac Coherent Light Source, are now able to provide diffractive imaging of atomic structure dynamics [17–21]. The field of timeresolved electron microscopy [22–27], which has imaged reaction front propagation in reactive multilayer foils [28] and the dynamics of phase transitions [20, 29, 30], crystallization [31–34], and potentially nano-catalysts [35], is now being pushed towards the ultrafast (i.e., subnanosecond) regime [25, 36–38]. An important experimental attribute of these research instruments is their ability to acquire sufficient data on a single shot; as a result, irreversible dynamic processes may be studied with high space-time resolution.

The performance of such cutting-edge research instruments is fundamentally dependent upon the quality of the electron pulses produced by their front-end laser-driven electron guns;

in particular, the transverse electron beam quality. In pulsed electron beam diffraction, the transverse beam quality (or focal spotsize-divergence product) directly determines the fidelity of the measured diffraction pattern, and hence the ability to observe time-dependent changes to it. Future high brightness x-ray sources are expected to require an order of magnitude improvement in the spatial quality of their front-end electron pulses [39] as this allows for a stronger interaction over the length of the undulator region where the x-rays are generated [40]. In single-shot time-resolved electron microscopy, the incident transverse electron beam quality together with the (aberration-free) numerical aperture of the objective lens determine the smallest focal spot size on the specimen, and hence the spatial resolving power since the Rose criterion dictates that ∼1000 electrons/pixel on a CCD-based detector are required for adequate image quality [41].

In the transverse spatial dimension, a high quality (i.e., high transverse brightness [42, 43]) electron pulse is characterized by a low rms transverse emittance [44]; commonly defined as $\epsilon_T = \Delta x \Delta p_T/(m_0 c)$, where Δx is the rms transverse pulse size, Δp_T is the rms transverse momentum of the electrons in the pulse, m_0 is the free electron mass, and c is the speed of light in vacuum. As the rms transverse emittance is conserved in propagation through perfect (i.e., non-aberrating) electron optics [44], its value at the photocathode should be minimized. However, the initial electron beam size, Δx_{cath}, is limited by either the optical laser focusing conditions (perhaps also the photocathode optical damage threshold) or screening of the guns acceleration field E_{cath} on the photocathode surface [42, 45–48]. In the short pulse limit, when

the incident laser pulse duration is less than the time of flight down the gun axis, the latter short-pulse Child's law limit restricts the photoemitted pulse charge to less than $\epsilon_0 E_{cath}(\Delta x_{cath})^2$, where ϵ_0 is the vacuum permittivity, if spatial and temporal electron pulse distortion is to be avoided [42,49]. As a result, the limiting initial normalized transverse electron pulse brightness is proportional to $E_{cath}/(\Delta p_T)^2$, which favors the use of RF photo-guns due to their much higher acceleration fields. The alternative is to significantly reduce the rms transverse momentum, Δp_T, of the electrons generated by the laser-driven electron source [50,51].

In the ideal metal approximation, in which the metal photocathode's electrons are assumed to have the free electron mass m_0 and the associated pure parabolic energy dispersion, a remarkably simple expression for the rms transverse momentum can be derived analytically [52,53]; $\Delta p_{T0} = \sqrt{\frac{m_0(\hbar\omega-\phi)}{3}}$, where the excess photoemission energy $\Delta E = \hbar\omega - \phi$ and ϕ is the effective work function of the photocathode surface. This expression is in good agreement with measurements of Δp_T for those photocathode material for which the 'ideal' metal approximation is reasonable [54], even though its analytical derivation also assumes a constant density of state, which is only a good approximation if the Fermi energy $E_F \gg \Delta E$. The analytical derivation of Δp_{T0} in Ref [52] and [53] also writes the total electron momentum inside inside (p^{in}_{total}) and outside (p^{out}_{total}) as $p^{in}_{total} = \sqrt{2m_0(E+\hbar\omega)}$ and $p^{out}_{total} = \sqrt{2m_0(E+\hbar\omega-E_F-\phi)}$ for the photoemitted electron initially at a state energy E between $E_F - \Delta E$ and E_F. From the momentum consideration point of view, during the inelastic electron photo collision associated with photon absorption (i.e., excitation of the electron to energy $E+\hbar\omega$), this can not be the case since

the initial electron momentum near the Fermi level $p \approx p_F = \sqrt{2m_0 E_F}$ is much greater than the typical UV photon momentum $\hbar\omega/c$. Indeed, for band-to-band electron excitation in solid state materials, such as semiconductors [55], the photon momentum is generally neglected in the description of the optical transition.

Moreover, the reality is that most metals do not have such a perfect spherical Fermi surface and instead their band structures near Fermi level are much more complex. As a result, Δp_{T0} is not generally in good agreement with experimentally determined values of the rms transverse momentum, $\Delta p_{T,expt.}$ [56], with larger deviations accompanied by more complex and distorted band structures. In addition, the experimental $\Delta p_{T,expt.}$ results do not support the notion that Δp_T is only a function of the excess energy ΔE; that is to say, there must be some other factors that affect Δp_T. In fact, the Δp_T evaluation should be on a case-by-case basis as the distribution of escaping electrons should be related to the real electronic band structure and its local density of states — physical effects that are also omitted in Ref. [52] and [53]. In order to elucidate the fundamental role that the band structure (and its dispersion) plays in determining the emission properties of solid-state photocathodes, I will introduce a density functional theory [57] (DFT) based photoemission Δp_T simulation which shows good agreement with the experimental measurements of rms transverse momentum for the polycrystalline metals such as Mg, Be, Mo, Cr, W, V, Ta, Nb, Ag and Cu [56]. It is also important to mention that polycrystalline samples used in Ref. [56] have arbitrary combinations of single crystal orientation on their surfaces. Due to the fact that work function, band structure and local density of states are

all dependent upon crystal orientation, it is almost impossible to ascertain how a polycrystalline metal photocathode would behave in detail from atomic scale theory. Instead, it is possible to determine the photoemitting electron states of single crystal and develop a theoretical model to describe and predict its emission properties.

Density functional theory has been demonstrated as a powerful tool for the investigation of both metal and semiconductor electronic properties. The purpose of the present investigation is to provide a promising DFT-based photoemission model for both metal and semiconductor photocathodes. With such a photoemission model, benchmarked to experimental data, the prediction of the six-dimensional (three space and three momentum) properties of electron pulses generated from photocathodes is possible, as is the potential to design photocathode materials for particular emission attributes. The latter should be useful for UED, Ultrafast Electron Microscopy (UEM) and FELs where performance improvements can be expected with reduced divergence (i.e., brightness) electron pulses; in other words, through the use of photocathodes with a low intrinsic transverse emittance and hence Δp_T.

In Chapter 2, I will introduce an overview of basic photocathode theory, which includes the three-step and one-step photoemission models, an analytical derivation of Δp_T, quantum efficiency and brightness, and ideal photocathode selection criteria. Importantly, the discussion of the effect of the transmission flux over the work function barrier on the rms transverse momentum of emitted electrons is directly applicable to the method of evaluating Δp_T in the

presented photoemission model. Together with the electronic-structure calculations based on DFT, this allows the complex emission properties of different metal photocathodes to be accurately simulated.

In Chapter 3, I outline the DFT methods associated with evaluating the electronic properties of crystalline photocathodes as well as the algorithm of the DFT–based photoemission model for simulating the intrinsic transverse momentum distribution of the photoemitted electrons from photocathodes. I will present the details of the *ab initio* method for band structure, Fermi surface, and work function calculations. Emphasis is placed on how to relate the electronic properties of the photocathode material under investigation to the transverse momentum distribution of the photoelectrons emitted from it. The resulting DFT computational analysis can then be readily extended to the BCC, FCC and HCP metals to explain the lower than expected values of Δp_T observed in the experimental measurements. In addition, the effect of a finite electron temperature (T_e) on Δp_T is also investigated by applying Fermi–Dirac statistics. This effect is of great importance in understanding the temperature sensitivity of photocathodes. The presented DFT-based theoretical analysis clearly indicates that Δp_T is intrinsically dependent on the material's electronic band structure; that is, the characteristics of the state or band from which the electron is photoemitted.

In Chapter 4, I apply the DFT photoemission model to determine the photoemission properties of body-centered cubic (BCC) photocathodes. A case-by-case analysis of each BCC pho-

tocathode includes the calculation of (i) electronic band structures along high symmetry points and lines, (ii) three and two dimensional Fermi surfaces in the first Brillouin zone, and (iii) the work function of different crystal faces in the [110] zone. With a knowledge of these electronic properties, I demonstrate the rms transverse momentum of alkali metals indeed agrees with $\Delta p_{T0} = \sqrt{m_0(\hbar\omega - \phi)/3}$ [52, 53], because their parabolic bands and quasi-spherical Fermi surfaces meet the analytical requirement of the prior analysis. This is especially true of potassium — a metal with its near spherical Fermi surface and free electron effective mass close to the vacuum mass m_0. Then I also apply the DFT photoemission model to determine the emission properties of Group Vb (V, Nb, and Ta) and Group VIb (Cr, Mo, and W) elemental metal photocathodes, and explain their lower than expected Δp_T values. As various UV laser photon energies are used in different research groups, a calculation of the rms transverse momentum as a function of photon energy, $\hbar\omega$, at different electron temperature, T_e, will also be presented for the Group Vb and Group VIb photocathodes to compare with and facilitate further experimental measurements. Moreover, I will explain why photoemission from the Group Vb metals is predicted to be significantly less temperature sensitive than from the Group VIb metals. Finally, I perform virtual crystal approximation calculation to build Mo_xNb_{1-x} crystal alloy system to show that such photocathodes which could generate continuous Δp_T.

In Chapter 5, I concentrate on the different photoemission properties of face-centered cubic metal photocathodes, such as noble metals (Cu, Ag and Au) and p-block (Al and Pb) transition metal FCC photocathodes. First, I determine the crystal structure and electronic properties of

the different groups. Unlike the BCC Group Vb and Group VIb photocathodes, FCC metals exhibit obvious band structure and Fermi surface diversification among Groups VIIIB, IB and IIIA, and this cause a large Δp_T variation. In addition, I present surface state photoemission using Ag(111) as an exemplar, and derive a surface state photoemission model to simulate the resultant 'cone-like' electron beam emission. This method extends the DFT–based model and provides a means to analyze photoelectron beam generation from hollow cone illumination [58, 59].

In Chapter 6, I explain the emission properties of hexagonal close-packed (HCP) metals. First, I present the bulk properties and electronic properties of the 15 HCP metals; they include two alkaline earth metals (Be and Mg) and thirteen *d*-block transition HCP metals (Cd, Co, Hf, Os, Re, Ru, Sc, Tc, Tl, Ti, Y, Zn and Zr). Seven HCP metals (Be, Hf, Mg, Sc, Ti, Y, and Zr) are selected as potential photocathodes from the 15 HCP metals according to the photocathode selection criteria. Unlike BCC and FCC metals, one of the important characteristics of HCP photocathode are their anisotropic properties; that is to say, HCP metals exhibit a strong photoemission anisotropy due to the uniaxial nature of their electronic properties. I illustrate that this photoemission anisotropy is reflected in the electron transverse momentum distribution for $(10\bar{1}0)$ face emission. In contrast, a symmetric transverse momentum results for emission from the (0001) face. Emission from the (0001) face of all seven selected HCP metals is discussed, and a more detailed analysis of Be(0001) photocathodes is presented where a robust surface

state [60–64] can contribute to photoemission.

In Chapter 7, I introduce semiconductor photocathodes and a previous excited-state thermionic emission measurement on a GaSb photocathode [65]. Armed with a background knowledge of semiconductor photocathodes and the developed metal photocathodes model, I predict and evaluate the properties of a proposed extremely bright laser-driven photocathode electron source — PbTe(111) single crystal which should have very low Δp_T for emitted electron pulses. The DFT-based model is extended to p-type semiconductors in order to evaluate the properties of such new photocathode materials selected for their optimal electron emission and robust operation under UV irradiation.

I also note that my work on the rms transverse momentum, Δp_T, of elemental metal photocathodes has allowed a database to be accumulated that should provide a benchmark for the emission properties of photocathodes. This database is made available to the community through a UIC sever; http://people.uic.edu/∼tli27/Database.html.

CHAPTER 2

PHOTOEMISSION PHYSICS

This chapter provides an overview of the theory behind photoemission on which my DFT photoemission model is based. Section 2.1 will give an introduction to the photoemission effect, and Section 2.2 will address the photoemission models [52, 66–68] and basic photocathode theory concepts. In Section 2.3, I will discuss the boundary conditions, transmission flux, and the theoretical formalisms for determining the rms transverse momentum, Δp_T, of the emitted electrons. The latter parameter, Δp_T, will be discussed throughout the whole thesis and as it plays an important role in describing the quality of the electron beam generated from a photocathode. Section 2.4 will discuss the derivation of thermal emittance for photoelectric emission followed by the three-step model, and approach to evaluating the quantum efficiency focusing on D.H.Dowell's theory [52] and J.F.Schmerge's theory [53, 69]. In addition, a brief introduction to beam brightness will also included in this section. In Section 2.5, I will generalize and outline the ideal photocathode selection criteria to give a common photocathode standard for thermionic and photoelectric emission.

2.1 Introduction

In 1905, Albert Einstein published the paper 'On the electrodynamics of moving bodies' [70], and theorized that the energy in each quantum of light was equal to the angular frequency (ω)

multiplied by the reduced Planck constant ($\hbar$). A photon above a certain threshold frequency has the required energy to eject a single electron, creating the observed photoemission effect. This discovery led to the quantum revolution in physics and earned Einstein the Nobel Prize in Physics in 1921. His mathematical description of the photoelectronic effect can be written as

$$KE_{max} = \hbar\omega - \phi_{eff}, \tag{2.1}$$

where KE_{max} is the maximum kinetic energy of a photoemitted electron in vacuum, also called the excess energy (ΔE), and ϕ_{eff} is the effective work function defined by the minimum energy required to photoemit an electron from the surface. In the three dimensional case, the KE_{max} is the summation of transverse electron kinetic energy (parallel to the photocathode surface) and longitudinal electron kinetic energy (perpendicular to the photocathode surface),

$$KE_{max} = \Delta E = \frac{\vec{p_{T0}}^2}{2m_0} + \frac{\vec{p_{z0}}^2}{2m_0}, \tag{2.2}$$

where $\vec{p}_{T0}$ and $\vec{p}_{z0}$ are the electron transverse and longitudinal electron momenta in vacuum, respectively. The maximum possible transverse momentum for the photomitted electrons, when $p_{z0} = 0$, is simply given by

$$p_{T,max} = \sqrt{2m_0\Delta E}. \tag{2.3}$$

At this value of the transverse momentum, the transmission efficiency over the photoemission barrier is zero since $p_{z0} = 0$.

2.2 Photoemission Models

The three step (semi-classical) photoemission model was first described by Berglund and Spicer [71] in 1964. This model breaks down the complex process of photoemission into three separate steps; (i) electrons are first optically excited into states of higher energy after photon energy absorption, (ii) they transport in these intermediate states of the solid, with or without scattering, and move to the surface of the solid, (iii) electrons transmit out of the solid and escape into of the spectral vacuum. As shown in Figure 2.1, starting from energy scheme point of view, after electrons with initial total energy E absorb a photon of energy $\hbar\omega$, electrons may have large enough total energy to overcome work function potential barrier ϕ and transport to vacuum if E is within the interval $[E_F - \Delta E,\ E_F]$, where the Fermi level E_F is the highest energy level can be occupied inside solid, and the excess energy ΔE is defined as $\hbar\omega - \phi$. This representation emphasizes that direct interband optical transitions are involved during the photoemission processes; that is, it requires a real intermediate state where the intrinsically excited electron is able to reside. The three-step model has been proved to be an effective tool for the investigation of photoemission properties for GaAs [65], CsK_2Sb [72] and Cu(111) [73].

The one-step photoemission model assumes an instantaneous emission into the vacuum via a virtual excited state. As shown in Figure 2.2, the virtual state to which the absorbed photon

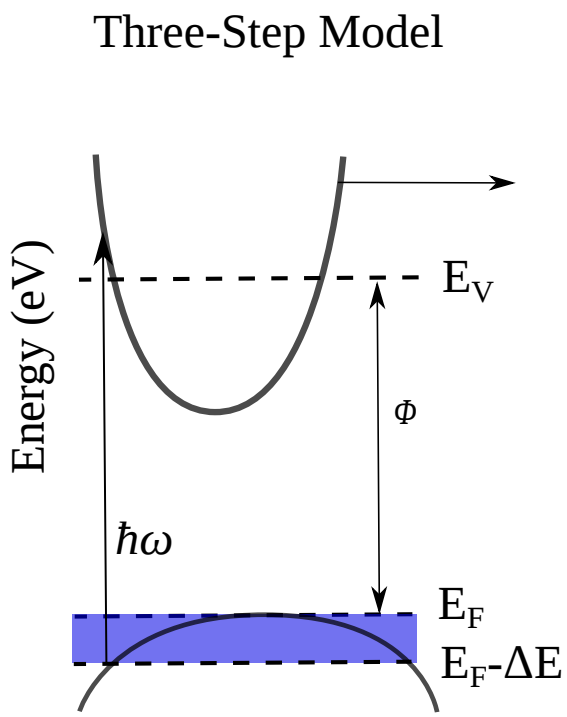

Figure 2.1: Schematic of the three-step model of photoemission; 1) electron absorbs photon energy $\hbar\omega$. 2) it is transported to the surface in a real intermediate band, and 3) it escapes into the vacuum. E_F is the highest energy level an electron may have at zero temperature. The blue region is the $(E_F - \Delta E, E_F)$ energy interval. ϕ is the work function, defined as the energy offset between vacuum energy E_V and Fermi energy E_F.

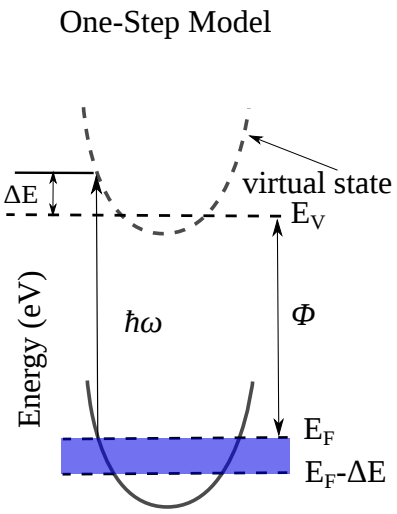

Figure 2.2: Schematic representation of one-step photoemission model. The virtual state is above the Fermi level and plotted in dashed line. When the photon energy is high enough, electrons are directly photoemitted.

energy $\hbar\omega$ excites the electron may photoemit when E + $\hbar\omega > E_F + \phi$. The escaping electrons will be those whose component of kinetic energy normal to the surface is sufficient to overcome the work function potential barrier, other electrons are totally reflected back to the bulk. In the UV photon energy regime, the momentum of the photon is small compared to the total electron momentum and can therefore be neglected ($\hbar\omega/c \ll p_{tot}$), allowing the electron momentum to be unchanged during photon absorption inside the solid. At the vacuum-side interface, the transverse momentum of electron is conserved in propagation into the vacuum, that is

$$\vec{p}_T = \vec{p}_{T0}, \tag{2.4}$$

where p_T and p_{T0} are transverse momentum in solid and outside, respectively. However, the work function potential step reduces the component of the kinetic energy perpendicular to the surface, so the longitudinal momentum is not conserved as the electron crosses the surface.

For an isotropic beam with electron effective mass m^*, one can write the overall energy conservation as

$$\hbar\omega + \frac{p_z^2 + p_T^2}{2m^*} = E_F + \phi + \frac{p_{z0}^2 + p_T^2}{2m_0}, \tag{2.5}$$

where p_z and p_{z0} are the longitudinal momentum of the excited electrons normal to the surfacein bulk and vacuum, respectively. When p_{z0} equals zero and the transverse momentum has its maximum value $p_{T,max} = \sqrt{2m_0(\hbar\omega - \phi)}$, p_z can be written as

$$\begin{aligned} p_z^2 &= 2m^*[E_F + \phi - \hbar\omega + (\frac{1}{2m_0} - \frac{1}{2m^*})2m_0(\hbar\omega - \phi)] \\ &= 2m^*[E_F - \frac{m_0}{m^*}(\hbar\omega - \phi)] \\ &= p_F^2 - p_{T,max}^2 \\ p_F &= \sqrt{2m^* E_F}, \end{aligned} \tag{2.6}$$

where p_F is the electron momentum at Fermi level. Then the maximum value of the internal photoemission angle, θ_{in}^{max}, can be expressed as

$$tan\theta_{in}^{max} = \frac{p_{T,max}}{p_z} = \sqrt{\frac{\hbar\omega - \phi}{(\frac{m^*}{m_0})E_F - (\hbar\omega)}}. \tag{2.7}$$

As $(cos_{in}^{max}\theta)^2 = \frac{1}{(tan_{in}^{max}\theta)^2+1}$, we have

$$\begin{aligned} cos^2\theta_{in}^{max} &= \frac{1}{\frac{\Delta E}{\frac{m^*}{m_0}E_F - \Delta E} + 1} \\ cos\theta_{in}^{max} &= \sqrt{\frac{(\frac{m^*}{m_0}E_F) - \Delta E}{(\frac{m^*}{m_0}E_F)}} \\ &\text{where } \frac{m^*}{m_0}E_F - \Delta E \geq 0. \end{aligned} \tag{2.8}$$

The above equation determines the possible directions of photoelectrons inside the crystal and represents the one-step model photoemission criteria. Most metals' photoemission in the vacuum ultraviolet (UV) regime can be simulated by the quantum mechanical one-step model. In Appendix A, I present a more sophisticated derivation of θ_{in}^{max}.

2.3 Δp_T Due to $T(p_z, p_{z0})$

Electrons change their angles of propagation with respect to the interface or refract as they move from the photocathode material to the outside vacuum. This is because the transverse momentum p_T is conserved at the solid-vacuum interface, whereas the longitudinal momentum is not conserved due to energy conservation in this direction (z) — the effect of the work function barrier. So, both the conservation of transverse momentum at the surface (Equation 2.4) and overall energy conservation (Equation 2.5) determine which electrons may be photoemitted. Figure 2.3 depicts the electron momentum relationships for the instantaneous (one-step) photoemission process that determine directly the range of the electron transverse momentum distribution (and hence limit Δp_T) of the photocathode emission. As discussed in Section 2.2,

there is a virtual excited state which maintains the energy-momentum dispersion of the energy band from which the electrons are photoexcited, and the excited electron can be emitted as long as its total energy component perpendicular to surface is sufficient enough to overcome effective work function in the (ijk) crystalline direction of photoemission. If all the excess photoemission energy, $\Delta E = \hbar\omega - \phi$, is in the transverse direction (emission angle of $\pi/2$), the electron's components in the vacuum are $p_{z0} = 0$ and $p_{T,max} = \sqrt{2m_0\Delta E}$. For transverse momentum larger than $p_{T,max}$, electrons are reflected back into the photocathode material from the work function barrier.

Aside from conservation of transverse momentum and energy, the influence of a potential step during the propagation of a beam of particles also needs to be considered carefully. There is a net particle (electron) flow across the work function barrier, which can be derived by differentiating the probability density, $P(z,t) = |\psi(z,t)|^2$, so that the Schrodinger equation can be written as

$$\frac{\partial P(z,t)}{\partial t} + \frac{\partial j(z,t)}{\partial z} = 0, \tag{2.9}$$

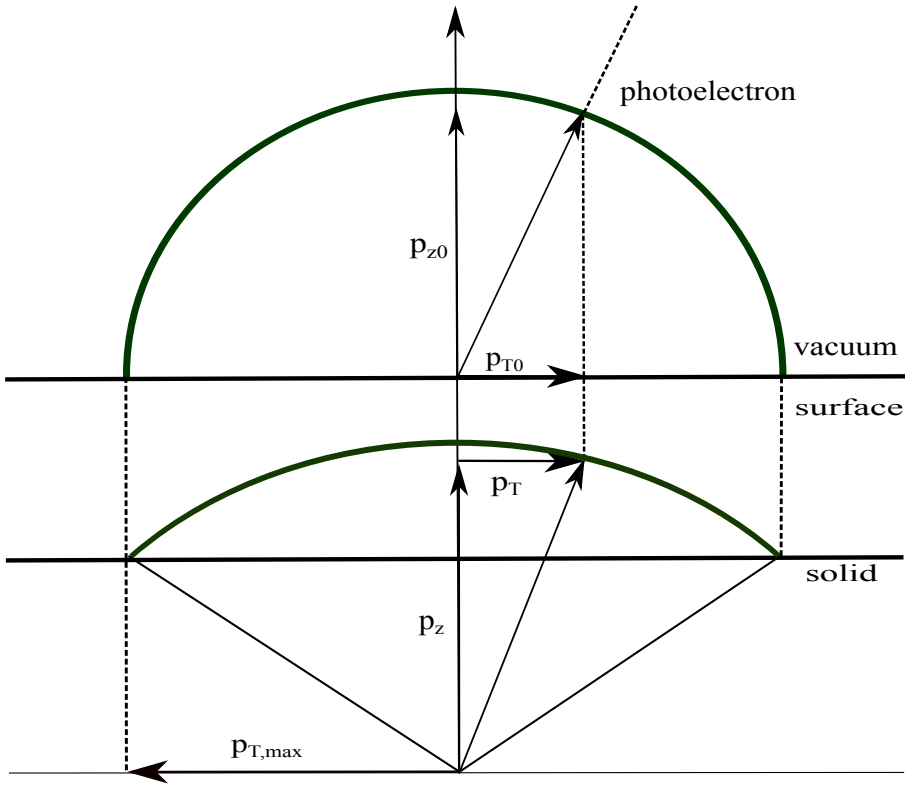

Figure 2.3: Illustration of the escape conditions for the an instantaneous (one-step) photoemission process. The photoelectron has transverse (longitudinal) momentum p_{T0} (p_{z0}). The electron inside photocathode has transverse (longitudinal) momentum p_T (p_z). The thick solid lines give the openings of the internal and external escape cones, respectively. Transverse momenta are labeled with right arrows, and the maximum transverse momentum is labeled with left arrow.

where $j(z,t)$ is identified as the probability current. Assuming a plane wave is associated with a constant (time-dependent) flux in the longitudinal direction, then the probability current can be written as

$$\begin{aligned} j(z,t) &= \frac{\hbar}{2m_z^* i}(\psi^* \frac{\partial \psi}{\partial z} - \frac{\partial \psi^*}{\partial z}\psi) \\ &= \frac{\hbar}{2m_z^* i}(\psi^* \frac{\partial \psi}{\partial z} - c.c) \\ &= |A|^2 \frac{p_z}{m_z^*}, \end{aligned} \tag{2.10}$$

where m_z^* is the magnitude of the local longitudinal effective mass, and the amplitude A is given by $\sqrt{m_z^* j/p_z}$ for a given value of the flux j. In longitudinal transmission direction case, let us assume that an electron with longitudinal momentum p_z inside photocathode is incident upon an effective work function step of height ϕ_{eff} at the vacuum-cathode surface and is transmitted into the vacuum with momentum p_{z0}. The corresponding wave function and boundary conditions are given by

$$\begin{aligned} &\psi_{in}(z) = e^{ip_z z/\hbar} + re^{-ip_z z/\hbar}, \text{inside photocathode} \\ &\psi_{out}(z) = te^{ip_{z0} z/\hbar}, \text{outside photocathode} \\ &\frac{\partial}{\partial z}\psi_{in}|_{z=0} = \frac{\partial}{\partial x}\psi_{out}|_{z=0} \\ &\psi_{in}|_{z=0} = \psi_{out}|_{z=0} \end{aligned} \tag{2.11}$$

where r and t are reflected and transmitted amplitudes, respectively. Solving the above set of equations, allows the transmission amplitude to be expressed as,

$$t = \frac{2p_z}{p_z + p_{z0}}. \tag{2.12}$$

The incident and transmitted fluxes as well as the transmittivity T are then given by

$$\begin{aligned} &\text{incident flux} = |A|^2 \frac{p_z}{m_z^*} \\ &\text{transmitted flux} = |At|^2 \frac{p_{z0}}{m_0} \\ &T = \frac{\text{transmitted flux}}{\text{incident flux}}. \end{aligned} \tag{2.13}$$

The solution of the above equations gives

$$\begin{aligned} T &= \frac{|At|^2 \frac{p_{z0}}{m_0}}{|A|^2 \frac{p_z}{m_z^*}} = \frac{m_z^*}{m_0} \frac{4p_z p_{z0}}{(p_z + p_{z0})^2} \\ \frac{1}{m_z^*} &= |\frac{\partial^2 E(p_T, p_z)}{\partial p_z^2}|, \end{aligned} \tag{2.14}$$

where the magnitude longitudinal effective mass m_z^* is used to account for both 'electron-like' (positive dispersion) and 'hole-like' (negative dispersion) of the emitting band(s). The close relationship between the band dispersion E($\hbar\vec{k}$=$\vec{p}_z$+$\vec{p}_T$) below the Fermi level in the photocathode material and the photoemitted electron transmitted flux is clearly evident in Equation 2.14.

Imposition of the boundary condition and derived transmission flux of electrons over the photoemission barrier allows evaluation of Δp_T. The rms tranverse momentum of electron beam is defined as [68, 74]

$$\Delta p_{T,x} = \sqrt{< p_T^2 > - < p_T >^2}, \tag{2.15}$$

where the angle brackets refer to expectation values of p_T^2 over the entire beam, and usually for planar photocathode, $< p_T >^2 = 0$. Using cartesian coordinates, $< p_T^2 >$ can be written as

$$< p_T^2 >= \frac{\int_{E_F-\Delta E}^{E_F} \int_0^{p_{x,max}} \int_0^{p_{y,max}} \int_{p_{z,min}}^{p_{z,max}} dp_x dp_y dp_z dE (p_x^2 + p_y^2)^{3/2} h(E, p_x, p_y, p_z)}{\int_{E_F-\Delta E}^{E_F} \int_0^{p_{x,max}} \int_0^{p_{y,max}} \int_{p_{z,min}}^{p_{z,max}} dp_x dp_y dp_z dE (p_x^2 + p_y^2)^{1/2} h(E, p_x, p_y, p_z)} \tag{2.16}$$

$$h(E, p_x, p_y, p_z) = T.n(E, p_x, p_y, p_z)$$

where $h(E, p_x, p_y, p_z)$ is the momentum distribution function used to describe the 'shape' of photoemitting electron states; it determines the distribution of possible photoemitting electronic energy states in terms of the product of the local density of states (LDOS) $n(E, p_x, p_y, p_z)$ and the transmission coefficient T. Equation 2.16 can also be simplified and expressed in terms of a normalized numerical summation based on p_T

$$< p_T^2 >= \frac{\sum_E \sum_{p_T} \sum_{p_z} h(E, p_T, p_z) p_T^3 \delta p_T \delta p_z \delta E}{2 \sum_E \sum_{p_T} \sum_{p_z} h(E, p_T, p_z) p_T \delta p_T \delta p_z \delta E}, \tag{2.17}$$

where $p_T = \sqrt{p_x^2 + p_y^2}$. Every quantity in Equation 2.17 is given by discrete value, and therefore $<p_T^2>$ can be evaluated by accumulating the product of p_T^3 and its localized distribution divided

by the normalization factor. According to the Equation 2.15, the rms transverse momentum Δp_T can then be evaluated by square root of Equation 2.17;

$$\Delta p_T = \sqrt{\frac{\sum_{E}\sum_{p_T}\sum_{p_z} h(E, p_T, p_z) p_T^3 \delta p_T \delta p_z \delta E}{2\sum_{E}\sum_{p_T}\sum_{p_z} h(E, p_T, p_z) p_T \delta p_T \delta p_z \delta E}}. \tag{2.18}$$

2.4 RMS Transverse Emittance, Quantum Efficiency and Brightness

The general definition of the rms transverse emittance [44, 75] is given in

$$\epsilon_T = \frac{1}{m_0 c}\sqrt{\langle x^2\rangle\langle p_x^2\rangle - \langle x p_x\rangle^2}. \tag{2.19}$$

where $\langle x\rangle$ and $\langle p_x\rangle$ are the averages taken over the whole electron beam distribution of electrons with respect to position x and momentum p_x, and c is the speed of light in vacuum. The above question is very widely used in describing laboratory beams and simulating both theoretical and experimental results [76]. In the transverse spatial dimension, improvements in producing a high quality (more coherent) electron pulse is characterized by a reduction in rms transverse emittance, which may be expressed as

$$\epsilon_T = \frac{1}{m_0 c}\Delta x \Delta p_T, \tag{2.20}$$

for a spatially symmetric beam where $\langle xp_x \rangle = 0$. Here Δx is the rms transverse pulse size and Δp_T is the rms transverse momentum. This quantity is conserved in a perfect (i.e., non-aberrating) propagation system. As a reduction in the source size Δx is limited either by the laser spot size on photocathode or short-pulse Child's law [77], $\Delta x \geq \sqrt{\frac{Nqd}{\pi\epsilon_0 V_{DC}}}$, where N is the number of electrons/pulse, V_{DC} is the potential of DC gun, d is the DC gun acceleration gap, q is the particle charge, and ϵ_0 is the vacuum permittivity. Thus, significant improvements in the quality of beam through a reduction in the rms transverse momentum Δp_T could be an ideal route to ultra-bright photocathodes.

For single-photon photoemission, the standard theoretical expression of Δp_T [52, 68] is

$$\Delta p_{T0} = \sqrt{\frac{m_0(\hbar\omega - \phi)}{3}}. \tag{2.21}$$

Since this quantity is an intrinsic property of the emission source, Equation 2.21 seems to indicate that the only chance to minimize Δp_T is to reduce the excess photoemission energy $\Delta E{=}\hbar\omega - \phi$; but in fact it is not so. The solenoid scan measurements of $\Delta p_{T,expt.}$ conducted by B.L.Rickman *et al.* on ten different elemental photocathodes with 4.75eV photons are clearly inconsistent with Equation 2.21 [56]. In particular, the measured rms transverse momentum for polycrystalline Ag ($\Delta p_{T,Ag}{=}0.235{\pm}0.005\sqrt{m_0 eV}$) and W ($\Delta p_{T,W}{=}0.150{\pm}0.005\sqrt{m_0 eV}$) differ by a factor of ~ 1.6 even though both their work functions are 4.64±0.02eV. Further, for the Group Vb metals (V, Nb and Ta), Δp_{T0} as given by Equation 2.21 would require a factor of

$\sim$5 reduction in the ΔE in order to be consistent with $\Delta p_{T,expt.}$. In Chapter 3, I will present a photoemission analysis, using the full electronic band structure of the metal photocathodes, that provides the explanation for this discrepancy.

The quantum efficiency (QE) is an important practical parameter for photoemission as it signifies the probability of electron emission when a single photon strikes the photocathode—the number of emitted electrons per incident photon. The QE is then the number of electrons that could escape divided by the total number of electrons summed over excess energy and the maximum solid angle times the fraction of laser energy actually absorbed in the cathode. The analytical expression for QE determined by J.F.Schmerge [69] can be written as

$$QE = (1-R)\frac{\int_{E_F-\Delta E}^{E_F}\int_0^{\theta_{max}}\int_0^{2\pi} N_{electron} sin\theta d\theta d\Phi dE}{\int_{E_F-\Delta E}^{E_F}\int_0^{\pi/2}\int_0^{2\pi} N_{electron} sin\theta d\theta d\Phi dE}, \tag{2.22}$$

where $N_{electron}$ is the electron energy distribution which is assumed to be a Fermi-Dirac distribution, θ_{max} is the maximum angle that an electron can approach with respect to the surface normal and be emitted, and R is the power reflectance of the laser radiation at the photocathode surface which is angle and polarization dependent. In order to evaluate an exact quantum efficiency value, Equation 2.22 must be numerically integrated, or it may be solved approximately with a simplified electron energy distribution. From the band theory point of view, in the one-step photoemission model described in Section 2.2, the QE would then also be propor-

tional to the integration of the product of the band density of states per volume per unit energy $n(E,\vec{p})$ and the transmission efficiency over the photoemission barrier $T(E,\vec{p})$

$$QE \propto \int_{\Omega_p}\int_0^{p_{max}}\int_{E_F+\phi-\hbar\omega}^{E_F} n(E,\vec{p})T(E,\vec{p})p^2 dE d\vec{p} d\Omega_p, \tag{2.23}$$

where the transmission factor $T(E,\vec{p})$ (Equation 2.14) is a function of longitudinal momentum (p_z and p_{z0}). It is interesting to note that any changes to the transverse momentum of the electrons inside the metal would have no effect on the QE. Thus, the QE is a measure of the longitudinal momentum distribution, which agrees with D.H.Dowell's conclusion about the measurement of QE [52].

As a figure of merit of an electron beam, brightness ($\overline{B}$) has been introduced using a number of different definitions [78]. Conventionally, the brightness can be expressed in terms of the peak current divided by the square of the transverse emittance [79, 80], which can be related to the widely used definition of average brightness

$$\overline{B} = \frac{2I}{\pi^2\epsilon_T^2} = \frac{2Im_0^2c^2}{\pi^2\Delta x^2\Delta p_T^2} \propto \frac{E_{cath}}{\Delta p_T^2}. \tag{2.24}$$

The equation above indicates that brightness can be thought of as the peak current flux (I) per unit of mean square transverse momentum. As the rms transverse emittance ($\epsilon_T = \frac{1}{m_0c}\Delta x\Delta p_T$) is conserved through perfect electron optics [44], its value should be minimized in order to achieve a high brightness value. However, the initial electron beam size (spot size), Δx, is

limited by either the optical laser focusing conditions or screening the gun's acceleration field on the photocathode surface E_{cath} [76, 81–84] as presented in Chapter 1.

2.5 Ideal Photocathode Selection Criteria

Metallic photocathodes are very attractive and widely applicable in TEMs, DTEMs and XFELs, because most of them are very robust and vacuum compatible (allowing operation at pressures of $>10^{-9}$Torr), have good response time [85] ($<$ 1ps) and long life time, and accept higher than 100 MV/m surface electric fields; but they have a relatively high work function (>4.00eV, and so need UV light) and a relatively very low QE ($< 10^{-4}$). In the best of cases, with special surface treatment [82], the QE is at most of the order of 0.1% using incident photons at 266 nm. Unfortunately, this performances degrades as the photocathode surface contaminates in the RF gun. The lifetime does not exceed few days; however, it is generally possible to restore the initial properties. Nonetheless, the low QE of metallic photocathodes implies the use of a high laser power density at the surface. In contrast, some semiconductor photocathodes have relatively lower work function (work in visible light or UV light), and a high QE ($> 5\%$); but they require very good vacuum conditions ($\sim 10^{-12}$Torr or better) such as ultra-high vacuum (UHV) or even extremely high vacuum (XHV) [86, 87] to operate and extend lifetime. Nowadays, the majority of effort to achieve a high quality electron beam is directed towards high brightness photocathode materials, such as Group Vb metals [88], LaB_6 semiconductor [89], and GaAs-GaAsP strain compensated superlattice [90] for the generation

of spin polarized electron beams.

Although, in principle, almost all elemental metals could be employed as photocathodes given the appropriate UV laser radiation source (i.e., incident photon energy), differences in their physical and chemical characteristics will dictate their utility. Ideally, a photocathode material should possess a work function that allows photoemission with readily available UV laser sources, be robust and chemically stable, have a sufficiently high melting point, and be free of magnetic effects:

1. *Work function.* Although modern laser systems are capable of generating radiation throughout most of the infrared, visible, and UV spectral regions, the most readily accessible wavelengths are the harmonics of solid-state lasers such as Ti:sapphire (emitting at ca. 800nm), Nd:Yttrium Aluminum Garnet (YAG) (1064nm), and Yb:fiber based systems (∼1040nm). As the efficient generation of harmonics shorter than ∼250nm is complicated by the availability of suitable UV transparent nonlinear crystals, desired photocathodes have work functions less than $\hbar\omega \approx 4.7$ eV (i.e., the third harmonic of Ti:sapphire or the fourth harmonic of Nd:YAG).

2. *Robustness, vapor pressure, and chemical stability.* The metal photocathode should also be hard enough to allow for a good surface figure to be attained by polishing (to avoid surface roughness effects [91]), be vacuum compatible, and be sufficiently inert chemically to allow for operation at vacuum pressures greater than 10^{-9} Torr (as routinely found in electron micro-

scopes). The hardness criterion rules out for example potassium, sodium, and thallium, which are soft metals, while the high vapor pressures of Cd and Zn ensure that they are not vacuum compatible if the effects of desorption contamination are to be avoided [92]. Chemical stability is also an important criterion, especially if surface oxidation causes a significant change in the photocathode work function [93], for example, face-centered cubic metals Ca and Sr are ruled out by this criterion.

3. *Melting point and optical damage.* Metal photocathodes with melting points above ∼1,000K are also preferred for short electron pulse generation as laser induced heating [65, 94] can be significant. Of course, this form of optical damage may be preceded by other forms of laser radiation induced damage that are generally dependent upon the optical surface quality of the photocathode.

4. *Magnetism.* Magnetic metals such as hexagonal close-packed metal Co, and the face-centered cubic metals Ni and Fe, do not generally perform well as low emittance photocathode materials, primarily because the trajectory of photoemitted electrons is strongly affected by the metals' local surface magnetic field [95].

From a practical point of view, the electron beam with an isotropic transverse momentum distribution on the transverse plane is preferred instead of that with bivariate transverse momentum distribution. As will be shown in this thesis, this means that an ideal crystal orientation

of the photocathode is one that has a symmetric electronic band cross section at the Fermi level; for example, the (001) crystal orientation is preferred for BCC, FCC and (0001) for HCP metals.

CHAPTER 3

THE DENSITY FUNCTIONAL THEORY BASED PHOTOEMISSION MODEL

In this chapter, I will present a first-principles analysis of photoemission from metal photocathodes to demonstrate a strong band structure dependence to the rms transverse momentum of the photoemitted electrons. As silver is a well known and widely used photocathode [96–98] with a single band across the Fermi level, evaluation of its photoemission characteristics as an exemplar provides a canonical test case that can be compared to both prior theoretical and experimental results [71, 98–100]. In Section 3.1, I detail the *Ab initio* method, which requires a fundamental knowledge of the electronic properties of the photocathode material such as its band structure E($\vec{k}$), LDOS $n(E, \vec{k})$ and work function $\phi(ijk)$. In Section 3.2, along with introducing the DFT based photoemission model, I illustrate how the electron transverse momentum distribution established as well as the method employed to extract Δp_T from the crystal momentum map. In addition, I explain the electron temperature effect on the Δp_T.

3.1 The *Ab initio* Method

First-principles calculations of electronic properties within DFT are carried out using the PWscf code of the Quantum-ESPRESSO suite [101]. Ultrasoft pseudopotentials (USPP) with the local density approximation (LDA) [102–104] are utilized to render the computations tractable as well as to enhance efficiency. It is worth mentioning that the results of my analysis are not changed if the generalized gradient approximation (GGA) is used instead [105]. In order to deal with the sharp discontinuity in k-space between occupied and unoccupied states, we use a Monkhorst-Pack [106] set of special k-points and Marzari-Vanderbilt smearing [107] with a broadening of 0.02 Ryd. Relativistic, including spin-orbit coupling, approximations are included for the $4d$, $5d$ and $6p$ transition metals [108], where relativistic corrections to their electric properties are significant [109, 110]. Non-relativistic calculations are performed on the other metals.

Density functional approaches typically focus on finding the minimum total energy for a particular configuration, which means that convergence tests always need to be performed before calculating the real electronical properties. Even though more plane waves can be used to describe the crystal system if more calculation accuracy is required, it is also necessary to find a balance between computational cost and calculation accuracy. Therefore, for the optimal lattice constant calculation, the experimental lattice parameter is first employed as the input, and subsequently the convergence test is performed for the kinetic energy cut-off for wave-functions, kinetic energy, charge density for the potential and the uniform grid of k-points to insure that

the ground state energy is within the energy convergence tolerance of 10^{-4}eV (0.1meV).

For the case of Ag, the total energy is monotonically decreasing with increasing kinetic energy cut-off — a behavior that is a direct result of the variational principle [111]. The total energy asymptotically tends to its converged value at a 395eV cut-off energy, which is enough to guarantee $\pm 10^{-4}$eV convergence tolerance. With the lattice constant and kinetic energy cutoff fixed, the convergence of absolute energies with respect to a uniform k-point grid is guaranteed by increasing the k-sampling points. The convergence result shows that a 15×15×15 k-point grid is sufficient for the FCC silver to achieve the convergence tolerance. After computing the total energy of the metal at lattice constant interval [$a_{expt.}$-0.50, $a_{expt.}$+0.50] Bohr in increments of 0.01 Bohr (1 Bohr = 0.529 $\mathring{A}$), the lattice constant with the minimum total energy was labeled as the metal's theoretical lattice constant. My DFT calculated lattice constant, $a_{Ag,DFT}$ = 7.57 Bohr, is within 2% of the experimental value, $a_{Ag,expt.}$ = 7.72 Bohr. The DFT evaluated optimal lattice constant is used as the lattice constant input for the subsequent band structure, Fermi surface, LDOS, and work function calculations. The FCC Ag crystal with the optimal lattice constant is represented using XCrySDen [112] in Figure 3.1.

3.1.1 Band Structure and Local Density of States

For the band structure calculation, the algorithm is the following: 1) The k-path of interest for band structure is generated using Xcrysden [112]. 2) A self-consistent field (SCF) calculation [113] is performed using the theoretical optimized lattice constant to determine the

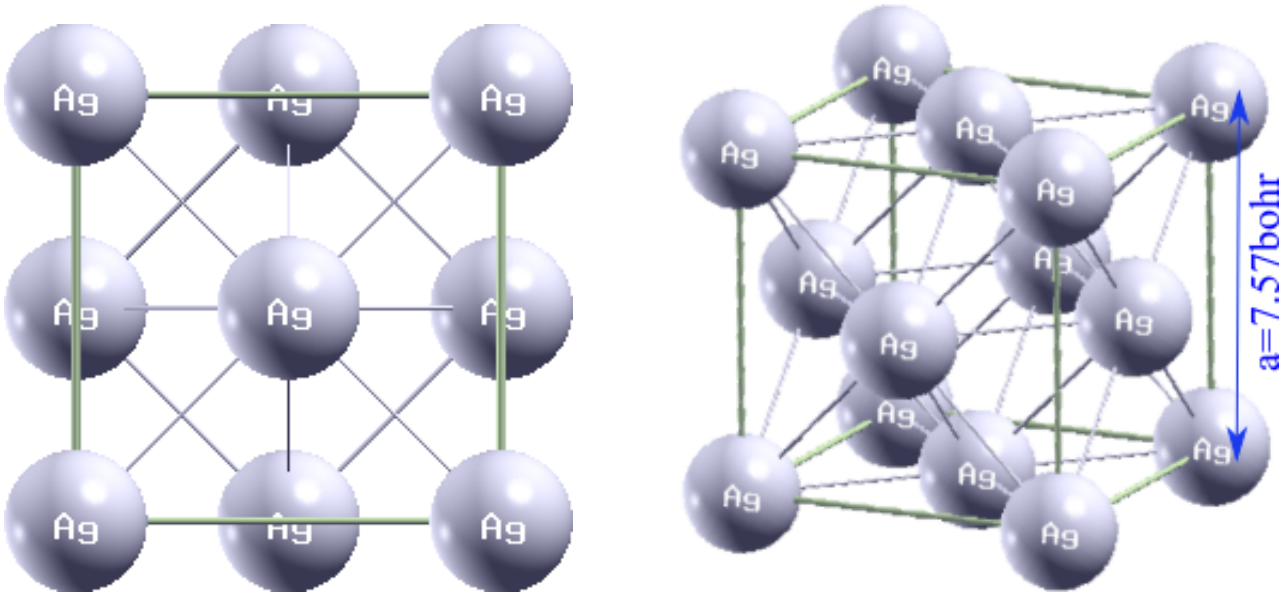

Figure 3.1: FCC Ag crystal structure with DFT calculated a=7.57 Bohr lattice constant. The left panel is the top view; The right panel is (45^o, 45^o, 45^o) aerial view. FCC structure has lattice points on the faces of the cube, and each face gives exactly one half atom contribution to the FCC unit cell. Together with the corner lattice points contributes, there are a total of 4 atoms per unit cell (1/8×8 from the corners plus 1/2×6 from the faces).

self-consistent density and potential. 3) A non-SCF calculation with the desired k-path and number of bands is conducted to evaluate each chosen k-point's eigenvalues and eigenvectors (wave functions). 4) Finally, the calculated E($\vec{k}$) data is extracted to produce a Fermi surface file that can be read by GNUplot [114] along the high symmetry points and lines in the first Brillouin zone. For the LDOS calculations, I employed the following procedure: 1) The lower and upper energy values around the Fermi level (E_{min} and E_{max}) as well as the energy grid step are first specified. 2) The first Brillouin zone is then sampled by an automatically generated uniform k-point grid. 3) An improved tetrahedron method for Brillouin-zone integrations [115]

and simple Gaussian energy level broadening [116] are therefore employed to calculate LDOS, $n(E, \vec{k})$.

For the band structure calculation of Ag, 200 uniform k-points are chosen along the symmetry points and lines in the first Brillouin zone of the FCC system. The parameters used to achieve the optimized lattice constant, $a = 7.57$ Bohr, are then used to perform the band structure calculation. The result is shown in Figure 3.2 and is with 98% in agreement with previous experimental $E(\vec{k})$ dispersion results [66, 71, 117]. The Ag energy band dispersion curves $E(\vec{k})$ are plotted along the k-path $\Gamma \xrightarrow{\Delta} X \xrightarrow{Z} W \xrightarrow{Q} L \xrightarrow{\Lambda} \Gamma \xrightarrow{\Sigma} K$ in the first Brillouin zone, where Δ, Z, Q, Λ and Σ are symmetry lines with the line lengths $\overline{\Gamma X}$=2π/a, $\overline{XW}$=π/a, $\overline{WL}$=$\sqrt{2}\pi$/a, $\overline{L\Gamma}$=$\sqrt{3}\pi$/a and $\overline{\Gamma K}$=3$\pi/\sqrt{2}$a, respectively. Due to the low-lying excited d-band, the dispersions of the 'electron-like' bands that cross the Fermi level (dashed line) are generally close to parabolic. Nonetheless, as shown in later chapters, it is often necessary to define an effective mass at the Fermi level, $m^* = \hbar^2(\frac{d^2E}{dk^2}|_{k=k_F})^{-1}$, which gives 1.03$\pm$0.01$m_0$, 0.39$\pm$0.01$m_0$ and 0.94$\pm$0.01m_0 [118] for the Δ_1, Σ_1, and Λ_1 bands, respectively.

3.1.2 Fermi Surface

The calculation of Fermi surface proceeds as follows: 1) A SCF calculation is performed to determine the Fermi energy using Gaussian smearing and Gaussian broadening for metals [116]. 2) A $n_x \times n_y \times n_z$ ($n_{x,y,z}$ are positive integers) uniform k-point grid is imposed on the 3D irreducible Brillouin zone rather than the first Brillouin zone to dramatically reduce

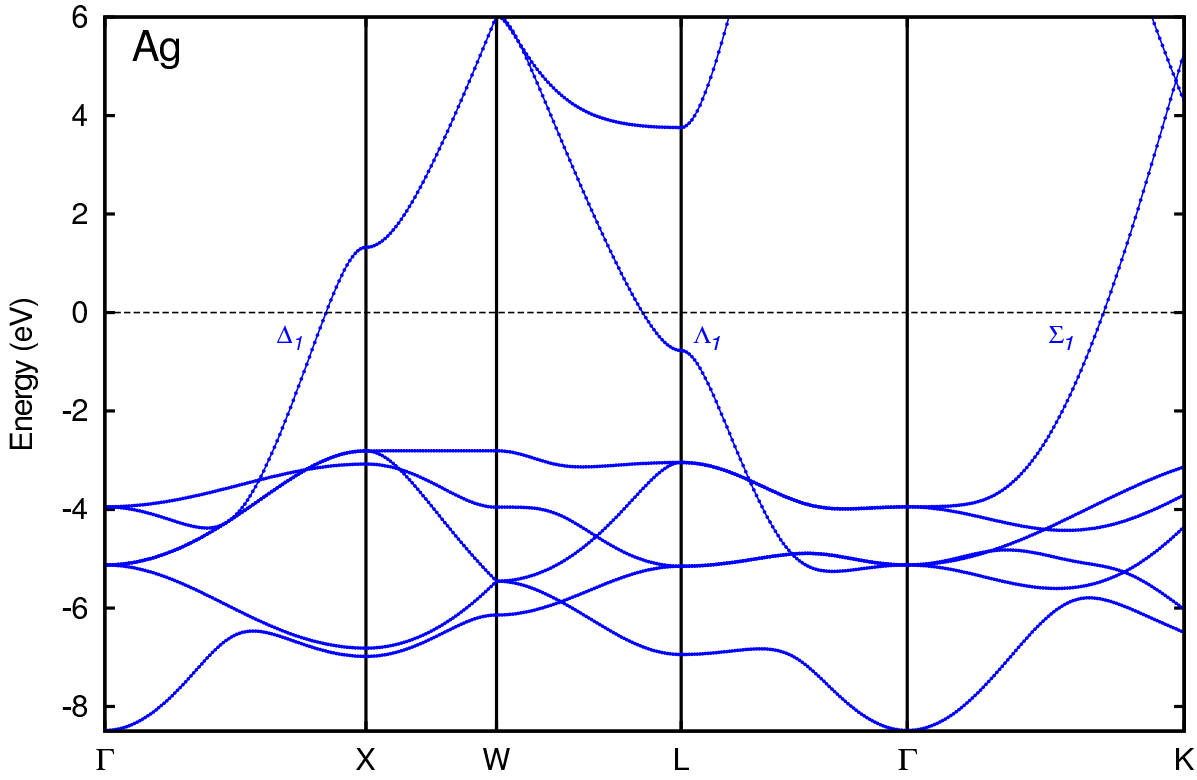

Figure 3.2: Ag band structure along high symmetry points. The Fermi level is shifted to zero energy and labeled with a dashed line. In [001] ($\Gamma_1 \rightarrow$ X) and [110] ($\Gamma_1 \rightarrow$ K) directions, the Δ_1 band and Γ_1 band cross Fermi level. In the [111] ($\Gamma_1 \rightarrow$ L) direction, the Λ_1 is 0.77eV below the Fermi level.

computational costs. The total number of k points (the value of $n_x \times n_y \times n_z$) should be larger than 1000 in order to have sufficient data points to clearly vizualize the 3D Fermi surface. 3) A band structure calculation is then performed using the $n_x \times n_y \times n_z$ uniform k points. 4) The calculated E(k_x, k_y, k_z) data is used to produce a Fermi surface file that can be read by XCrySDen graphical user interface [112] in the first Brillouin zone.

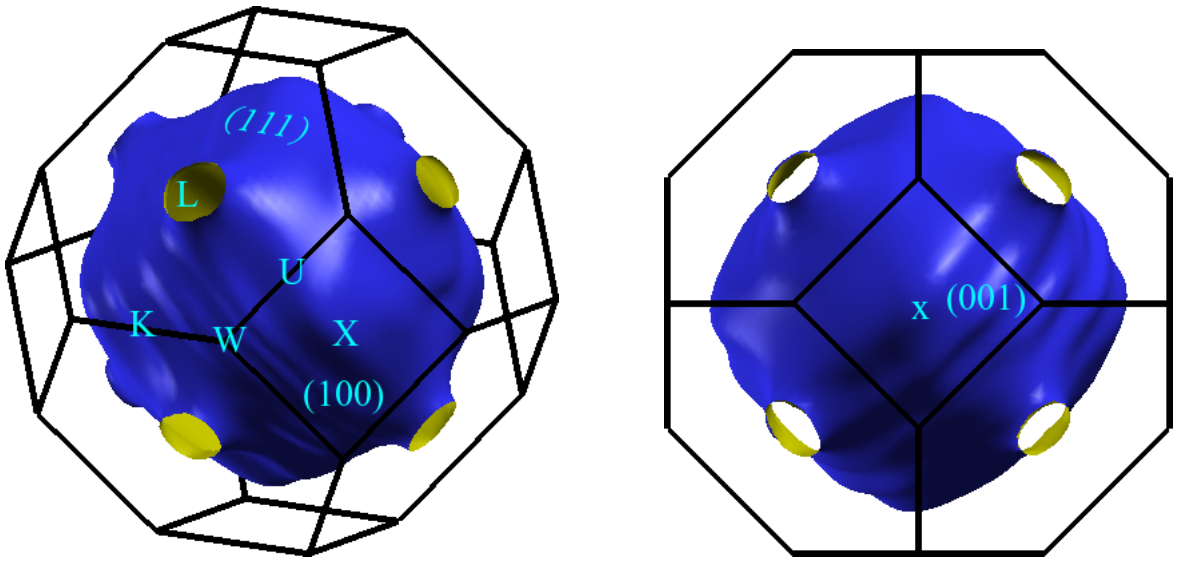

Figure 3.3: Fermi surface of Ag in the first Brillouin zone. The polyhedron (black solid lines) represents the first Brillouin zone of the FCC system. It consists of a near to perfect 'belly' sphere, centered at Γ point, which connects to the L point along the [111] direction.

The Fermi surface evaluation for Ag is based on a plane-wave basis set with 21×21×21 uniform k-grid points sampling the irreducible Brillouin-zone. The 3D Fermi surface of Ag as well as the first Brillouin zone of a simple FCC lattice is shown in Figure 3.3 with the high symmetry points and crystal faces labeled; the (001) surface and the (111) surface are perpendicular to k_z-axis and $\Gamma - L$ axis, respectively. The radius of the principal sphere ('belly') is $2.81\sqrt{m_0 eV}$ along Γ–X. There is a 'neck' in the (111) plane (U–L–K). The shape of the 'neck' is a circle with a radius of $0.51\sqrt{m_0 eV}$ along L–K direction. Otherwise, the Ag Fermi surface is quite spherical. For most photocathode materials, however, the crystal Fermi surface is quite

complex and highly asymmetric (i.e., non-spherical and a multi-band combination) which can increase the complexity of the electron emission analysis.

3.1.3 The Thin-Slab Work Function Evaluation

The work function ϕ of a metal is defined as the minimum energy to exact an electron from the metal surface;

$$\phi = E_{vac} - E_F, \tag{3.1}$$

where E_{vac} is the vacuum energy level, defined as the electrostatic potential outside the metal surface, and E_F is the Fermi energy. Thus, the value of work function can be evaluated for the metal surface by determining the energetic difference between the vacuum and Fermi level using the thin-slab technique [119–122]. Consequently, the calculation of work function is separated into two parts; 1) calculation of the Fermi energy E_F of the slab, which can be done through a SCF calculation and 2) the evaluation of the potential energy at the vacuum level. The vacuum length should be large enough to ensure that the average potential is nearly flat in the vacuum.

To summarize, the basic DFT procedure to assess the work function of metals is as follows: 1) Construct thin-slabs consisting of a film formed by a few atomic layers parallel the crystalline plane (ijk) of interest. It is not straightforward to construct such a slab without visualizing it first, particularly for high index crystal planes, so I employed XCrysDen to visualize crystalline and supercell structures [112]. This ensured that all of the slab models studied were of the correct crystal geometry. 2) Perform a SCF calculation to find the Fermi energy in the crystal-

oriented slab. It is well known that the some equilibrium atomic positions in a crystal surface may be different from those in the ideal bulk-terminated surface [123]. Therefore, if necessary, a relaxation calculation is performed first at the beginning to find the equilibrium geometry of the surface [124]. 3) Calculate the average of macroscopic potential to determine the vacuum level. 4) Determine final work function by evaluating the difference in the Fermi and vacuum level energies.

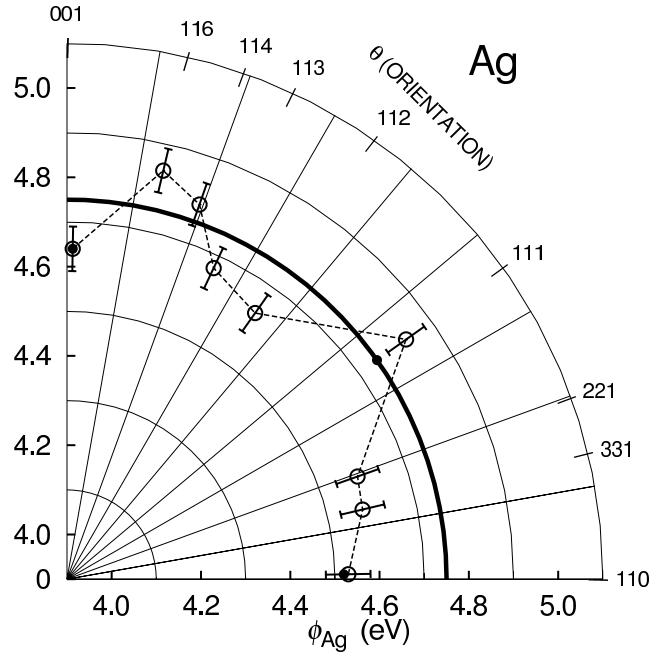

Figure 3.4: Polar plot of the photoelectric work function of Ag in [110] zone. Open circles with ±0.05 eV error bars stand for the values of thin-slab calculated work function for the high-index surfaces (112), (113), (114), (116), (221) and (331) as well as the low-index surfaces (111), (100), and (110); solid circles stand for literature values [125]; the solid line stands for 4.75 eV photon energy.

For the Ag work function calculation, I employ unrelaxed slabs consisting of 8-12 atomic layers separated by a 15 $\mathring{A}$ vacuum region, which is sufficient to ensure that both the vacuum and average crystal potential reach equilibrium, thus allowing the work function to be determined from the energetic difference within an accuracy of typically ± 0.05eV. Even if significantly more computational intensive surface relaxation effects are included, neither the LDA or GGA exchange-correlation potentials appear to offer any less uncertainty than those of experimental values [125, 126]. The calculated work function results are displayed in the form of a polar plot from the (001) face to the (110) face in Figure 3.4, they are in good agreement with the experimental data [125] (solid circles).

Knowledge of the photoelectric work function in the (ijk) crystalline direction is required to determine which occupied states may contribute to photoemission and thus the efficiency of electron photoemission from those states. There is clearly significant variation in $\phi_{(ijk)}$ over a range of about 0.3 eV from a minimum of 4.53 eV for the (110) face to a maximum of 4.83 eV for the (116) face. For instance, for a photon energy $\hbar\omega = 4.75$ eV (solid line in Figure 3.4), the (111), (116) and (114) faces possess work functions greater than $\hbar\omega$. As a result of this variation in $\phi_{(ijk)}$, a polycrystalline photocathode will, in general, generate an intrinsically inhomogeneous electron beam — some microcrystalline faces not emitting, while others emit with ranging efficiency and different values of the rms transverse momentum Δp_T. I will detail the effect of work function anisotropy on photoemitting energy states and incorporate this complexity into

the DFT-based photoemission analysis of elemental metals presented in Chapters 4–6.

3.2 DFT-Based Photoemission Model

From a knowledge of the band structure of the metal photocathode (i.e., the electronic state dispersion $E(\vec{k})$ and local density of states $n(E,\vec{k})$) and the work function anisotropy $\phi_{(ijk)}$, it is straightforward to determine the momentum components of the photoemitted electron and the weighted (by $n(E,\vec{k})$) probability of its emission from a particular crystal face over the work function barrier, $T(\vec{p_z},\vec{p_{z0}})$, where $\vec{p_{z0}} = \hbar\vec{k_{z0}}$ is the longitudinal momentum of the emitted electron in the vacuum. As the momentum of the incident UV photon is negligible in comparison to the momentum of the electron in the crystal ($\hbar k \gg \hbar\omega/c$) [50,56], the governing energy-momentum relationship for an instantaneous (one-step) photoemission process involving a virtual optically-excited state is

$$\hbar\omega + E(p_z, p_T) = \phi_{(ijk)} + \frac{1}{2m_0}(p_{z0}^2 + p_T^2), \tag{3.2}$$

where the Fermi level is defined as zero energy. In Equation 3.2, the electron momentum is written in terms of its longitudinal component $\vec{p_z} = \hbar\vec{k_z}$ ($\vec{p_{z0}} = \hbar\vec{k_{z0}}$) perpendicular to the (ijk) emission surface in the metal (vacuum), and its transverse component $\vec{p_T} = \hbar\vec{k_T}$ parallel to the

surface which is conserved during the emission process [44]. The flux transmission probability over the work function barrier may be expressed as

$$T = \frac{m_z^*}{m_0}\frac{4p_z p_{z0}}{(p_z + p_{z0})^2}; \;\; \frac{1}{m_z^*} = |\frac{\partial^2 E}{\partial p_z^2}|, \tag{3.3}$$

where the magnitude of the local effective mass in the emission direction, m_z^*, is used to account for both 'electron-like' (positive dispersion) and 'hole-like' (negative dispersion) of the emitting band(s). The close relationship between the band dispersion $\mathrm{E}(\hbar\vec{k} = \vec{p_z} + \vec{p_T})$ below the Fermi level in the photocathode material and the photoemitted electron momentum distribution is clearly evident from Equation 3.2 and Equation 3.3. In particular, if the band dispersion restricts electrons with high values of p_T from being emitted (an imaginary p_{z0}), then a reduced value of the emitted rms transverse momentum Δp_T should result.

3.2.1 DFT-Based Δp_T Analysis

In this section, I show that the symmetry of the electron transverse momentum distribution photoemitted from Ag(001) results from highly symmetric electron energy bands in Ag for the (001) emission direction. The subsequent photoemission analyses presented in Chapters 4, 5, 6, and 7 show that such symmetric electron bands are not the norm.

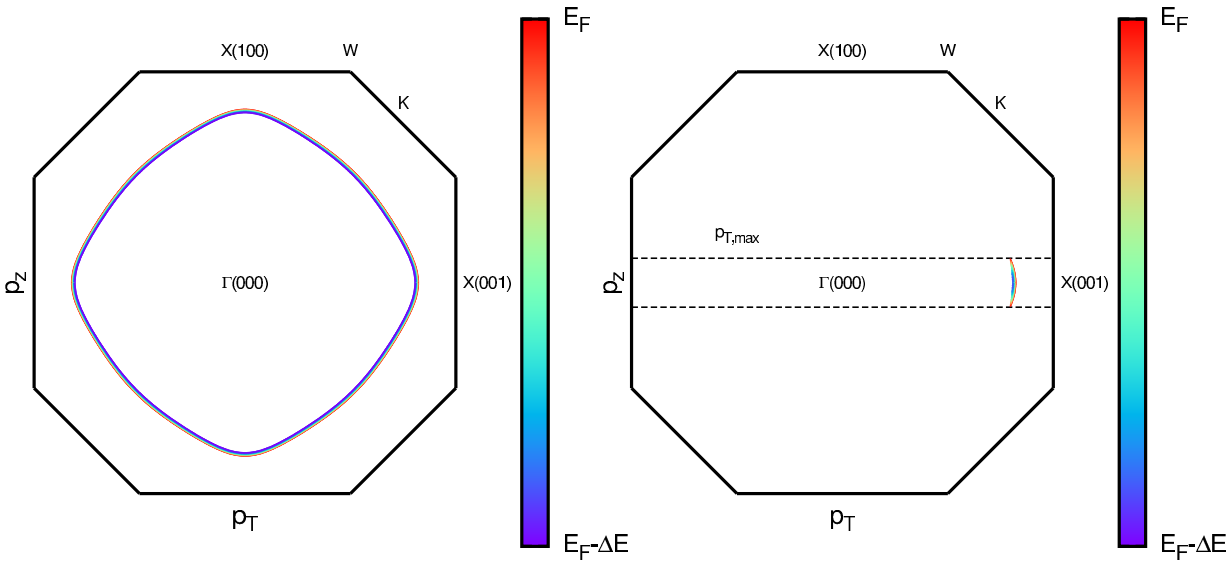

(a) (b)

Figure 3.5: Ag [100] ($\Gamma \rightarrow X(100)$) direction photoemission E($\vec{p}$) states for the (001) transverse crystal direction. The black solid line is the intersection of (100) plane of Brillouin zone. In the left panel, the $X(100) \rightarrow \Gamma \rightarrow X(001)$ plane colored contour represents the excess energy states with energy increasing from $E_F - \Delta E$ to E_F as the contour color becomes red. In the right panel, the dashed lines indicate $p_{T,max}$, and the colored contour means electronic states that may photoemit with [100] as the p_z direction and [010] as p_T direction.

For each photoemission crystal face (ijk), there are in general two corresponding primary transverse crystal directions and emission from the energy bands in these directions is evaluated separately due to the directional dependence of the Brillouin Zone (BZ) intersection. As shown in Figure 3.5 and Figure 3.6, for Ag(001) face photoemission, (010) and (110) are the two primary transverse crystal faces. Their planar intersections with the FCC BZ generate 'octagon-like' (Figure 3.5) and 'hexagon-like' (Figure 3.6) two dimensional crystal momentum cross-sections, respectively. With 4.75 eV incident photon energy (0.13 eV excess energy), using

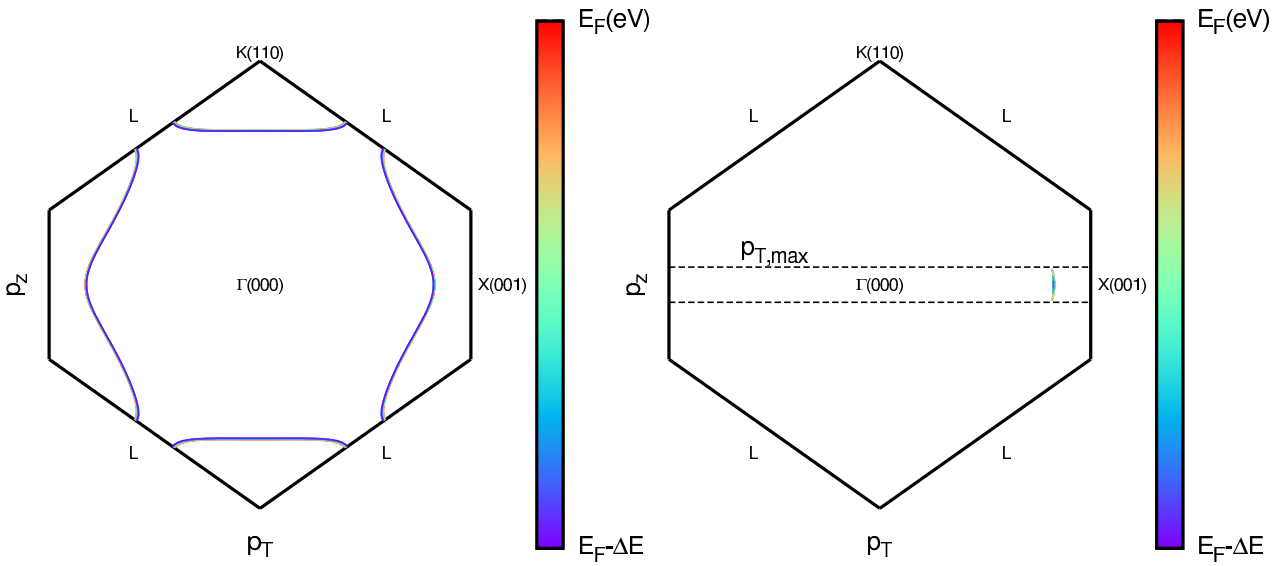

Figure 3.6: Ag [100] ($\Gamma \rightarrow X(100)$) direction photoemission E($\vec{p}$) states for the (110) transverse crystal direction. The black solid line is the intersection of (110) plane of Brillouin zone. In the left panel, the $X(100) \rightarrow \Gamma \rightarrow K(110)$ plane colored contour represents the excess energy states with energy increasing from $E_F - \Delta E$ to E_F as the contour color becomes red. In the right panel, the dashed lines indicate $\pm p_{T,max}$, and the colored contours show the electronic states that may photoemit with [100] as the p_z direction and [110] as the p_T direction.

.

Equation 2.3, the maximum transverse momentum is given by $p_{T,max} = 0.51\ \sqrt{m_0 eV}$, which is represented by the dashed lines in Figure 3.5(b) and Figure 3.6(b). At this value of the transverse momentum, the transmission efficiency over the photoemission barrier, $T(p_z, p_{z0})$, is zero since $p_{z0} = 0$. Applying the boundary conditions discussed in Section 2.3, the photoemitting electron energy states confined by $p_{T,max}$ have 'crescent-like' shape and are plotted in Figure 3.5(b) and Figure 3.6(b) using a colored energy contour palette from $E_F - \Delta E$ (blue) to E_F (red). As the transverse momentum p_T is reduced, more electron states below the Fermi

level can contribute to photoemission with those states nearest Fermi level having the largest local density of states $n(E, \vec{k})$ for this 'electron-like' band and the highest values of $T(p_z, p_{z0})$. As expected from the near spherical Fermi surface (Figure 3.3), the emission states are highly symmetric about the emission direction [001] for Ag. Due to this high symmetry in Ag's band structure for the $K \overset{\Sigma}{\leftarrow} \Gamma \overset{\Delta}{\rightarrow} X$ path, the resulting weighted transverse momentum distributions of the photoemitted electrons are also nearly identical along the (010) and $(1\bar{1}0)$ crystal momentum directions (Figure 3.7(a)).

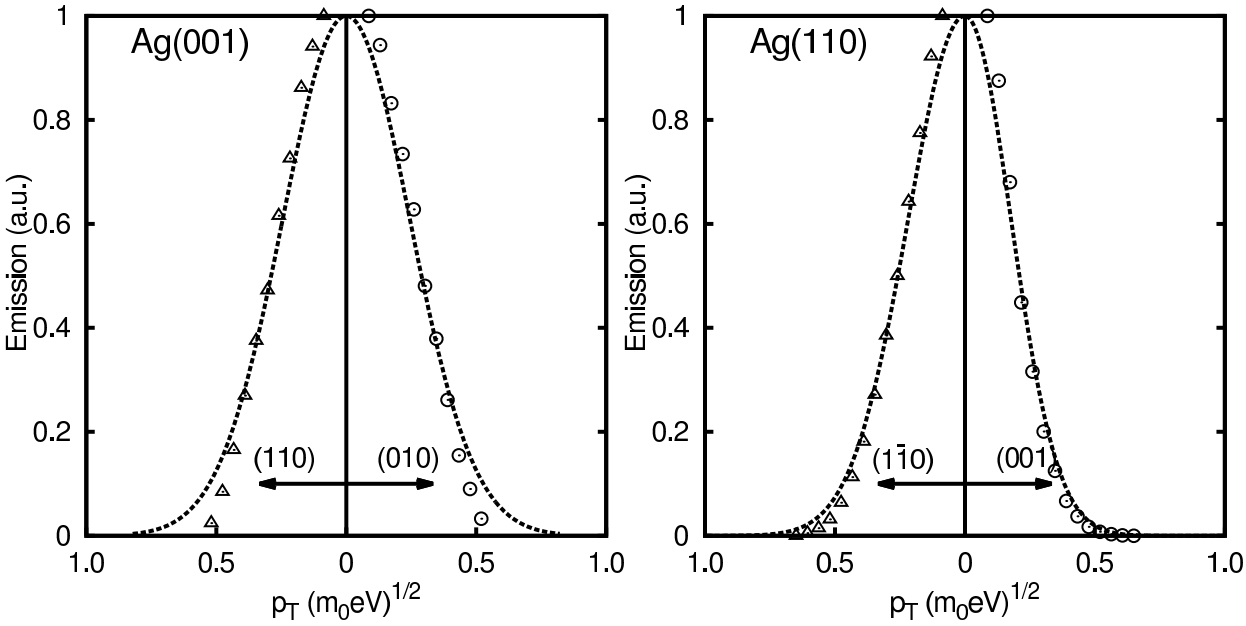

(a) (b)

Figure 3.7: (a) p_T distributions of Ag(001) crystal photoemission; transverse momentum distributions of the photoemitted electrons in the (010) and (110) directions. (b) p_T distributions of Ag(110) crystal photoemission; transverse momentum distributions of the photoemitted electrons in the (001) and (110) directions. The dashed lines are the Gaussian fits and guides to eye.

The rms transverse momentum Δp_T is readily evaluated from the photoemitting states momentum-energy distribution showing Figure 3.8 by integrating over the product $n(E,\vec{p})T(p_z,p_{z0})$ at constant p_T followed by standard methods to find the variance in p_T. As shown in Figure 3.7, both the (110) and (010) emission faces' data are well fitted to a normal distribution $e^{-p_T^2/2\sigma^2}$ independently (dashed line) to show that the p_T distributions are close to 'bell-shaped'. The spatially averaged values of the rms transverse momentum $\Delta p_{T,(001)}$ extracted from these p_T distributions using Equation 2.18 are both 0.202 $\sqrt{m_0 eV}$ for the (010) and the (110) transverse momentum directions; both values are close to the $0.235\sqrt{m_0 eV}$ experimental value of polycrystalline silver [56]. Furthermore, they are consistent with that predicted by prior analysis [52,53]: $\Delta p_{T0} = \sqrt{m_0 \Delta E/3} = 0.208\ \sqrt{m_0 eV}$. This agreement is to be expected since the analyses in Ref. [52] and [53] use spherically symmetric bands with an electron mass equal to m_0 and a constant density of states: All are good approximations for Ag(001) as the crystal orientation has an effective mass $1.03\pm0.01 m_0$ [99] at the Fermi level (within 3% of m_0), and its Fermi energy of 6.31 eV [127] is sufficiently greater than the employed 0.13 eV excess photoemission energy which ensures that the approximation of a constant electron density distribution is reasonable.

For the case of (110) crystal face emission, there exists a slight asymmetry in the transverse momentum distribution (Figure 3.7(b)) that results from the 'dagger-like' distribution of photoemitting energy states (Figure 3.8(b)). With 4.75 eV incident photon energy ($\Delta E =$ 0.22 eV), the calculated Δp_T values are 0.174 $\sqrt{m_0 eV}$ and 0.169 $\sqrt{m_0 eV}$ for (001) and $(1\bar{1}0)$

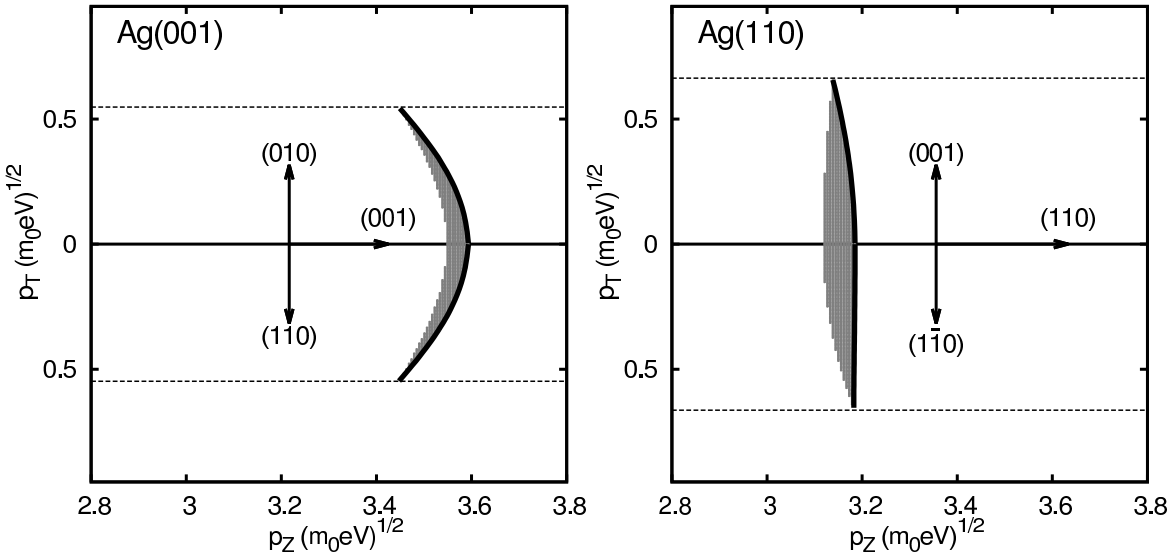

Figure 3.8: (a) Ag(001) and (b) Ag(110) face photoemitting energy states contours. Crystal momentum map of the electronic states (shaded regions) below the Fermi level (solid line) that may photoemit within $p_{T,max} = \sqrt{2m_0\Delta E}$ (dashed lines). For Ag(001), the transverse crystal orientations are (010) and (110); for Ag(110), the transverse crystal orientations are (001) and (1$\bar{1}$0)

transverse momentum faces, respectively. The non-equal Δp_T values are due to the fact that there exists a distortion to the otherwise near spherical Fermi surface in the (110) direction that also is manifest in a significantly lower electron effective mass of $0.39(\pm 0.01)m_0$ [99]. However, the values calculated of Δp_T also differ from the experimental Δp_T value for Ag [56] by 26%. That is almost certainly because the experiment in Ref. [56] used a polycrystalline Ag sample whose most prevalent surface can be expected to be (001) [128]. Therefore, the properties of the generated electron beam can be expected to be intrinsically dominated by the (001) direction photoemission rather than the (110) direction photoemission. In addition, both of these evalu-

ations of Δp_T are, of course, determined in the 'zero temperature' limit; that is, for an electron temperature $T_e \to 0$, so that no electrons occupy states above the Fermi level. The experiment was conducted at room temperature ($T_e \to 300$K), which will have higher Δp_T value than that for zero temperature. In my DFT-based analysis, this restriction may be lifted by the inclusion of the Fermi-Dirac function as discussed in the next section.

3.2.2 Temperature Dependence of Δp_T

So far, the evaluations of the rms transverse momentum have been determined in the zero temperature limit; that is, for an electron temperature $T_e \to 0$ so that no electrons occupy states above the Fermi level. For a temperature dependent DFT-based Δp_T analysis, the Fermi-Dirac function $f_D(E, T_e) = (1 + e^{(E-E_F)/k_B T_e})^{-1}$ needs to be included, where k_B is Boltzmann's constant, to describe the occupation of the electronic states around the Fermi energy E_F, albeit for the band structure evaluated for a 'zero temperature' crystal (i.e., where lattice vibrations (phonons) are frozen out). K. L. Jensen, who first recognized the effect of electron temperature on the angular integration part of electron transverse momentum [53], introduces the Fermi-Dirac function $f_D(E, T_e)$ as a temperature multiplier to $< p_T^2 >$, where $E \in [E_F - \Delta E, \infty]$. In reality, the Fermi–Dirac function gives the distribution of identical fermions over single-particle energy states, where no more than one fermion can occupy a state. When electrons with energy E reside in an associated local density of states $n(E, p_T, p_z)$ (i.e. the number of states per unit energy range per unit volume), the average number of fermions per unit energy range per unit

volume can be expressed as $n(E, p_T, p_z) f_D(E, T_e)$.

In a real metal photocathode, electrons may distribute above the $E_{F,T_e=0}$ as the electron temperature increases. Prior experimental results obtained for two-photon driven thermionic emission from gold [129] indicate that laser-induced heating [130] of the electron distribution in metal photocathodes does indeed increase the emitted Δp_T — an effect that is generally overlooked in both direct current and radio frequency (RF) guns. In the sub-picosecond ultrafast limit, the effect of such laser-induced heating is readily evaluated since it typically takes a few picoseconds for the heat deposited into the electron distribution to be transferred to the phonons [131]. Therefore, the temperature multiplier $f_D(E, T_e)$ should be brought into the p_T integration over the transverse momentum distribution for the interval E$\in[E_F - \Delta E, \infty]$, giving the following electron temperature dependent expression for $<p_T^2>$;

$$< p_T^2 >= \frac{\int_{E_F-\Delta E}^{\infty} \int_0^{p_{x,max}} \int_0^{p_{y,max}} \int_{p_{z,min}}^{p_{z,max}} dp_x dp_y dp_z dE (p_x^2 + p_y^2)^{3/2} n(E, p_x, p_y, p_z) f_D(E, T_e)}{\int_{E_F-\Delta E}^{\infty} \int_0^{p_{x,max}} \int_0^{p_{y,max}} \int_{p_{z,min}}^{p_{z,max}} dp_x dp_y dp_z dE (p_x^2 + p_y^2)^{1/2} n(E, p_x, p_y, p_z) f_D(E, T_e)}, \tag{3.4}$$

where $p_{x,max}$, $p_{y,max}$ and $p_{z,max}$ are the maximum values for the momenta of three principal directions, $f(p_x, p_y, p_z)$ is the electron distribution, and $p_T = \sqrt{p_x^2 + p_y^2}$. The above equation can be simplified and modified for numerical means in terms of summations using step changes for p_T, p_z and E (δp_T, δp_z and δE);

$$\Delta p_T = \sqrt{\frac{1}{2} \frac{\sum_E \sum_{p_T} \sum_{p_z} f(p_T, p_z) p_T^3 n(E, p_T, p_z) f_D(E, T_e) \delta p_T \delta p_z \delta E}{\sum_E \sum_{p_T} \sum_{p_z} f(p_T, p_z) p_T n(E, p_T, p_z) f_D(E, T_e) \delta p_T \delta p_z \delta E}}. \tag{3.5}$$

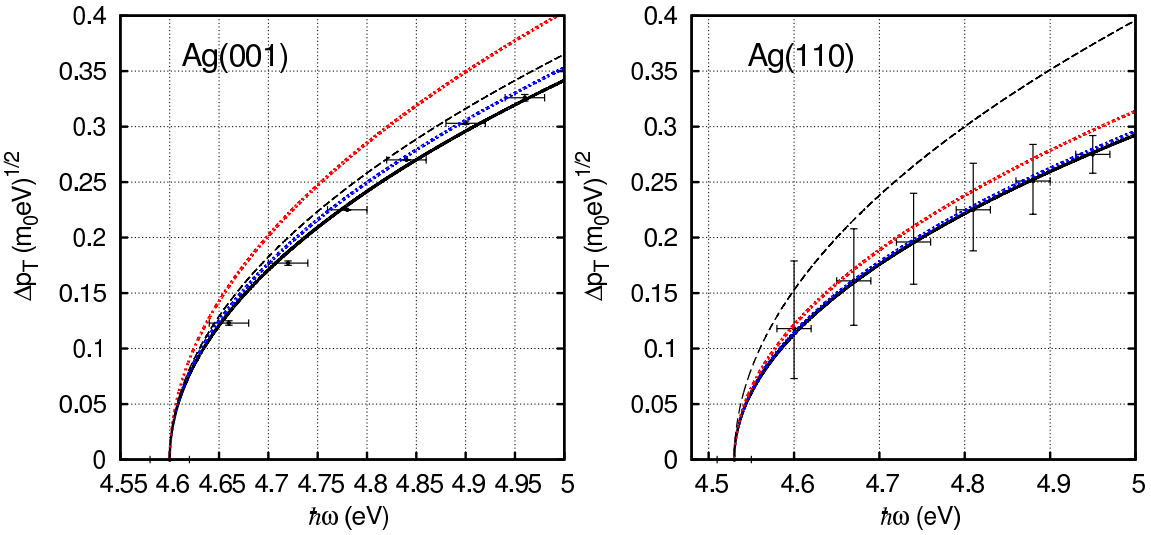

(a) (b)

Figure 3.9: $\Delta p_T(\hbar\omega)$ of Ag(001) and Ag(110) at 0K, 300K and 1234K (the melting point [132]). The data points are the DFT photoemission model extracted Δp_T values as a function of $\hbar\omega$. (a) $\Delta p_T(\hbar\omega)$ of (010) transverse momentum face for Ag(001). (b) $\Delta p_T(\hbar\omega)$ of $(1\bar{1}0)$ transverse momentum face for Ag(110). The solid lines (blue and red dot-dashed lines) are the $\Delta p_T = A\sqrt{m_0 \Delta E}$ fit to the $T_e \to 0$K (T=300K and T=1234K) data points. The black dashed lines are the expected form of $\Delta p_{T0} = \sqrt{m_0(\hbar\omega - \phi)/3}$ from Refs. [52] and [68]

Figure 3.9 shows the dependence of Δp_T on the incident photon energy $\hbar\omega$ for Ag evaluated by the discussed DFT-based photoemission simulation at three different electron temperatures T_e; 0K, 300K, 1234K (the melting point of silver [133]). In keeping with the prior photoemission analyses, which give $\Delta p_{T0} = \sqrt{m_0(\hbar\omega - \phi_{(ijk)})/3}$ (dashed line), a least squares method is used to fit the function $p_T = A\sqrt{m_0(\hbar\omega - \phi_{(ijk)})}$ (solid line) to the $T_e \to 0K$ DFT-based data points. The extracted values of A are 0.540 and 0.427 for Ag(001) (Figure 3.9(a)) and Ag(110) (Figure 3.9(b)) face emission, respectively. The blue dot-dashed lines, just above the solid line, show the fits to the result of calculating $\Delta p_T(\hbar\omega)$ for the Ag(001) and Ag(110) faces

TABLE I: Summary of emission property results for Ag(001) and Ag(110).

Metal	p_z direction	p_T direction	A(0 K)	A (300 K)	A (1234 K)
Ag	001	010	0.540	0.558	0.638
Ag	001	110	0.540	0.558	0.638
Ag	110	001	0.427	0.432	0.458
Ag	110	$1\bar{1}0$	0.420	0.428	0.456

with the DFT-based photoemission simulation when T_e = 300K (data points not shown). The increase (or change) in Δp_T is only around 3.2% in this case since ΔE and E_F are both much greater than $k_B T_e$; that is to say that the additional partially populated states above the Fermi level are a small perturbation in the photoemission simulation. When T_e is at silver's melting point 1234K, $k_B T_e$ is equal to 0.106eV and the effect of the higher electron temperature results in an increase in Δp_T of around 11.4% for Ag(001) and 6.0 % for Ag(110) in Δp_T with corresponding A values of 0.638 and 0.458 shown in Table I. As ΔE for Ag(001) is smaller than for Ag(110), increasing electron temperature will have less effect on $\Delta p_{T,(110)}$ and $\Delta p_{T,(001)}$ as reflected in Figure 3.9. We note that the Boltzmann tail of the Fermi-Dirac distribution will allow photoemission for $\hbar\omega < \phi_{(001)}$ [134], essentially photo-assisted thermionic emission with $\Delta p_T \approx \sqrt{m_0 k_B T_e} = 0.177(m_0 eV)^{1/2}$ for T_e=300K, but this effect is not considered here as the emission efficiency is much reduced. Furthermore, although the relative efficiency of different crystal faces of the same metal photocathode could be determined, the DFT-based photoemission analysis as described cannot determine the absolute emission efficiency since electron scattering rates that limit the lifetime of the virtual excited electronic state have not

been included.

CHAPTER 4

BODY-CENTERED CUBIC METAL PHOTOCATHODES

In Chapter 3, the DFT-based photoemission model has been introduced in detail. The purpose of this chapter is to investigate the emission properties for Alkali, Group Vb and Group VIb body-centered cubic (BCC) elemental photocathodes as well as to demonstrate the effect of band structure, work function, and electron temperature on the emission properties of BCC metal photocathodes. The results not only indicate the reasons for the previous standard model's success in explaining photoemission from idealized metal photocathodes (the alkali metals) [52, 53], but also explain the lower than expected Δp_T measurements for Group Vb (V, Nb and Ta) and VIb (Cr, Mo and W) BCC metals [50, 54].

In Section 4.1, the prior theoretical approaches and the DFT-based photoemission simulations will be compared using potassium as an exemplar. In Section 4.3 and Section 4.2, I will introduce the more practical BCC elemental photocathodes (Group Vb and Group VIb) and show the influence of their band complexity on photoemission. A comparison between Vanadium Group and Chromium Group metals shows a strong temperature insensitivity for the Vanadium Group photocathodes. In section 4.4, I will present an example of photocathode design using the BCC Mo_xNb_{1-x} alloy, which is able to generate a continuous variation in Δp_T.

4.1 Alkali Metals

The alkali metals are the first group of the periodic table and have only one electron in their outer shell. They are not found uncombined in nature, because these soft metals readily lose their outer electron in ionic bonding with other materials; that is to say, they may chemically interact before and after inserted into a laser-driven electron gun, and so do not meet the ideal photocathode criteria (See Section.2.5). Even though alkali metals are not ideal photocathodes, they are of particular importance for understanding the conditional accuracy of Dowell's expression for Δp_T which is derived based on a parabolic relationship between the electron's energy E and its wave-vector $\vec{k}$.

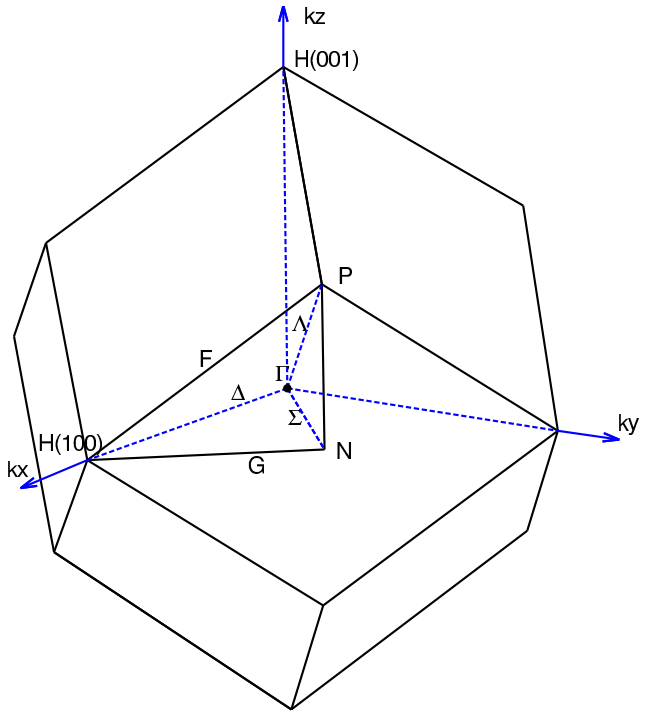

Figure 4.1: BCC Brillouin zone

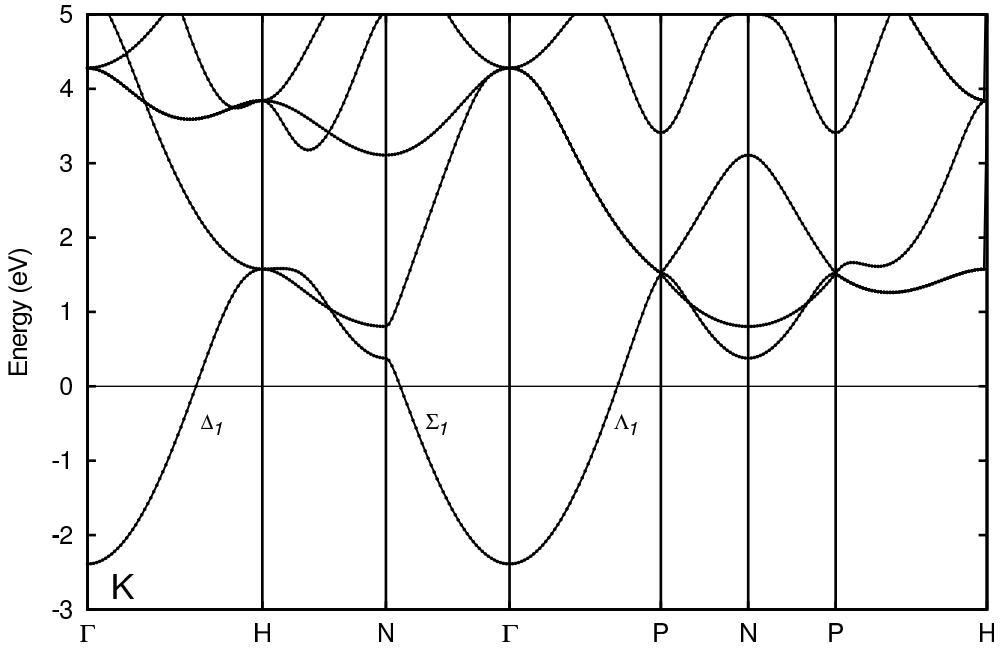

Figure 4.2: DFT calculated band structure of potassium along high symmetry points and lines of the first BZ of the BCC lattice. The horizontal line at zero energy represents the calculated Fermi energy. The Δ_1, Σ_1, and Λ_1 bands cross the Fermi level.

The energy bands and Fermi surfaces of alkali metals have been the object of many theoretical investigations [135, 136]; the similarity of the alkali metals to ideal metals provides an opportunity for a quantitative test of the nearly free electron model as a description of the electronic band structure of a solid. Among these monovalent metals, the Fermi surfaces of sodium, potassium and rubidium are closest to spherical; lithium and cesium, on the other hand, are believed to have relatively more anisotropic Fermi surfaces [137–140]. Experimentally, A.C. Thorsen and J.O. Reitz have performed de Haas-van alphen (dHvA) and transverse magnetoresistance measurements on potassium, and the results show that the effective mass of

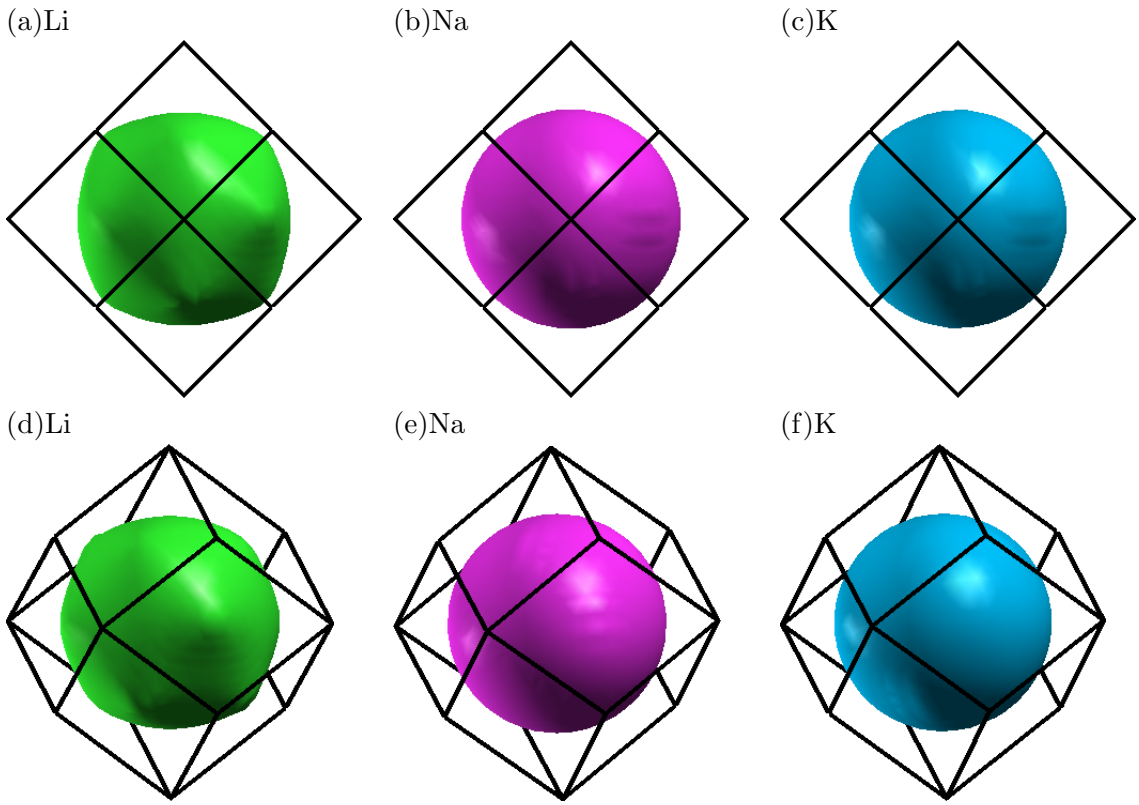

Figure 4.3: Alkali Metal Fermi surface. Two projected ((a)—(c) and (d)—(f)) of the alkali metal reciprocal lattice showing the shape of Li, Na, and K Fermi surfaces.

electrons in potassium is close to the free electron mass ($m^* \approx m_0$), and that potassium could be used as an idealized metallic model for free conduction electrons. Thus, the free-electron model [141] can be a suitable starting point for the evaluation of the potassium Fermi surface.

In alkali metals with the BCC crystal structure, where the conventional unit cell of side a contains two atoms with one free electron each, the Fermi surface is inside the empty-lattice in

the extended-zone scheme. When working in the reduced-zone scheme, the Fermi surfaces of individual bands are obtained by reducing the Fermi surface to the first Brillouin zone (See Figure 4.1). Among the points located on the boundaries of the rhombic dodecahedron Brillouin zone of the BCC lattice, the face center at N=$\frac{2\pi}{a}(\frac{1}{2},\frac{1}{2},0)$ is closest to the zone center at $0.71\frac{2\pi}{a}$ from the Γ point, while the face corner at H=$\frac{2\pi}{a}$(1,0,0) is furthest from the Γ point.

Our DFT calculation optimized lattice constant a for K is 9.51 Bohr, which differs from $a_{expt.}$ = 9.88 Bohr by only 3% [142]. In the ground state, a system of N electrons occupies states with the lowest possible energies; all the occupied states lie inside a sphere of radius k_F, and the energy at the surface of this sphere is defined as the Fermi energy E_F. The magnitude of the wavevector k_F and the Fermi energy are related by the equation $E_F = \frac{\hbar^2 k_F^2}{2m_0}$, and the radius of the Fermi sphere is expressed as

$$k_F = \frac{2\pi}{a}(\frac{3z}{4\pi})^{1/3}, \tag{4.1}$$

where z is the number of free electrons per atom; for potassium case, z=1. According to the equation above, the Fermi momentum in the monovalent metal is $p_{\text{Fermi}} = 2.137\sqrt{m_0 eV}$ [143]. This is 10% smaller than the distance $\overline{\Gamma N} = 2.437\sqrt{m_0 eV}$, which means that the Fermi sphere is entirely inside the first BZ. The calculated band structure for K, shown in Figure 4.2, clearly indicates that photoemission in the [001], [110] and [111] directions will be associated with the near parabolic Δ_1, Σ_1 and Σ_1 bands, respectively. Further, the potassium Fermi surface

(See Figure 4.3) result obtained by our DFT calculation shows that the Fermi momentum is $2.161\sqrt{m_0 eV}$, which differs from p_{Fermi} by only 1.12%, and that the associated electron effective mass at the Fermi level is within 10% of m_0.

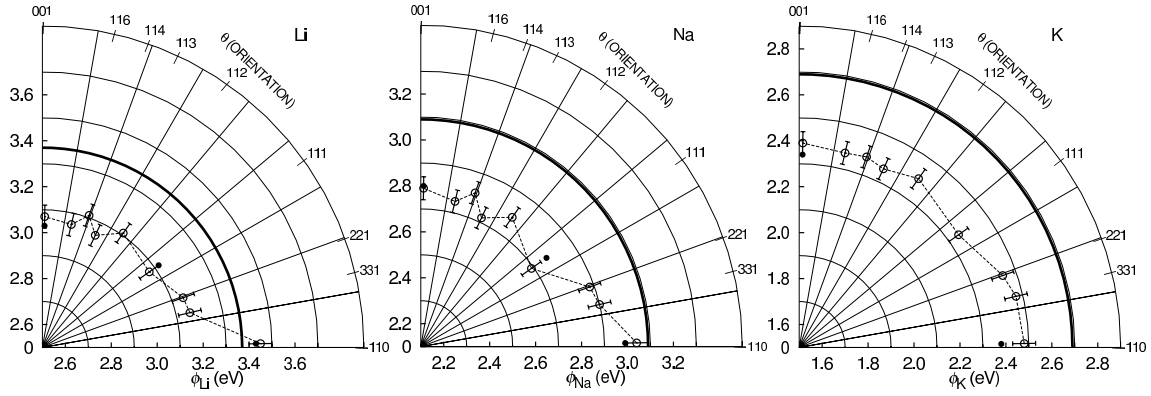

Figure 4.4: Polar plots of the photoelectric work function of alkali metals (Li, Na and K) in [110] zone.

Besides the idealized Fermi surface and band structure, potassium also possesses almost isotropic work function values. The [110] zone polar plots of Figure 4.4 show the DFT calculated work function values for Li, Na, and K evaluated using the thin-slab method (open circles). The solid circles indicate the available experimental results [121, 142, 144–146], which are in good agreement with the DFT calculated results. Potassium has relatively low work functions (generally <3.0 eV) which would allow photoemission using green laser light. Except for the (110) crystal face, the work function deviation among the other faces is within ±0.1 eV for all the metals; that is, the value of the work function does not show strong crystal orientation (ijk) dependence. If the Fermi energy is defined as the zero energy level, for photoemission from

the (001) face of K with an excess energy ΔE=0.3 eV ($\phi_{(001)} = 2.39$ eV, $\hbar\omega = 2.69$ eV), the maximum internal angle for which an electron can escape is $\theta^{in}_{max} = 19.51^o$ (See Equation 2.7). This is consistent with the confined internal photoemission angle $\theta^{in}_{max,DFT} = 19.73^o$ determined from the DFT model as shown in Figure 4.5. As it clearly should, the intrinsic isotropy of alkali metals' band structure, Fermi surface, and work function will result in isotropic photoemission properties.

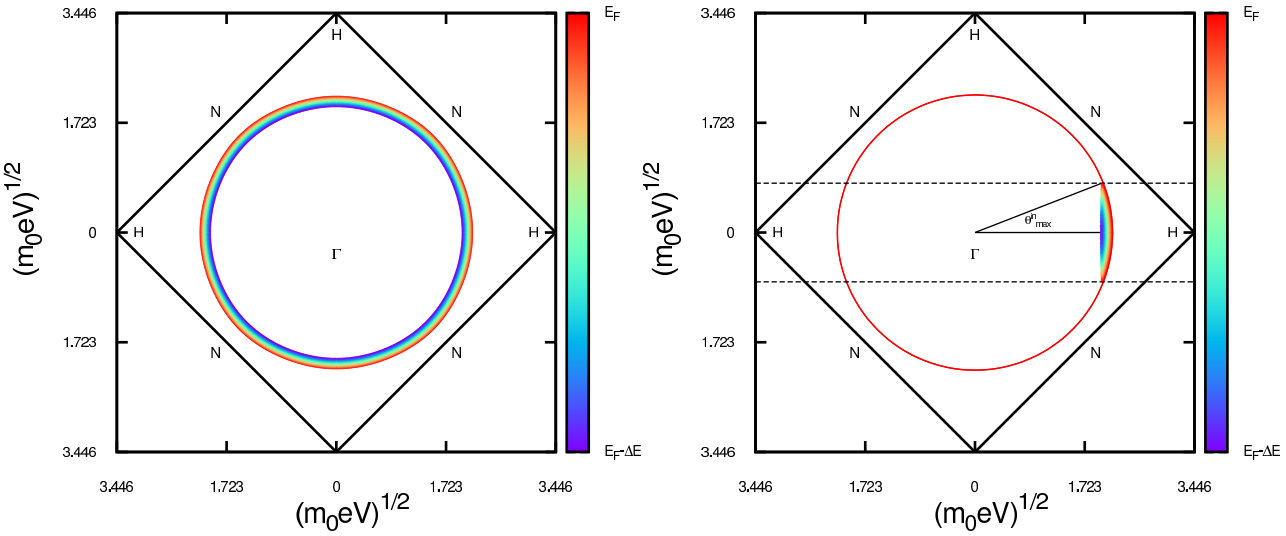

Figure 4.5: Photoemission analysis for emission from the (001) face potassium when $\hbar\omega = 2.69$ eV and $\phi_{(001)} = 2.39$ eV. Cartesian coordinates are in units of $\sqrt{m_0 eV}$. In the left panel, the concentric circles are the energy contours from $E_F - \Delta E$ (blue line) to E_F (red line). In the right panel, the red circle with radius $2.161\sqrt{m_0 eV}$ is photoemission Fermi surface intersection on (001) plane; the 'circular sector' represents the electronic states which may photoemit with $p_{T,max} = 0.775\sqrt{m_0 eV}$.

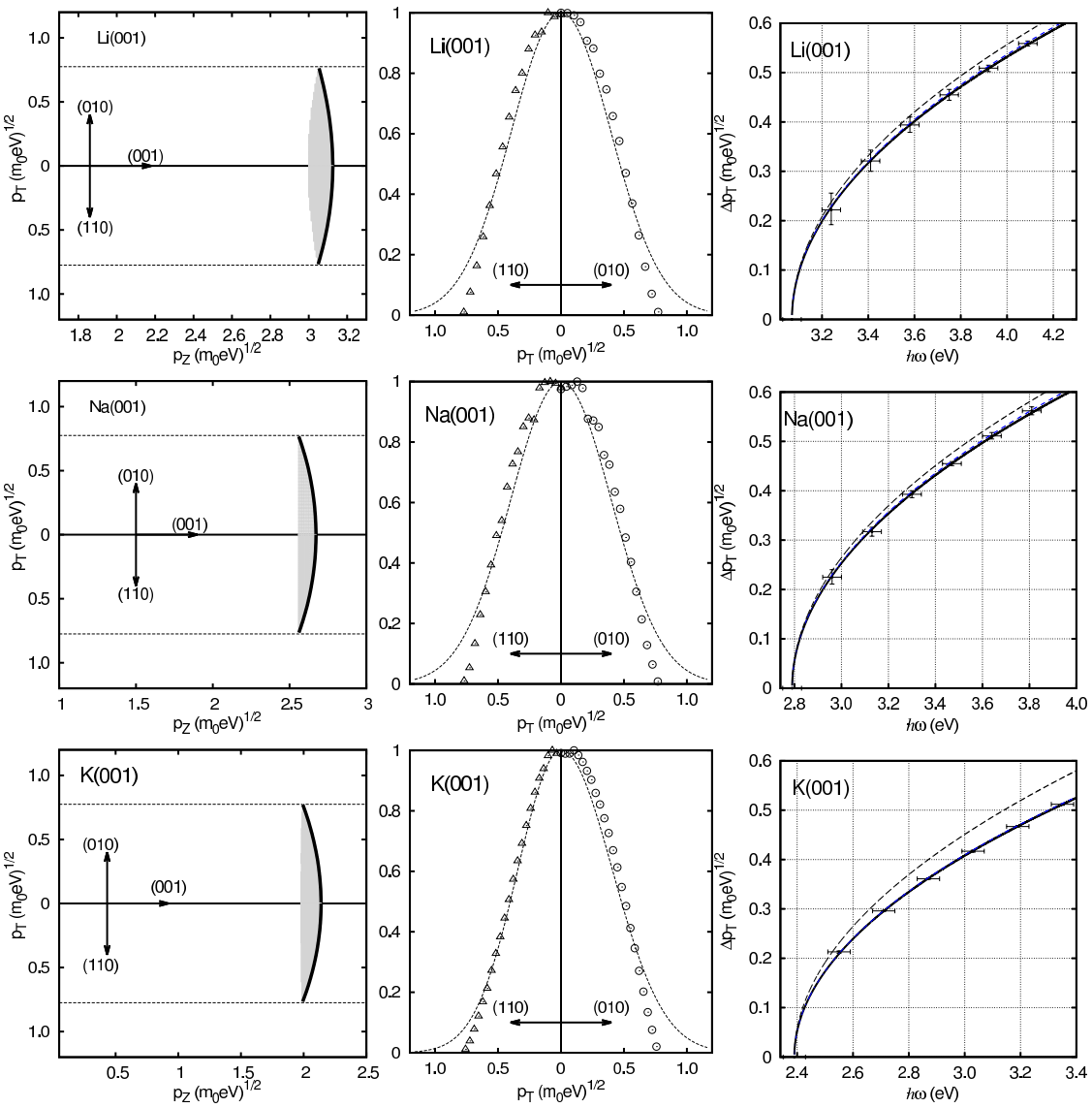

Figure 4.6: Results from the DFT-based photoemission analysis for the (001) face of the alkali metals (Li, Na and K).

The first two columns of Figure 4.6 display the result of the DFT-based photoemission simulation for the (001) face of potassium, sodium and lithium when the incident photon energy is 2.69 eV. The first column shows the electronic states that contribute to the photoemission (shaded region) below the Fermi level (solid line) along two crystal momentum directions ((010) and (110)) transverse to the (001) emission direction. As expected from the near spherical Fermi surface, the emission states are highly symmetric about the emission direction for this metal. The dashed lines in the first column of Figure 4.6 indicate the maximum possible transverse momentum for the photoemitted electrons, which is defined as $p_{T,max} = \sqrt{2m_0\Delta E}$. At this value of the transverse momentum, the transmission efficiency over the photoemission barrier, $T(p_z, p_{z0})$, is zero since $p_{z0} = 0$, so that the transverse momentum distributions of the emitted electrons terminate at $p_{T,max.}$. As the transverse momentum p_T is reduced, more electron states below the Fermi level can contribute to photoemission with those states nearest the Fermi level having the largest local density of states $n(E, \vec{k})$ and the highest values of $T(p_z, p_{z0})$.

Due to the high symmetry of the alkali metals' band structures, the resulting weighted transverse momentum distributions of the photoemitted electrons are also nearly identical along the (010) and (110) crystal momentum directions (second column of Figure 4.6). The spatially-averaged values of the rms transverse momentum Δp_T extracted from these p_T distributions for (001) emission of alkali metals are shown in Table II. The extracted Δp_T are consistent with those predicted by the prior analysis of Dowell and Jensen [52, 53], $\Delta p_T = \sqrt{m_0\Delta E/3}$. This agreement is to be expected since the previous analysis uses spherically symmetric bands with

an electron mass equal to m_0 and a constant density of states: all are good approximations for Li, Na, and K as they have an effective electron mass at the Fermi level within 10% of m_0 [147], and their Fermi energies [127] are sufficiently greater than the employed excess photoemission energy which ensures that the approximation of a constant density of states is reasonable.

TABLE II: Emission properties of alkali metals with ΔE=0.3 eV.

	Δp_{T0} $(\sqrt{m_0 eV})$	$\Delta p_{T,DFT}$ $(\sqrt{m_0 eV})$	A	crystal face
Li	0.316	0.286	0.523	(001)
	0.286	0.316	0.523	(110)
	0.316	0.286	0.523	(111)
Na	0.316	0.286	0.523	(001)
	0.286	0.316	0.523	(110)
	0.316	0.286	0.523	(111)
K	0.316	0.286	0.523	(001)
	0.286	0.316	0.523	(110)
	0.316	0.286	0.523	(111)

The dependence of Δp_T on the incident photon energy $\hbar\omega$ determined by the DFT-based photoemission simulation is also in close agreement with the analysis in Refs. [52] and [68]. The third column of Figure 4.6 shows this dependence using a fit (solid line) to the DFT-derived data points of the form $\Delta p_T = A\sqrt{m_0(\hbar\omega - \phi_{(001)})}$ (dashed line) for (001) emission. The extracted values of A differ from $1/\sqrt{3}$ by only 10%. Both of these evaluations of the rms transverse momentum are, of course, determined in the zero temperature limit; that is, for an electron temperature $T_e \to 0$ so that no electrons occupy states above the Fermi level. In our DFT-based analysis, this restriction may be lifted by the inclusion of the Fermi-Dirac function $f(E) = 1/(1+exp[-(E_F - E)/k_B T_e])$ to describe the occupation of the electronic states around

the Fermi energy E_F, albeit for the band structure evaluated for a 'zero temperature' crystal (i.e., where lattice expansion and vibrations are neglected). The dot-dashed line in third column of Figure 4.6, just above the solid line, shows the fit to the result of calculating $\Delta p_T(\hbar\omega)$ for the (001) face with the DFT-based photoemission simulation when T_e=300K (data points not shown). The increase (or change) in Δp_T is only of the order of 1% in this case since ΔE and E_F are both much greater than $k_B T_e$; that is to say that the additional partially populated states above the Fermi level are a small perturbation in the photoemission simulation. We note that the Boltzmann tail of the Fermi-Dirac distribution will allow photoemission for $\hbar\omega < \phi_{(001)}$ [65], essentially photo-assisted thermionic emission with $\Delta p_T \approx \sqrt{m_0 k_B T_e}$ for T_e=300 K, but this effect is not considered here as the emission efficiency is much reduced. In addition, the DFT-based photoemission analysis as described cannot determine the absolute emission efficiency since the matrix element for photoexcitation into the virtual excited electronic state and electron scattering rates that may limit the lifetime of that emitting state have not been included.

In summary, the DFT-evaluated emission properties of alkali photocathodes are in agreement with prior analytical expressions of Δp_T within a 9% error. In Sections 4.2 and 4.3, I will outline the same photoemission analysis for the single crystal orientation (001) of Group Vb (V, Nb and Ta) and Group VIb (Mo, Cr and W) photocathodes, for which previous analytical method have not provided accurate values for Δp_T.

4.2 Group VIb Photocathodes

Several authors [148–151] have carried out electronic band structure calculations for the Group VIb transition metals. These calculations appear to be reliable since the Fermi surfaces determined from them are supported by measurements [152, 153] on both Tungsten and Molybdenum. Calculations for the $3d$ transition metals and experiments on the high-field galvanomagnetic properties of Niobium and Tantalum [154] suggest that the rigid-band model is reasonable for these metals. If this assumption is made, many of the features of the Group VIb and Vb metals' electron bands can be considered to be similar.

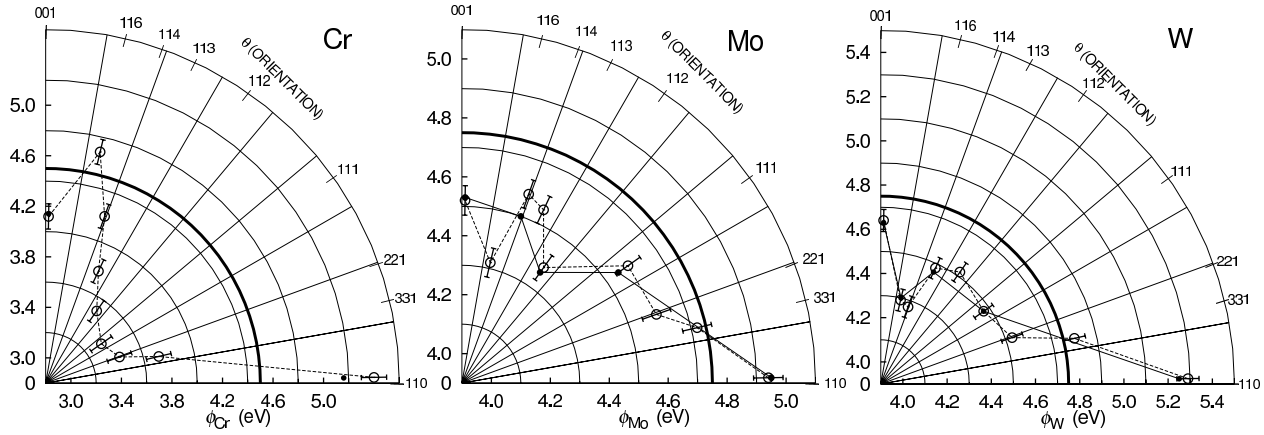

Figure 4.7: Polar plot of Group VIb work function in [110] zone from (001) to the (110) face for the Group VIb metals (Cr, Mo and W): Theoretical thin-slab DFT-based evaluations (open circles); literature values for Cr [155, 156], Mo [125, 157] and W [125, 158] (solid circles); and the 4.75eV UV photon energy (bold solid line).

The Group VIb metals (Cr, Mo, and W) are attractive photocathode materials due to their hardness [159], high melting points [160–162], and relative chemical inertness. Our evaluations of the band structure for these bcc metals, which agree with prior calculations [163–165], reveal

that the Fermi level in these metals crosses several bands: the Δ_2, $\Delta_{2'}$ and Δ_5 bands. As these bands are also somewhat anisotropic in momentum space, as evidenced by the highly distorted Fermi surface, photoemission will be more complex than for potassium. Fortunately, for all three metals, some experimental data is available for the work function anisotropy $\phi(ijk)$ [125, 155, 156, 158, 166–168] to compare with our thin-slab evaluations. Figure 4.7 displays the evaluated work functions (open circles) for different crystal faces in the form of a 'polar plot' from (001) to (110), which includes all major orientations expected on the face of a polycrystalline photocathode, together with prior experimental measurements of $\phi(ijk)$ (solid circles) for Cr [125, 155, 166], Mo [121, 125], and W [125, 158]. Our DFT-based thin-slab evaluations are clearly in good agreement with the literature values within the estimated ± 50 meV uncertainty of the calculations. The data also clearly shows that crystal faces close to the (110) orientation of these bcc metals will not emit electrons under our experimental conditions (See Section 2.3) as $\phi_{(ijk)}$ is greater than the employed 4.75 eV UV laser photon energy (indicated by the bold solid line in Figure 4.7). Nonetheless, for the polycrystalline photocathodes used in our measurements of Δp_T, the generated electron beam should be intrinsically inhomogeneous with microcrystalline faces closer to the (001) direction dominating the emission. Further, for polycrystalline BCC metal surfaces, the (001) crystal face can be expected to be most prevalent [169, 170] and hence likely dominate the photoemission properties; typically, for a mechanically worked, in our case polished BCC metal, the (112) face is the next most frequent covering $\sim$10% of the surface, while the (111) microcrystal faces only cover a few percent [169,170]. Careful analysis of the band structure of the Group VIb metals further supports

the approximation that the (001) crystal face will dominate the photoemission process, since emission from the (111) crystal face involves only one band whereas four sets of electronic states from three bands crossing the Fermi level contribute to photoemission in the (001) direction. The theoretical analysis presented here will therefore be restricted to (001)-face emission.

The results from the DFT-based analysis for photoemission from the (001) faces of Cr, Mo, and W with $\hbar\omega = 4.75$eV are presented in Figure 4.8. The first column for each metal shows the electronic states (shaded regions) below the Fermi level (solid line) that may contribute to photoemission as function of the internal crystal momentum in the (001) direction ($\vec{p_z}$) and two transverse momentum ($\vec{p_T}$) directions along the (100) and (110) crystal directions. Four separate sets of electronic states from the three bands [163–165] that cross the Fermi level contribute to photoemission from the (001) face for all three metals; the 'hole-like' Δ_2 band (negative dispersion) and 'electron-like' $\Delta_{2'}$ band (positive dispersion) electronic states from the Fermi surface 'lens' at low p_Z, and two 'electron-like' states at higher p_Z that are degenerate with the Δ_5 band at p_T=0. In all three cases, the bands are fairly symmetric about the (001) direction, which leads to relatively isotropic transverse momentum distributions (central panel in Figure 4.8), and hence electron beams with uniform intrinsic divergence. The spatially-averaged values of Δp_T extracted from these momentum distributions are listed in Table III together with the values of $\Delta p_{T0} = \sqrt{m_0 \Delta E/3}$ computed using $\phi_{(001)}$ and $\hbar\omega = 4.75$ eV. In all cases, Δp_{T0} is greater than the results of the DFT photoemission simulation ($\Delta p_{T,DFT}$), and the latter are in better agreement with our experimental measurements of $\Delta p_{T,expt}$ for poly-

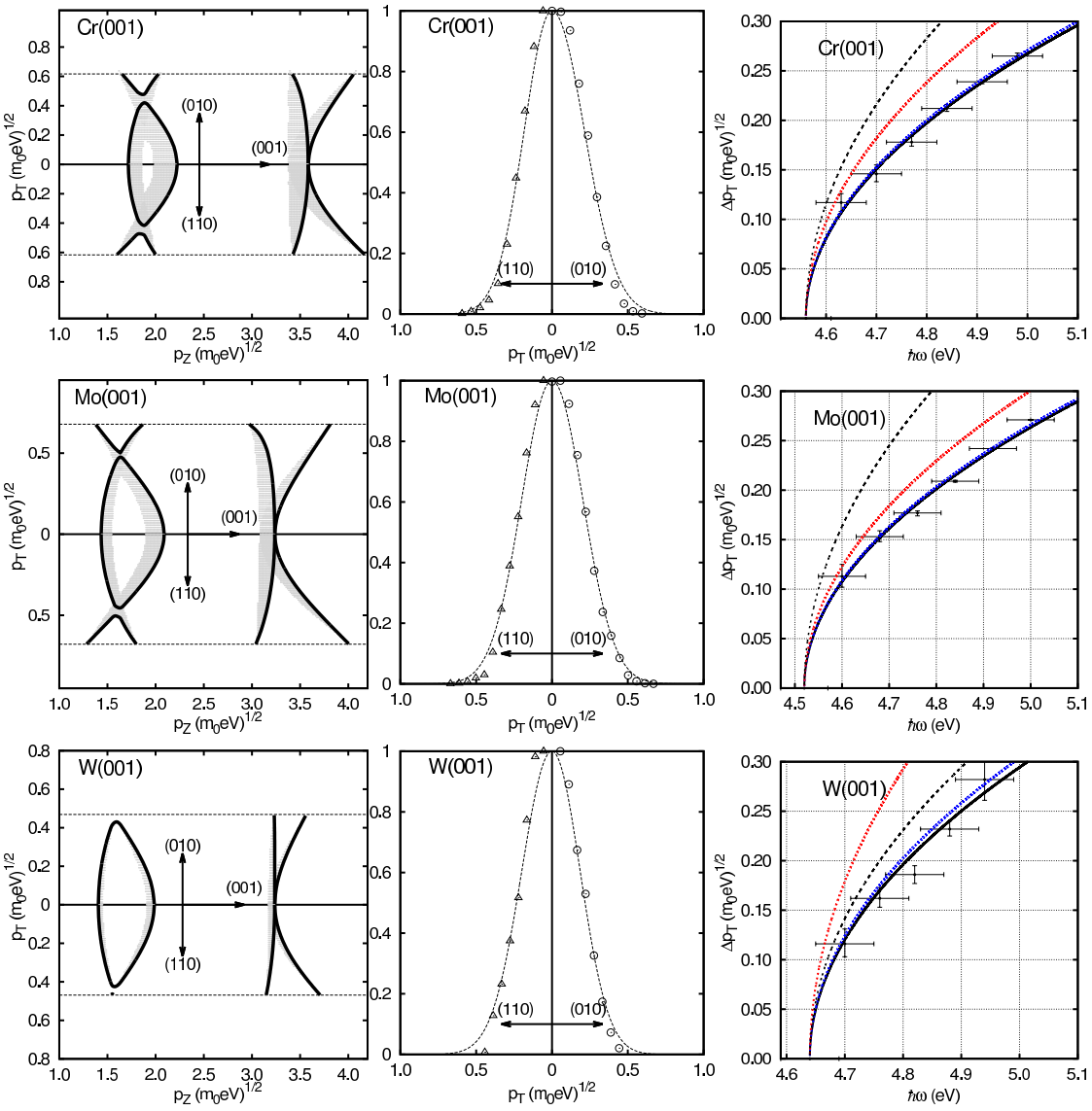

Figure 4.8: Excess energy contours, transverse momentum distributions and the $\Delta p_T(\hbar\omega)$ plots for Cr, Mo and W in (001) crystal orientation. The results from the DFT-based photoemission analysis for the (001) face of the Group VIb metals (Cr, Mo and W). Left panel: Crystal momentum map of the electronic states (shaded regions) below the Fermi level (solid line) that may photoemit within $p_{T,max} = \sqrt{m_0 \Delta E}$ (dashed lines) for the transverse (010) and (110) crystal directions. Center panel: Transverse momentum distribution of the photoemitted electrons in the (010) and (110) directions (Gaussian fits are guides to the eye). Right panel: Incident photon energy dependence of the rms transverse momentum Δp_T for electron temperatures $T_e \to 0$ (data points with solid line fit); $\Delta p_T = A\sqrt{m_0 \Delta E}$, T_e =300K and the melting points of each metal (dot-dashed lines), together with the expected form of $\Delta p_T = \sqrt{(\hbar\omega - \phi)/3}$ (black dashed line).

crystalline Group VIb photocathodes. Comparison with the K(001) calculation (Figure 4.6), which was consistent with Δp_{T0}, reveals that the reduced rms transverse momentum for Cr, Mo, and W (001)-face emission is due to the Group VIb metals' band structure; specifically, the involvement of both 'electron-like' and 'hole-like' electronic states and the generally stronger band dispersions. The fact that $\Delta p_{T,DFT}$ is smallest for W(001) emission is fundamentally related to the restriction placed on $p_{T,max.} = \sqrt{2m_0(\hbar\omega - \phi_{(001)})}$ (dashed lines in the first column of Figure 4.8) by the higher value of $\phi_{(001)}$ for Tungsten. On the other hand, the ∼15% difference in $\Delta p_{T,DFT}$ for Cr(001) and Mo(001) emission, which have almost the same work function, is evidently related to a higher relative emission local state density (shaded regions in the first panel of Figure 4.8) in Cr at low values of p_T. The resultant 40% reduction in the rms transverse momentum over Δp_{T0} for Cr(001) equates to a reduction in the rms solid angle of divergence (and hence brightness enhancement) for an electron beam by a factor of 2.8.

TABLE III: Emission properties of Group VIb metals.

Metal	$\phi_{(001,DFT)}$ (eV)	$\Delta p_{T,DFT}$ $(\sqrt{m_0 eV})$	Δp_{T0} $(\sqrt{m_0 eV})$	A	$\Delta p_{T,expt}$ [171] $(\sqrt{m_0 eV})$
Cr	4.56(±0.05)	0.168(±0.020)	0.252(±0.03)	0.403	0.155(±0.005)
Mo	4.52(±0.05)	0.177(±0.019)	0.276(±0.03)	0.380	0.200(±0.005)
W	4.64(±0.05)	0.160(±0.034)	0.191(±0.03)	0.491	0.150(±0.005)

The third column in Figure 4.8 shows the theoretical dependence of Δp_T on the incident photon energy $\hbar\omega$ for $T_e \to 0$ (data points) together with the form predicted by $\Delta p_{T0} = \sqrt{m_0(\hbar\omega - \phi_{(001)})/3}$ (dashed line) [52, 68]. For all three metals, the theoretical data is a good

fit to $\Delta p_T = A\sqrt{m_0(\hbar\omega - \phi_{(001)})}$ (solid line), giving $A_{Cr(001)} = 0.34$, $A_{Mo(001)} = 0.47$, and $A_{W(001)} = 0.46$ — values significantly less than 0.577. Also shown in the third column of Figure 4.8 is the fitted form of $\Delta p_T(\hbar\omega)$ when T_e equals 300K and the melting point of each metal (dot-dashed lines, data points not shown) evaluated using the Fermi-Dirac function to describe the occupation of the electronic states generated by the zero temperature DFT band structure calculations. As for (001)-face alkali metal photoemission (Figure 4.6), the evaluated $\Delta p_T(\hbar\omega)$ at $T_e = 300$ K is indistinguishable from that at 0 K within the uncertainty of the DFT-based photoemission simulations. The rms transverse momentum of the emitted electrons does increase for electron temperatures at the melting points of the Group VIb metals with, as would be expected, the increase in Δp_T being most dramatic for W which has the lowest excess photoemission energy, $\Delta E = 0.12$ eV, and the highest melting point at 3680K ($k_B T_e = 0.31$ eV). This increase is, of course, primarily due to the temperature-dependent partial population of the states above the Fermi level which can lead to significant emission from states with transverse momenta beyond $p_{T,max}$.

4.3 Group Vb Photocathodes

Although in general somewhat more reactive than the Group VIb metals [172], the Group Vb metals (V, Nb, and Ta) are also attractive photocathode materials due again to their hardness [159] and high melting points [173–175]. Moreover, as shown in Figure 4.9, they have lower polycrystalline work functions than their Group VIb counterparts, which translates to a higher photoemission quantum efficiency [52, 176]; for polycrystalline photocathodes at $\hbar\omega$=4.75eV,

it has been observed that the Group Vb metals have an efficiency a factor of ∼2 greater than the Group VIb metals [50]. This is the primary reason for the use of Ta photocathodes in DTEMs [177, 178]. It is also noteworthy that, unlike the Group VIb elements, V, Nb, and Ta are all superconducting and so are directly compatible with superconducting laser-driven guns [179, 180].

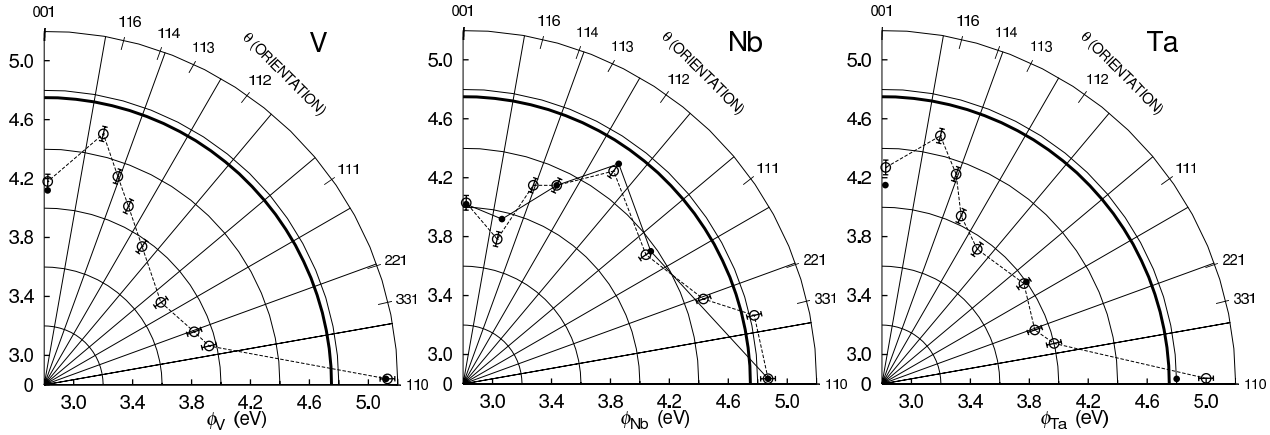

Figure 4.9: Polar plot of V, Nb and Ta work function in [110] zone.

Our band structure calculations for the BCC Group Vb elements are again in good agreement with prior evaluations [125, 156, 167, 168] and show that the Fermi level crosses only the Δ_2 band in these metals. This band corresponds to the central 'jack' of the Fermi surface around the Γ point of the band structure [148, 181, 182] and is therefore quite anisotropic. Our evaluations of the work function anisotropy $\phi_{(ijk)}$ for the Group Vb metals using the thin-slab method [183] are also in agreement with available data within the estimated ±50 meV uncertainty of the theoretical calculations; as shown in Figure 4.9, which displays the evaluated

work functions (open circles) for different crystal faces from (001) to (110) together with the prior experimental measurements of $\phi_{(ijk)}$ (solid circles) for V [125,167,168], Nb [125,156], and Ta [125]. As with the Group Vb elements, $\phi_{(110)}$ is greater than our 4.75 eV photon energy (bold solid line) and their BCC crystal structure means that the (001) microcrystalline face will again likely be the most prevalent [169,170] and hence dominate the photoemission properties of polycrystalline Group Vb photocathodes.

Figure 4.10 displays the results from the DFT-based analysis for photoemission from the (001) faces of V, Nb, and Ta when $\hbar\omega$=4.75 eV. The crystal momentum depiction of the electronic states capable of photoemission (shaded regions) below the Fermi level (solid line) in the left panel for each element clearly shows that emission is only from the 'hole-like' states associated with the 'jack-shaped' Fermi surface centered on the Γ-point of the Brillouin zone. With the exception of Nb at low values of p_z, where band dispersion rather than $p_{T,max.} = (2m_0\Delta E)^{1/2}$ (dashed line) limits emission in the (110) direction, the emitting states are nonetheless again quite symmetric about the primary (001) crystal direction. As a result, the transverse momentum distributions for the emitted electrons from all three Group Vb metals (second column in Figure 4.10) are very symmetric — the asymmetry in the emission states of Nb not being a significant factor as electronic states with low values of p_z and high values of p_T have a substantially lower photoemission probability than the other states. This is especially true for photoemission from this 'hole-like' state since, unlike 'electron-like' states with positive dispersion,

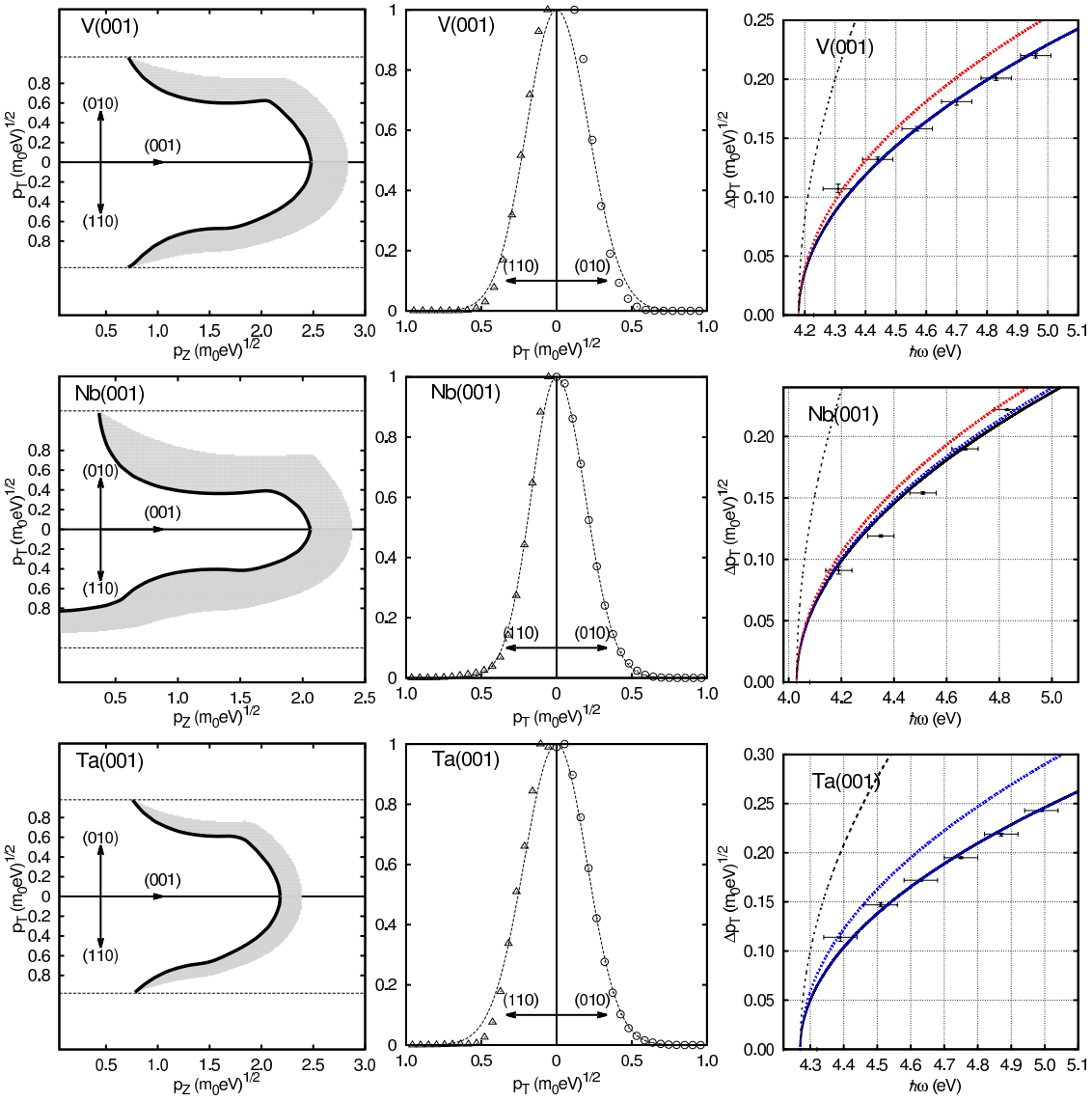

Figure 4.10: Excess energy contours, transverse momentum distributions and the $\Delta p_T(\hbar\omega)$ plots for V, Nb and Ta in (001) crystal orientation. The results from the DFT-based photoemission analysis for the (001) face of the Group VIb metals (Cr, Mo and W). Left panel: Crystal momentum map of the electronic states (shaded regions) below the Fermi level (solid line) that may photoemit within $p_{T,max} = \sqrt{m_0 \Delta E}$ (dashed lines) for the transverse (010) and (110) crystal directions. Center panel: Transverse momentum distribution of the photoemitted electrons in the (010) and (110) directions (Gaussian fits are guides to the eye). Right panel: Incident photon energy dependence of the rms transverse momentum Δp_T for electron temperatures $T_e \to 0$ (data points with solid line fit); $\Delta p_T = A\sqrt{m_0 \Delta E}$, T_e =300K and the melting points of each metal (dot-dashed lines), together with the expected form of $\Delta p_T = \sqrt{(\hbar\omega - \phi)/3}$ (black dashed line).

higher transverse crystal momenta mean lower energy. The net result, as shown in Table IV, is also a much lower spatially–averaged rms transverse momentum for emission from the (001) face of the Group Vb metals than would be expected from $\Delta p_{T0} = \sqrt{m_0 \Delta E/3}$ [52,68] evaluated using the listed values of $\phi_{(001)}$. The extracted values of $\Delta p_{T,DFT}$ are, however, close to our experimental measurements of Δp_T for polycrystalline Group Vb photocathodes.

TABLE IV: Emission properties of Group Vb metals.

Metal	$\phi_{(001,DFT)}$ (eV) (eV)	Δp_{T0} ($\sqrt{m_0 eV}$)	$\Delta p_{T,DFT}$ ($\sqrt{m_0 eV}$)	A	$\Delta p_{T,expt}$ [171] ($\sqrt{m_0 eV}$)
V	4.18(±0.05)	0.440±0.02	0.191±0.003	0.253	0.183(±0.005)
Nb	4.03(±0.05)	0.490±0.02	0.204±0.002	0.240	0.185(±0.005)
Ta	4.27(±0.05)	0.400±0.02	0.200±0.002	0.288	0.185(±0.005)

The third column for each element in Figure 4.10 again shows the theoretical dependence of Δp_T on the incident photon energy $\hbar\omega$ for $T_e \rightarrow 0$ (data points) together with the form predicted by $\Delta p_{T0} = \sqrt{m_0 \Delta E/3}$ [52, 68] (dashed line). Fitting $\Delta p_T = A\sqrt{m_0(\hbar\omega - \phi)}$ to the theoretical data (solid line) gives $A_{V(001)} = 0.28$, $A_{Nb(001)} = 0.23$, and $A_{Ta(001)} = 0.26$ – values less than half of 0.577. This means that the rms solid angle of emission from the (001) crystal face of Group Vb metal photocathodes will be 4-5x less than expected. Surprisingly, and very unlike their Group VIb counterparts (Figure 4.8), when T_e equals 300 K or even the melting point of each metal (dot-dashed lines in the right panel of Figure 4.10; data points not shown) the values of $\Delta p_T(\hbar\omega)$ evaluated using the DFT-based analysis are not increased appreciably. This interesting result is fundamentally related to the dispersion of the emitting

electronic state. For this 'hole-like' state, increasing T_e serves to partially populate states above the Fermi level with generally lower values of Δp_T (first panel of Figure 4.8), thereby leaving Δp_T relatively unchanged. The small $\sim$10% increase in $\Delta p_{T,DFT}(\hbar\omega)$ evaluated for V(001) and Ta(001) emission at their melting point temperatures is primarily due to contributions from energetic partially populated states above the Fermi level around $p_{T,max.}$. Thus, photoemission from the Group Vb metals is significantly less temperature sensitive than from the Group VIb metals.

4.4 BCC Alloy Photocathodes

The above analysis of the emission properties of the BCC transition metals implies a strong dependence of their electronic band structure (Fermi surface) on the Δp_T. The Fermi surface of the Group Vb transition metals and Group VIb transition metals are similar, especially along major crystal orientations such as (001) and (111), and it is the Fermi level position that fundamentally determines the value of Δp_T. This is because the position of Fermi level not only affects the shape of photoemitting energy contours but also the LDOS associated with photoemission. To tentatively realize Δp_T manipulation through positioning E_F, I employ the Mo_xNb_{1-x} alloy system [151, 184] which allows a continuous shifting of Fermi level by tuning the composition x that then changes the photoemitting states of the alloy system generating a relationship between Δp_T and x. This section will present this extensive investigation of the Mo_xNb_{1-x} alloy system to demonstrate one method of photocathode design aimed at discov-

ering photocathode materials exhibiting low Δp_T emission values.

4.4.1 Mo_xNb_{1-x} Alloy

There have been a number of studies on BCC alloys [151,184–186]. These previous research work has been dedicated to understand the electronic properties of the binary BCC Mo–Nb alloy system, which forms a continuous BCC solid solution. It is well known that these alloys not only have temperature insensitive elastic constants, chemical inertness, and no intermediate phases, but also are stable against high temperatures and pressures over the whole composition range [151,185].

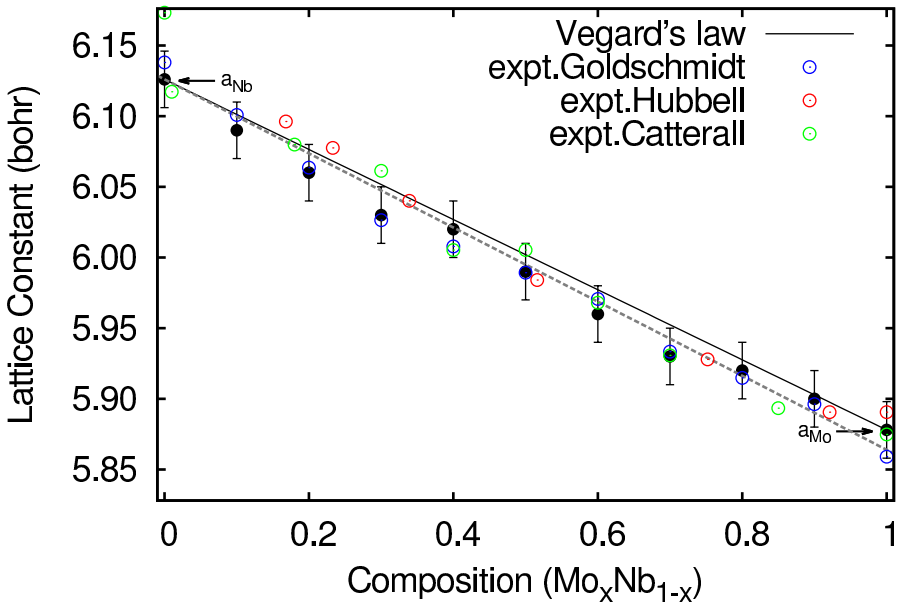

Figure 4.11: Mo_xNb_{1-x} bimetal's lattice constant as a function of x. Solid line is the Vegard's law, dashed line is the least square fit of DFT calculated lattice constant, which differs from Vegard's law by only 5.7%.

The virtual crystal approximation (VCA) construction method [187] is employed for the combination of two metals' pseudopotentials according to the composition of Mo_xNb_{1-x}, an alloy made of Mo of fraction x and Nb molecules of fraction 1-x. As the pseudopotential methods have matured, the correct or optimal way to implement the VCA has become less obvious. For the case of LDA, using the USPP generated by Vanderbilt [103], the implementation is straightforward: the potential of the virtual system made from the Mo_xNb_{1-x} alloy is generated simply by compositionally averaging the potentials of the Mo and Nb compounds. It is important to emphasize that since we construct a single potential at the atomic level, the use of our VCA pseudopotentials in solid state calculations requires no additional computational effort. In this Averaged Descreened Potentials VCA (ADPVCA) approach [187], two independent atomic pseudopotentials V_{ps}^{Mo} and V_{ps}^{Nb} are constructed. These descreened potentials are then averaged according to

$$V_{ps}^{\mathrm{ADPVCA}} = (1-x)V_{ps}^{\mathrm{Nb}} + xV_{ps}^{\mathrm{Mo}}. \tag{4.2}$$

For creating useful 'mixed' pseudopotentials in the quantum-ESPRESSO computational routine, the two original potential files have to be compatible and be the same type of pseudopotential — an requirement that is met by using the USPP of D.Vanderbilt [188]. After generating the new pseudopotential for Mo_xNb_{1-x} by VCA, we run the optimal lattice constant test for Mo_xNb_{1-x} with an x step of 0.1. Then, band calculations are performed to determine a con-

tinuous band structure.

The calculated lattice constant results as shown in Figure 4.11 agree with Vegard's law [189] $a(x) = xa_{\mathrm{Mo}} + (1-x)a_{\mathrm{Nb}}$. The experimental measurements by Goldschmidt and Brand [190] and Catterall, Barker [191] and Hubbell [185] are also included for comparison; these experimental measurements have been conducted over the whole range of compositions (0-100 atomic % Mo) in $\mathrm{Mo}_x\mathrm{Nb}_{1-x}$ alloys. My lattice constant calculations (black solid circles) are in good agreement with experimental values; all the data points show only a small deviation from the Vegards law, i.e., $a_{A_{1-x}B_x} = (1-x)a_A + xa_B$, where $a_{A_{1-x}B_x}$, a_A and a_B are the equilibrium lattice parameters of alloy $A_{1-x}B_x$ and the constituent pure elements A and B, respectively. If necessary, a configuration average test is performed in order to ensure that the VCA is realistic for the real disordered system.

Generally, the energy dispersions of $\mathrm{Mo}_x\mathrm{Nb}_{1-x}$ have great similarities and appear to be intermediate between those of the two pure $4d$ metals; not only are the dispersion shape of their electronic bands similar to that of pure Mo and Nb metals, but also their Fermi level is located between the two elemental metal's Fermi level. The result of band structure calculation is shown in Figure 4.12, with the Fermi level of Mo, Nb, and the $\mathrm{Mo}_{0.5}\mathrm{Nb}_{0.5}$ alloy indicated. The Fermi levels are calculated assuming all the electrons outside the closed shell to be valence electrons. As a result, the metal with the most valence electrons, Mo, has its Fermi level above that with the least, Nb, with the alloy between the two. My DFT calculated band structure of

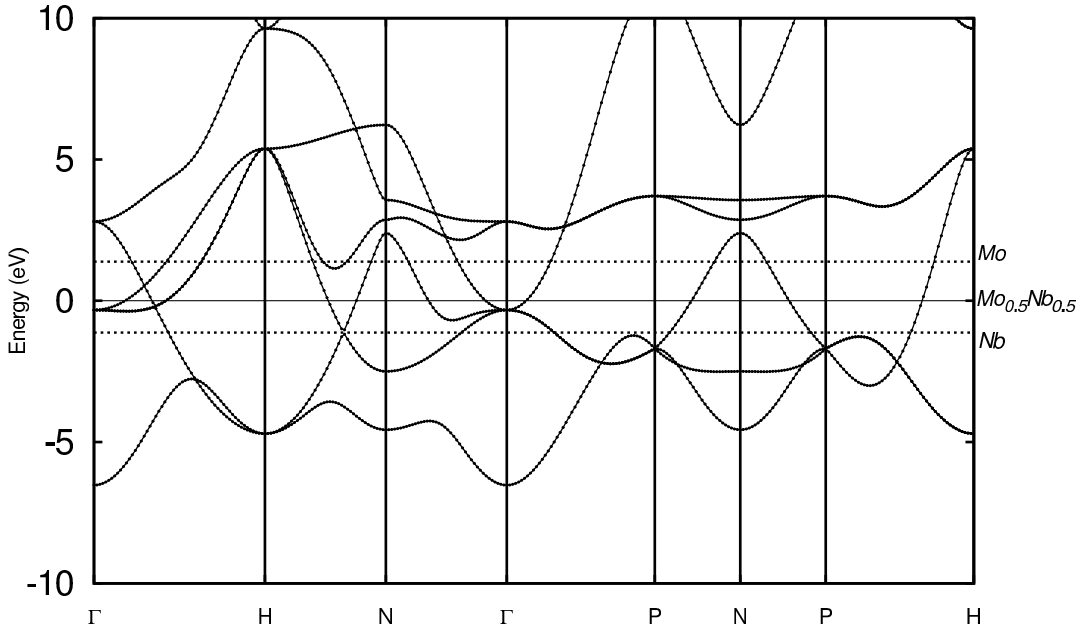

Figure 4.12: Calculated Mo_xNb_{1-x} bimetal's band structure along high symmetry points and lines. The Fermi level of $Mo_{0.5}Nb_{0.5}$ sets the zero point energy by solid line; the Fermi levels of Niobium and Molybdenum are indicated by the dot dashed lines.

$Mo_{0.5}Nb_{0.5}$ alloy is in a good agreement with previous calculation [151].

The work function of the $Mo_xNb_{1-x}(001)$ can be approximately expressed as [186]

$$\begin{aligned}\phi_{\text{Alloy}} &= x\phi_{\text{Mo}} + (1-x)\phi_{\text{Nb}} + x(1-x)[\frac{(\phi_{\text{Mo}} - \phi_{\text{Nb}})(\frac{\rho_{\text{Mo}}}{\rho_{\text{Nb}}} - 1)}{x\frac{\rho_{\text{Mo}}}{\rho_{\text{Nb}}} + (1-x)}] \\ &\approx x\phi_{\text{Mo}} + (1-x)\phi_{\text{Nb}},\end{aligned} \tag{4.3}$$

where ϕ_{Mo} and ϕ_{Nb} are the pure constituent work functions of Mo and Nb, receptively, and ρ_{Mo} and ρ_{Nb} are the pure constituent total densities of states. For the (001) orientation,

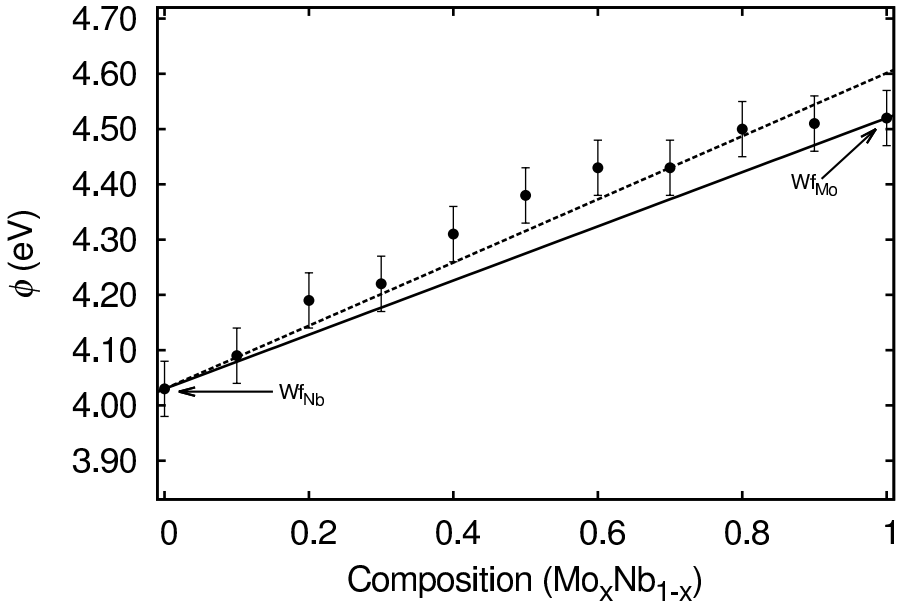

Figure 4.13: Mo_xNb_{1-x} bimetal's work function of (001) face as a function of x. Solid line is the linear relationship of Equation 4.3, and dashed line is the least squares fit of thin-slab method calculated work function, which differs from $\phi^{\text{Mo}}_{(001)}x + (1-x)\phi^{\text{Nb}}_{(001)}$ by 16%.

$\rho_{\text{Nb}} \approx \rho_{\text{Mo}}$ [186, 192]. The result of the thin-slab evaluated work function is shown in Figure 4.13. It can be seen that the work functions of the Mo_xNb_{1-x} alloy system generally follow a linear function of composition x indicated by Equation 4.3, which is in solid line and has slope of 0.45. The dot dashed line is the linear fit of the DFT calculated work functions of the Mo_xNb_{1-x} alloy system, and its slop is 0.52. The 16% difference implies that Equation 4.3 is a rough estimation for the relationship between composition x and the work function, and the discrepancy could be explained by a more sophisticated estimation — the image force model [193].

4.4.2 Photocathode Design

For photoemission from the (001) crystal face of Mo_xNb_{1-x} system with 4.75 eV photon energy, the (110) and (010) sections of the resulting photoemitting contours of $Mo_xNb_{1-x}(001)$ in the repeated reduced zone scheme are shown in Figure 4.14. It is clear that there is a continuous evolution of the emitting states (shaded regions) as the composition x changes from 0.1 (nearly 'Nb-like' as in Figure 4.10) to 0.9 (nearly 'Mo-like' as in Figure 4.8) due to the continous variation of $\phi_{(001)}$ and E_F with x. When x $\leq$ 0.2, the crystal momentum depiction of the electronic states capable of photoemission (shaded regions) below the Fermi level (solid line) clearly shows that the emission is only from the 'hole-like' states associated with the 'Nb-like' Fermi surface. When 0.3 $\leq$ x $\leq$ 0.6, the effect of the 'Mo-like' Fermi surface becomes cause so that the emission is from both the 'hole-like' states associated with 'Nb-like' Fermi surface and the 'electron-hole' mixed states associated with 'Mo-like' Fermi surface. When 0.7 $\leq$ x $\leq$ 0.9, the effect of 'Mo-like' Fermi surface dominates the photoemitting electronic states so that Mo_xNb_{1-x} has 'Mo-like' photoemitting energy state contours. It is important to note that the slightly asymmetry in Mo_xNb_{1-x} emission states results from the asymmetry in the emission states of Nb, and it is not a significant factor of the transverse momentum distribution since electron states with low value of p_z and high values of p_T have lower photoemission probability than the other states.

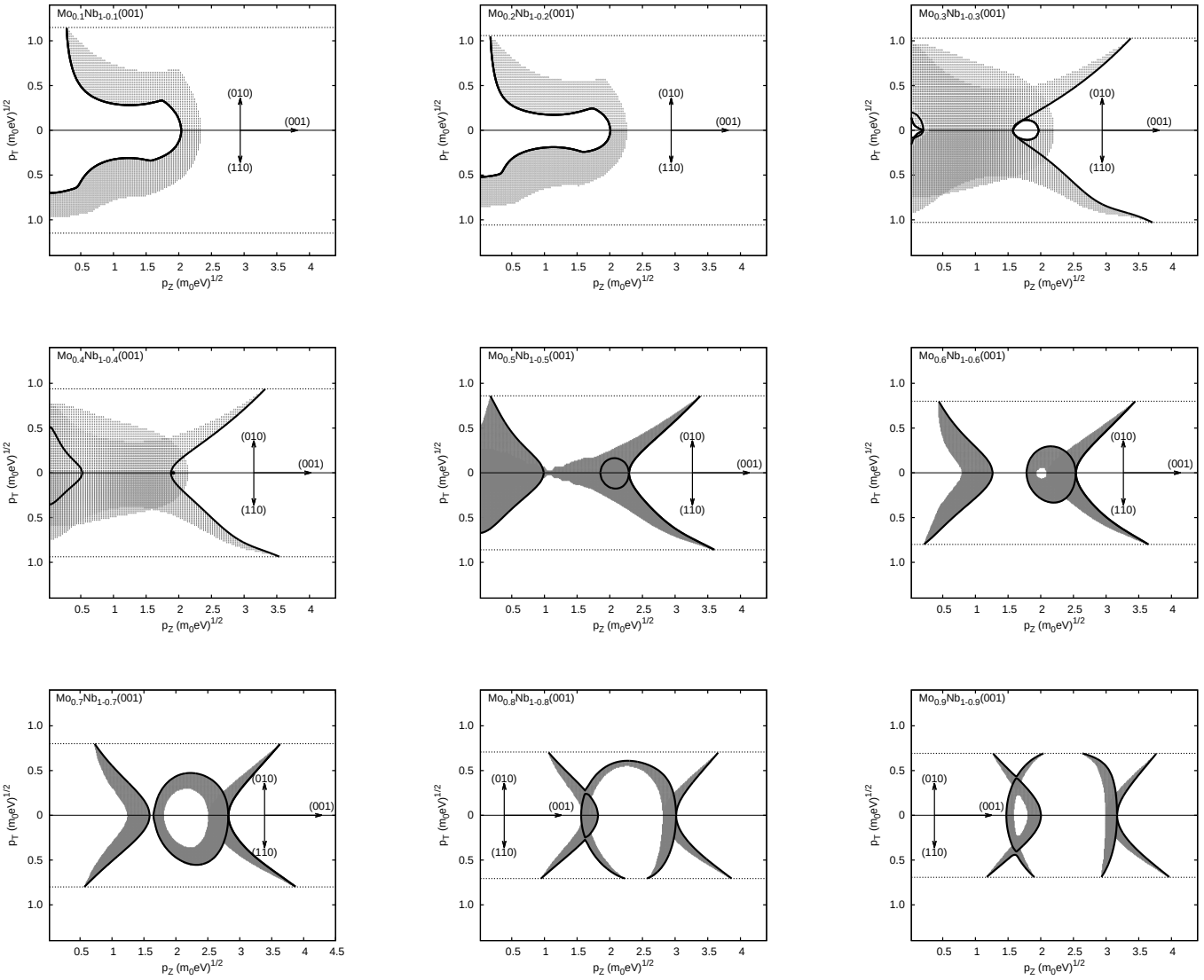

Figure 4.14: Photoemitting energy contours of Mo_xNb_{1-x} alloys as the composition factor x changes from 0.1 to 0.9 in steps of 0.1. The electron states (shaded regions) below the Fermi level (solid lines) that may photoemit with in $p_{T,max} = \sqrt{m_0 \Delta E}$ (dashed lines) for the transverse (010) and (110) crystal directions.

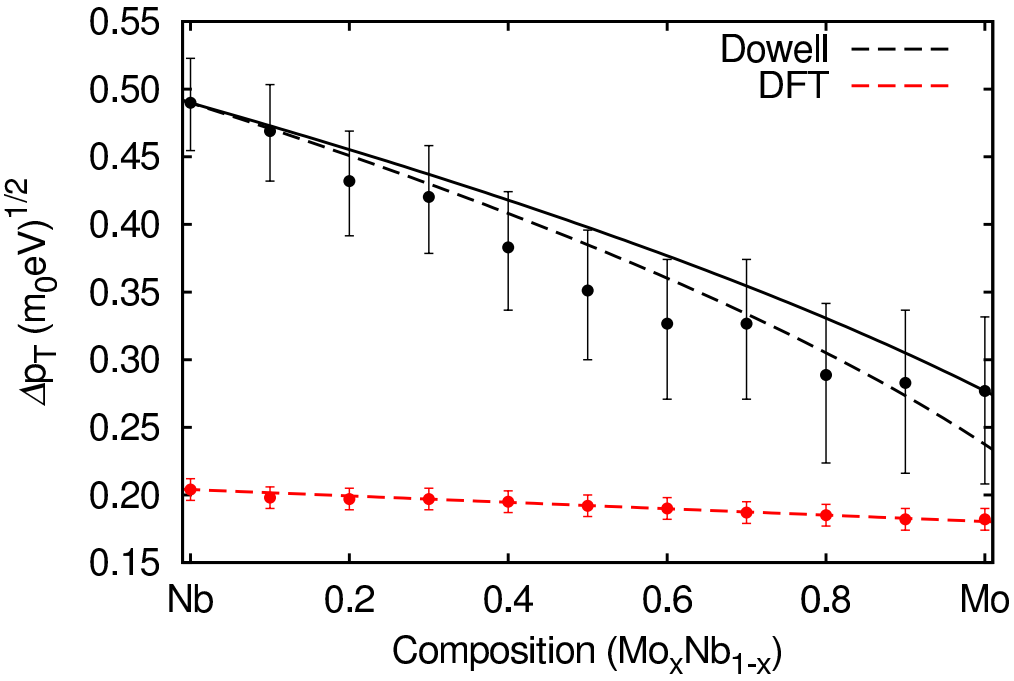

Figure 4.15: Δp_{T0} and $\Delta p_{T,\mathrm{DFT}}$ values as a function of composition x. The dashed black and red lines are the theoretical curve by Equation 4.5 and Equation 4.4, respectively. The solid black dots are the theoretical calculated Δp_{T0} by $\Delta p_{T0} = \sqrt{m_0(\hbar\omega - \phi)/3}$ [52, 53] using DFT calculated $\mathrm{Mo}_x\mathrm{Nb}_{1-x}(001)$ work functions. The solid black line fit is a guide to the eye. The red dots are the DFT calculated $\Delta p_{T,\mathrm{DFT}}$.

Based on the photoemission model for BCC elemental photocathodes, the DFT evaluated values of $\Delta p_{T,\mathrm{DFT}}$ at $\hbar\omega = 4.75$ eV with respect to the composition x are shown in Figure 4.15 using red dots. As expected, the $\Delta p_{T,\mathrm{DFT}}$ values are decreasing from $0.204\sqrt{m_0 eV}$ to $0.177\sqrt{m_0 eV}$ as the composition x increases, the error bars come from the ± 0.05eV work function uncertainty, which generates $\pm 0.004\sqrt{m_0 eV}$ uncertainty in $\Delta p_{T,\mathrm{DFT}}$. A linear fit of

$\Delta p_{T,\mathrm{DFT}}$ values is in red dashed line, which has a slope of 0.027. Therefore, the DFT-based analysis of the $\Delta p_T(x)$ for the $\mathrm{Mo}_x\mathrm{Nb}_{1-x}$ alloy can be written as

$$\Delta p_{T,\mathrm{DFT}}(x) = \Delta p^{\mathrm{Mo}}_{T,(001)} x + \Delta p^{\mathrm{Nb}}_{T,(001)}(1-x), \tag{4.4}$$

where $\Delta p^{\mathrm{Mo}}_{T,(001)}$ and $\Delta p^{\mathrm{Nb}}_{T,(001)}$ are the rms transverse momentum values of pure Mo(001) and Nb(001), respectively. As the the alloy composition factor x changes from 0 to 1, the Δp_T of $\mathrm{Mo}_x\mathrm{Nb}_{1-x}$ continuously approaches the Δp_T of Mo, which indicates a continuous Δp_T of such Bi-metals. The slope of such monotonical increasement as a function of x and is proportional to $\Delta p^{\mathrm{Mo}}_{T,(001)} - \Delta p^{\mathrm{Nb}}_{T,(001)}$. Despite excess energy change of a factor of $\sim$2 from Nb to Mo, the $\Delta p_{T,\mathrm{DFT}}(x)$ values have little change — only $0.027\sqrt{m_0 e\overline{V}}$, which is due to the 'smooth' transition from the 'hole-like' band (Δ_2) in Nb to the 'electron-like' and 'hole-like' bands (Δ_2, $\Delta_{2'}$ and Δ_5) in Mo as shown in Figure 4.14. Similarly, combining Dowell's theory [52, 53] and Vegard's law (Equation 4.3), the expected square root relationship between Δp_{T0} and x can be expressed by

$$\Delta p_{T0}(x) = \sqrt{\frac{m_0[\hbar\omega - \phi_{\mathrm{Mo}(001)} x - \phi_{\mathrm{Nb}(001)}(1-x)]}{3}}. \tag{4.5}$$

This square root dependence is plotted by black dashed line in Figure 4.14 using the DFT calculated Mo(001) and Nb(001) work functions. The black dots are the theoretical evaluated $\Delta p_{T,0}$ by Equation 4.5 using DFT calculated work functions for $\mathrm{Mo}_x\mathrm{Nb}_{1-x}(001)$. The error bars again correspond to the DFT evaluated $\pm$0.05eV work function uncertainty. The $\Delta p_{T0}(x)$ values are generally a factor of 2.0$\sim$2.5 greater than the $\Delta p_{T,\mathrm{DFT}}(x)$ values. This interesting

result is fundamentally consistent with the the ratio of $1/\sqrt{3}$ to the fitting A values for Nb and Mo (See Table IV and Table III).

In addition, the recent solenoid scan measurement [50] and the monotonic variation of Mo_xNb_{1-x}'s $\Delta p_{T,\mathrm{DFT}}$ shown in Figure 4.15 indicate that, among Group Vb and Group Vb metals, Nb obtains the best QE (η_{PE}) as well as the lowest Δp_T. These parameters together with Equation 2.24 may help us qualitatively evaluate the the brightness of a photocathode, which can be expressed as

$$B \sim \frac{\eta_{PE}}{(\Delta p_T)^2}. \tag{4.6}$$

According to the the above figure of merit, the brightness is largest for Vb metals, especially Nb. Also it is clear that the drawback of choosing Mo_xNb_{1-x} alloy photocathodes is that the Mo component in the Mo_xNb_{1-x} alloy system has low QE and relatively high Δp_T compared with Nb. In addition, Group Vb photocathodes are preferred due to T_e insensitive resulting from their strong inward bending Δ_2 band. Therefore there is no read gain for high brightness for the Mo_xNb_{1-x} alloys.

CHAPTER 5

FACE-CENTERED CUBIC METAL PHOTOCATHODES

In Chapter 3, the FCC metal Ag has been used as the exemplar to illustrate the DFT-based photoemission model. FCC is an important crystal structure, and there are ten elemental FCC metals (Al, Ag, Au, Ca, Cu, Pb, Pd, Pt, Rh, and Sr) that have this structure. Three of them could be used as photocathodes (Au, Rh, Pt, and Pd have very high work functions; Ca and Sr are very reactive). Au has high work function, but it will be discussed for the sake of the completeness of noble metals' photoemission investigation. In this chapter, I will apply the photoemission model to investigate the four remaining FCC photocathodes; two noble metals (Cu and Au) and two p-block metals (Al and Pb). Aside from the fact that the direct photoemission is dominant for most FCC photocathodes, photoemission from a surface state has also been observed for the (111)-face of noble metals [194–198]. The optical properties of the (111) surface state will be extensively reviewed both experimentally and theoretically [199, 200], and a surface state DFT evaluation will be performed to show that the photocathode generated hollow cone illumination (HCI) can be realized.

In Section 5.1, I will extend the DFT analysis from Ag to Au and Cu. In Section 5.2, I will present HCI based on Ag(111) single crystal emission, and show the schematic procedure to generate a 'cone-like' electron beam. As Δp_T data on photoemission from the Ag(111) face surface state is lacking in the photocathode community, my DFT calculation fills this vacancy.

Emphasis will be placed on a discussion of the surface state photoemission and the resulting Δp_T analysis and results obtained with it. In Section 5.3, the DFT-based photoemission analysis is used for the evaluation of the emission properties of p-block FCC photocathodes.

5.1 Noble Metal Photocathodes

Noble metal photocathodes with low emittance (high brightness) are nowadays routinely used as electron sources for laser-driven high-gradient guns [65, 69]. That is because these metals are resistant to corrosion, easy to fabricate, reliable and tolerant to contamination, and have uniform emission, high operating life time and a fast response time. The other principal reason for the wide use of noble metals as photocathodes is, of course, the wealth of available information about them. For example, the electronic properties of noble metals have been thoroughly investigated by cyclotron resonance, XPS experiments, X-ray emission experiments, ARUPS experiments and dHvA measurements [67, 201, 202]. Each experimental method mentioned above has been extensively applied to the field of photoemission physics and the results have been found to fit a consistent and entirely reasonable picture of the metal's Fermi surface. The disadvantages of noble metal photocathodes are their low QE (of the order of $10^{-6} \sim 10^{-4}$) and the need for a UV drive laser (> 4.60eV), which limits these photocathodes for applications requiring less than 1 mA average current [203].

The first BZ of an FCC lattice has a truncated octahedron shape as shown in Figure 5.1. Noble metals only have one free electron per atom so that the BZ is only half filled. The

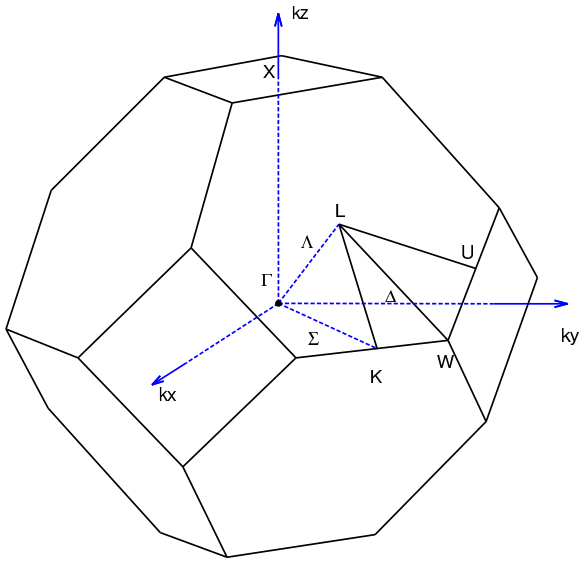

Figure 5.1: FCC Brillouin zone

structural and electrical properties of both the bulk and surfaces of noble metals were previously investigated theoretically and experimentally [66, 67, 100]. The calculated band diagrams for copper and gold are shown in Figure 5.2. The relatively flat bands lying about 2eV below the Fermi surface are associated principally with d atomic states, whereas the bands lying at higher energy are associated principally with s and p atomic states. The d bands are fully filled and the s bands are half-filled; thus, the volume contributed by the d bands is enclosed by the Fermi surface formed by the s bands. The equivalent Fermi surface radius then equals the average of Δ_1 (Γ–X) and Σ_1 (Γ–K) radii of the Fermi energy surface, values for which are shown in Table V both from Ref [96] and my DFT calculations. The unequal (100) face and (110) face radii indicate a distortion of the nominally spherical noble metal Fermi surface. In

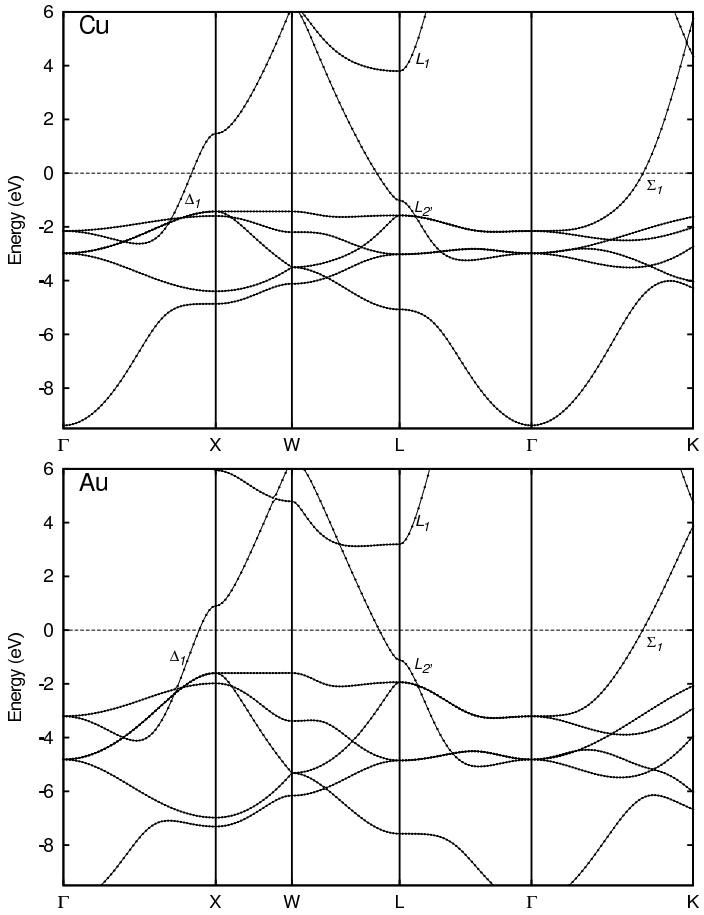

Figure 5.2: Copper and Gold band structures along high symmetry points and lines. Fermi level at zero energy is marked with dashed line.

addition, contact is established between the Fermi surface and the BZ boundaries in the <111> directions ($\overline{\Gamma L}$). These contact areas correspond to the energy gap at the zone boundary along the high symmetry line Λ. To further examine the consistency of the Fermi surface calculations by DFT, the effective masses corresponding to the (001), (110) and (111) faces are determined using $m^* = (\frac{\partial^2 E(\vec{p})}{\partial^2 \vec{p}})^{-1}$. The noble metal's Fermi surface is constructed of three major parts; a

TABLE V: The Fermi surface radii of Ag, Al and Cu (in units of $\frac{2\pi}{a}$).

	face	DFT	Expt.
Cu	(001)	0.81	0.83[a]
	(110)	0.72	0.74[a]
Ag	(001)	0.80	0.82[a]
	(110)	0.73	0.75[a]
Au	(001)	0.87	0.88[a]
	(110)	0.73	0.74[a]

[a]Reference [96]

'dog's bone' orbit from the contours in the (111) plane, a 'neck' orbit from contours in the (110) plane (the hexagonal face), and a 'belly' orbit from the contours in (100) plane [97, 204, 205]. These three orbits are shown in Figure 5.3 and the results from the effective masses calculations corresponding to the orbits are listed in Table VI. It can be seen that Ag, whose Fermi surface is closest to a perfect sphere (See Figure 3.3), has effective mass values close to m_0, while Cu whose Fermi surface is furthest from a perfect sphere (See Figure 5.3) has an effective mass much less than m_0. The DFT evaluated effective masses are all within 10% of the experimental values. Unlike potassium whose band structures could be completely defined by the E versus $\vec{p}$ diagram calculated along the principal crystal directions, the distorted spherical Fermi surfaces of the noble metals suggests that a DFT-based emission analysis will be required to evaluate their Δp_T.

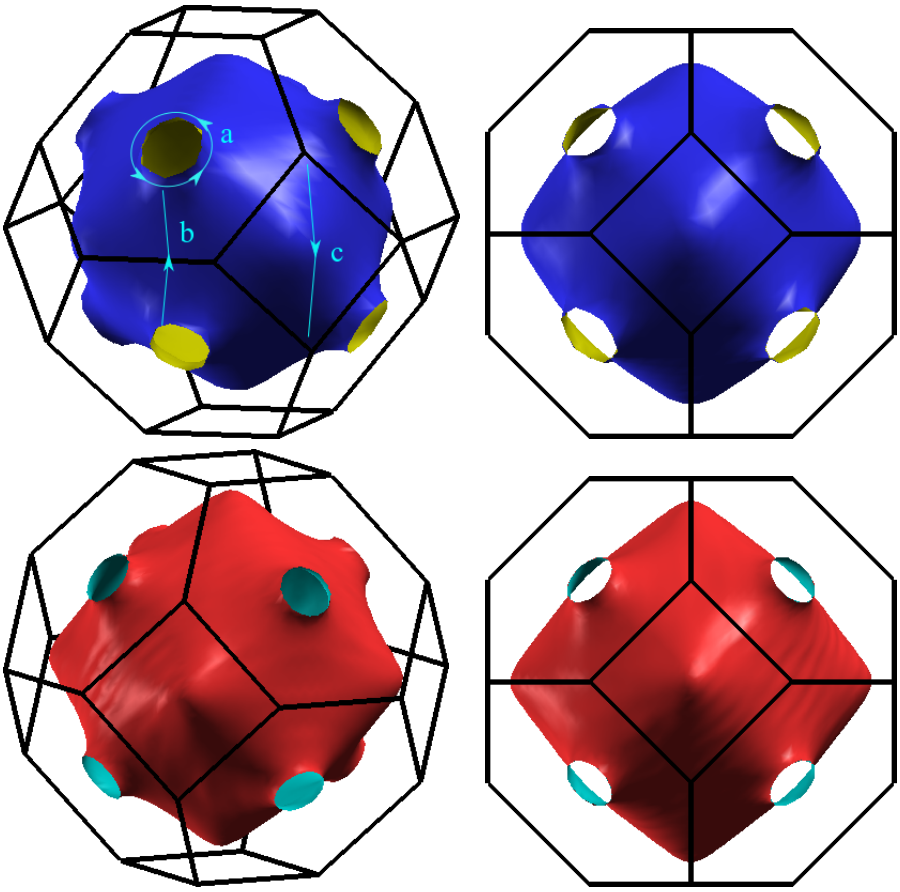

Figure 5.3: Cu and Au Fermi surfaces. Two projections of the noble metals reciprocal lattice show the shape of Cu and Au Fermi surfaces. The orbits considered are labeled by light blue lines: (a) dog's bone orbit, (b) neck orbit, and (c) central belly orbit.

TABLE VI: The effective mass of Ag, Al and Cu (in units of m^*/m_0).

	face	DFT	Expt.
Cu	(100)	0.47	0.49±0.02[a]
	(110)	0.50	0.53±0.02[a]
	(111)	0.42	0.45±0.02[a]
Ag	(001)	1.00	1.03±0.01[b]
	(110)	0.35	0.39±0.01[b]
	(111)	0.89	0.94±0.01[b]
Au	(001)	0.96	0.99±0.01[c]
	(110)	0.45	0.48±0.01[d]
	(111)	1.03	1.08±0.01[c]

[a]Reference [202]
[b]Reference [99]
[c]Reference [205]
[d]Reference [206]

The results of evaluating the photoelectric work functions of noble metals with respect to crystal orientation using the thin-slab method [183], are shown in Table VII. The calculated work functions are within 10% of experimental values [209,210], with any absolute discrepancies being in the vicinity of 0.1eV. Nonetheless, for these metals the calculated theoretical values are consistent and appear to be reliable; indeed, they are in very good agreement with experimental values. For bulk Au, a $\hbar\omega$=5.36 eV (231 nm) photon energy is the minimum energy required to overcome the photoelectric work function barrier. Due to this high work function value, there are no literature values of the rms transverse momentum Δp_T value for photoemission from Au with an excess energy greater than zero. For Cu and Ag, a $\hbar\omega$=4.75eV (261nm) UV laser can be used to photoemit from the (100) and (110) crystal faces. The Δp_T of an electron beam emitted

TABLE VII: The work function of Ag, Al, Au, and Cu (in units of eV).

	face	Expt.	DFT
Cu	(100)	4.59[b]	4.64±0.05
	(110)	4.48[b]	4.52±0.05
	(111)	4.94[b]	5.02±0.05
Al	(001)	4.41[b]	4.52±0.05
	(110)	4.28[b]	4.36±0.05
	(111)	4.24[b]	4.20±0.05
Ag	(001)	4.64[c]	4.64±0.05
	(110)	4.52[c]	4.53±0.05
	(111)	4.75[d]	4.83±0.05
Au	(001)	5.47[c]	5.52±0.05
	(110)	5.37[c]	5.36±0.05
	(111)	5.31[c]	5.50±0.05

[a]Reference [207]
[b]Reference [121]
[c]Reference [125]
[d]Reference [208]

from polycrystalline Cu and Ag surfaces irradiated by the 4.75eV picosecond laser pulses has been measured by the solenoid scan technique [56], and the measured Δp_T values for polished Ag and Cu photocathodes are $0.235\sqrt{m_0 eV}$ and $0.130\sqrt{m_0 eV}$, respectively. The polycrystalline nature of the measured noble metal photocathodes implies a crystal orientation randomness to the samples, so that the strict theoretical expression for $\Delta p_{T,\text{average}}$ must be expressed as

$$\Delta p_{T,\text{average}} = \sum_i \sum_j \sum_k x_{(ijk)} \Delta p_{T,(ijk)}, \tag{5.1}$$

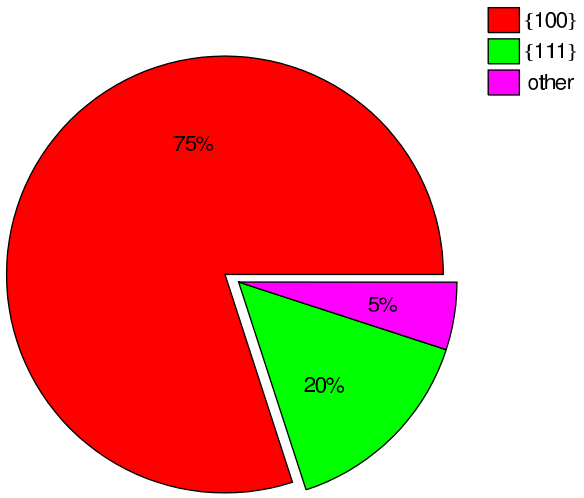

Figure 5.4: General crystal orientation percentage for polycrystalline FCC metal [209].

where $x_{(ijk)}$ is the weight of (ijk) crystal orientation and $\sum_i\sum_j\sum_k x_{(ijk)}=1$. The general $x_{(ijk)}$ distribution of FCC polycrystalline is displayed in Figure 5.4, which indicates that (100) and (110) are the two prevalent crystal faces and, hence, are expected to dominate the photoemission from polycrystalline noble metals [209]. Therefore, it is possible to consider an average Δp_T using an analysis that is restricted to (001) and (110) face emission.

TABLE VIII: DFT evaluated photoemission properties of Cu and Au.

Metal	face	$\Delta p_{T,DFT}$ $(\sqrt{m_0 eV})$	Δp_{T0} $(\sqrt{m_0 eV})$	$A_{T=0K}$
Cu	(100)	0.170	0.191	0.445
	(110)	0.198	0.288	0.444
Au	(100)	0.208	0.278	0.425
	(110)	0.168	0.361	0.245

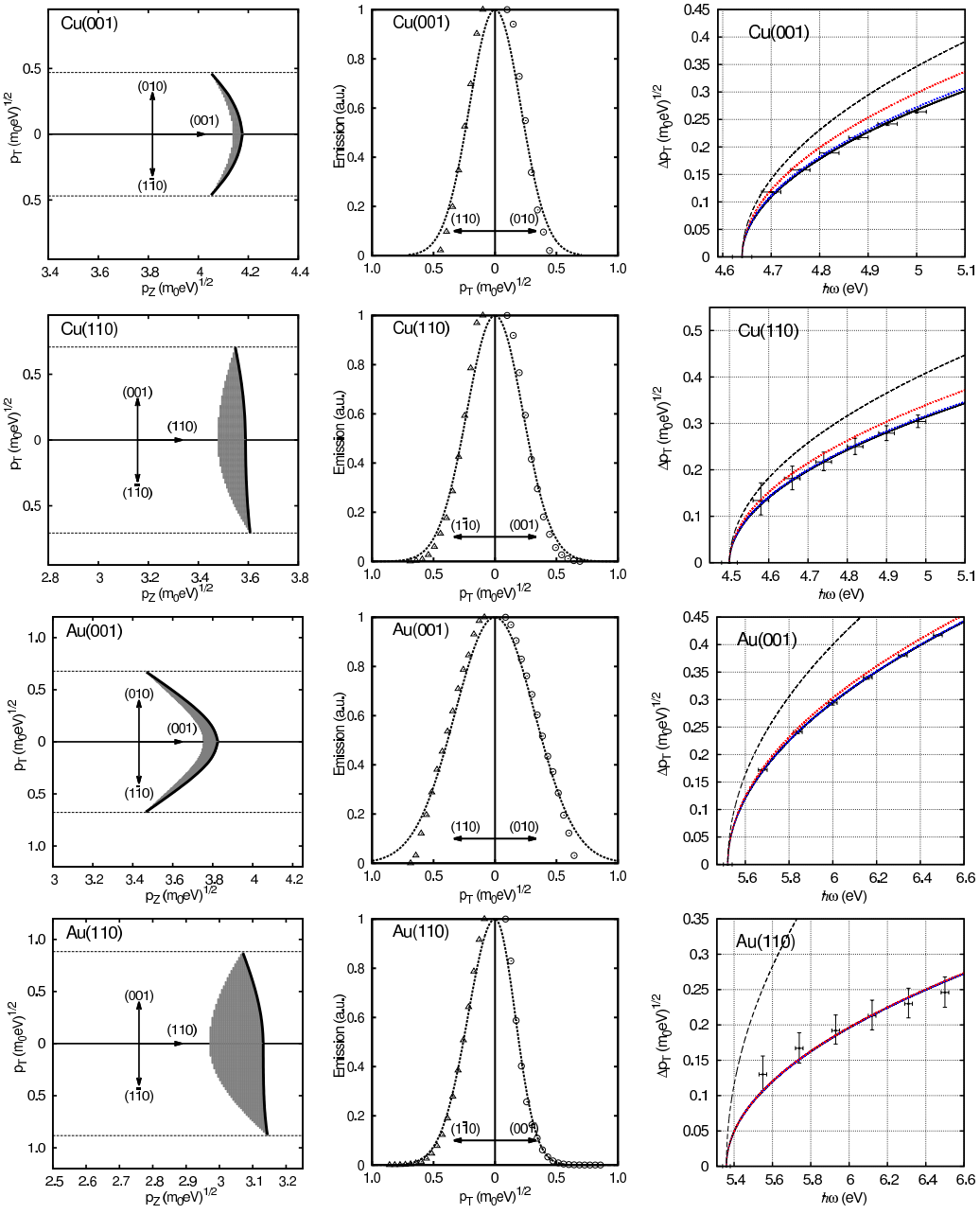

(a) (b) (c)

Figure 5.5: The results from the DFT-based photoemission analysis for the (001)/(110) face of Cu and Au. (a) Crystal momentum map of the electronic states (shaded regions) below the Fermi level (solid line) that may photoemit within $p_{T,max} = \sqrt{m_0 \Delta E}$ (dashed lines) for the transverse (010)/(001) and (110)/(1$\bar{1}$0) crystal directions. (b) Transverse momentum distribution of the photoemitted electrons in the (010)/(001) and (110)/(1$\bar{1}$0) directions. (c) Incident photon energy dependence of the rms transverse momentum Δp_T for electron temperatures $T_e \to 0$ (data points with solid line fit); $\Delta p_T = A\sqrt{m_0 \Delta E}$, T_e =300K and the melting points of each metal (dot-dashed lines), together with the expected form of $\Delta p_T = \sqrt{(\hbar\omega - \phi)/3}$ (black dashed line).

The DFT-based photoemission model described in Chapter 3 is used to evaluate Δp_T for Cu and Au. The results for photoemission from the (001) and (110) faces of Cu and Au are shown in Figure 5.5. The spatially-averaged values of Δp_T extracted from the excess energy contours are calculated using $\hbar\omega$=4.75 eV for Cu and $\hbar\omega$=5.77 eV for Au, and the results are listed in Table VIII. The theoretical data is a good fit to $\Delta p_T = A\sqrt{m_0(\hbar\omega - \phi)}$, giving the A values within 79% of 0.577 for Ag all cases expect Au(110) where A value within 42% of 0.577. In the $\Delta p_T(\hbar\omega, T_e)$ plot (Figure 5.5(c)), the rms transverse momentum is evaluated under 0 K, 300 K and the melting point, where the melting temperature for Cu (Au) is 1363K (1336K) [132]. As would be expected, the increase in Δp_T due to electron temperature increase is weak (strong) for Au (Cu) which has the large (small) excess photoemission energy; both metals have inward bent 'electron-like' energy states. Owing to the high degree of symmetry of Fermi surface in the FCC Brillouin zone, a relatively isotropic transverse momentum distribution is dominant in the prevalent crystal orientations.

5.2 Hollow Cone Illumination

In recent years, axial hollow cone illumination has gained great interest at high resolutions in conventional transmission electron microscopes since it eliminates phase contrast artifacts from an image, thus making high resolution electron microscopy (HREM), bright-field imaging and dark-field electron microscopy (DFEM) much more reliable [58, 211, 212]. The previous method of producing HCI employs annular condenser apertures [213], circular condenser apertures [214], or an electronic cone illumination method [213, 215], which impose several instrumental limi-

tations. It is therefore important to consider an alternative method of producing hollow cone illumination which minimizes such limitations and enables the corresponding microscopy to be performed routinely. Aside from the needed instrument improvements, it is inevitable that the standard methods of producing cone illumination mask the electron beam and therefore decrease its brightness. In this sense, a photocathode that directly generates the required hollow-cone beam for HCI would be quite attractive.

5.2.1 Introduction to Surface State

Previous literatures have indicated that there are surface states in the Surface Brillouin Zone (SBZ) for Ag(111), Cu(111) and Au(111) [197, 199, 200, 216]. Due to the presence of a crystal surface, bulk-forbidden electronic single-particle states may arise leading to a band in the corresponding projected bulk band gap. These so-called surface states are highly localized perpendicular to the surface, and form a (quasi) two-dimensional electron band. Typically, surface states exist if their character is similar to a bulk state, but shifted in energy by the surface perturbation. Because the occupied part of the surface state is far away from the surface Brillouin-zone (SBZ) boundary, its dispersion can be regarded as identical for all in-plane directions. As shown in Figure 5.6, the SBZ is a two dimensional hexagonal structure for the (111) FCC crystal face ($k_z = 0$), and it is centered at $\overline{\Gamma}$ point with $\overline{\Gamma M}$ and $\overline{\Gamma K}$ directions as $\vec{k_x}$ and $\vec{k_y}$, respectively; that is to say, the surface state disperses with momentum parallel to the surface p_x and p_y but not with perpendicular momentum p_z (momentum is restricted with the in-plane vector $\vec{p_T} = \vec{p_x} + \vec{p_y}$). According to Ref. [199], [217], and [218], it is the surface state

which can play an essential role in noble metal (111) face photoemission because, for a clean (111) surface, the photoemission intensity reaches a speak at E_F - $E_{ss,min}$, where $E_{ss,min}$ is the surface state band energy minimum [204]. Surface states can therefore dominate emission from the (111) faces of noble metals.

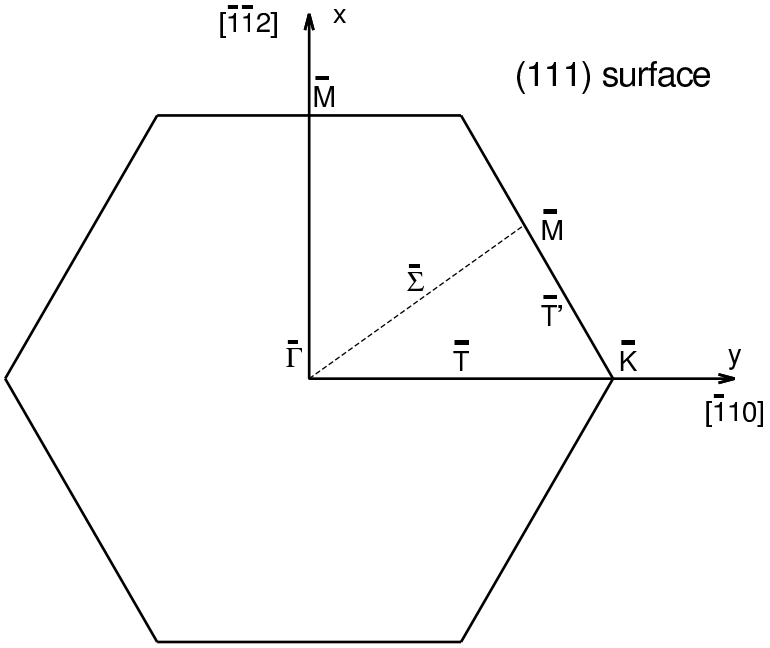

Figure 5.6: FCC (111) Surface Brillouin Zone

A successful method of distinguishing surface state and bulk photoemission features and determine the former's properties is to use a DFT-based surface band calculation within the slab model to extract the slab's band structure and inspect its energy dispersion properties, and thereby find the surface state band that is located between Fermi level and bulk bands. First, a (111)-face supercell comprising the multi-layer slab and suitable vacuum region needs

to be constructed. Second, band structure calculation along the $\overline{\Gamma M}$ and $\overline{\Gamma M}$ directions is performed. Third, the bulk bands are projected onto the k_x-k_y plane and plotted together with surface bands to determine the allowed surface states. As the surface energy dispersion relations are described in the SBZ (See Figure 5.6), in order to estimate where a surface state is, one can project the bulk bands into the two-dimensional Brillouin zone and then look for gaps that might accommodate such a state among the bulk states. The surface bands are the highest-energy partially occupied bands that fall below the Fermi level E_F only for limited regions of the momentum-space. The electronic states of these surface bands are usually well localized in the vicinity of the surface. The electrons occupying such a region of allowed $k_x - k_y$ space require the least energy to overcome the summation of the work function and transverse energy required to escape the material as photoelectrons. When the laser photon energy is high enough to liberate these electrons but insufficient to reach the next energy band, an electron beam suitable for HCI can then be generated by emission from the single assessed surface state.

5.2.2 (111)-Face Emission From Ag

For Ag(111), there is an $s - p$ gap at $\overline{\Gamma}$, where a Shockley-type surface state was observed by R. Paniago, G. Nicolay, and S. D. Kevan *et al.* [199, 200, 216]. The L-gap $s - p$ surface state dispersion was obtained by measuring the energy of the surface state as a function of the external electron angle θ. In contrast to the experimental investigations, I use a well-converged basis set and a k-mesh of 17×17×1 points in the two-dimensional irreducible Brillouin zone and modeled the surface by employing a periodic slab of 9 atomic layers separated by 15 $\mathring{A}$ of vac-

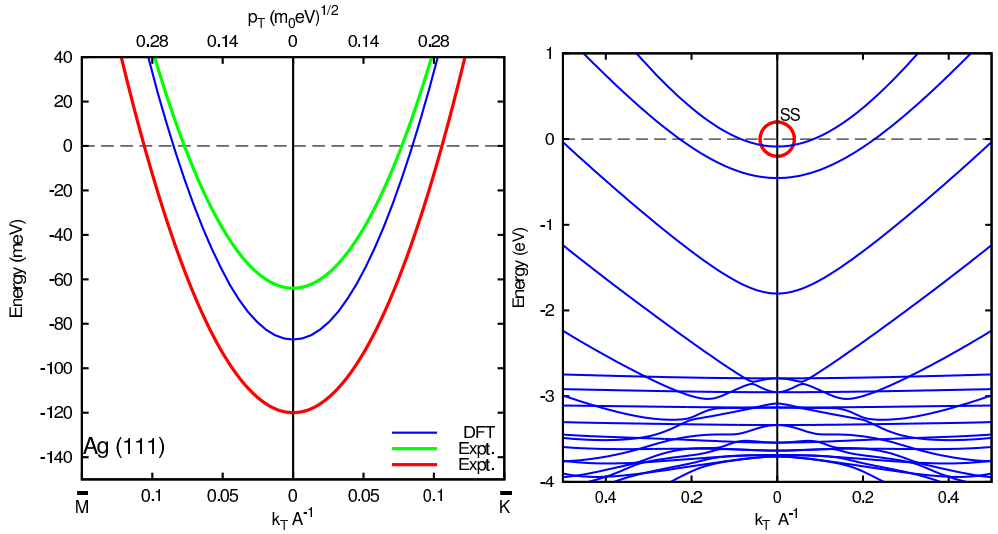

Figure 5.7: Energy dispersion relation for the Ag(111) Surface state. Results of the band-structure calculation along the $\overline{\Gamma M}$ direction for a 9-layer slab of Ag(111). The Fermi level has been adjusted to zero level. (a) The comparison between the DFT calculated surface band (blue solid line) with the experimental measured surface bands. The green solid line is Nicolay's result; the red solid line is Kevan's result. (b) The surface band dispersions are plotted in blue solid lines. The surface state is highlighted by red circle.

uum. The thin slab band calculation [183] is implemented by quantum-ESPRESSO using the LDA [103] pseudopotential. Results of the band structure calculation along the $\overline{\Gamma M}$ direction for the 9 layer slab of Ag(111) is shown in Figure 5.7(b). In order to be consistent with the experimental measurement unit, I plot the band dispersion in terms of E($\vec{k}$). In Figure 5.7(b), the blue solid lines give the slab's band dispersion by DFT at $T_e = 0$, and the Fermi level has been adjusted to zero (dashed line), the allowed surface surface is highlighted by the red circle. In Figure 5.7(a), I compare my DFT calculation (blue solid line) with the experimental Ag(111) surface state measurement of Nicolay [199] (green solid line) and by Kevan [200] (red

solid line). The DFT calculated surface state is between the two experimental surface states, which again demonstrates that there is a good agreement between experiment and theory.

The surface state, with its parabolic dispersion about the $\overline{\Gamma}$ point of the SBZ, is 62 meV below the Fermi level with effective mass $m^* = 0.40\ m_0$ in both the $\overline{\Gamma} \rightarrow \overline{\mathrm{K}}$ and $\overline{\Gamma} \rightarrow \overline{\mathrm{M}}$ directions, and has a Fermi wavevector value of $k_F = \pm 0.08\ \mathring{A}^{-1}$ [200]. The DFT-based surface state dispersion shown in Figure 5.7 gives the surface state band minimum ∼70 meV below E_F, and $m^*/m_0 = 0.42$. The DFT evaluated occupied part of the surface state ($k_F = 0.077\ \mathring{A}^{-1}$) is far away from the surface Brillouin-zone boundary ($k_{\overline{\Gamma M}} = 0.577\ \mathring{A}^{-1}$), and its dispersion can be regarded as identical for all in-plane directions. Therefore, we restrict most of our following discussion to the dispersion along the $\overline{\Gamma M}$ and $\overline{\Gamma K}$ directions, denoted as the $\vec{p_x}$ and $\vec{p_y}$ directions with the in-plane vector $\vec{p_T} = \vec{p_x} + \vec{p_y}$.

The minimum energy required to photoemit from the surface state, $E_{(111)}$, is the sum of FCC (111) face work function $\phi_{(111)}$ and the (111) Fermi level transverse momentum offset $p_F^2/2m_0$;

$$E_{(111)} = \phi_{(111)} + p_F^2/2m_0, \tag{5.2}$$

as in this case, $m^* < m_0$ (See Equation 2.5). Consequently, since $p_F = 0.245\ \sqrt{m_0 eV}$, photoemission from the Ag(111) surface state is predicted to only occur when $\hbar\omega > \phi_{(111)} + 0.03$ eV, where $\phi_{(111)} = 4.83$ eV. This means that photoemission from the surface state of Ag(111) will first occur from states around the Fermi level as this requires the least energy.

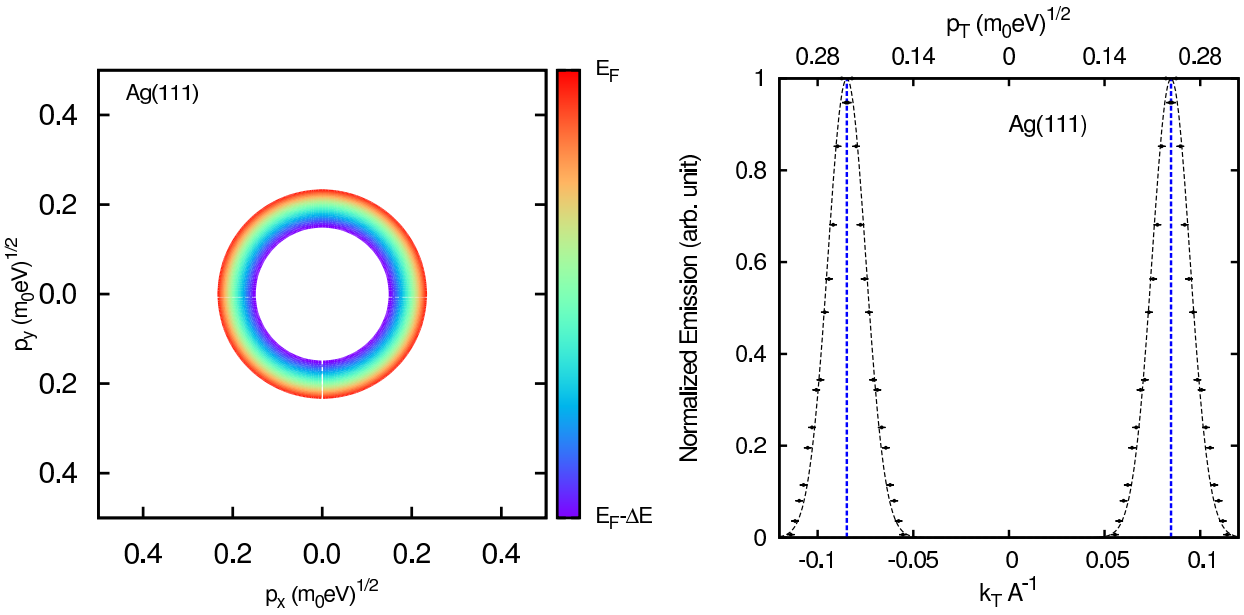

(a) (b)

Figure 5.8: (a) Ag(111) surface state constant energy contour with $\Delta E = 35$ meV. The outmost red contour is the two dimensional surface state Fermi surface contour with radius $0.220\sqrt{m_0 eV}$. The innermost blue contour is the $E_F - \Delta E$ constant energy contour with radius $0.190\sqrt{m_0 eV}$. (b) Ag(111) surface state transverse momentum distribution with $\Delta E = 35$ meV. Dashed line Gaussian fits are guides to eye.

From energy dispersion point of view, the surface state band structure is a single upward parabola; that is to say, the two dimensional Fermi surface map in the p_x — p_y plane consists of only one single circle at the maximum p_T value — $\hbar k_F$. For an excess energy of $\Delta E = 35$ meV, the resulting energy contour for the Ag(111) surface state has the 'ring-like' shape as shown in Figure 5.8(a); the two dimensional photoemitting energy contours reside inside the L-gap of the projected bulk band states in p_T-space.

The surface state photoemission energy-momentum relationship for an one-step photoemission process can be written as

$$\frac{(p_x^2 + p_y^2)}{2m_0} + \phi_{(111)} + \frac{p_{z0}^2}{2m_0} = \hbar\omega + E(p_x, p_y), \tag{5.3}$$

where p_x and p_y are the transverse momentum components ($p_T = \sqrt{p_x^2 + p_y^2}$), p_{z0} is the longitudinal momentum in vacuum and E(p_x, p_y) is initial electron state energy. An intrinsic emittance calculation may thus be obtained from the transverse momentum distribution of photoemitting energy contours. After application of Equation 5.3 and Equation 3.3, the resulting transverse momentum distribution displayed in Figure 5.8(b) shows the L-gap surface state photoemission. The Δp_T of the 'ring-like' emission peaks is $0.029\sqrt{m_0 eV}$ for $\Delta E = 35$meV. It can be seen that the transverse momentum distribution is symmetric with respect to $\overline{\Gamma}$ and has maxima close to p_F, which is consistent with experimental measurements.

As the emitted transverse momentum distribution is in the form of a ring with a radius k_F = $0.077\mathring{A}^{-1}$, its acceleration in an electron gun to an axial momentum of p_0 will generate a hollow cone beam with a semi-angle $\theta_{HCI} \approx p_F/p_0$. That is, using the DFT-based thin-slab model, I show that the Ag(111) surface state photoemission with an excess energy of 35meV will produce a HCI beam. The useful range of excess energies for Ag(111) generation of HCI is $0 \sim 62$ meV, which will require accurately tunable UV laser; Ag(111) alloys such as Cu-Ag (111) could overcome this hurdle. It is also important to mention that when the surface state

band effective mass is greater than the free electron mass, photoemission from the surface state will first occur from states around the $\overline{\Gamma}$ point as this requires the least energy — I will discuss this surface state photoemission situation in Section 6.4.

5.3 *p*-block Transition Metal Photocathodes

In addition to the noble metals, other elemental metals with a FCC crystal structure also include two alkaline earth metals (Ca and Sr), two *p*-block metals (Al and Pb), and three *d*-block metals (Pd, Rh and Pt). According to the ideal photocathode criteria, among these other FCC metals, only Al and Pb are potential photocathodes. This is because calcium is quite reactive for a metal, strontium is a soft metallic element that is highly reactive chemically, and the *d*-block FCC metals have very high work functions (> 5.00 eV). Specially, Pd(100) and Pt(100) have work functions of 5.90±0.01 eV [219] and 5.82±0.15 eV [220], respectively, which would require sub-200nm photons for photoemission and Rh(100) with a 5.25eV work function [221] would require the 216nm (5.75eV) 5^{th} harmonic of a Nd:YAG laser [222] for photoemission. Moreover, photoemission using deep UV laser radiation can lead to laser damage and therefore reduce the life time of the photocathode. On the other hand, Al and Pb have relatively low work functions (< 4.5 eV) as shown in Table IX, where the DFT calculated values are compared to available measured values. These two photocathode materials are therefore suitable for use with the 4^{th} harmonic of Nd:YAG and 3^{rd} harmonic of Ti: sapphire ($\hbar\omega = 4.67$eV).

TABLE IX: Summary of work function and Δp_{T0} of p-block metals.

	Surface	$\phi_{expt.}$(eV)	ϕ_{DFT}(eV)	Δp_{T0}
Al	(100)	4.41[a]	4.39	0.337
	(111)	4.24[a]	4.20	0.412
	(110)	4.06[a]	4.28	0.480
Pb	(100)	3.95[b]	4.00	0.516
	(111)	3.85[b]	3.95	0.548
	(110)	3.80[b]	3.89	0.563

Reference[a] [125]
Reference[b] [223]

The Fermi surfaces of Pb and Al are somewhat more complex than the noble metals due to both s and p state contributions to the occupied valence bands under Fermi level [224]. Consequently, their band structures are dominated by a parabolic dispersion in the center of BZ which is strongly modified near zone boundaries. The Fermi surface complexity of these two p-block metals is reflected in the energy relationships, E(p_z, p_T) of the electron states that can contribute to photoemission. The results of the DFT-based analysis for photoemission from (001) and (110) faces are shown in Figure 5.9. For each element, Figure 5.9(a) shows the electronic states (shaded regions) below the Fermi level (solid line) that may contribute to photoemission as function of the internal crystal momentum in the (001) and (110) directions (p_z) and their transverse momentum (p_T) directions. One set of electronic states from the p band that cross the Fermi level contribute to photoemission from the (001) and (110) crystal faces for both metals. For emission from the (001)-face of both Al and Pb, the state

distribution is fairly symmetric about the $\Gamma - X$ direction. For Al(001), the emission is from the Δ_1 'electron-like' band centered at Γ point [225]. On the other hand, Pb(001) emission is from the Δ_6 'hole-like' band. In both cases, the transverse momentum distribution of the emitted electrons is very symmetric (Figure 5.9(b)). Emission from the (110)-face of both Al and Pb involves two 'electron-like' bands. In Al (Pb) case, the Σ_1 (Σ_5^+) and Σ_3 (Σ_5^-) bands are associated with the (110) photoemission, and these two bands are not symmetric with respect to Γ–K direction. For (100) face emission, the symmetric p_T distribution is ascribed to isotropically distorted Fermi surface. Compared with Al(100)'s p_T distribution, Pb(100)'s p_T distribution in the [110] direction has slightly longer tail than that in [010] direction, but the minor difference does not result in an obvious Δp_T difference between the (010) and (110) transverse directions. All the contributing bands for both metals are fairly symmetric about the (001) crystal direction, but are not as symmetric about the (110) direction, which leads to relatively isotropic transverse momentum distributions for (001)-face emission and somewhat anisotropic transverse momentum distributions for the (110) direction (Figure 5.9(b)). The spatially averaged values of Δp_T extracted from these calculated momentum distributions are listed in Table X together with the values of $\Delta p_{T0} = \sqrt{m_0 \Delta E/3}$ [52, 53]. In all cases, Δp_{T0} is greater than the results of the DFT photoemission simulation.

Figure 5.9(c) shows the theoretical dependence of Δp_T on the incident photon energy $\hbar\omega$ for $T_e \to 0$ (data points) together with the form predicted by $\Delta p_{T0} = \sqrt{\Delta E m_0/3}$ (black dashed

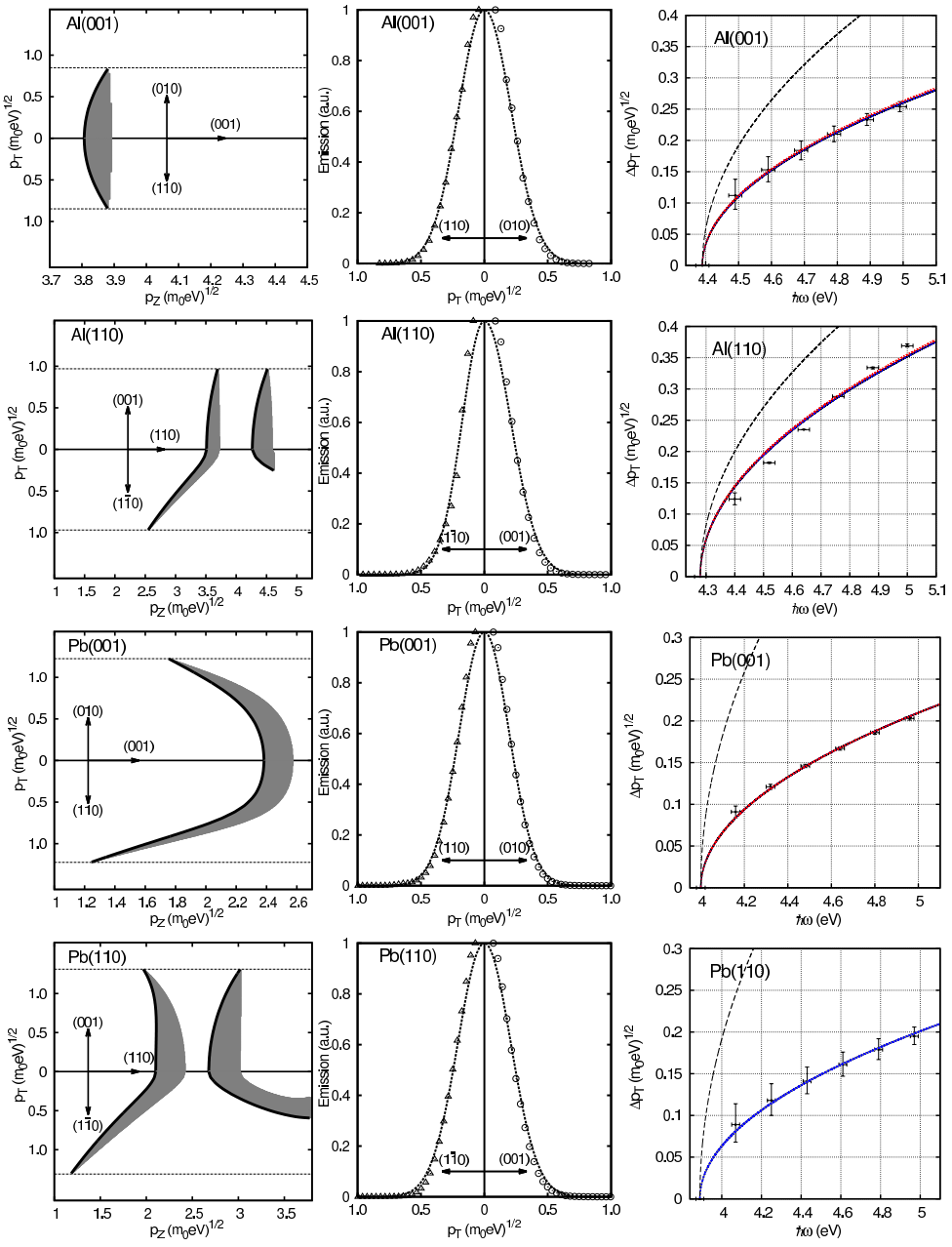

Figure 5.9: The results from the DFT-based photoemission analysis for the (001)/(110) face of Al and Pb. (a) Crystal momentum map of the electronic states (shaded regions) below the Fermi level (solid line) that may photoemit within $p_{T,max} = \sqrt{m_0 \Delta E}$ (dashed lines) for the transverse (010)/(001) and (110)/(1$\bar{1}$0) crystal directions. (b) Transverse momentum distribution of the photoemitted electrons in the (010)/(001) and (110)/(1$\bar{1}$0) directions. (c) Incident photon energy dependence of the rms transverse momentum Δp_T for electron temperatures $T_e \to 0$ (data points with solid line fit); $\Delta p_T = A\sqrt{m_0 \Delta E}$, T_e =300K and the melting points of each metal (dot-dashed lines), together with the expected form of $\Delta p_T = \sqrt{(\hbar\omega - \phi)/3}$ (black dashed line).

TABLE X: Summary of emission property results for Al and Pb.

Metal	face	A(0K)	A(300K)	A(melting point)	$\Delta p_{T,DFT}(\sqrt{m_0 eV})$
Al	(100)	0.333	0.333	0.337	0.200
Al	(110)	0.414	0.415	0.418	0.196
Pb	(100)	0.210	0.210	0.210	0.203
Pb	(110)	0.191	0.191	0.191	0.199

Melting points for Al and Pb are 993K and 601K [226], respectively.

line). For both metals, the theoretical data are a good fit to $\Delta p_T = A\sqrt{(\hbar\omega - \phi)m_0}$ (solid line), giving the A values shown in Table X, which are significantly less than 0.577. The dashed line is the fitted form of $\Delta p_T(\hbar\omega)$ when T_e equals 300 K evaluated using the Fermi-Dirac function to describe the occupation of the electronic states generated by the zero temperature DFT band structure calculations (data points not shown). The rms transverse momentum of the emitted electrons does not increase significantly for electron at room temperatures. Also shown in Figure 5.9(c), is the fit to $\Delta p_T(\hbar\omega)$ at the melting point of each metal (dot-dashed line), which are again not significantly different to $\Delta p_T(\hbar\omega, T_e \to 0)$ since the excess photoemission energy $\Delta E \gg k_B T_e$ are at the melting point. As before (Chatpers 3 and 4), thermionic emission of the tail of the Fermi distribution when $\hbar\omega < \phi$ is not included as the photoemission efficiency is much reduced.

Table X summarizes the values of $A_{(ijk)}$ extracted from the fits to the $\Delta p_T(\hbar\omega, T_e)$ DFT data in Figure 5.9(c) for each of the stated transverse directions for both the (001) and (110) crystal faces of Al and Pb. The two p-block FCC metals are predicted to have some emission

anisotropy for the (110) faces while emission from their (001) faces should be isotropic in to which 5% — a trend that is consistent with the isotropy associated with the photoemitting states (Figure 5.9(b)).

CHAPTER 6

HEXAGONAL CLOSE–PACKED METAL PHOTOCATHODES

In Chapter 4 and 5, I discussed the emission properties of BCC and FCC photocathodes. Many BCC and FCC metals are very attractive photocathodes, but they do not generally show the influence of Brillouin zone anisotropy on Δp_T; that is, they do not possess Fermi surface with uniaxial or biaxial symmetry that could result in intrinsic Δp_T anisotropy. In this chapter, I calculate the lattice constants, work functions, Fermi surfaces and Δp_T of HCP metal crystal photocathodes, which are intrinsically anisotropic. In addition, emission from (0001)-oriented Be is examined due to the presence of a strong surface state, photoemission from which generally produces a relatively isotropic rms transverse momentum distribution since the basal plane band dispersion is quite isotropic.

A DFT-based analysis of photoemission on HCP metals is developed and the calculated rms transverse momentum (Δp_T) values are in good agreement with the available experimental data on polycrystalline Beryllium [56] and Magnesium [227]. In Section 6.1, the lattice constants and work functions of the 15 elemental HCP metals are examined and compared with the available experimental values. In Section 6.2, along with the evaluation of Δp_T on selected HCP metals (Be, Hf, Mg, Sc, Ti, Y, and Zr), I demonstrate the dependence of Δp_T on the basal plane and prism plane photoemission, the latter directly demonstrating the connection between the anisotropic electronic properties of HCP metals and anisotropic transverse momentum distribu-

tions of emitted electrons. In Section 6.3, the photoemission from the Mg(0001) face that may generate an electron beam with an isotropic transverse momentum distribution are described in detail. In Section 6.4, emission from the (0001) face of the seven HCP metals is discussed, and a more detailed analysis of Be(0001) photocathodes is presented where a robust surface state [60–64] can contribute to photoemission. In Section 6.5, the (0001)-face emission from Hf, Sc, Ti, Y, and Zr metals are also discussed.

6.1 Physical and Electronic Property Anisotropy

The hexagonal crystal structure has four lattice constants that differ with direction; identical a_1, a_2 and a_3 constants in the hexagonal band plane, and the c in the perpendicular direction. The lattice constant c is always greater than a, and for an ideal HCP crystal structure $c/a \approx 1.633$. For the lattice constant calculation, ultrasoft pseudopotentials within the local density approximation [188] are used for all 15 HCP metals; the results of our analysis are not changed if the GGA [105] is used instead. A sampling of 10×10×6 Monkhorst-Pack [106] set of special k-points and Marzari-Vanderbilt smearing [228] with a broadening of 0.02 Ryd is employed and, for the $4d$, $5d$ and $6p$ metals, relativistic approximations are included [109, 110]. In addition, ferromagnetic collinear local spin density approximation (LSDA) has been used to find the optimized geometry of HCP Co due to its magnetic property [229]. The DFT-based calculations were all initiated using the experimental lattice parameters for each HCP metal and then tested for total energy convergence to a tolerance of 10^{-4} eV. Minimization of the total energy then yields the theoretical optimized lattice constants a and c that are compared in Table XI to their

experimental values.

The comparison of the DFT-generated lattice constants with the experimental values in Table XI not only shows good agreement, but also reveals a wide range in the c/a lattice constant ratio from 1.567 for Be to 1.886 for Cd. This ratio range is related to electronic state mixing and hence anisotropy in the electronic band structure. In the divalent HCP metals Be, Mg, Zn, and Cd the p valence electron levels are closest to the occupied s levels whereas electrons in the d levels are energetically well separated from both in Zn and Cd. As a consequence, in Be and Mg, high-symmetry s-p mixing is linked to a preferred formation of the energy band near the Fermi level, and thus, electronic band structures with close to parabolic dispersion below the Fermi level. However, there is no similarity between the alkali metal's close to spherical Fermi surfaces and those of Be and Mg [55] due to the latter's non-cubic crystal symmetry and the fact that two valence electrons ensure that their Fermi surfaces enclose twice the volume in momentum space. Nonetheless, Mg with a c/a lattice constant ratio of 1.624 is within 1% of ideal close packing where $c/a = 1.633$. In contrast, for Cd and Zn there is a significant mixing contribution from the d states which leads to large non-ideal c/a ratios of 1.886 and 1.896, respectively. For Tl, the only $6p$ HCP transition metal, $c/a = 1.599$; its Fermi surface consists of three non-spherical structures [238] and its Fermi energy lies in an almost pure $6p$ band above the top of the s band. According to the extensive investigations by F. Batallan et al. [232], R.A. Deegan [239], and D.G. Pettifor [240], the electronic bands of the other ten d-block transition metals ($3d$ (Co, Sc and Ti), $4d$ (Ru, Tc, Zr and Y) and $5d$ (Hf, Re and Os))

TABLE XI: Calculated lattice constants of the 15 HCP metals compared with the experimental literature values.

	Expt. (a.u.)	Expt. c/a	DFT (a.u.)	DFT c/a
Be	a=4.32	1.567 [230]	a=4.20	1.590
	c=6.77		c=6.68	
Cd	a=5.63	1.886 [231]	a=5.48	1.896
	c=10.62		c=10.39	
Co	a=4.74	1.571 [232]	a=4.52	1.617
	c=7.45		c=7.31	
Hf	a=6.04	1.579 [109]	a=5.88	1.594
	c=9.54		c=9.37	
Mg	a=6.06	1.625 [233]	a=5.89	1.642
	c=9.85		c=9.67	
Os	a=5.17	1.579 [109]	a=5.17	1.571
	c=8.16		c=8.12	
Re	a=5.22	1.609 [234]	a=5.04	1.587
	c=8.40		c=8.00	
Ru	a=5.10	1.582 [109]	a=5.16	1.663
	c=8.07		c=8.58	
Sc	a=6.24	1.591 [235]	a=6.03	1.589
	c=9.93		c=9.52	
Tc	a=5.18	1.585 [236]	a=5.11	1.624
	c=8.21		c=8.30	
Tl	a=6.53	1.599 [237]	a=6.40	1.608
	c=10.44		c=10.29	
Ti	a=5.58	1.586 [235]	a=5.36	1.612
	c=8.85		c=8.64	
Y	a=6.89	1.572 [235]	a=6.61	1.587
	c=10.83		c=10.49	
Zn	a=5.01	1.804 [231]	a=4.83	1.888
	c=9.04		c=9.12	
Zr	a=6.10	1.595 [109]	a=5.91	1.636
	c=9.73		c=9.67	

are primarily d-like and not parabolic near Fermi level. They have low lying d levels leading to a s-p and d synthesized band structures with the c/a ratios from 1.540 to 1.609. The large variation in the c/a lattice constant ratios and associated electronic band structure details for the HCP elemental metals generates anisotropic Fermi surfaces and energy-momentum relationships $E(\vec{k})$, and thus asymmetric local densities of states $g(E, \vec{k})$, in addition to considerable work function anisotropy, $\phi_{(ijkl)}$ — all of which are involved in photoemission for any particular crystal direction.

Knowledge of the photoelectric work function and its anisotropy is the second requirement for our DFT-based photoemission analysis. We evaluate $\phi_{(ijkl)}$ using the thin-slab method [122] which requires knowledge of the atomic potentials, their lattice positions in the ABAB z-direction hexagonal stacking (Table XI), and the metal's Fermi level acquired from the bulk DFT band structure calculations. In our evaluations of $\phi_{(ijkl)}$, unrelaxed slabs generally consisting of 8-13 atomic layers separated by a 15Å vacuum region are employed as this is sufficient to ensure that both the vacuum and average crystal potential reach equilibrium. The work function may then be determined from the energetic difference between the Fermi and the vacuum levels to a calculation uncertainty of typically ± 0.05 eV. We note that even though small surface layer relaxations are expected for both (0001) and $(10\bar{1}0)$ faces [241], the surfaces of the HCP metals are also known to be less likely to reconstruct at low temperatuers [242]. Moreover, although the LDA can be expected to represent the better choice of exchange-correlation functional if a better match to experimental values of $\phi_{(ijkl)}$ is desired, our calculations indicate that even

with surface relaxations, neither the LDA nor the GGA exchange-correlation functional appear to represent a more accurate choice [241]. The results obtained from the unrelaxed thin-slab simulations for work functions of the (0001) and $(10\bar{1}0)$ crystal faces for all 15 HCP elemental metals are shown in Table XII, together with available experimental and theoretical values from the literature. The tabulated data clearly shows that the intrinsic anisotropic nature of HCP metals also results in a strong crystal orientation dependence of the work function.

As mentioned in Chapter 3, the DFT-based theoretical analysis clearly indicates that Δp_T is dependent on the characteristics of the state or band form which the electrons are photoemitted. The electronic band structures of HCP metals show strong anisotropy, as has been demonstrated by previous theoretical and experimental studies of their electronic properties [167,231,244,248,253–259]. For example, HCP metals have 'electron-like' (upward parabola) bands and 'hole-like' (downward parabola) bands that cross the Fermi level along both abscissa (Γ – K or Γ – M) directions (See Figure 6.1) such as the Σ_3, Σ_5, T_4 and T_5 bands, and the ordinate (Γ – A) direction (See Figure 6.1) such as the Δ_8 bands for Zinc; but not all HCP metals have bands that cross the Fermi level in the ordinate direction, for example Be. In addition, open orbits (non-closed Fermi surface) have been found by dHvA measurements on the Fermi surfaces of Co (0001), Tl $(10\bar{1}0)$ and Tl (0001) [232,237]. The complexity of the HCP Fermi surface highlights the advantage of DFT-based investigations of the properties of HCP photocathodes, since they are able to evaluate the real material's electronic band structure and Fermi surface so that Δp_T can be quantitatively extracted from the intrinsic electron transverse

TABLE XII: Work functions of the 15 HCP metals

	Surface	ϕ (eV)	Method	ϕ_{DFT} (eV)
Be	(P)[a]	3.92 [243]	Expt.	
	(P)	4.98 [210]	Expt.	
	(0001)	5.10 [244]	Expt.	5.61
		5.40 [245]	Theory	
		5.62 [167]	Theory	
	$(10\bar{1}0)$			3.88
Cd	(P)	4.22 [210]	Expt.	
	(0001)	4.00 [246]	Expt.	4.17
	$(10\bar{1}0)$			4.76
Co	(P)	5.00 [210]	Expt.	
	(0001)	5.55 [247]	Expt.	5.62
Hf	(P)	3.90 [210]	Expt.	
	(0001)			4.51
	$(10\bar{1}0)$			3.63
Mg	(P)	3.66 [210]	Expt.	
	(0001)	4.05 [248]	Theory	3.87
		3.70 [245]	Expt.	
	$(10\bar{1}0)$			3.79
Os	(P)	4.83 [210]	Expt.	
	(0001)			5.62
	$(10\bar{1}0)$			4.94
Re	(P)	4.96 [210]	Expt.	
	(0001)	5.22-5.77 [249]	Expt.	5.35
	$(10\bar{1}0)$	5.75 [210]	Expt.	5.67
Ru	(P)	4.71 [210]	Expt.	
	(0001)	5.40 [250]	Expt.	5.37
	$(10\bar{1}0)$			4.59
Sc	(P)	3.50 [210]	Expt.	
	(0001)			3.81
	$(10\bar{1}0)$			3.10
Tc	(P)	4.88 [210]	Expt.	
	(0001)			5.15
	$(10\bar{1}0)$			4.31
Tl	(P)	3.84 [210]	Expt.	
	(0001)			3.90
	$(10\bar{1}0)$			3.93
Ti	(P)	4.33 [210]	Expt.	
	(0001)	4.60($\pm$0.2) [251]	Expt.	4.72
	$(10\bar{1}0)$			3.63
Y	(P)	3.10 [210]	Expt.	
	(0001)			3.60
	$(10\bar{1}0)$			3.08
Zn	(P)	4.33 [210]	Expt.	
	(0001)	4.15 [248]	Theory	4.43
	$(10\bar{1}0)$			5.04
Zr	(P)	4.05 [210]	Expt.	
	(0001)	4.26-4.51 [252]	Theory	4.42
	$(10\bar{1}0)$			3.59

(P)=Polycrystalline

momentum distribution inside HCP metals.

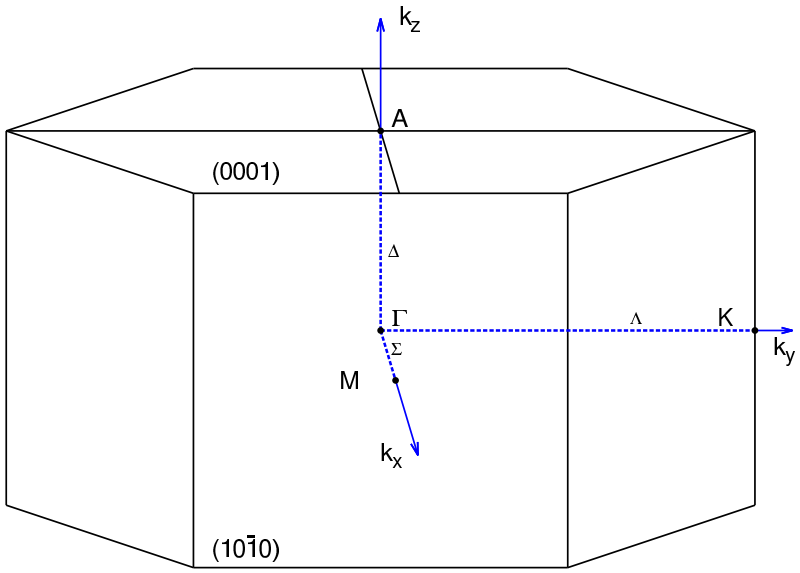

Figure 6.1: The first Brillouin zone of a simple hexagonal lattice.

The emitted electron's rms transverse momentum also depends foundamentally on the photoemission excess energy, so that, for a constant photon energy $\hbar\omega$, an anisotropic photocathode work function leads to a variation in Δp_T with respect to the different micro-crystal orientations in a polycrystalline photocathode. For instance, the work functions of Rhenium are well known as a function of crystal orientation by previous experimental work function measurements [236], and the values vary from a minimum value or Re(2111) of 4.70±0.04eV to a maximum value for Re(1010) 5.95±0.15eV. Based on the calculated work functions and the photocathode selection criteria in Section 2.5, I will restrict the analysis of the photoemission characteristics of elemental HCP metal photocathodes to Be, Hf, Mg, Sc, Ti, Y, and Zr. The fact that the HCP

crystal structure is intrinsically anisotropic, and hence, so is the electronic crystal band structure, immediately suggests that the momentum distribution of electrons photoemitted from the (0001) crystal face should be different to that emitted from the $(10\bar{1}0)$ face. The $(10\bar{1}0)$ crystal orientation will be used to illustrate that the anisotropic electronic properties of HCP metals causes emission anisotropy.

6.2 $(10\bar{1}0)$-Face Emission

The preferred crystal orientations for HCP metals are the $(10\bar{1}0)$ and (0001) faces which will therefore dominate the constitution of HCP polycrystalline sample [260]. As, in general, $\phi_{(10\bar{1}0)} < \phi_{(0001)}$ (Table XII), one expects the emission properties of the $(10\bar{1}0)$ face to play an important role in determining the characteristics of HCP metal photocathodes. The thin-slab analysis [183] indicates that $\phi_{(10\bar{1}0)}$ ranges from 3.08 eV for Y to 3.88 eV for Be (See Table XII). As a result, for incident 4.75 eV (or even 4.67 eV) UV photons, one might expect efficient ($\sim 10^{-4}$ quantum efficiency [227]) isotropic photoemission since the maximum possible transverse momentum $p_{T,max.} = (2m_0\Delta E)^{1/2}$ of around 1.5 $(m_0\text{eV})^{1/2}$ should allow access to many electronic states in the metal photocathodes. However, as shown below, the highly anisotropic band structure (due to the symmetry of HCP crystals) can play a major role in determining the rms transverse momentum Δp_T of the photoemitted electrons, even generating beams with a highly elliptical divergence symmetry from the $(10\bar{1}0)$ face.

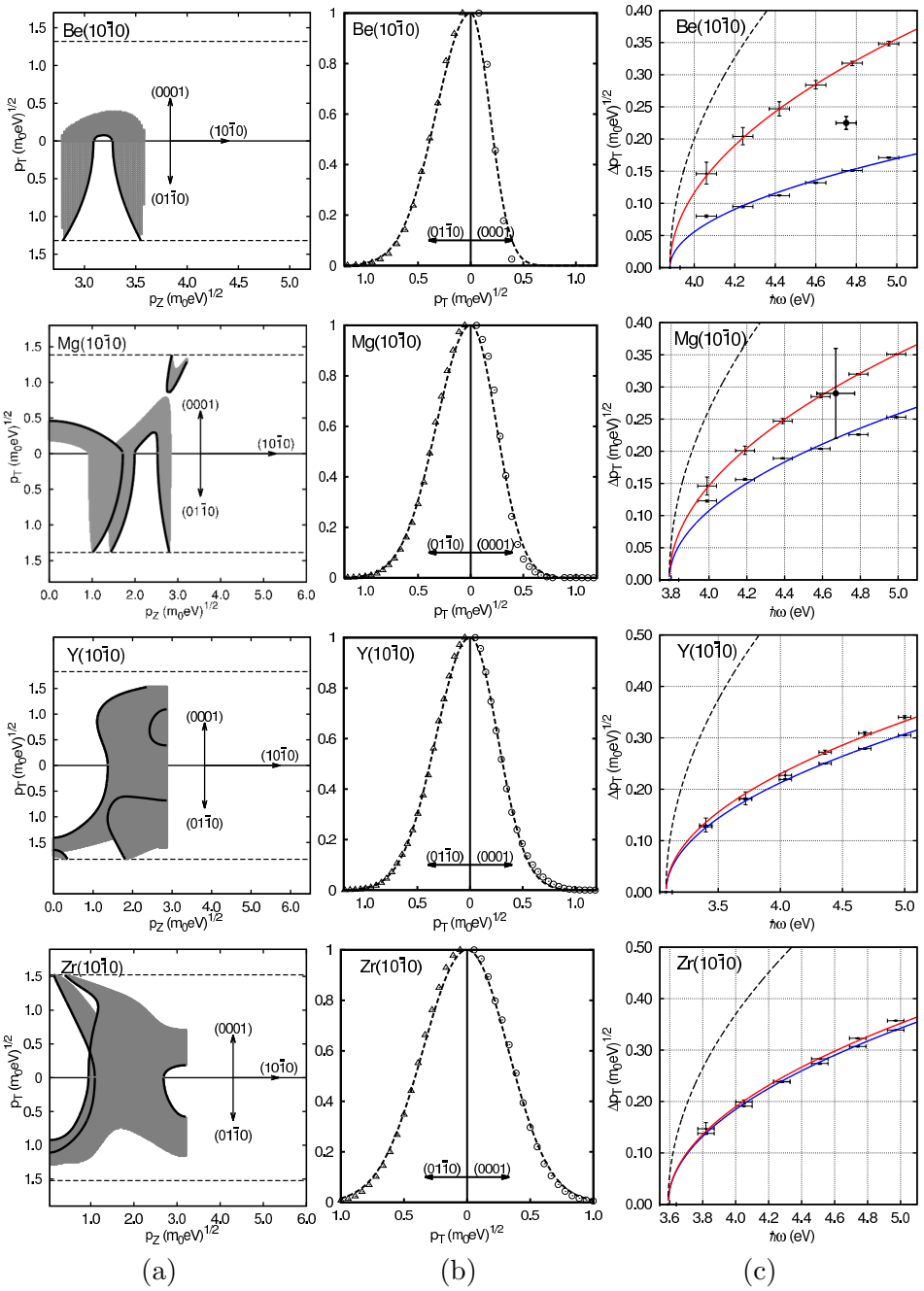

Figure 6.2: Emission properties for the (10$\bar{1}$0) face of Be, Mg, Y and Zr metals. (a) Crystal momentum map of the electronic states (shaded regions) below the Fermi level (solid line) that may photoemit within $p_{T,max.} = \sqrt{2m_0\Delta E}$ (dashed lines) for the transverse (0001) and (01$\bar{1}$0) crystal directions. (b) Transverse momentum distributions of the photoemitted electrons in the (0001) and (01$\bar{1}$0) directions (Gaussian fits are guides to the eye). (c) Incident photon energy dependence of the rms transverse momentum Δp_T for electron temperatures $T_e \to 0$ (data points with solid red line fit, for (01$\bar{1}$0) crystal direction and solid blue line fit for (0001) crystal direction), together with the expected form of $\Delta p_T(\hbar\omega)$ from Refs. [52] and [68] (dashed line). Black circles show the measured Δp_T data from Refs. [56] and [227] for Be and Mg, respectively.

Figure 6.2 displays the results obtained from the DFT-based photoemission simulation for the $(10\bar{1}0)$ face of Be, Mg, Y and Zr when $\hbar\omega$=4.75 eV. In each case, Figure 6.2(a) shows the electronic states (shaded regions) below the Fermi level (solid line) that contribute to photoemission along the (0001) and $(01\bar{1}0)$ crystal momentum directions perpendicular to the $(10\bar{1}0)$ emission direction. An acute asymmetry of the contributing states in transverse momentum p_T, caused by the energetic position of the Fermi level in the HCP band structure, is immediately evident, with Be being the most asymmetric and Zr the most symmetric. For Be$(10\bar{1}0)$ emission, the 'hole-like' dispersion of the contributing Δ_2 band in the (0001) direction is so strong that emission ceases for $p_T > 0.4$ $(m_0\text{eV})^{1/2}$, even though electron emission up to $p_{T,max.} = 1.319$ $(m_0\text{eV})^{1/2}$ (dashed line) from the same band is possible in the $(01\bar{1}0)$ momentum direction. The Δ_2 band also contributes to the state asymmetry for Mg emission although to a somewhat lesser extent as some photoemission is now also possible at $p_{T,max.} = 1.386$ $(m_0\text{eV})^{1/2}$ (dashed line) in the (0001) transverse momentum direction due to the T_2 and T_4 bands [261]. There is also an additional anisotropic contribution to photoemission from Mg from the 'electron-like' Σ_1 band at lower values of p_z. For Y, a large number of predominantly 'hole-like' electronic states, that are more isotropically distributed about the $(10\bar{1}0)$ emission direction than in Be and Mg and extend to $p_{T,max.}$=1.828 $(m_0\text{eV})^{1/2}$ (dashed line) in both the transverse (0001) and $(01\bar{1}0)$ crystal momentum directions, will contribute to the photoemission. For the $(10\bar{1}0)$ face of Zr, photoemission with $\hbar\omega$=4.75 eV is possible up to $p_{T,max.} = 1.523$ $(m_0\text{eV})^{1/2}$ (dashed line) in all transverse directions and the contributing states appear to be even more symmetrically distributed about the $(10\bar{1}0)$ emission direction. The photoemitting states for both Y

and Zr are terminated by the MK edge of Brillouin zone at $p_z = 2.93$ $(m_0\text{eV})^{1/2}$ and $p_z = 3.21$ $(m_0\text{eV})^{1/2}$, respectively.

The trend of decreasing anisotropy from Be, through Mg and Y, to Zr is reflected in the transverse momentum distributions of the emitted electrons shown in Figure 6.2(b). For example, for Be$(10\bar{1}0)$ emission at the considered 4.75 eV photon energy, the calculated rms transverse momentum for photoemitted electrons parallel to the (0001) crystal direction, $\Delta p_{T,(0001)}$= 0.147 $(m_0\text{eV})^{1/2}$, is a factor of more than two lower than that for the $(01\bar{1}0)$ crystal direction, $\Delta p_{T,(01\bar{1}0)} = 0.312$ $(m_0\text{eV})^{1/2}$. For the $(10\bar{1}0)$-face of Mg, this ratio in the directional rms transverse momenta of the emitted electrons is reduced to ∼1.4, and it is further reduced for Y and Zr, with emission from the latter being close to isotropic. All the values of Δp_T extracted from the DFT analysis are also significantly lower than that expected from the isotropic single-band theory of Dowell and Jensen [52, 68]; namely, $\Delta p_{T0} = \sqrt{m_0 \Delta E/3}$ evaluated using the listed values of $\phi_{(10\bar{1}0)}$ determined from the thin-slab calculation [183] (from Table XII). This is primarily due to the contribution of 'hole-like' bands to photoemission for this HCP crystal orientation; unlike 'electron-like' bands, 'hole-like' states below the Fermi level are generally at higher p_T which reduces the available excess energy and hence the transmission efficiency over the work function barrier.

Figure 6.2(c) displays the photon energy dependence of both $\Delta p_{T,(0001)}$ and $\Delta p_{T,(01\bar{1}0)}$ determined by the DFT-based analysis for $(10\bar{1}0)$-face emission from the Be, Mg, Y and Zr HCP

crystalline photocathodes. The theoretical data points, which reflect the ±0.05 eV uncertainty in the work function evaluation, are well fit by $\Delta p_T = A\sqrt{(m_0 \Delta E)}$ (solid lines) for electrons emitted with p_T in both the (0001) and $(10\bar{1}0)$ crystal directions. Also shown by the dashed lines is the trend in $\Delta p_{T0}(\hbar\omega)$ from the analysis of Dowell and Jensen ($A = 0.577$) [52,68] which, in all four cases, predicts a value of the rms transverse momentum that is on average a factor of 2 greater than that determined by our analysis. The DFT-based photoemission analysis is, however, consistent with the available experimental data for polycrystalline Be [50, 56] and Mg [227] photocathodes, which are expected to preferentially expose $(10\bar{1}0)$ microcrystalline faces [260]. For Mg with $\hbar\omega = 4.66$ eV, Wang et al. [227] report an upper limit on the normalized transverse emittance of 0.40(±0.1) mm.mrad/mm, which equates to $\Delta p_T = 0.290(\pm 0.07)$ $(m_0\text{eV})^{1/2}$ — a value that is plotted in Figure 6.2(c) for Mg$(10\bar{1}0)$ emission with an estimated ±0.1 eV uncertainty in the effective work function due to both the uncertainty in the value of $\phi_{(10\bar{1}0)}$ and the Schottky effect in the employed RF gun. Similarly, the span of the two directional transverse values of Δp_T predicted for Be$(10\bar{1}0)$ emission is consistent with the value of $0.225(\pm 0.01)$ $(m_0\text{eV})^{1/2}$ (also plotted in Figure 6.2(c)) determined for a polycrystalline Be photocathode using the solenoid scan technique with a 20kV DC photo-gun and 4.75 eV photons [50, 56].

Table XIII summarizes the values of $A_{(0001)}$ and $A_{(01\bar{1}0)}$ (in terms of $A_{(0001)}$) extracted from the fits to the $\Delta p_T(\hbar\omega)$ DFT data in Figure 6.2(c), together with results obtained for $(10\bar{1}0)$-face emission from HCP Hf, Sc, and Ti. The two Group IIa elements (Be and Mg) are predicted

to have the largest anisotropy in the rms transverse momentum of the emitted electrons, while emission from both the Group IIIb (Sc and Y) and Group IVb (Ti, Zr, and Hf) elements should be isotropic in Δp_T to within 10% — a trend that is consistent with anisotropy associated with the photoemitting states (Figure 6.2(a)). The fact that all the values of $A_{(ijkl)}$ are around half of the $1/\sqrt{3}$ factor derived in Refs. [52] and [68] suggests that these seven $(10\bar{1}0)$-face emitting HCP elemental metal photocathodes will have a brightness $\sim 4\times$ larger than expected.

TABLE XIII: Photoemission properties of $(10\bar{1}0)$-face HCP metals.

	$\phi_{(10\bar{1}0)}$ (± 0.05 eV)	$A_{(0001)}$	$A_{(01\bar{1}0)}/A_{(0001)}$
Be	3.88	0.160	2.10
Mg	3.79	0.241	1.33
Sc	3.10	0.221	1.05
Y	3.08	0.222	1.08
Ti	3.63	0.295	1.04
Zr	3.59	0.287	1.03
Hf	3.63	0.281	1.08

We also note that in accordance with the results for the BCC and FCC elemental metal photocathodes (See Chapter 4) and 5, the DFT-based photoemission analysis indicates that the electron temperature $T_e = 300$K has little effect on Δp_T up to the melting points [226] of the four investigated HCP metal photocathodes. In particular, the values of A in $\Delta p_T = A\sqrt{m_0 \Delta E}$ do not change by more than about 1%, which is well within the intrinsic uncertainty of the simulation technique. To a large extent, this temperature insensitivity is due to the preponderance of 'hole-like' states for $(10\bar{1}0)$-face emission, for which higher electron temperatures generate

occupation in higher energy states with lower p_T that therefore do not contribute to significant increase in Δp_T.

6.3 Magnesium (0001)-Face Emission

In general, it is only photoemission from the HCP (0001)-face that may generate an electron beam with an isotropic transverse momentum distribution. In contrast to the HCP $(01\bar{1}0)$ face, the HCP (0001) face is more isotropic due to the hexagonal shape of HCP basal plane. As a result, the transverse momentum distribution of HCP (0001) crystal orientation is quite isotropic about the [0001] axis of symmetry and the photoemission direction. In this section, I take Mg(0001) emission as an exemplar, for which the work function (See Table XII) allows photoemission for incident 4.75eV photons. As in the previous analysis presented in this thesis, the DFT-based photoemission model outlined in Chapter 3 is used to evaluate the rms transverse momentum Δp_T of the emitted electrons.

Figure 6.3 displays the DFT based photoemission simulation results for emission from the (0001) face of magnesium ($\phi_{(0001)} = 3.87(\pm 0.05)$ eV). Figure 6.3(a) illustrates the electronic states that contribute to the photoemission (shaded region) below the Fermi level (solid line) along two crystal momentum directions $(10\bar{1}0)$ and $(01\bar{1}0)$ transverse to the (0001) emission direction when the incident photon energy is 4.75 eV; that is, for an excess energy ΔE $=0.88(\pm 0.05)$ eV. As expected from the band structure calculations [233, 261], the emission states in the basal plane of this HCP metal are 'electron-like' (positive dispersion) and highly

symmetric about the (0001) emission direction for this metal. The dashed line in Figure 6.3(a) indicates the maximum possible transverse momentum for the photoemitted electrons, which is simply given by $p_{T,max.} = (2m_0\Delta E)^{1/2} \approx 1.327\ (m_0\text{eV})^{1/2}$. At this value of the transverse momentum, the transmission efficiency over the photoemission barrier, $T(p_z, p_{z0})$, is zero since $p_{z0} = 0$, so that the transverse momentum distributions of the emitted electrons terminate at $p_{T,max.}$. As the transverse momentum p_T is reduced, more electron states below the Fermi level can contribute to photoemission with those states nearest the Fermi level having the largest local density of states $g(E, \vec{k})$ and the highest values of $T(p_z, p_{z0})$.

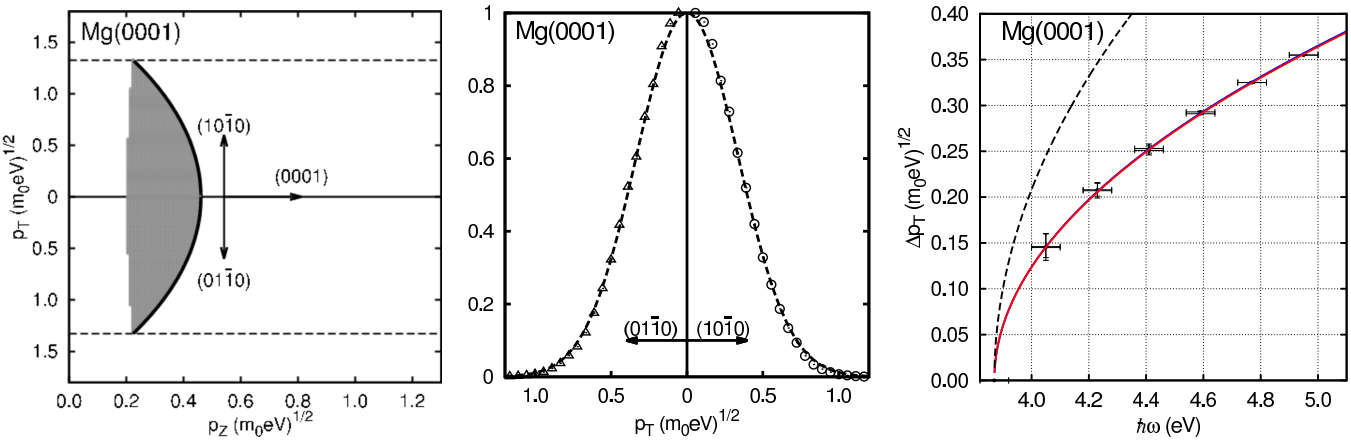

(a) (b) (c)

Figure 6.3: Mg(0001) photoemission analysis for $\hbar\omega = 4.75$eV. (a) Crystal momentum map of the electronic states (shaded regions) below the Fermi level (solid line) that may photoemit within $p_{T,max.} = \sqrt{2m_0\Delta E}$ (dashed lines) for the transverse (10$\bar{1}$0) and (01$\bar{1}$0) crystal directions; (b) Transverse momentum distributions of the photoemitted electrons in the (10$\bar{1}$0) and (01$\bar{1}$0) directions (Gaussian fits are guides to the eye); (c) Incident photon energy dependence of the rms transverse momentum Δp_T for electron temperatures $T_e \to 0$ (data points with solid red line fit; $\Delta p_T = A\sqrt{m_0\Delta E}$), $T_e = 300$K (dot-dashed line), together with the expected form of $\Delta p_T(\hbar\omega)$ from Refs. [52] and [68] (dashed line).

The high transverse symmetry of the Γ_4^- emission band about the (0001) crystal direction ensures that the resulting weighted transverse momentum distributions of the photoemitted electrons are nearly identical along the $(10\bar{1}0)$ and $(01\bar{1}0)$ crystal momentum directions (Figure 6.3(b)). The spatially-averaged value of the rms transverse momentum Δp_T extracted from these p_T distributions for Mg(0001) emission is $0.322(\pm 0.008)$ $(m_0\text{eV})^{1/2}$ — a value which is only 60% of that predicted by prior analyses [52, 68]; $\Delta p_{T0} = 0.542(\pm 0.015)$ $(m_0\text{eV})^{1/2}$. The explanation for the lower than expected value of Δp_T is associated with the energetic position and dispersion of the Γ_4^- electron band. Our band structure calculations indicate that the energetic minimum of this band at the Γ point is only 1.2 eV below the Fermi level. As a result, for $\Delta E \approx 0.9$ eV, nearly all the available states along the (0001) crystal direction at $p_T = 0$ are accessed, generating a gibbous, rather than crescent (See Figure 4.6, Figure 4.8, Figure 4.10, Figure 5.5 and Figure 5.9), shape to the shaded region in Figure 6.3(a). Thus, disproportionately more states at lower p_T emit than at higher p_T, which yields a reduced value of Δp_T.

Figure 6.3(c) displays the dependence of Δp_T on the incident photon energy $\hbar\omega$ predicted by the DFT-based simulation for photoemission from Mg(0001). The solid line is a fit to the theoretical data points of the form $\Delta p_T = A\sqrt{m_0(\hbar\omega - \phi_{(0001)})}$, giving a value for A of 0.343. Comparing this value of A with 0.577 from $\Delta p_{T0} = \sqrt{m_0 \Delta E/3}$ (dashed line in Figure 6.3(c)),

again indicates that the rms transverse momentum from Mg(0001) is a factor of ∼1.7 less than expected from prior analyses [52, 68]. Both of these evaluations of Δp_T are, again, determined in the 'zero temperature' limit; that is, for an electron temperature $T_e \to 0$, so that no electrons occupy states above the Fermi level. The dot-dashed line (just above the solid line) in Figure 6.3(c) shows the predicted form of $\Delta p_T(\hbar\omega)$ when $T_e = 300$K (data points not shown) which is evaluated by including the Fermi-Dirac function $f(E) = 1/(1+\exp[-(E_F - E)/k_B T_e])$, where k_B is Boltzmann's constant, to describe the occupation of the electronic states around the Fermi energy E_F, albeit for the 'zero temperature' crystal band structure. The increase (or change) in Δp_T is less than 1% in this case since ΔE and the value of E_F measured from the bottom of the Γ_4^- band are both much greater than $k_B T_e$; that is to say that the additional partially populated states above the Fermi level are a very small perturbation in the photoemission simulation. Even if T_e is increased to 923K, the melting point of Mg [226], the theoretical increase in Δp_T is insignificant compared to the uncertainties on the DFT-based photoemission simulation. We note that the Boltzmann tail of the Fermi-Dirac distribution will allow photoemission for $\hbar\omega < \phi_{(0001)}$ [65], essentially photo-assisted thermionic emission, but this effect is again not considered here as the emission efficiency will be much reduced.

6.4 Berillium (0001)-Face Emission

Photoemission from the (0001) face of HCP metals generally produces a relatively isotropic rms transverse momentum distribution since the basal plane band dispersion is also quite isotropic, as shown for Mg(0001) in Figure 6.3. There are, however, complications that are

introduced by both the details of the electronic band structure, coupled with the required energy-momentum relationship (Equation 3.2), and the presence of two-dimensional surface states.

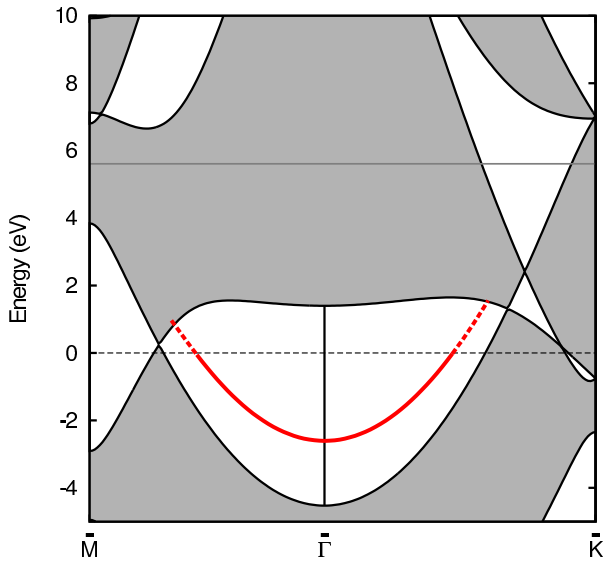

Figure 6.4: Calculated Be(0001) bulk and surface electronic states in the SBZ: Projected bulk states (grey shading) and the surface state below (solid red line) and above (dashed red line) the Fermi level (thin dashed line). The DFT evaluated vacuum level at $\phi_{(0001)}$=5.61 eV is indicated by a thin solid line.

In contrast to Mg, the Fermi level in Be and the Group IIIb metals (Sc and Y) does not cross the $\Gamma \rightarrow$ A direction of the Brillouin zone [262], meaning that there are no bulk electronic states that can photoemit electrons with zero transverse momentum p_T for the (0001) emission direction. As a result, the values of $\phi_{(0001)}$ evaluated from the energetic difference between the vacuum and Fermi levels (Table XII) will not reflect the actual bulk-state work function for the (0001) crystal face. The most extreme case is Be(0001) emission since, as shown in Figure 6.4,

the bottom of the occupied Γ_3^+ band with an effective mass greater than the free electron mass m_0 [263] is 4.6 eV below the Fermi level. As a result, the energy-momentum relationships governing the one-step photoemission process (Equation 3.2) dictate that the first electrons to be emitted from the bulk states originate near the Γ point and require a photon energy $\hbar\omega > \phi_{(0001)} + 4.6$ eV, giving an effective (0001)-face work function of about 10.2 eV — an energy well beyond common UV laser sources. Similar arguments associated with the position of the occupied bands in Sc and Y indicate that their thin-slab calculated values of $\phi_{(0001)}$ are also increased to give effective work functions of around 4.55 eV and 4.22 eV, respectively.

For sufficiently clean Be(0001) crystal faces, however, the effective work function will only be around 8.4 eV due to the existence of a strong two-dimensional surface state in the 6 eV energy gap between the lower occupied Γ_3^+ and upper unoccupied Γ_4^- bulk electronic bands [60–64]. This surface state, with its near-perfect parabolic dispersion about the $\overline{\Gamma}$ point of the SBZ, lies 1.8eV above the lower Γ_3^+ bulk band at zone center and its $\overline{\Gamma}$ point is 2.8 eV below the Fermi level [60–64]. Angle-resolved photoemission spectroscopy (ARPES) measurements [63] have indicated that the effective mass of the surface state is about $1.50m_0$; $m^* = 1.53m_0$ in the $\overline{\Gamma} \rightarrow \overline{\mathrm{M}}$ direction and $m^* = 1.45m_0$ in the $\overline{\Gamma} \rightarrow \overline{\mathrm{K}}$ direction. As for emission from the bulk states, this means that photoemission from the surface state of Be(0001) will first occur from states around the $\overline{\Gamma}$ point as this requires the least energy. Consequently, photoemission from the Be(0001) surface state is predicted to only occur when $\hbar\omega > \phi_{(0001)} + 2.8$ eV, where

$\phi_{(0001)}$=5.61 eV.

For the theoretical determination of the characteristics of the Be(0001) surface state within our DFT framework, thin-slab calculations employing the LDA pseudopotentials [188] in the Quantum-ESPRESSO code [101] are used. The surface is modeled in the two-dimensional irreducible SBZ with 13 atomic layers separated by 15 Å of vacuum — the slab configuration used to obtain a reasonable value for the work function for the Be(0001) surface, which then sets the energy scale for the two-dimensional quantum-confined surface state. Figure 6.4 shows the results of the computed Be(0001) surface state electronic structure in the two transverse symmetry directions ($\overline{\Gamma\mathrm{M}}$ and $\overline{\Gamma\mathrm{K}}$) of the SBZ along with the projected bulk states. The calculated minimum energy of the surface state (solid red line) at the $\overline{\Gamma}$ point is 2.83 eV below the Fermi level (dashed line), which is in good agreement with the experimental value of 2.8($\pm$0.05) eV [60–64]. Further, our evaluation of the Be(0001) surface state indicates that the dispersion of the confined state is quite isotropic with a transverse effective mass $m_T^* \approx 1.5m_0$, in agreement with prior work [63]. At the $\overline{\Gamma}$ point, the surface state band is calculated to be 1.92 eV above the minimum energy at the same crystal momentum of the lower bulk band Γ_3^+ from which the electrons in the surface state originate [60–64]. This 'zero point' energy ΔE_{ss} then allows evaluation of the longitudinal momentum of the electrons in the surface state; $p_z = \sqrt{2m_{ss}^* \Delta E_{ss}}$ $\approx 2.4\ (m_0\mathrm{eV})^{1/2}$, if one assumes $m_{ss}^* \approx 1.5m_0$ is also the effective electron mass of the surface state in the z direction (i.e., the (0001) crystal direction).

With these assumed constant values of p_z and m_z for the emitting state, all required parameters in our DFT photoemission analysis are defined; in particular, those associated with the flux transmission probability over the work function barrier (Equation 2.14). The predicted p_T distribution of the emitted electrons for an excess energy $\Delta E = 0.3$ eV (a photon energy $\hbar\omega = 8.74$ eV (142 nm)) is shown in Figure 6.5. As $m_T^* > m_0$ and the surface state has a constant density of states $g(E, \vec{k})$, electrons are predominantly photoemitted from the $\overline{\Gamma}$ point and no electrons may be emitted beyond $p_{T,max} = \sqrt{2m_0\Delta E} \approx 0.77\ (m_0\text{eV})^{1/2}$. In practice, $T(p_z, p_{z0})$ severely curtails emission beyond $p_T = 0.5\ (m_0\text{eV})^{1/2}$, resulting in a predicted value of $\Delta p_{T,\text{Be(0001)}} = 0.141(\pm 0.05)\ (m_0\text{eV})^{1/2}$. As expected from the isotropic dispersion of the two-dimensional surface state, the p_T distribution is also symmetric with respect to $p_T = 0$. If its effective mass were less than m_0, the one-step analysis would predict emission peaked at $p_T = \sqrt{2m^*E_F}$, which may then directly produce an electron beam suitable for hollow cone illumination [58, 211, 212].

6.5 (0001)-Face Emission From Other HCP Metals

Surface states also exist on the (0001) face of other HCP metals [264,265], but are less robust than that of Be(0001). In the case of Mg(0001) [266, 267], the Fermi level cuts the upper Γ_4^- band ensuring that there are filled bulk states around the $\overline{\Gamma}$ point of the SBZ which contribute to and dominate the photoemission as shown in Figure 6.3. For Sc and Y, our DFT-based analysis indicates that clean (0001) crystal surfaces of these elemental metals should also have

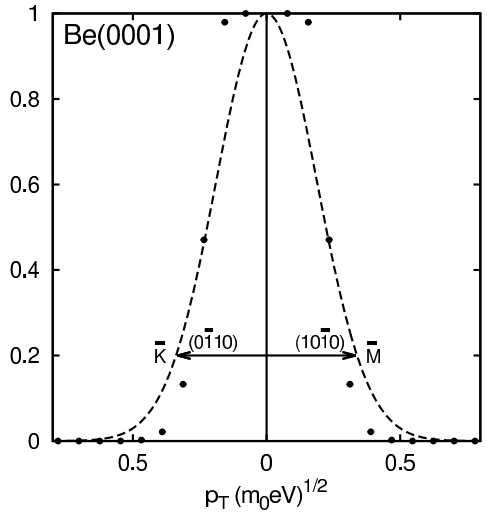

Figure 6.5: Evaluated electron transverse momentum distributions (solid circles) in the $\overline{\mathrm{M}}$ and $\overline{\mathrm{K}}$ directions of the SBZ (the bulk $(10\bar{1}0)$ and $(01\bar{1}0)$ directions) for photoemission from the Be(0001) surface state with $\hbar\omega$=8.74 eV. (Gaussian fit is guide to the eye (dashed line).)

a surface state. To our knowledge, however, there have been no experimental studies on either Sc(0001) or Y(0001) to compare with and verify our calculations.

The simulation of bulk state photoemission from the (0001) faces of the Group IVb metals (Ti, Zr, and Hf) is complicated, much more so than for their $(10\bar{1}0)$ faces, by the positioning of the Fermi level in the DFT evaluated band structure. The reason for this is the close proximity of the Γ_3^+ band to the Fermi level in the $\Gamma \rightarrow$ A direction; that is, whether or not the Γ_3^+ band cuts the Fermi level in this direction. Our DFT calculations suggest that it does not, which results in their being no emitting bulk states with $p_T = 0$. On the other hand, the work of D.A. Papaconstantopoulos [262] indicates that it does, while the Fermi surface database from the

University of Florida [268] shows a Fermi surface along the $\Gamma \rightarrow$ A direction for Ti and Hf, but not for Zr. As the one-step photoemission process is sensitive to the details of the electronic band structure near the Fermi level, either further more accurate theoretical calculations or, ideally, detailed ARPES (or Δp_T) measurements are needed to determine the photoemission properties of the (0001) faces of the Group IIIb metals.

The use of such a state can be dependent upon the cleanliness of the laser-driven electron gun since chemical contamination of the photocathode surface may destroy environmentally sensitive surface states. Similar considerations also affect the use of bulk elemental hcp metal photocathodes and together with impractical high work functions, low melting points, and magnetic effects effectively restrict the choice to only a handful of elemental hcp metals: Be, Mg, Sc, Ti, Y and Zr. Bi-metal hcp compounds may well overcome many such issues.

CHAPTER 7

SEMICONDUCTOR PHOTOCATHODES

The previous investigations (Chapter 3 - 6) into the photoemission properties of different crystal structure metal photocathodes (BCC, FCC and HCP) have shown that the DFT-based metal photoemission model provides good agreement with the experimental measurements of photoemission properties; in particular, the work function and the emitted electrons' transverse momentum distribution. As a narrow transverse momentum distribution with a low Δp_T increases the brightness of a photocathode, the DFT-based analysis technique is now being used to search for and evaluate potential high brightness photocathode materials. Based on the prior knowledge of the properties of lead chalcogenides [269–272] and the theoretical evaluations of metal photocathodes, the (111) face of PbTe is an extremely attractive photocathode material — it is also well-known as a thermoelectric material with a number of attractive properties such as relative insensitivity to oxidation, low resistivity and long lifetime [273–275].

In Section 7.1, I present an overview of semiconductor photoemission properties, including a previous analysis of excited-state thermionic emission (ESTE) from p-type GaSb(001) and InSb(001) single crystals. In Section 7.2, I evaluate the electronic properties of lead chalcogenides with special emphasis on the (111) face emission due to the very low effective mass on Λ_6^+ 'hole-like' valence band in the L valley. I also present the DFT-based calculations of the electronic properties of lead salts. In Section 7.3, I evaluate the rms transverse momentum

of (111)-oriented PbTe single crystals and compare the results of PbTe(111) with other known photocathodes as well as a cold atom electron source and show that the PbTe(111) single crystal is a potential high brightness photocathode.

7.1 Introduction to Semiconductor Photoemission Properties

Semiconductors as laser-driven electron sources can have high-spin polarization [276] and excellent QEs [277] and, in fact, hold the record for the highest QEs ever achieved so far [278]. However, compared to metals, many semiconductors are not prompt emitters with response times from 1-10 picoseconds or more. In stark contrast to the limited quantum efficiency of metals (which in the case of copper, for instance, is only 0.014% even at a UV drive laser wavelength of 266 nanometers [82]), the quantum efficiency of semiconductors can be quite good, of the order of 1-50% [277, 279], depending on the material choice and drive laser wavelength; for example, GaAs(001) at 800nm [280–282] and CsKTe at 262nm [283]. Generally, such high quantum efficiency semiconductor photocathodes operate in the negative electron affinity (NEA) regime where the electrons are excited into the condition band of the material whose energy minimum is above the vacuum level thus allowing nearly all photoexcited electrons to 'fall out' of the cathode surface.

Although less efficient, the related process of ESTE has been observed by J.A.Berger *et al.* in undoped GaSb(100) and moderately p-type InSb(100) using UV pulses ($\hbar\omega = 4.75$ eV) with a duration of $\sim$ 4ps [65]. Here, The known properties of the two semiconductors [284–286]

allowed one to determine that photoemission was due to therminonic emission from hot electron distribution photoexcited into the upper Γ_8 conduction band, as $\phi_{(100)} > \hbar\omega$ for both semiconductors. As shown in Figure 7.1, with photon energy $\hbar\omega$, the valence bands (heavy hole, light hole, and split-off bands) can directly populate the upper Γ_8 conduction band located at 3.77eV and 3.59eV above the valence band maximum (VBM) in GaSb and InSb [286]. With $0.3m_0$ ($0.5m_0$) effective mass m^* for the Γ_8 band of GaSb (InSb), the initially average excess energy $E_{electron}$ above the Γ_8 band is 0.35eV (0.41eV), which corresponds to a photoexcited electron temperature T_e of 4,200K (4,920K). The results is a well-populated Boltzmann tail extending above the vacuum level located at an effective work function ϕ_{eff} of 0.99eV (1.18eV) above the Γ_8 conduction band minimum. Using a the Boltzmann distribution, one can deduce that a $\exp[-\phi_{eff}/k_BT_e]$~0.06 fraction of the hot electron population is above the vacuum level and so can produce the observed thermionic emission. The dependence of Δp_T on m^* is then readily explained through a consideration of energy and momentum conservation in transmission across a boundary with a potential step associated with ϕ_{eff} [65], and it can be expressed by $\Delta p_T = \sqrt{m^* k_B T_e}$.

In contrast to ESTE, one-step photoemission (Section 2.2) in narrow-gap semiconductors with low effective band masses m^*, which requires photon energy greater than the E_F to vacuum offset, is also of great interest and and has been recently observed by B. L. Rickman *et al* in PbTe(111). It is also well known that the lead chalcogenides represent an important family of materials which have applications such as thermoelectric performance at high-temperature [287];

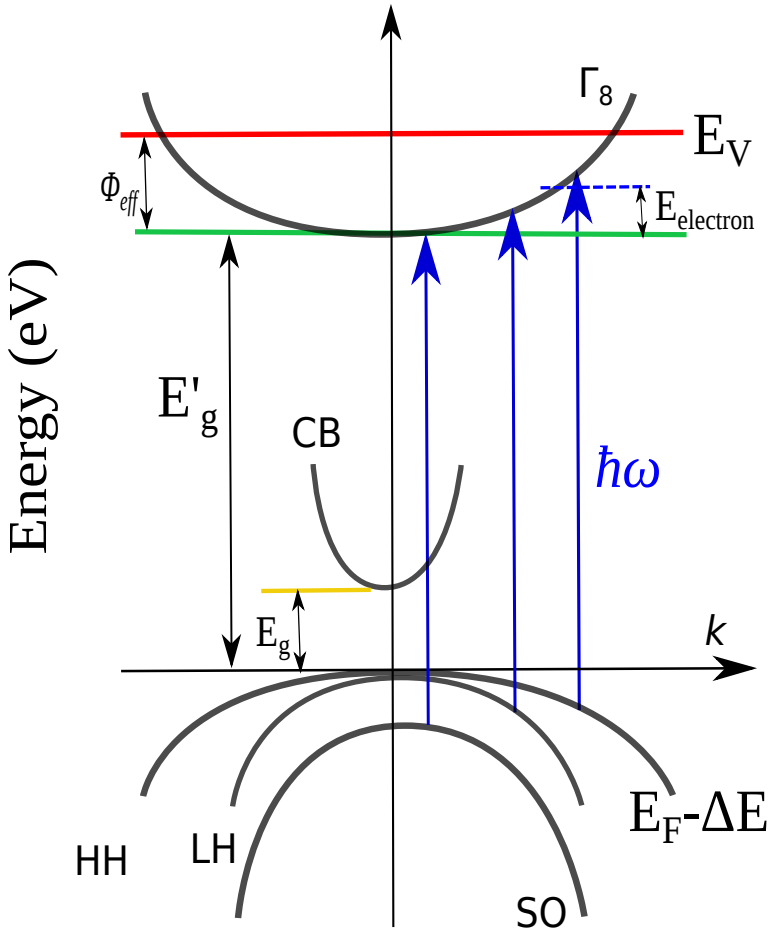

Figure 7.1: Schematic of ESTE in III-antimonides. The vacuum level, conduction band minimum (CBM), Γ_8 band minimum are in red, green, yellow solid line, respectively. E_g is the band gap between CBM and the valence band maximum (VBM); E_g' is the band gap between the Γ_8 band minimum and VBM; ϕ_{eff} is the energy offset between vacuum level and Γ_8 band minimum. $E_{electron}$ is defined to be the initially average excess energy above the Γ_8 band minimum. The three valence bands (heavy hole, light hole, and split-off bands) are labeled by HH, LH, and SO, respectively.

conversion of heat and electricity [288], and the generation electricity from waste heat [289]. The lead salts PbX (X=S, Se, Te) are well-studied narrow-gap semiconductors, as they can be employed both as an infrared detector [290, 291] and a thermoelectric material [273, 292]. In a bid to gain further insight to the use of PbX (X=S, Se, Te) compounds for future high brightness electron sources, I report here a benchmark study of the photoemission properties of these semiconductors, focusing particularly on the (111) crystal orientation relevant to low Δp_T performance.

7.2 *p*-type Lead Chalcogenides

A number of recent investigations, both experimental and theoretical, have aimed to gather insight into super-high brightness photocathodes [276, 293, 294]. According to our investigation of emission properties of metal photocathodes published in Journal of Applied Physics [171] and Physical Review ST Accelerators and Beams [295], photoemission from a low m^* 'hole-like' electron band is likely to result in low Δp_T, and rms transverse momentum for emission from such band is almost electron temperature independent. The prior theoretical calculations of the electronic properties of lead chalcogenides in the rocksalt crystal structure implemented the quasiparticle self-consistent approach [269, 296], the augmented-plane-wave method [270] and $\vec{k} \cdot \vec{p}$ perturbation theory [297]. Together with experimental measurements [298–303], these calculations show that the band structures of lead salts have a 'hole-like' valence band with very low effective mass at the L valley. These previous studies also show that the band structures of PbSe, PbS and PbTe are generally similar with minor differences in the spacing of the various

valence and conduction bands. The valence and conduction band extrema both occur at the L point of the BZ, and the 'hole-like' Λ_6^+ valence band is relatively well isolated from other occupied bands at the high symmetry L point. Both the conduction Λ_6^- and valence band Λ_6^+ extrema have low effective masses. Importantly, the electron states in the neighborhood of the vicinity of L point dominate the transport and optical properties of lead salts [304]. Below, for the purposes of the photoemission simulation, I revisit the electronic calculation of PbX compounds by DFT in detail, and confirm and supplement the results of earlier investigations.

Bulk PbX (X=S, Se and Te) have a rock-salt crystal structure with experimental low-temperature equilibrium lattice constants of $5.909\mathring{A}$, $6.098\mathring{A}$, and $6.428\mathring{A}$, respectively [269]. As shown in Figure 7.2, each of the two atom types in the rock-salt structure forms a separate face-centered cubic lattice. To carry out DFT calculations for a bulk crystal, the electronic wave function is described by plane-wave-basis sets with a kinetic energy cutoff of 28 Ry, and the energy cutoff for the charge density was set to 280 Ry. A threshold of 10^{-4} Ry/Bohr on the force for the ionic relaxation and 0.05GPa on the pressure for the cell relaxation were used. Note that although GGA is more complex and indeed gives better bulk properties than LDA, it is well-known that LDA works better than GGA for certain classes of systems and properties, in particular for calculating the properties of many nonmetallic systems [305]. This is because LDA shows a better cancellation of errors between surface exchange and correlation energies [306, 307]. Therefore, LDA is selected as the exchange-correlation functional for the lead salt calculations. The DFT lattice constant convergence is performed using a LDA pseu-

dopotential [188], and the DFT calculated lattice constants are generally within 4.0% of the experimental values as shown in Table XIV.

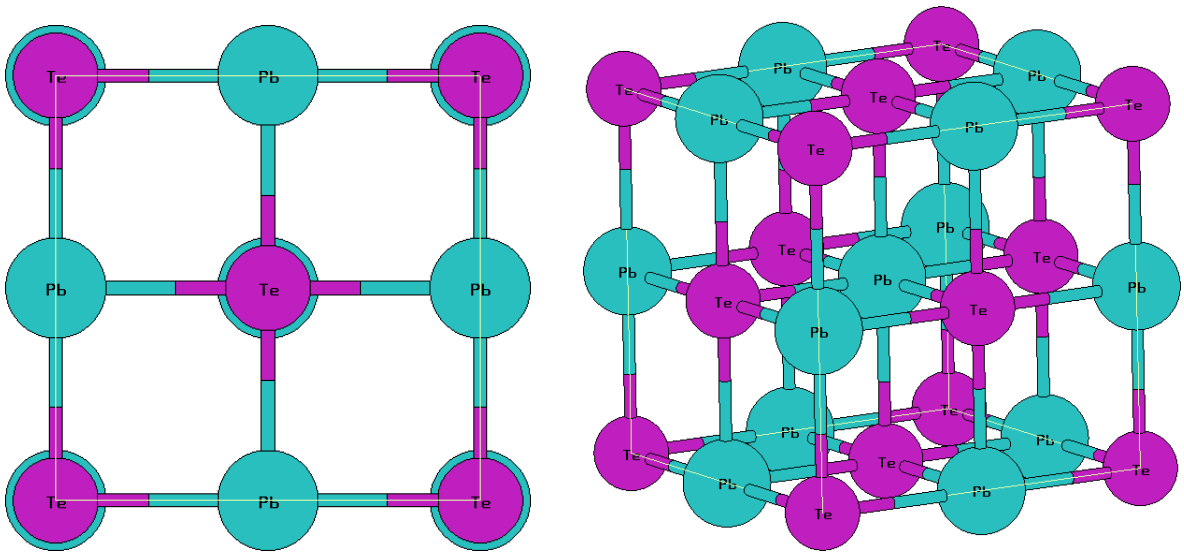

Figure 7.2: PbTe rock-salt crystal structure. Left panel is the top view; right panel is the (45^o, 45^o, 45^o) viewing angle. In rock-salt IV-VI compounds, each IV and VI atom is separated by a/2.

TABLE XIV: Lattice constants and hole effective masses (transverse to the Γ - L direction) for lead chalcogenides.

	Expt.(a.u) [308]	Expt.(a.u) [309]	DFT(a.u)	$m^*_{T,Expt.}/m_0$ [298]
PbS	11.22	11.20	11.01	0.075
PbSe	11.57	11.56	11.31	0.034
PbTe	12.21	12.18	12.01	0.022

For the band structure calculations, using the theoretical lattice constants, the self-consistent energy is computed by integration over a 6×6×6 k-mesh in the first BZ with energy cutoff 340eV. Full-relativistic effects are included in the DFT calculations, while spin-orbit coupling

is included during the plane wave self-consistency iterations. The states around the gap are dominated by Pb and X highly hybridized p bands [269]. As shown in Figure 7.3, the average direct band gap is 2-3eV, while the minimum band gap occurs at the L point with similar values of 0.30eV, 0.25eV, 0.26eV for PbX(X=S, Se, and Te), respectively. The DFT calculated lead salts' band structures are generally within 5% of the experimental low temperature values [310], especially, it shows the agreement about the remarkable spiky Λ_6^+ valence band in the vicinity of L point in both L–K and Γ–L directions. The experimental measured transverse effective masses (m_T^*) [298] for the Λ_6^+ band ('hole-like') displayed in Table XIV show that m_T^* of lead salts are less than $0.1m_0$, which is a factor of around 10 less than that of elemental metals. A close look at the effective masses obtained for the Λ_6^+ band indicates that, among these semiconductors, PbTe owns the lowest $\mathrm{m}_T^* = 0.022m_0$. This makes PbTe(111) an attractive single crystal photoemission material.

The (111) surfaces of the lead salt compounds are terminated by either lead or chalcogen surface atoms. Although for the pure lead salts these surfaces are unreconstructed under all conditions, the chemical composition of the surface may be determined by measuring the intensity of the specularly reflected electron beam in reflection high-energy electron diffraction [311], which clearly indicates that a surface dipole moment is formed naturally from alternatively terminated Pb and X layers. For calculating the work function for the (111) cleavage face in PbX compounds, it is possible to build 'effectively charged' lead salt slabs in three different

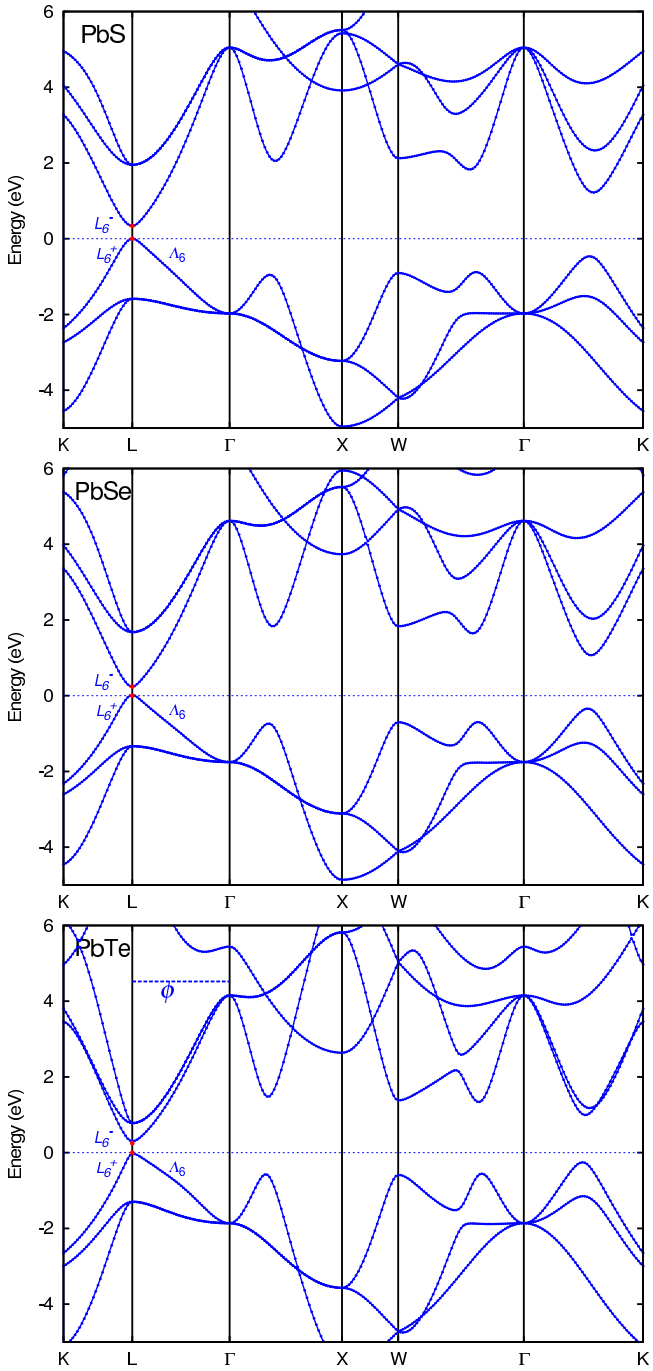

Figure 7.3: PbX (X=S, Se and Te) band structure along major high-symmetry points and lines with E_F (black dashed line) at zero energy placed at the top of the VBM. The CBM (L_6^-) and VBM (L_6^+) are labeled by red dots. $\Gamma \rightarrow L$ is the [111] direction which has the Λ_6^+ band with a low m_T^* below the Fermi level. For the PbTe band plot, the calculated (111) face work function is indicated by a blue dashed line. The VBM state is an even L_6^+ state, while the CBM state is an odd L_6^- state.

ways based on the terminations of (111) cleaved surfaces: 1) X terminated layers on both sides; 2) Pb terminated layers on both sides; 3) X terminated and Pb terminated on one side each. These charged-slabs will result in different work functions due to the different dipole slab terminations. In order to simulate the relationship between work function and slab termination configuration, DFT work function calculation are performed on all three slab configurations. For all the slab configurations, the Fermi level is pinned just above the VBM by using 0.02 Ry Gaussian spreading; therefore, the evaluated work function is defined as the energy offset from the VBM to vacuum level. To ensure the accuracy of our work function calculations, the vacuum thickness is enlarged from 10 to 15$\mathring{A}$, the (1×1) supercell thickness (n) is increased from 7 to 11 atomic layers together with $n \times n \times 1$ Monkhorst Pack points [106], to ensure that the work function values converge within 0.05eV. Dipole correction is added so that the contributions from electrostatic interaction due to the periodic boundary conditions is taken into consideration.

As shown in Table XV, the work function values increase as the slab termination changes from metal to chalcogen, which is consistent with the trend in the work function values from polycrystalline Pb (4.25eV) to the chalcogens (Se (5.90eV) and Te (4.95eV)) [125]. Khokhlov indicates that at elevated temperatures the lead salt (111) surfaces prefer to be metal terminated [312], but all types of termination exist. Therefore, the work functions of lead salts are as a function of the distribution of termination configurations, thus explaining the large (∼0.4eV) variation in the experimentally measured values of $\phi_{(111)}$. Typical work functions of

the three possible dipole configurations (Pb, Chalcogen, and Pb/Chalcogen) are generally less than 4.75eV thus allowing photoemission for 261nm ($\hbar\omega = 4.75$eV) UV laser pulses obtained by harmonic conversion of a diode-pumped, 63MHz repetition rate, femtosecond Yb:KGW laser [313].

TABLE XV: PbS(111), PbSe(111) and PbTe(111) work functions in eV.

	Expt.	DFT (Pb)	DFT (Chalcogen)	DFT (Pb/Chalcogen)
PbS(111)	4.80[a] –5.20[b]	4.49	4.79	4.58
PbSe(111)	4.48[c]	4.38	4.74	4.53
PbTe(111)	4.10[d]–4.60[e]	4.21	4.54	4.30

[a]Reference [314]
[b]Reference [315]
[c]Reference [271]
[d]Reference [316]
[e]Reference [317]

The special feature of PbX compounds in the interior of the first BZ can reveal the electronic properties of PbX compounds in both transverse and longitudinal point views. As is well known, the Fermi level of semiconductor is pinned by its impurities — the dopant. For undoped or weakly p-typed (111)-oriented lead salt single crystal, the Fermi level is just above the top of 'hole-like' band dispersions at the L point (VBM). Unlike elemental metals, that have electron bands across the Fermi level and available electron states at the Fermi energy, semiconductors do not have such an energy surface if the Fermi level is placed in the band gap. So, instead, in Figure 7.4 I plot the hole surface at a constant energy E=E_F - 0.30eV in the BZ for all three PbX compounds using a $20 \times 20 \times 20$ uniform k-grid imposed on the 3D irreducible BZ. This is thus equivalent in photoemission with an excess energy $\Delta E = 0.3$eV, irrespective of crystal orientation and emission boundary conditions. It is clear that in [111] direction ($\Gamma \rightarrow L$)

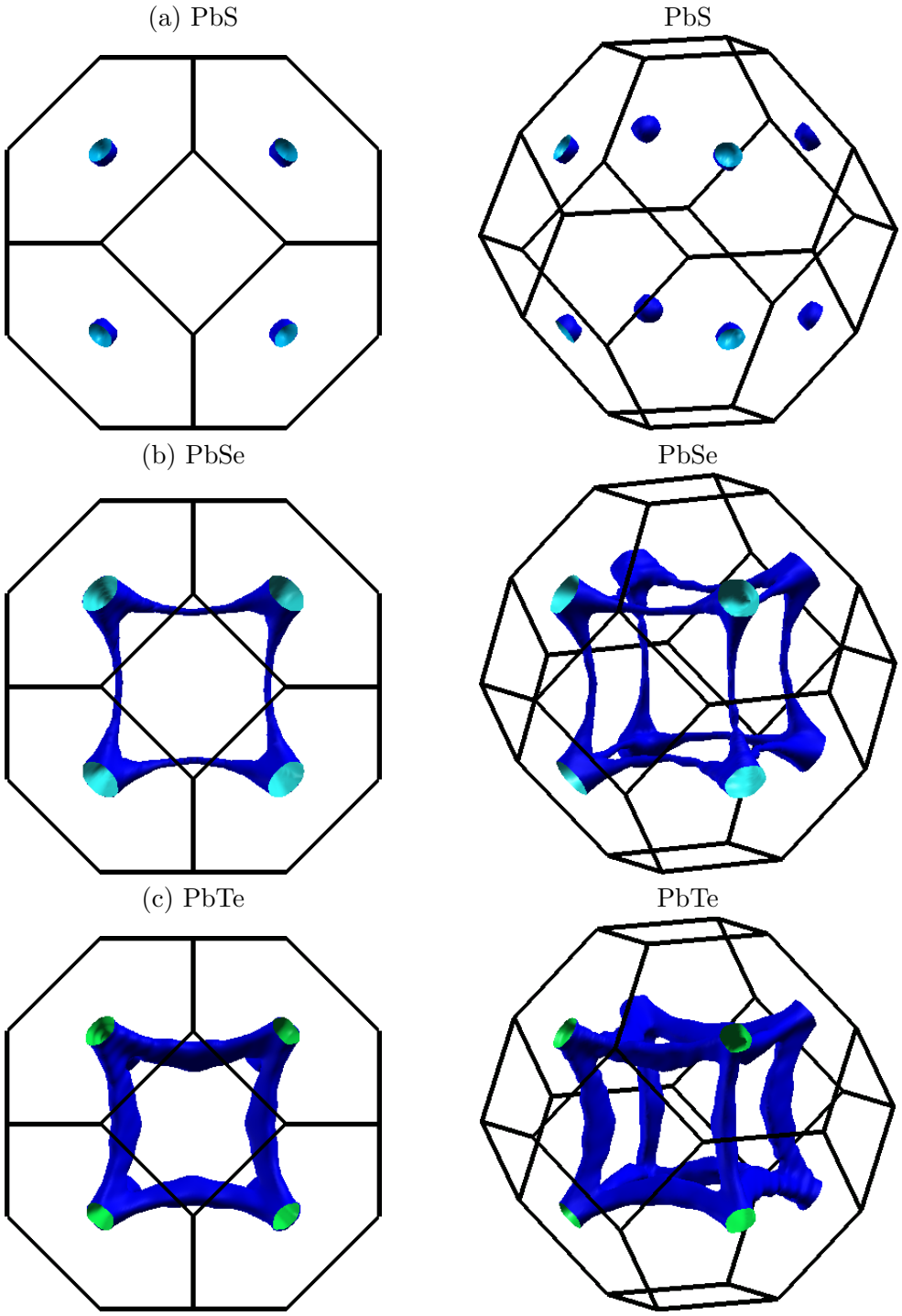

Figure 7.4: The E_F-ΔE energy surface for PbX (X=S, Se and Te) with $\Delta E = 0.3$eV. The right panel is top view; the left panel is the (45^o, 45^o, 45^o) aerial view. The surface is isotropically distributed about the Γ–L axis.

there is a small 'muffin-tin' like surfaces (blue circle) with radii of $0.22\sqrt{m_0eV}$, $0.25\sqrt{m_0eV}$, and $0.20\sqrt{m_0eV}$ for PbS, PbSe and PbTe, respectively.

Figure 7.5 shows the PbTe(111) face momentum distributions in the transverse $(\bar{1}10)$ and $(1\bar{1}2)$ directions where $\Delta E = 0.3$eV. The photoemitting contours are condensed and located at the edge of L point with a 'muffin-tin' shape in the first BZ. For $\Delta E = 0.3$eV, the theoretical $\Delta p_{T,max}$ equals $0.775\sqrt{m_0eV}$, which is indicated by the red dashed lines. Clearly, the 'hole-like' Λ_6^+ valence band itself plays the dominant role in confining the maximum transverse momentum within the band tip so that the transverse momentum does not spread from 0 to 0.775 $\sqrt{m_0eV}$. The energy surfaces displayed in Figure 7.5 for the same ΔE indicate that this will also be the case for (111)-face emission in the other PbX salts. In fact, the low values of m_T^* for the $\Lambda 6^+$ band in all three lead chalcogenides salts limit p_T to less than half of $p_{T,max} = \sqrt{2m_0(\Delta E)}$ — a band bending constraint on p_T that is not present in most metals and their alloys. This important characteristic of PbX(111) photocathodes will lead to the emission of well converged (low Δp_T) electron beams.

7.3 Δp_T Analysis of PbTe(111)

The thin-slab work function analysis in Section 7.2 indicates that $\phi_{(111)}$ ranges from 4.21 eV to 4.54eV for PbTe (See Table XV) — within ±0.1eV of the reported experimental range

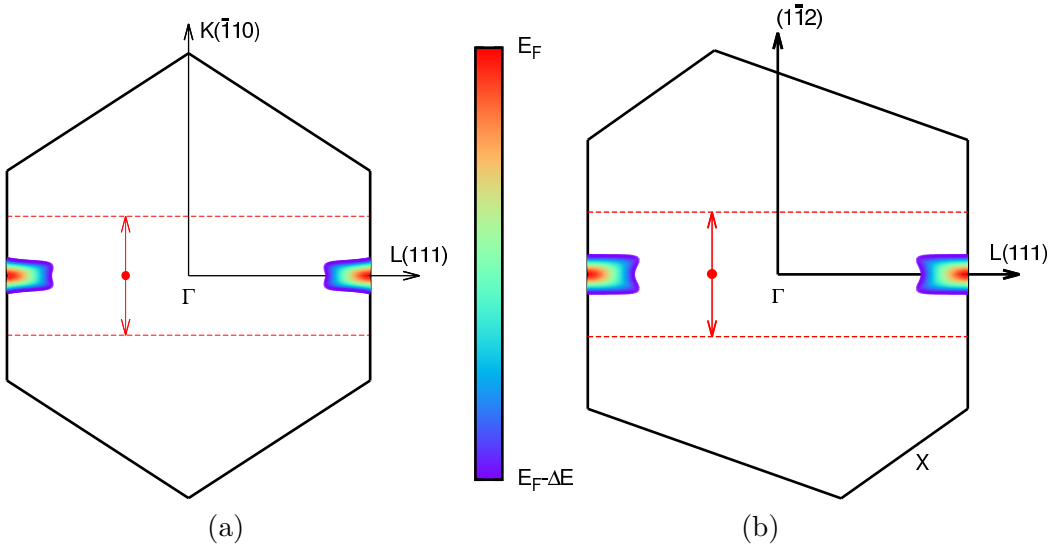

Figure 7.5: PbTe(111) face photoemitting electron energy states contour for excess energy ΔE = 0.3eV. The $p_{T,max}$ values are labeled by the red dashed lines. The color palette from red to blue indicates the energy level from E_F to $E_F - \Delta E$. (a) The $(\bar{1}10)$ transverse momentum face. (b) The $(1\bar{1}2)$ transverse momentum face.

of 4.10 to 4.60eV. As a result, for incident 4.75eV (or even 4.67eV) UV photons, photoemission since the maximum possible transverse momentum $p_{T,max.} = (2m_0\Delta E)^{1/2}$ of around 0.54∼1.14 $(m_0\text{eV})^{1/2}$ should allow access to many electronic states in the PbTe(111) photocathodes. However, as shown below, the Λ_6^+ band structure (due to the low m_T^*) can play a major role in determining the maximum transverse momentum $p_{T,max}$ as well as Δp_T of the photoemitted electrons.

Figure 7.6 displays the results from the DFT-based analysis for photoemission from the (111) face of PbTe with $\hbar\omega$ = 4.75eV using the work function calculated for the Te termi-

nated slab, i.e, 4.54eV. The crystal momentum depiction of the photoemitting electronic states (shaded regions) ΔE=0.21eV below the Fermi level (solid line) in Figure 7.6(a) clearly shows that emission is from the 'hole-like' states associated with the Λ_6^+ band Fermi surface centered on the Γ-point of the Brillouin zone. The emitting states are very isotropic about the primary [111] direction and have p_T maximum of $0.21\sqrt{m_0 eV}$, which is a factor of nearly 3 less than the value expected from $p_{T,max} = \sqrt{2m_0(\Delta E)}$. As a result, the transverse momentum distribution for the emitted electrons (See Figure 7.6(b)) is quite narrow. In addition, I note that unlike the III-Antimonies, the PbTe band structure calculation (Figure 7.3) indicates that there are no upper conduction band minimum within in 3eV of the vacuum energy — thus eliminating the possible of ESTE with higher p_T. For the work functions associated with the three termination configurations (See Table XV), the calculated Δp_T of PbTe(111) is $0.067\sqrt{m_0 eV}$, $0.125\sqrt{m_0 eV}$, and $0.152\sqrt{m_0 eV}$ for the Te, Te/Pb, and Pb terminated slabs, respectively. As expected, with the same incident photon energy, a Te terminated PbTe(111) single crystal photocathode is predicted to have the lowest Δp_T as it also has the smallest ΔE.

The expected transverse momentum distribution of a cold atom photoelectron source at 14(±2)K [318] is shown in Figure 7.7 (black dashed line), assuming a Gaussian distribution of the form $\exp[-\frac{p_T^2}{2\Delta p_T^2}]$ with Δp_T evaluated using $\sqrt{m_0 k_B T} = 0.0347 \pm 0.0131\sqrt{m_0 eV}$. For comparison, the transverse momentum distributions of Te terminated PbTe(111) and Cr(001) (See

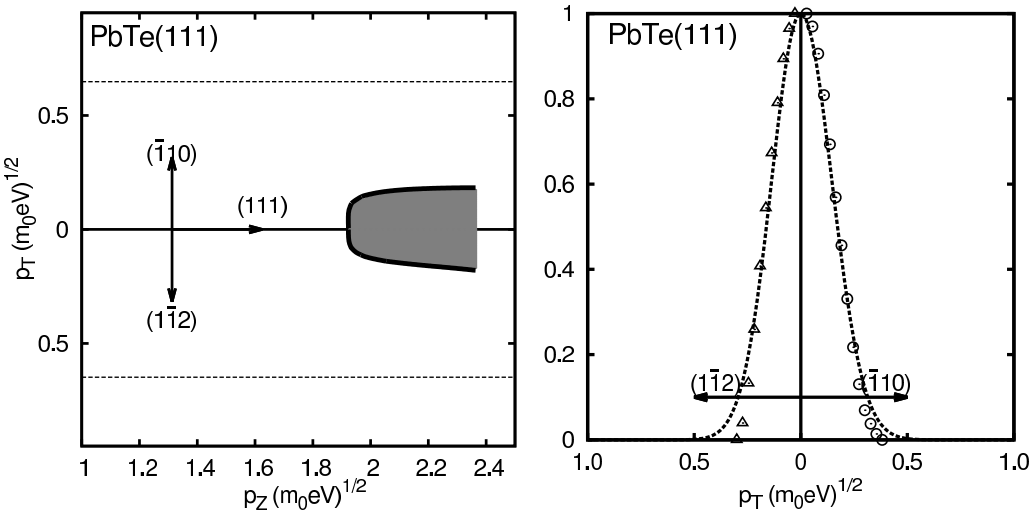

(a) (b)

Figure 7.6: Te terminated PbTe(111) photoemission states and transverse momentum distribution under $\hbar\omega = 4.75$eV: (a) Crystal momentum map of the electronic states (shaded regions) 0.21eV below the Fermi level (solid line) that may photoemit within the real $p_{T,max}$ (dashed line) for the transverse $(1\bar{1}2)$ and $(1\bar{1}0)$ crystal directions; (b) Transverse momentum distributions of the photoemitted electrons in the $(1\bar{1}2)$ and $(1\bar{1}0)$ directions (Gaussian fits are guides to the eye).

Chapter 4) are also displayed in Figure 7.7 with the solid green and pink lines, respectively. For a 300K solid planar photocathode, PbTe(111)'s predicted Δp_T is only a factor of 2 more than that of the cold atom source, and a factor of 1/2 less than that of Cr(001). According to the expression for Δp_T for thermionic electron emission $\sqrt{m_0 k_B T}$ [52], Te terminated PbTe(111) is close to a 50K electron source. It is important to note that the DFT evaluated Δp_T for PbTe(111) is at zero temperature. So the experimental measured value may be above this value due to temperature effects (e,g. thermal excitation across the band gap), sample termination configuration, and other factors (e.g., oxidation and Schottky effect) which can

affect the effective work function. It is, however, notable that the transmission flux probability, $T(p_z, p_z 0)$, over the work function barrier is significantly larger for PbTe(111) emission than most metals. This is because the combination of a relatively small longitudinal effective mass m_z^* and the additional crystal momentum at the L point VBM allows emission close to $p_{z0} = p_z$ where $T(p_z, p_z 0)$ is maximized. On the other hand, the density of possible excited states is less in PbTe than most metals due to the much smaller effective mass of the VB in PbTe. The net result is that the QE of PbTe is expected to be comparable to that of a metal.

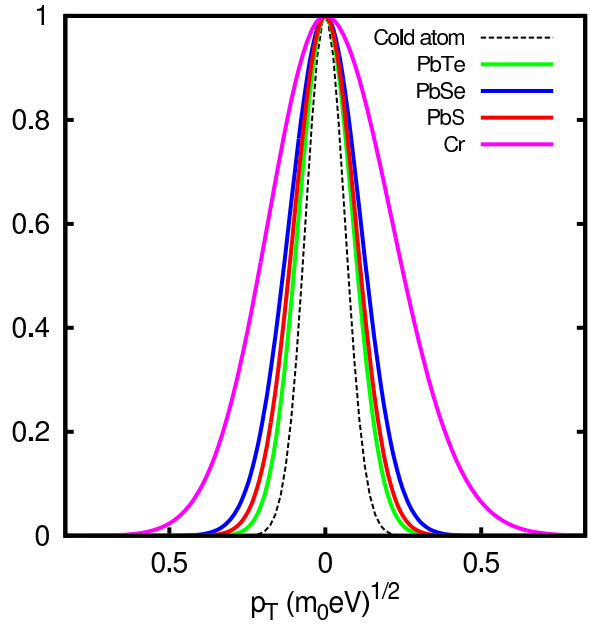

Figure 7.7: Comparison of transverse momentum distributions among the lead salt (111) faces, Cr(001) face and the cold atom source of Ref. [318].

In practice, the brightness of a next-generation cold electron unstructured photoemission source cannot arbitrarily increase as Δp_T is reduced. J. M. Maxson has already anticipated such a limit to be approached in the next generation of high brightness electron sources producing intense beams [319]; namely, the thermally induced disorder [319] limits in which any 'cold' electron gas quickly equilibrates its temperature so that the kinetic energy associated with the rms momenta of electrostatic the electron state potential energy associated with their rms separation. For a $\sim$50K PbTe(111) photocathode, this could limit the density of the generated electron pulse to $10^{19} m^{-3}$. There are numerous solid-state compounds that could be used as photocathodes, my work in this chapter has outlined an essential requirement for an ultra-low Δp_T planar solid-state photoemitter; namely, ideally a low m^* 'hole-like' band, the Te terminated PbTe(111) single crystal is an example of this approach to new photocathode discovery. The computational complexity in determining accurate work function values for solid-state compounds results from surface terminations (as shown in Table XV), oxidation, etc.) means that a more direct connection of my DFT-based photoemission simulation to experiment will require *situ* measurement [320] of the photocathode work function during experiments (such as the solenoid scan technique [50, 56]) aimed at determining Δp_T. Therefore, a tunable UV laser radiation source will be needed to realize such exciting avenue for future research.

CHAPTER 8

CONCLUSIONS

This thesis describes the emission properties of BCC, FCC, HCP, and semiconductor photocathodes using a DFT-based model and analysis. The presented DFT-based analysis of the properties of photocathodes clearly indicates that the rms transverse momentum Δp_T of electrons photoemitted in a one-step quantum mechanical process [67, 321] is fundamentally dependent upon the dispersive nature of the electronic bands from which they originate. Furthermore, this approach is unprecedented in fully and satisfactorily explaining both bulk and surface state photoemission, and as such it is a vital tool in the research and development of future photocathode materials aimed at producing low-emittance pulsed-electron sources. Not only does band structure play a crucial role in the physics of photoemission, as it clearly should, but that it is nearly impossible to accurately predict the functionality of a photocathode without such knowledge.

8.1 DFT Modeling

Chapter 3 describes the DFT-based model and analysis for photoemission that is used to calculate and interpret the rms transverse momentum (Δp_T) of the photoemitted electron beam. In addition to its expected dependence on the excess photoemission energy, $\Delta E = \hbar\omega - \phi$, the transverse momentum distribution of the emitted electrons is influenced by the electron band

dispersion, the local density of states (determined from the band structure calculation), the transmission flux over the work function barrier, and electron temperature. Further complicating the photoemission simulation is work function anisotropy; a thin-slab technique is employed to evaluate ϕ for different crystal orientations. As anticipated, the DFT-based photoemission model shows both analytically (Equation 3.4) and quantitatively (Equation 3.5) that Δp_T increases as the the temperature of the electrons T_e in the bands increase.

8.2 BCC Photocathodes

Chapter 4 explains the lower than expected rms transverse electron momentum measured for the BCC Group Vb and Group VIb elemental metals, and shows that a continuous variation in Δp_T can be obtained using the Mo_xNb_{1-x} alloy system. In this chapter, my DFT-based photoemission analysis is carefully benchmarked against prior formalisms [52, 53] using potassium — a BCC metal with a near spherical Fermi surface. Extension of the DFT-based analysis to Cr, Mo, W, V, Nb and Ta BCC metals has revealed a strong band structure dependence to the Δp_T of emitted electron beams. In particular, for photoemission from the (001) crystal face of these metals with 4.75eV photons, the Group Vb elements (V, Nb, and Ta) have significantly lower than expected values of Δp_T due to emission from 'hole-like' electronic states associated with the 'jack-shaped' Fermi surface around the Γ-point of the Brillouin zone. The results obtained for (001)-face emission using the DFT-based analysis are very consistent with our group's experimental measurements of Δp_T using the solenoid scan technique [56] for polycrystalline Cr, Mo, Nb, Ta, V, and W photocathodes under 261 nm UV irradiation. The Mo_xNb_{1-x} alloy

system has a continuous variation in the position of the Fermi level in the BCC band structure and value of the work function with respect to the composition x. This generates a continuous variation in Δp_T from $0.177\sqrt{m_0 eV}$ to $0.204\sqrt{m_0 eV}$ as x is tuned from 0 to 1.

8.3 FCC Photocathodes

Chapter 5 describes the photoemission properties of two noble metals (Cu and Au) and two p-block FCC metals (Al and Pb). The Fermi surface, effective mass, and band structures for the (100), (110), and (111) faces are evaluated and are in good agreement with the current literature dataset associated with the electronic properties of the four FCC metals. A surface state DFT evaluation has also been performed to show that photocathode generated hollow cone illumination (HCI) can be realized through the use of a Ag(111) single crystal with 0.03eV excess energy. In case of $m^* < m_0$, the minimum energy required to photoemit from the surface state, $E_{(111)}$, is the sum of FCC (111) face work function $\phi_{(111)}$ and the (111) Fermi level transverse momentum offset $p_F^2/2m_0$ (Equation 5.2). The local Δp_T width of the 'ring-like' emission from Ag(111) surface state peaks is $0.029\sqrt{m_0 eV}$.

8.4 HCP Photocathodes

The presented DFT-based analysis of the properties of photocathodes clearly indicates that the rms transverse momentum Δp_T of electrons photoemitted in a one-step quantum mechanical process [67, 321] is fundamentally dependent upon the dispersive nature of the electronic bands from which they originate. Chapter 6 shows that this is particularly true of the HCP

metals — the most common crystal structure amongst the elemental metals — since the crystal symmetry, and hence electronic band structure, is intrinsically anisotropic. Whereas emission from the basal plane, the (0001)-face, usually generates an isotropic transverse momentum distribution (Figure 6.3) due to hexagonal face symmetry, emission from the generally most prevalent $(10\bar{1}0)$-face in polycrystalline hcp metals can be quite anisotropic (Figure 6.2). As the rms transverse momentum Δp_T is dependent on the excess photoemission energy, knowledge of the work function for each crystal emission face, $\phi_{(ijkl)}$, is also critical to the DFT-based photoemission simulation. A standard thin-slab evaluation method for ϕ [183], which employs the atomic crystal potential from the band structure calculations, is shown to provide values in good agreement with literature values. The average of the resulting anisotropic values of Δp_T obtained from the theoretical simulation for the most prevalent $(10\bar{1}0)$-face of Be and Mg are consistent with experimental measurements [50, 56, 227].

Emission from the strong surface state of the Be(0001) face [60–64] is also analyzed. As the effective mass m^* associated with the dispersion of this two-dimensional state is greater than m_0 and fairly symmetric, the transverse momentum distribution of the photoemitted electrons is maximized at and quite symmetric about $p_T = 0$ (the $\overline{\Gamma}$ point of the SBZ). If its effective mass were less than m_0, the one-step analysis would predict emission peaked at $p_T = \sqrt{2m^* E_F}$, which may then directly produce an electron beam suitable for hollow cone illumination [58, 211, 212] — as were shown for the surface state on Ag(111) (Chapter 5)

8.5 Semiconductor Photocathodes

Chapter 7 discusses the ESTE from p-type III-antimonide semiconductor single crystals such as GaSb(100) and InSb(100), and also evaluates the emission properties of a class of attractive high brightness semiconductor photocathodes — the lead chalcogenides. Based on the DFT band structure and work function evaluations of the lead salts and previous investigations [269, 270, 296–303], Te terminated PbTe(111) single crystal is demonstrated to be an ultra-low Δp_T photocathode. This properties results from an important characteristic, namely, a very low transverse effective mass for the Λ_6^+ valence band. The predicted Δp_T of $0.067\sqrt{2m_0eV}$, which is only a factor of 2 more than that of a 14±2K cold atom source [318], as it is the equivalent of a 50K electron source from a planar 300K solid state photocathode.

8.6 The Δp_T of Elements and its Periodicity

The DFT photoemission model has been applied to the whole periodic table so that the Δp_T of almost all potential elemental photocathodes have been evaluated as shown in Appendix B. This Δp_T compilation should serve to significantly elucidate the emission properties of elemental photocathodes both macroscopically and microscopically.

APPENDICES

Appendix A

ANALYTICAL DERIVATION OF ΔP_T

Maximum internal photoemission angle is expressed in terms of transverse effective mass m_t^* and longitudinal effective mass m_l^*, which is

$$\begin{aligned} cos_{max}^{in}\theta &= \frac{\sqrt{2m_l^*(E_F+\phi-\hbar\omega)}}{\sqrt{2m_l^*E_l+2m_t^*E_t}}. \\ &= \frac{\sqrt{2m_l^*(E_F+\phi-\hbar\omega)}}{\sqrt{2m_l^*(E_F+\phi-\hbar\omega)+2m_t^*(E-E_F-\phi+\hbar\omega)}} \\ &= \frac{\sqrt{m_l^*(\chi)}}{\sqrt{m_l^*(\chi)+m_t^*(E-\chi)}}, \end{aligned} \tag{A.1}$$

$$tan\theta_{max}^{in} = \sqrt{\frac{m_t^*(E-\chi)}{m_l^*\chi}} = |\frac{p_t}{p_l}| = |\frac{k_t}{k_l}| \tag{A.2}$$

where $E = E_l + E_t$ and $\chi = E_F + \phi - \hbar\omega$.

Transverse momentum p_T is defined as

$$p_T = \sqrt{2m_t\chi + 2m_l(E-\chi)}sin\theta cos\Phi. \tag{A.3}$$

Appendix A (Continued)

According to the definition of root mean square, $\Delta {p_T}^2$ is

$$\begin{aligned}\Delta {p_T}^2 &= \frac{\int_{\chi}^{E_F} p_T^2 dE \int_{cos^{in}_{max}\theta}^{1} d(cos\theta) \int_0^{2\pi} d\Phi}{\int_{\chi}^{E_F} dE \int_{cos^{in}_{max}\theta}^{1} d(cos\theta) \int_0^{2\pi} d\Phi} \\ &= \frac{\int_{\chi}^{E_F} 2m_t\chi + 2m_l(E-\chi) sin^2\theta cos^2\Phi dE \int^{1}_{\frac{\sqrt{m_l^*(\chi)}}{\sqrt{m_l^*(\chi)+m_t^*(E-\chi)}}} d(cos\theta) \int_0^{2\pi} d\Phi}{\int_{\chi}^{E_F} dE \int^{1}_{\frac{\sqrt{m_l^*(\chi)}}{\sqrt{m_l^*(\chi)+m_t^*(E-\chi)}}} d(cos\theta) \int_0^{2\pi} d\Phi}\end{aligned} \tag{A.4}$$

The angular integration can be done separately and are given by

$$\begin{aligned}\frac{\int_0^{2\pi} cos^2\Phi d\Phi}{\int_0^{2\pi} d\Phi} &= \frac{1}{2} \\ \int sin^2\theta d(cos\theta) &= cos\theta - \frac{1}{3}cos^3\theta\end{aligned} \tag{A.5}$$

Substituting these integrals into equation Equation A.4 results in the following expression for the square of the rms transverse momentum:

$$\begin{aligned}\Delta {p_T}^2 &= \frac{\int_{\chi}^{E_F} [\frac{2}{3} - \frac{\sqrt{m_l^*(\chi)}}{\sqrt{m_l^*(\chi)+m_t^*(E-\chi)}} + \frac{1}{3}(\frac{\sqrt{m_l^*(\chi)}}{\sqrt{m_l^*(\chi)+m_t^*(E-\chi)}})^3][2m_t^*\chi + 2m_l^*(E-\chi)]dE}{\int_{\chi}^{E_F}[1 - \frac{\sqrt{m_l^*(\chi)}}{\sqrt{m_l^*(\chi)+m_t^*(E_F-\chi)}}]dE} \\ &= \frac{1}{3}\frac{(E-\chi)(\sqrt{E_F m_t^* + m_l^*\chi - m_t\chi} - \sqrt{m_l^*\chi})^2}{\frac{(\sqrt{E_F m_t^* + m_l^*\chi - m_t\chi} - \sqrt{m_l^*\chi})^2}{m_t^*}} \\ &= \frac{(E_F-\chi)m_t^*}{3} \\ &= \frac{(\hbar\omega - \phi)m_t^*}{3}.\end{aligned} \tag{A.6}$$

Therefore, $\Delta p_T = \sqrt{\frac{(\hbar\omega-\phi)m_t^*}{3}}$.

Appendix B

THE ΔP_T OF THE ELEMENTS AND ITS PERIODICITY

TABLE XVI: The Δp_T of the elements and its periodicity. The work functions are given by Ref. [125] unless otherwise indicated. Lattice constants are given by Ref. [322] unless otherwise indicated. indicated.

Element	ϕ (eV)	$\hbar\omega$ (eV)	Crystal	lattice (a.u.)	Δp_T ($\sqrt{m_0 eV}$)	$\frac{\Delta p_{T,DFT}}{\Delta p_{T0}}$	(i,j,k)	$\frac{m^*}{m_0}$
Ag	4.52(110) 4.14(110) [323] 4.22(001) [323] 4.46(111) [323] 4.74(111)	4.75	fcc	a=7.72(Expt.) a=7.57(DFT)	0.277(Dowell) 0.202(DFT)	0.96	(110)	1.06 [97]
Al	4.41	4.75	fcc	a=7.65 a=7.53	0.336 0.200	0.55	(100)	1.18 [324]
Au	5.37	5.60	fcc	a=7.71 a=7.64	0.277 0.208	0.85	(110)	1.03 [205]
Ba	2.70	3.00	bcc	a=9.51 a=9.01	0.316 0.192	0.61	(001)	0.38-0.74 [325]
Be	3.92	4.75	hcp	a=4.32;c=6.77 [230] a=4.20;c=6.68	0.525 0.312	0.594	$(10\bar{1}0)$	0.16-0.18 [326]
Bi	4.50 [327]	4.75	rho.	a=8.81 [328] α=57.35^o;z=0.468 a=8.45 α=57.33^o;z=0.473	0.288 0.174 	0.604	(111)	0.05-0.25 [329, 330]

rho. = rhombohedral; tet. = tetragonal; * = magnetic element.

Appendix B (Continued)

Element	ϕ (eV)	$\hbar\omega$ (eV)	Crystal	lattice (a.u.)	Δp_T ($\sqrt{m_0 eV}$)	$\frac{\Delta p_{T,DFT}}{\Delta p_{T0}}$	(i,j,k)	$\frac{m^*}{m_0}$
Cd	4.22	4.75	hcp	a=5.63;c=10.62 [231] a=5.48;c=10.39	0.420 0.220	0.524	$(10\bar{1}0)$	0.14-0.40 [329, 331]
Co*	5.0	5.20	hcp	a=4.74;c=7.45 [232] a=4.52;c=7.31	0.258 0.208	0.806	$(10\bar{1}0)$	0.10-0.35 [332]
Cr	4.5 4.46(P) [155] 4.57(100) [166] 5.08(110) [166]	4.75	bcc	a=5.50 a=5.28	0.288 0.168	0.683	(001)	0.20-0.40 [333]
Cs	2.14	2.44	bcc	a=11.61 a=10.91	0.316 0.302	0.95	(001)	1.3 [334]
Cu	4.48(100)	4.75	fcc	a=6.83 a=6.65	0.300 0.170	0.656	(110)	1.37-1.52 [202]
Fe*	4.67	4.75	bcc	a=5.41 a=5.20	0.163 0.147	0.90	(001)	
Li	2.90(P) 2.49(P) [145] 3.12(111) [335] 3.03(001) [335] 3.43(110) [335]	3.20	bcc	a=6.63 a=6.37	0.316 0.286	0.905	(001)	2.10 [144]
Hf	3.90	4.75	hcp	a=6.04;c=9.54 [109] a=5.88;c=9.37	0.532 0.300	0.573	$(10\bar{1}0)$	

rho. = rhombohedral; tet. = tetragonal; * = magnetic element.

Appendix B (Continued)

Element	ϕ (eV)	$\hbar\omega$ (eV)	Crystal	lattice (a.u.)	Δp_T ($\sqrt{m_0 eV}$)	$\frac{\Delta p_{T,DFT}}{\Delta p_{T0}}$	(i,j,k)	$\frac{m^*}{m_0}$
In	4.12	4.75	tet.	a=8.61;c=9.32	0.458	0.382	(111)	0.30 [329, 336]
				a=8.40;c=9.72	0.175			
Ir	5.76	5.90	fcc	a=7.25	0.283	0.740	(001)	0.28-0.91 [337]
				a=7.2	0.209			
K	2.30(P)	2.60	bcc	a=10.07	0.316	0.905	(001)	1.3 [142]
				a=9.51	0.286			
	2.34(100) [167]							
	2.38(110) [167]							
Mg	3.66	4.75	hcp	a=6.06;c=9.85 [233]	0.602	0.516	$(10\bar{1}0)$	0.16-0.36 [338]
				a=5.89;c=9.67	0.313			
Mn*	4.10	4.75	bcc	a=5.40	0.465	0.47	(001)	
				a=5.16	0.219			
Mo	4.53	4.75	bcc	a=5.95	0.271	0.653	(001)	0.31-0.38 [339]
				a=5.88	0.177			
Na	2.75(P)	3.05	bcc	a=8.11	0.316	0.905	(001)	1.25 [146]
	2.80(001) [121]			a=7.67	0.286			
	2.99(110) [121]							
	2.77(111) [121]							

rho. = rhombohedral; tet. = tetragonal; * = magnetic element.

Appendix B (Continued)

Element	ϕ (eV)	$\hbar\omega$ (eV)	Crystalline	lattice (a.u.)	Δp_T ($\sqrt{m_0 eV}$)	$\frac{\Delta p_{T,DFT}}{\Delta p_{T0}}$	(i,j,k)	$\frac{m^*}{m_0}$
Nb	4.02(001) [156]	4.75	bcc	a=6.24	0.493	0.40	(001)	0.57-0.97 [148]
				a=6.13	0.204			
	4.87(110) [156]							
	4.36(111) [156]							
	4.63(112) [156]							
	4.29(113) [156]							
	3.95(116) [156]							
Ni*	5.22	5.50	fcc	a=6.66	0.305	0.627	(100)	0.26-1.00 [340]
				a=6.48	0.184			
Os	4.83	5.10	hcp	a=5.22;c=8.04 [109]	0.300	0.577	$(10\bar{1}0)$	0.23 [341]
				a=5.17;c=8.12	0.173			
Pb	4.25	4.75	fcc	a=9.36	0.408	0.497	(100)	0.52 [342]
				a=9.21	0.203			
Pd	5.12	5.50	fcc	a=7.35	0.355	0.600	(100)	0.63-1.30 [343]
				a=7.26	0.213			
Po	4.70	5.00	cubic	a=6.35	0.316	0.665	(001)	
				a=6.20	0.210			
Pt	5.65	5.90	fcc	a=7.72	0.287	0.728	(100)	2.1 [344]
				a=7.35	0.209			
Rb	2.16	2.46	bcc	a=10.55	0.316	0.95	(001)	1.23-1.61 [345]
				a=10.13	0.302			
Re	4.96	5.10	hcp	a=5.22;c=8.40 [234]	0.311	0.518	$(10\bar{1}0)$	0.12-0.50 [346]
				a=5.04;c=8.00	0.161			
Rh	4.98	5.10	fcc	a=7.19	0.408	0.571	(100)	0.91-1.47 [347]
				a=7.10	0.233			
Ru	4.71	5.10	hcp	a=5.22;c=8.04 [109]	0.216	0.808	$(10\bar{1}0)$	0.24-0.47 [341]
				a=5.16;c=8.58	0.198			
Sb	4.70	5.00	rho.	a=8.48 [328]	0.316	0.559	(111)	0.05-0.52 [329]
				α=57.23^o;z=0.467				
				a=8.10	0.361			
				α=57.23^o;z=0.469				

rho. = rhombohedral; tet. = tetragonal; * = magnetic element.

Appendix B (Continued)

Element	ϕ (eV)	$\hbar\omega$ (eV)	Crystalline	lattice (a.u.)	Δp_T ($\sqrt{m_0 eV}$)	$\frac{\Delta p_{T,DFT}}{\Delta p_{T0}}$	(i,j,k)	$\frac{m^*}{m_0}$
Sc	3.50	4.75	hcp	a=6.24;c=9.93 [235]	0.645	0.434	$(10\bar{1}0)$	4.1 [348]
				a=6.03;c=9.52	0.280			
Si	4.91	5.10	diamond	a=10.26	0.251	0.550	(001)	0.19-0.43 [349, 350]
				a=10.20	0.138			
Sn	4.42	4.75	tet.	a=10.96;c=5.95	0.331	0.559	(111)	0.1-2.0 [329, 351]
				a=10.92;c=5.91	0.269			
Ta	4.15	4.75	bcc	a=6.24	0.447	0.456	(001)	0.60-0.84 [352]
				a=6.16	0.204			
Tc	4.88	5.10	hcp	a=5.18;c=8.21 [236]	0.270	0.722	$(10\bar{1}0)$	2.0-5.0 [353]
				a=5.11;c=8.30	0.195			
Tl	3.84	4.75	hcp	a=6.53;c=10.44 [237]	0.551	0.584	$(10\bar{1}0)$	0.35 [329]
				a=6.40;c=10.29	0.253			
Ti	3.63	4.75	hcp	a=5.58;c=8.85 [235]	0.611	0.513	$(10\bar{1}0)$	
				a=5.36;c=8.64	0.314			
V	4.30	4.75	bcc	a=5.73	0.387	0.49	(001)	0.86 [354, 355]
				a=5.53	0.191			
	5.12(110) [167]							
	4.12(100) [168]							
W	4.63	4.75	bcc	a=5.98	0.200	0.80	(001)	0.30 [356]
				a=5.92	0.160			
	4.46(113) [158]							
Y	3.10	4.75	hcp	a=6.89;c=10.83 [235]	0.741	0.426	$(10\bar{1}0)$	0.29-2.4 [357]
				a=6.61;c=10.49	0.316			
Zn	4.33	4.75	hcp	a=5.01;c=9.04 [231]	0.374	0.519	$(10\bar{1}0)$	0.2-0.22 [329]
				a=4.83;c=9.12	0.194			
Zr	4.05	4.75	hcp	a=6.10;c=9.73 [109]	0.483	0.673	$(10\bar{1}0)$	2.31-2.61 [358]
				a=5.91;c=9.67	0.325			

rho. = rhombohedral; tet. = tetragonal; * = magnetic element.

CITED LITERATURE

1. Mourou, G. and Williamson, S.: Picosecond electron diffraction. Applied Physics Letters, 41(1):44–45, July 1982.

2. Srinivasan, R., Lobastov, V., Ruan, C.-Y., and Zewail, A.: Ultrafast electron diffraction (UED). Helvetica Chimica Acta, 86(6):1761–1799, June 2003.

3. Siwick, B. J., Dwyer, J. R., Jordan, R. E., and Miller, R. J. D.: An atomic-level view of melting using femtosecond electron diffraction. Science, 302(5649):1382–1385, November 2003.

4. Cao, J., Hao, Z., Park, H., Tao, C., Kau, D., and Blaszczyk, L.: Femtosecond electron diffraction for direct measurement of ultrafast atomic motions. Applied Physics Letters, 83(5):1044–1046, August 2003.

5. Sciaini, G. and Miller, R. J. D.: Femtosecond electron diffraction: heralding the era of atomically resolved dynamics. Reports on Progress in Physics, 74(9):096101, September 2011.

6. Ruan, C.-Y., Vigliotti, F., Lobastov, V. A., Chen, S., and Zewail, A. H.: Ultrafast electron crystallography: Transient structures of molecules, surfaces, and phase transitions. Proceedings of the National Academy of Sciences of the United States of America, 101(5):1123–1128, February 2004.

7. Hastings, J. B., Rudakov, F. M., Dowell, D. H., Schmerge, J. F., Cardoza, J. D., Castro, J. M., Gierman, S. M., Loos, H., and Weber, P. M.: Ultrafast time-resolved electron diffraction with megavolt electron beams. Applied Physics Letters, 89(18):184109, October 2006.

8. Williamson, S., Mourou, G., and Li, J. C. M.: Time-resolved laser-induced phase transformation in aluminum. Physical Review Letters, 52(26):2364–2367, June 1984.

9. Sciaini, G., Harb, M., Kruglik, S. G., Payer, T., Hebeisen, C. T., Heringdorf, F.-J. M. z., Yamaguchi, M., Hoegen, M. H.-v., Ernstorfer, R., and Miller, R. J. D.: Electronic acceleration of atomic motions and disordering in bismuth. Nature, 458(7234):56–59, March 2009.

10. Tao, Z., Han, T.-R. T., Mahanti, S. D., Duxbury, P. M., Yuan, F., Ruan, C.-Y., Wang, K., and Wu, J.: Decoupling of structural and electronic phase transitions in vo_2. Phys. Rev. Lett., 109:166406, Oct 2012.

11. Siwick, B. J., Dwyer, J. R., Jordan, R. E., and Miller, R. J. D.: Femtosecond electron diffraction studies of strongly driven structural phase transitions. Chemical Physics, 299(23):285–305, April 2004.

12. Hanisch-Blicharski, A., Janzen, A., Krenzer, B., Wall, S., Klasing, F., Kalus, A., Frigge, T., Kammler, M., and Horn-von Hoegen, M.: Ultra-fast electron diffraction at surfaces: From nanoscale heat transport to driven phase transitions. Ultramicroscopy, 127:2–8, April 2013.

13. Harb, M., Ernstorfer, R., Hebeisen, C. T., Sciaini, G., Peng, W., Dartigalongue, T., Eriksson, M. A., Lagally, M. G., Kruglik, S. G., and Miller, R. D.: Electronically driven structure changes of si captured by femtosecond electron diffraction. Physical review letters, 100(15):155504, 2008.

14. Raman, R. K., Murdick, R. A., Worhatch, R. J., Murooka, Y., Mahanti, S. D., Han, T.-R. T., and Ruan, C.-Y.: Electronically driven fragmentation of silver nanocrystals revealed by ultrafast electron crystallography. Physical Review Letters, 104(12):123401, March 2010.

15. Williamson, J. C., Cao, J., Ihee, H., Frey, H., and Zewail, A. H.: Clocking transient chemical changes by ultrafast electron diffraction. Nature, 386(6621):159–162, March 1997.

16. Dudek, R. C. and Weber, P. M.: Ultrafast diffraction imaging of the electrocyclic ring-opening reaction of 1, 3-cyclohexadiene. The Journal of Physical Chemistry A, 105(17):4167–4171, 2001.

17. Chapman, H. N., Barty, A., Bogan, M. J., Boutet, S., Frank, M., Hau-Riege, S. P., Marchesini, S., Woods, B. W., Bajt, S., Benner, W. H., London, R. A., Plnjes, E., Kuhlmann, M., Treusch, R., Dsterer, S., Tschentscher, T., Schneider, J. R., Spiller, E., Mller, T., Bostedt, C., Hoener, M., Shapiro, D. A., Hodgson, K. O., van der Spoel, D., Burmeister, F., Bergh, M., Caleman, C., Huldt, G., Seibert, M. M., Maia, F. R. N. C., Lee, R. W., Szke, A., Timneanu, N., and Hajdu, J.: Femtosecond diffractive imaging with a soft-x-ray free-electron laser. Nature Physics, 2(12):839–843, December 2006.

18. Gaffney, K. J. and Chapman, H. N.: Imaging atomic structure and dynamics with ultrafast x-ray scattering. Science, 316(5830):1444–1448, June 2007.

19. Kern, J., Alonso-Mori, R., Tran, R., Hattne, J., Gildea, R. J., Echols, N., Glöckner, C., Hellmich, J., Laksmono, H., Sierra, R. G., et al.: Simultaneous femtosecond x-ray spectroscopy and diffraction of photosystem ii at room temperature. Science, 340(6131):491–495, 2013.

20. Schotte, F., Lim, M., Jackson, T. A., Smirnov, A. V., Soman, J., Olson, J. S., Phillips, G. N., Wulff, M., and Anfinrud, P. A.: Watching a protein as it functions with 150-ps time-resolved x-ray crystallography. Science, 300(5627):1944–1947, June 2003.

21. Neutze, R., Wouts, R., van der Spoel, D., Weckert, E., and Hajdu, J.: Potential for biomolecular imaging with femtosecond x-ray pulses. Nature, 406(6797):752–757, August 2000.

22. Bostanjoglo, O. and Horinek, W. R.: . Optik, 65(361), 1983.

23. Lobastov, V. A., Srinivasan, R., and Zewail, A. H.: Four-dimensional ultrafast electron microscopy. Proceedings of the National Academy of Sciences of the United States of America, 102(20):7069–7073, May 2005.

24. LaGrange, T., Armstrong, M. R., Boyden, K., Brown, C. G., Campbell, G. H., Colvin, J. D., DeHope, W. J., Frank, A. M., Gibson, D. J., Hartemann, F. V., Kim, J. S., King, W. E., Pyke, B. J., Reed, B. W., Shirk, M. D., Shuttlesworth, R. M., Stuart, B. C., Torralva, B. R., and Browning, N. D.: Single-shot dynamic transmission electron microscopy. Applied Physics Letters, 89(4):044105, July 2006.

25. Merano, M., Sonderegger, S., Crottini, A., Collin, S., Renucci, P., Pelucchi, E., Malko, A., Baier, M. H., Kapon, E., Deveaud, B., and Ganire, J.-D.: Probing carrier dynamics in nanostructures by picosecond cathodoluminescence. Nature, 438(7067):479–482, November 2005.

26. Bostanjoglo, O., Elschner, R., Mao, Z., Nink, T., and Weingrtner, M.: Nanosecond electron microscopes. Ultramicroscopy, 81(34):141–147, April 2000.

27. Bostanjoglo, O. and Weingärtner, M.: Pulsed photoelectron microscope for imaging laser-induced nanosecond processes. Review of scientific instruments, 68(6):2456–2460, 1997.

28. Kim, J. S., LaGrange, T., Reed, B. W., Taheri, M. L., Armstrong, M. R., King, W. E., Browning, N. D., and Campbell, G. H.: Imaging of transient structures using nanosecond in situ tem. Science, 321(5895):1472–1475, 2008.

29. Bostanjoglo, O. and Liedtke, R.: Tracing fast phase transitions by electron microscopy. physica status solidi (a), 60(2):451–455, 1980.

30. LaGrange, T., Campbell, G. H., Colvin, J. D., Reed, B., and King, W. E.: Nanosecond time resolved electron diffraction studies of the α β in pure ti thin films using the dynamic transmission electron microscope (dtem). Journal of materials science, 41(14):4440–4444, 2006.

31. Santala, M. K., Reed, B. W., Raoux, S., Topuria, T., LaGrange, T., and Campbell, G. H.: Nanosecond-scale time-resolved electron imaging during laser crystallization of GeTe. physica status solidi (b), 249(10):1907–1913, October 2012.

32. Santala, M. K., Reed, B. W., Raoux, S., Topuria, T., LaGrange, T., and Campbell, G. H.: Irreversible reactions studied with nanosecond transmission electron microscopy movies: Laser crystallization of phase change materials. Applied Physics Letters, 102(17):174105, April 2013.

33. Bostanjoglo, O., Tornow, R., and Tornow, W.: Nanosecond-exposure electron microscopy of laser-induced phase transformations. Ultramicroscopy, 21(4):367–372, 1987.

34. Bostanjoglo, O. and Schlotzhauer, G.: Impulse stimulated crystallization of sb films investigated by time resolved tem. physica status solidi (a), 68(2):555–560, 1981.

35. Masiel, D. J., Reed, B. W., LaGrange, T. B., Campbell, G. H., Guo, T., and Browning, N. D.: Time-resolved annular dark field imaging of catalyst nanoparticles. ChemPhysChem, 11(10):2088–2090, July 2010.

36. King, W. E., Campbell, G. H., Frank, A., Reed, B., Schmerge, J. F., Siwick, B. J., Stuart, B. C., and Weber, P. M.: Ultrafast electron microscopy in materials science, biology, and chemistry. Journal of Applied Physics, 97(11):111101, June 2005.

37. Armstrong, M. R., Boyden, K., Browning, N. D., Campbell, G. H., Colvin, J. D., DeHope, W. J., Frank, A. M., Gibson, D. J., Hartemann, F., Kim, J. S., King, W. E., LaGrange, T. B., Pyke, B. J., Reed, B. W., Shuttlesworth, R. M., Stuart, B. C., and Torralva, B. R.: Practical considerations for high spatial and temporal resolu-

tion dynamic transmission electron microscopy. Ultramicroscopy, 107(45):356–367, April 2007.

38. Armstrong, M. R., Reed, B. W., Torralva, B. R., and Browning, N. D.: Prospects for electron imaging with ultrafast time resolution. Applied Physics Letters, 90(11):114101, March 2007.

39. Kim, K.-J., Shvydko, Y., and Reiche, S.: A proposal for an x-ray free-electron laser oscillator with an energy-recovery linac. Physical Review Letters, 100(24):244802, June 2008.

40. Huang, Z. and Kim, K.-J.: Review of x-ray free-electron laser theory. Physical Review Special Topics - Accelerators and Beams, 10(3):034801, March 2007.

41. Rose, A.: Advances in electronics and electron physics. Academic Press, 1:131–166, 1948.

42. Bazarov, I. V., Dunham, B. M., and Sinclair, C. K.: Maximum achievable beam brightness from photoinjectors. Physical Review Letters, 102(10):104801, March 2009.

43. Rhee, M. J.: Refined definition of the beam brightness. Physics of Fluids B: Plasma Physics (1989-1993), 4(6):1674–1676, June 1992.

44. Reiser, M.: Theory and design of charged particle beams. John Wiley & Sons, 2008.

45. Valfells, ., Feldman, D. W., Virgo, M., OShea, P. G., and Lau, Y. Y.: Effects of pulse-length and emitter area on virtual cathode formation in electron guns. Physics of Plasmas (1994-present), 9(5):2377–2382, May 2002.

46. Child, C. D.: Discharge from hot CaO. Physical Review (Series I), 32(5):492–511, May 1911.

47. Langmuir, I.: The effect of space charge and initial velocities on the potential distribution and thermionic current between parallel plane electrodes. Physical Review, 21(4):419–435, April 1923.

48. SrinivasanRao, T., Fischer, J., and Tsang, T.: Photoemission studies on metals using picosecond ultraviolet laser pulses. Journal of Applied Physics, 69(5):3291–3296, March 1991.

49. Anderson, T., Tomov, I. V., and Rentzepis, P. M.: Laserdriven metal photocathodes for picosecond electron and xray pulse generation. Journal of Applied Physics, 71(10):5161–5167, May 1992.

50. Rickman, B. L., Berger, J. A., Nicholls, A. W., and Schroeder, W. A.: Erratum: Intrinsic electron beam emittance from metal photocathodes: The effect of the electron effective mass [phys. rev. lett. **111** , 237401 (2013)]. Phys. Rev. Lett., 113:239904, Dec 2014.

51. Prat, E., Bettoni, S., Braun, H.-H., Ganter, R., and Schietinger, T.: Measurements of copper and cesium telluride cathodes in a radio-frequency photoinjector. Phys. Rev. ST Accel. Beams, 18:043401, Apr 2015.

52. Dowell, D. H. and Schmerge, J. F.: Quantum efficiency and thermal emittance of metal photocathodes. Phys. Rev. ST Accel. Beams, 12:074201, Jul 2009.

53. Jensen, K. L., O'Shea, P. G., and Feldman, D. W.: Emittance of a photocathode: Effects of temperature and field. Physical Review Special Topics - Accelerators and Beams, 13(8):080704, August 2010.

54. Li, T., Rickman, B. L., and Schroeder, W. A.: Emission properties of body-centered cubic elemental metal photocathodes. Journal of Applied Physics, 117(13), 2015.

55. Kittel, C.: Introduction to solid state physics. Wiley, 2005.

56. Rickman, B. L., Berger, J. A., Nicholls, A. W., and Schroeder, W. A.: Intrinsic electron beam emittance from metal photocathodes: The effect of the electron effective mass. Phys. Rev. Lett., 111:237401, Dec 2013.

57. Parr, R. G. and Yang, W.: Density-functional theory of atoms and molecules, volume 16. Oxford university press, 1989.

58. Dinges, C., Kohl, H., and Rose, H.: High-resolution imaging of crystalline objects by hollow-cone illumination. Ultramicroscopy, 55(1):91–100, July 1994.

59. Kunath, W., Zemlin, F., and Weiss, K.: Apodization in phase-contrast electron microscopy realized with hollow-cone illumination. Ultramicroscopy, 16(2):123–138, 1985.

60. Feibelman, P. J.: First-principles calculation of the geometric and electronic structure of the be (0001) surface. Physical Review B, 46(4):2532, 1992.

61. Bartynski, R. A., Jensen, E., Gustafsson, T., and Plummer, E. W.: Angle-resolved photoemission investigation of the electronic structure of be: Surface states. Physical Review B, 32(4):1921–1926, August 1985.

62. Pohl, K., Cho, J.-H., Terakura, K., Scheffler, M., and Plummer, E. W.: Anomalously large thermal expansion at the (0001) surface of beryllium without observable interlayer anharmonicity. Physical review letters, 80(13):2853, 1998.

63. Boettger, J. C. and Trickey, S. B.: Electronic surface states in beryllium. Physical Review B, 34(6):3604, 1986.

64. Sprunger, P. T., Petersen, L., Plummer, E. W., Lgsgaard, E., and Besenbacher, F.: Giant friedel oscillations on the beryllium(0001) surface. Science, 275(5307):1764–1767, March 1997.

65. Berger, J. A., Rickman, B. L., Li, T., Nicholls, A. W., and Schroeder, W. A.: Excited-state thermionic emission in III-antimonides: Low emittance ultrafast photocathodes. Applied Physics Letters, 101(19):194103, November 2012.

66. Berglund, C. N. and Spicer, W. E.: Photoemission studies of copper and silver: Theory. Phys. Rev., 136:A1030–A1044, Nov 1964.

67. Courths, R. and Hüfner, S.: Photoemission experiments on copper. Physics Reports, 112(2):53–171, 1984.

68. Jensen, K. L., OShea, P. G., Feldman, D. W., and Shaw, J. L.: Emittance of a field emission electron source. Journal of Applied Physics, 107(1), 2010.

69. Schmerge, J. F., Clendenin, J. E., Dowell, D. H., and Gierman, S. M.: Rf gun photo-emission model for metal cathodes including time dependent emission. International Journal of Modern Physics A, 22(23):4069–4082, September 2007.

70. Einstein, A. et al.: On the electrodynamics of moving bodies. Annalen der Physik, 17(10):891–921, 1905.

71. Berglund, C. and Spicer, W.: Photoemission studies of copper and silver: Experiment. Physical Review, 136(4A):A1044–A1064, November 1964.

72. Kalarasse, L., Bennecer, B., and Kalarasse, F.: Optical properties of the alkali antimonide semiconductors cs3sb, cs2ksb, csk2sb and k3sb. Journal of Physics and Chemistry of Solids, 71(3):314–322, 2010.

73. Kevan, S.: Evidence for a new broadening mechanism in angle-resolved photoemission from cu (111). Physical review letters, 50(7):526, 1983.

74. Sacherer, F.: . IEEE Report No. IEEE NS-18, pages 1105–1107, 1971.

75. Rhee, M. J.: Refined definition of the beam brightness. Physics of Fluids B: Plasma Physics (1989-1993), 4(6), 1992.

76. Bazarov, I. V., Dunham, B. M., and Sinclair, C. K.: Maximum achievable beam brightness from photoinjectors. Phys. Rev. Lett., 102:104801, Mar 2009.

77. Valfells, ., Feldman, D. W., Virgo, M., OShea, P. G., and Lau, Y. Y.: Effects of pulse-length and emitter area on virtual cathode formation in electron guns. Physics of Plasmas (1994-present), 9(5), 2002.

78. Van Steenbergen, A.: Recent developments in high intensity ion beam production and preacceleration. Nuclear Science, IEEE Transactions on, 12(3):746–764, 1965.

79. Lejeune, C., Aubert, J., and Septier, A.: . Applied charged particle optics, 1980.

80. Lawson, J. D.: The physics of charged-particle beams. 2. 1988.

81. Anderson, T., Tomov, I. V., and Rentzepis, P.: Laser-driven metal photocathodes for picosecond electron and x-ray pulse generation. Journal of applied physics, 71(10):5161–5167, 1992.

82. Srinivasan-Rao, T., Fischer, J., and Tsang, T.: Photoemission studies on metals using picosecond ultraviolet laser pulses. Journal of applied physics, 69(5):3291–3296, 1991.

83. Langmuir, I.: The effect of space charge and initial velocities on the potential distribution and thermionic current between parallel plane electrodes. Phys. Rev., 21:419–435, Apr 1923.

84. Child, C. D.: Discharge from hot cao. Phys. Rev. (Series I), 32:492–511, May 1911.

85. Spicer, W. E. and Herrera-Gomez, A.: Modern theory and applications of photocathodes. In SPIE's 1993 International Symposium on Optics, Imaging, and Instrumentation, pages 18–35. International Society for Optics and Photonics, 1993.

86. Ichimura, S., Kokubun, K., Hirata, M., Tsukahara, S., Saito, K., and Ikeda, Y.: Measurement of outgassing characteristics from a vacuum chamber fabricated for pressure calibration in uhv/xhv region. Vacuum, 53(1):291–294, 1999.

87. Dylla, H.: The development of uhv and xhv for physics research. CERN Accelerator School, Platja DAro, Spain, pages 16–24, 2006.

88. Armstrong, M. R., Boyden, K., Browning, N. D., Campbell, G. H., Colvin, J. D., DeHope, W. J., Frank, A. M., Gibson, D. J., Hartemann, F., Kim, J. S., King, W. E., LaGrange, T. B., Pyke, B. J., Reed, B. W., Shuttlesworth, R. M., Stuart, B. C., and Torralva, B. R.: Practical considerations for high spatial and temporal resolution dynamic transmission electron microscopy. Ultramicroscopy, 107(45):356 – 367, 2007.

89. Kong, S., Kinross-Wright, J., Nguyen, D., and Sheffield, R.: Photocathodes for free electron lasers. Nuclear Instruments and Methods in Physics Research Section A: Accelerators, Spectrometers, Detectors and Associated Equipment, 358(13):272 – 275, 1995.

90. Nishitani, T., Nakanishi, T., Yamamoto, M., Okumi, S., Furuta, F., Miyamoto, M., Kuwahara, M., Yamamoto, N., Naniwa, K., Watanabe, O., et al.: Highly polarized electrons from gaas–gaasp and ingaas–algaas strained-layer superlattice photocathodes. Journal of applied physics, 97(9):094907, 2005.

91. Karkare, S. and Bazarov, I.: Effect of nanoscale surface roughness on transverse energy spread from gaas photocathodes. Applied Physics Letters, 98(9):094104, 2011.

92. Lee, G.: Materials for ultra-high vacuum. Fermilab, TM-1615, 1980.

93. Mahlman, G. W.: Work functions and conductivity of oxide-coated cathodes. Journal of Applied Physics, 20(2):197–202, 1949.

94. Chen, J., Tzou, D., and Beraun, J.: A semiclassical two-temperature model for ultrafast laser heating. International Journal of Heat and Mass Transfer, 49(12):307 – 316, 2006.

95. Jeon, E., Kim, J., Kim, Y., Ma, K., and Nam, J.: Magnetic field effects on the photocathode uniformity of hamamatsu r7081 photomultiplier tubes. Nuclear Instruments and Methods in Physics Research Section A: Accelerators, Spectrometers, Detectors and Associated Equipment, 697:46–51, 2013.

96. Coleridge, P. T. and Templeton, I. M.: Fermi-surface radii in copper, silver, and gold. Physical Review B, 25(12):7818–7819, June 1982.

97. Christensen, N. E.: An APW calculation for silver. physica status solidi (b), 31(2):635–647, January 1969.

98. Berglund, C. N. and Spicer, W. E.: Photoemission studies of copper and silver: theory. Physical Review, 136(4A):A1030, 1964.

99. Lewis, P. E. and Lee, P. M.: Band structure and electronic properties of silver. Physical Review, 175(3):795–804, November 1968.

100. Ballinger, R. A. and Marshall, C. a. W.: Study of potentials suitable for band structure calculations of the noble metals II. silver and gold. Journal of Physics C: Solid State Physics, 2(10):1822, October 1969.

101. et al., P. G.: Quantum espresso: a modular and open-source software project for quantum simulations of materials. Journal of Physics: Condensed Matter, 21(39):395502 (19pp), 2009.

102. Garrity, K. F., Bennett, J. W., Rabe, K. M., and Vanderbilt, D.: Pseudopotentials for high-throughput DFT calculations. Computational Materials Science, 81:446–452, January 2014.

103. Vanderbilt, D.: Soft self-consistent pseudopotentials in a generalized eigenvalue formalism. Phys. Rev. B, 41:7892–7895, Apr 1990.

104. Kresse, G. and Hafner, J.: Norm-conserving and ultrasoft pseudopotentials for first-row and transition elements. J. Phys.: Condens. Matter, 6:8245, Apr 1994.

105. Perdew, J. P., Burke, K., and Ernzerhof, M.: Generalized gradient approximation made simple. Phys. Rev. Lett., 77:3865–3868, Oct 1996.

106. Monkhorst, H. J. and Pack, J. D.: Special points for brillouin-zone integrations. Phys. Rev. B, 13:5188–5192, Jun 1976.

107. Marzari, N., Vanderbilt, D., De Vita, A., and Payne, M. C.: Thermal contraction and disordering of the al(110) surface. Phys. Rev. Lett., 82:3296–3299, Apr 1999.

108. Sigalas, M., Papaconstantopoulos, D., and Bacalis, N.: Total energy and band structure of the $3d$, $4d$, and $5d$ metals. Physical Review B, 45(11):5777–5783, March 1992.

109. Jepsen, O., Andersen, O. K., and Mackintosh, A. R.: Electronic structure of hcp transition metals. Physical Review B, 12(8):3084–3103, October 1975.

110. Soven, P.: Relativistic band structure and fermi surface of thallium. i. Phys. Rev., 137(6A):A1706–A1717, March 1965.

111. Ekeland, I.: On the variational principle. Journal of Mathematical Analysis and Applications, 47(2):324–353, 1974.

112. Kokalj, A.: Computer graphics and graphical user interfaces as tools in simulations of matter at the atomic scale. Computational Materials Science, 28(2):155 – 168, 2003. Proceedings of the Symposium on Software Development for Process and Materials Design.

113. Elstner, M., Porezag, D., Jungnickel, G., Elsner, J., Haugk, M., Frauenheim, T., Suhai, S., and Seifert, G.: Self-consistent-charge density-functional tight-binding method for simulations of complex materials properties. Physical Review B, 58(11):7260, 1998.

114. Janert, P. K.: Gnuplot in action. Manning, 2010.

115. Blöchl, P. E., Jepsen, O., and Andersen, O. K.: Improved tetrahedron method for brillouin-zone integrations. Phys. Rev. B, 49:16223–16233, Jun 1994.

116. Kresse, G. and Hafner, J.: Ab initio molecular dynamics for liquid metals. Physical Review B, 47(1):558, 1993.

117. Christensen, N. E.: The band structure of silver and optical interband transitions. physica status solidi (b), 54(2):551–563, 1972.

118. Joseph, A. S. and Thorsen, A. C.: Low-field de haas-van alphen effect in ag. Phys. Rev., 138:A1159–A1164, May 1965.

119. Lang, N. D. and Kohn, W.: Theory of metal surfaces: Work function. Phys. Rev. B, 3:1215–1223, Feb 1971.

120. Schulte, F. K.: Chemical potentials and workfunctions of metal surfaces in the theory of an inhomogeneous electron gas. Journal of Physics C: Solid State Physics, 7(20):L370, 1974.

121. Fall, C.: . Ab initio study of the work functions of elemental metal crystals, 1999.

122. Fall, C. J., Binggeli, N., and Baldereschi, A.: Deriving accurate work functions from thin-slab calculations. Journal of Physics: Condensed Matter, 11(13):2689, 1999.

123. Methfessel, M., Hennig, D., and Scheffler, M.: Trends of the surface relaxations, surface energies, and work functions of the 4d transition metals. Physical Review B, 46(8):4816, 1992.

124. Rossky, P., Doll, J., and Friedman, H.: Brownian dynamics as smart monte carlo simulation. The Journal of Chemical Physics, 69(10):4628–4633, 1978.

125. Michaelson, H. B.: The work function of the elements and its periodicity. Journal of Applied Physics, 48(11):4729, 1977.

126. Eastman, D. E.: Photoelectric work functions of transition, rare-earth, and noble metals. Phys. Rev. B, 2:1–2, Jul 1970.

127. Papaconstantopoulos, D. A.: Handbook of the band structure of elemental solids. Springer, 2014.

128. Dillamore, I. and Roberts, W.: Rolling textures in f.c.c. and b.c.c. metals. Acta Metallurgica, 12(3):281 – 293, 1964.

129. Logothetis, E. M. and Hartman, P. L.: Laser-induced electron emission from solids: Many-photon photoelectric effects and thermionic emission. Physical Review, 187(2):460–474, November 1969.

130. Peterman, E. J., Gittes, F., and Schmidt, C. F.: Laser-induced heating in optical traps. Biophysical journal, 84(2):1308–1316, 2003.

131. Semenov, A. D., Nebosis, R. S., Gousev, Y. P., Heusinger, M. A., and Renk, K. F.: Analysis of the nonequilibrium photoresponse of superconducting films to pulsed radiation by use of a two-temperature model. Physical Review B, 52(1):581–590, July 1995.

132. Cohen, L., Klement, W., and Kennedy, G.: Melting of copper, silver, and gold at high pressures. Physical Review, 145(2):519–525, May 1966.

133. Lide, D. R.: CRC handbook of chemistry and physics. CRC press, 2004.

134. Berger, J. A., Rickman, B. L., Li, T., Nicholls, A. W., and Andreas Schroeder, W.: Excited-state thermionic emission in iii-antimonides: Low emittance ultrafast photocathodes. Applied Physics Letters, 101(19), 2012.

135. Ham, F. S.: Energy bands of alkali metals. i. calculated bands. Phys. Rev., 128:82–97, Oct 1962.

136. Ham, F.: Energy bands of alkali metals. II. fermi surface. Physical Review, 128(6):2524–2541, December 1962.

137. H., B.: . Trans. metall. Soc. A.I.M.E., 227:546, 1963.

138. Dugdale, J.: Electrical resistivity at low temperatures. Science, 134:77–86, 1961.

139. Shoenberg, D. and Stiles, P.: The de haas-van alphen effect in alkali metals. In Proceedings of the Royal Society of London A: Mathematical, Physical and Engineering Sciences, volume 281, pages 62–91. The Royal Society, 1964.

140. Okumura, K. and Templeton, I.: The de haas–van alphen effect in rubidium. Philosophical Magazine, 7(79):1239–1241, 1962.

141. Sommerfeld, A.: Lectures on Theoretical Physics: Thermodynamics and statistical mechanics, volume 5. Academic Press, 1964.

142. Thorsen, A. C. and Berlincourt, T. G.: de haas-van alphen effect in potassium. Physical Review Letters, 6(11):617–618, June 1961.

143. Reitz, J. and Overhauser, A.: Magnetoresistance of potassium. Physical Review, 171(3):749–753, July 1968.

144. Hunt, M. B., Reinders, P. H. P., and Springford, M.: A de haas-van alphen effect study of the fermi surface of lithium. Journal of Physics: Condensed Matter, 1(37):6589, September 1989.

145. Anderson, P. A.: The work function of lithium. Phys. Rev., 75:1205–1207, Apr 1949.

146. Elliott, M. and Datars, W. R.: De haas-van alphen effect in sodium under pressure. Journal of Physics F: Metal Physics, 12(3):465, March 1982.

147. Lien, W. H. and Phillips, N. E.: Low-temperature heat capacities of potassium, rubidium, and cesium. Physical Review, 133(5A):A1370–A1377, March 1964.

148. Mattheiss, L. F.: Electronic structure of niobium and tantalum. Physical Review B, 1(2):373–380, January 1970.

149. Loucks, T. L.: Fermi surfaces of cr, mo, and w by the augmented-plane-wave method. Phys. Rev., 139:A1181–A1188, Aug 1965.

150. Lomer, W.: Fermi surface in molybdenum. Proceedings of the Physical Society, 84(2):327, 1964.

151. Powell, B. M., Martel, P., and Woods, A. D. B.: Lattice dynamics of niobium-molybdenum alloys. Phys. Rev., 171:727–736, Jul 1968.

152. Brandt, G. and Rayne, J.: Low-field de haas-van alphen studies of chromium group transition elements. Physical Review, 132(5):1945, 1963.

153. Girvan, R., Gold, A., and Phillips, R.: The de haas-van alphen effect and the fermi surface of tungsten. Journal of Physics and Chemistry of Solids, 29(9):1485–1502, 1968.

154. Fawcett, E., Reed, W., and Soden, R.: High-field galvanomagnetic properties of niobium and tantalum. Physical Review, 159(3):533, 1967.

155. Fu, C. L. and Freeman, A. J.: Surface ferromagnetism of cr(001). Phys. Rev. B, 33:1755–1761, Feb 1986.

156. Leblanc, R. P., Vanbrugghe, B. C., and Girouard, F. E.: Thermionic emission from a niobium single crystal. Canadian Journal of Physics, 52(17):1589–1593, 1974.

157. Jacobson, D. L. and Campbell, A. E.: Molybdenum work function determined by electron emission microscopy. Metallurgical and Materials Transactions B, 2(11):3063–3066, November 1971.

158. Surma, S. A.: Correlation of electron work function and surface-atomic structure of some d transition metals. physica status solidi(a), 183(2):307–322, 2001.

159. Tabor, D.: The hardness of metals, volume 10. ClarendonP, 1951.

160. Dubrovinskaia, N., Dubrovinsky, L., Saxena, S., and Sundman, B.: Thermal expansion of chromium (cr) to melting temperature. Calphad, 21(4):497–508, 1997.

161. Dandliker, R., Conner, R., and Johnson, W.: Melt infiltration casting of bulk metallic-glass matrix composites. Journal of materials research, 13(10):2896–2901, 1998.

162. Seydel, U. and Kitzel, W.: Thermal volume expansion of liquid ti, v, mo, pd, and w. Journal of Physics F: Metal Physics, 9(9):L153, 1979.

163. Iverson, R. J. and Hodges, L.: Molybdenum: Band structure, fermi surface, and spin-orbit interaction. Phys. Rev. B, 8:1429–1432, Aug 1973.

164. Laurent, D. G., Callaway, J., Fry, J. L., and Brener, N. E.: Band structure, fermi surface, compton profile, and optical conductivity of paramagnetic chromium. Phys. Rev. B, 23:4977–4987, May 1981.

165. Mattheiss, L. F.: Fermi surface in tungsten. Physical Review, 139(6A):A1893–A1904, September 1965.

166. Thomas, R. E. and Haas, G. A.: Diffusion measurements in thin films utilizing work function changes: Cr into au. Journal of Applied Physics, 43(12), 1972.

167. Skriver, H. L. and Rosengaard, N. M.: Surface energy and work function of elemental metals. Physical Review B, 46(11):7157–7168, September 1992.

168. Ohnishi, S., Fu, C., and Freeman, A.: Local spin density total energy study of surface magnetism: V (100). Journal of Magnetism and Magnetic Materials, 50(2):161 – 168, 1985.

169. Dillamore, I. and Roberts, W.: . Metall. Rev., 10, 1965.

170. Jacobson, D. and Campbell, A.: . Metall. Trans., 2:3063, 1971.

171. Li, T., Rickman, B. L., and Schroeder, W. A.: Emission properties of body-centered cubic elemental metal photocathodes. Journal of Applied Physics, 117(13), 2015.

172. Biocompatibility of -stabilizing elements of titanium alloys. Biomaterials, 25(26):5705 – 5713, 2004.

173. Xiyuan, Y., Xiaojian, Y., and Wangyu, H.: Molecular-dynamics study of thermodynamic melting of the vanadium (111) surface. Rare Metal Materials and Engineering, 35(4):562, 2006.

174. Akgerman, A., Anthony, R. G., Bullin, J. A., Eubank, P. T., and Hall, K. R.: Method for converting natural gas to liquid hydrocarbons. 2000. US Patent 6,130,260.

175. Kiessig, H. and Essmann, U.: Flow stress of pure niobium between 2200 k and the melting point 2741 k. Scripta metallurgica, 19(8):989–992, 1985.

176. Vecchione, T., Dowell, D., Wan, W., Feng, J., and Padmore, H.: Quantum efficiency and transverse momentum from metals.

177. Berger, J. A., Hogan, J. T., Greco, M. J., Schroeder, W. A., Nicholls, A. W., and Browning, N. D.: Dc photoelectron gun parameters for ultrafast electron microscopy. Microscopy and Microanalysis, 15(04):298–313, 2009.

178. Abellan, P., Woehl, T. J., Tonkyn, R. G., Andreas Schroeder, W., Evans, J. E., and Browning, N. D.: Implementing¡ i¿ in situ¡/i¿ experiments in liquids in the (scanning) transmission electron microscope ((s) tem) and dynamic tem (dtem). Microscopy and Microanalysis, 20(S3):1648–1649, 2014.

179. O'Hara, S., Sellers, G., and Anderson, A.: Influence of hydrogen on the thermal conductivities of superconducting nb and ta. Physical Review B, 10(7):2777, 1974.

180. Face, D., Ruggiero, S., and Prober, D.: Ion-beam deposition of nb and ta refractory superconducting films. Journal of Vacuum Science & Technology A, 1(2):326–330, 1983.

181. Laurent, D. G., Wang, C. S., and Callaway, J.: Energy bands, compton profile, and optical conductivity of vanadium. Physical Review B, 17(2):455–461, January 1978.

182. Petroff, I. and Viswanathan, C. R.: Calculation of the photoelectric emission from tungsten, tantalum, and molybdenum. Physical Review B, 4(3):799, 1971.

183. Fall, C. J., Binggeli, N., and Baldereschi, A.: Deriving accurate work functions from thin-slab calculations. Journal of Physics: Condensed Matter, 11(13):2689, 1999.

184. Jiang, C., Wolverton, C., Sofo, J., Chen, L.-Q., and Liu, Z.-K.: First-principles study of binary bcc alloys using special quasirandom structures. Physical Review B, 69(21):214202, June 2004.

185. Hubbell, W. C. and Brotzen, F. R.: Elastic constants of niobiummolybdenum alloys in the temperature range 190 to +100c. Journal of Applied Physics, 43(8):3306–3312, November 2003.

186. Ishii, R., Matsumura, K., Sakai, A., and Sakata, T.: Work function of binary alloys. Applied Surface Science, 169170:658–661, January 2001.

187. Ramer, N. J. and Rappe, A. M.: Virtual-crystal approximation that works: Locating a compositional phase boundary in pb(zr1-xTix)o3. Physical Review B, 62(2):R743–R746, July 2000.

188. Garrity, K. F., Bennett, J. W., Rabe, K. M., and Vanderbilt, D.: Pseudopotentials for high-throughput dft calculations. Computational Materials Science, 81:446–452, 2014.

189. Denton, A. R. and Ashcroft, N. W.: Vegards law. Physical Review A, 43(6):3161, 1991.

190. Goldschmidt, H. and Brand, J.: The constitution of the chromium-niobium-molybdenum system. Journal of the Less Common Metals, 3(1):44 – 61, 1961.

191. Kaufman, L. and Clougherty, E.: Metals for the space age, plansee proceedings (1964), f. Benesovsky Ed. Metallwerk Plansee, Reutte, Tyrol, Austria, page 722.

192. Gelatt Jr, C. and Ehrenreich, H.: Charge transfer in alloys: Agau. Physical Review B, 10(2):398, 1974.

193. Rothschild, J. A. and Eizenberg, M.: Work function calculation of solid solution alloys using the image force model. Phys. Rev. B, 81:224201, Jun 2010.

194. El-Fattah, Z. M. A., Matena, M., Corso, M., Ormaza, M., Ortega, J. E., and Schiller, F.: Modifying the cu(111) shockley surface state by au alloying. Physical Review B, 86(24), December 2012.

195. LaShell, S., McDougall, B., and Jensen, E.: Spin splitting of an au (111) surface state band observed with angle resolved photoelectron spectroscopy. Physical review letters, 77(16):3419, 1996.

196. Hsieh, T. C., John, P., Miller, T., and Chiang, T.-C.: Resonances in the photoemission cross section of a surface state: Results for ag (111). Physical Review B, 35(8):3728, 1987.

197. Brgi, L., Petersen, L., Brune, H., and Kern, K.: Noble metal surface states: deviations from parabolic dispersion. Surface science, 447(1):L157L161, 2000.

198. Smith, N. V.: Phase analysis of image states and surface states associated with nearly-free-electron band gaps. Physical Review B, 32(6):3549–3555, September 1985.

199. Nicolay, G., Reinert, F., Hfner, S., and Blaha, P.: Spin-orbit splitting of the l-gap surface state on au(111) and ag(111). Physical Review B, 65(3), December 2001.

200. Paniago, R., Matzdorf, R., Meister, G., and Goldmann, A.: Temperature dependence of shockley-type surface energy bands on cu (111), ag (111) and au (111). Surface science, 336(1):113–122, 1995.

201. Koch, J. F., Stradling, R. A., and Kip, A. F.: Some new aspects of cyclotron resonance in copper. Physical Review, 133(1A):A240–A252, January 1964.

202. Joseph, A. S., Thorsen, A. C., Gertner, E., and Valby, L. E.: Low-field de haas-van alphen effect in copper. Physical Review, 148(2):569–575, August 1966.

203. Dowell, D. H., Bazarov, I., Dunham, B., Harkay, K., Hernandez-Garcia, C., Legg, R., Padmore, H., Rao, T., Smedley, J., and Wan, W.: Cathode r&d for future light sources. Nuclear Instruments and Methods in Physics Research Section A: Accelerators, Spectrometers, Detectors and Associated Equipment, 622(3):685–697, October 2010.

204. Goldmann, A., Dose, V., and Borstel, G.: Empty electronic states at the (100),(110), and (111) surfaces of nickel, copper, and silver. Physical Review B, 32(4):1971, 1985.

205. Joseph, A. S., Thorsen, A. C., and Blum, F. A.: Low-field de haas-van alphen effect in gold. Physical Review, 140(6A):A2046–A2050, December 1965.

206. Bosacchi, B., Ketterson, J. B., and Windmiller, L. R.: Measurement and inversion of de haas-van alphen data in gold. Phys. Rev. B, 4:1197–1210, Aug 1971.

207. Ma, X.: Ab-initio study of the work functions of elemental metal surfaces.

208. Farnsworth, H. and Winch, R.: Photoelectric work functions of (100) and (111) faces of silver single crystals and their contact potential difference. Phys. Rev., 58:812–819, Nov 1940.

209. Barrett, C. S. and Massalski, T. B.: Structure of metals, volume 92. McGraw-Hill New York, 1966.

210. Michaelson, H. B.: The work function of the elements and its periodicity. J. Appl. Phys, 48(11), 1977.

211. Krakow, W. and Howland, L. A.: A method for producing hollow cone illumination electronically in the conventional transmission microscope. Ultramicroscopy, 2:53–67, 1976.

212. Kondo, Y., Ito, T., and Harada, Y.: New electron diffraction techniques using electronic hollow-cone illumination. Japanese Journal of Applied Physics, 23(3A):L178, March 1984.

213. Krakow, W. and Howland, L. A.: A method for producing hollow cone illumination electronically in the conventional transmission microscope. Ultramicroscopy, 2:53–67, 1977.

214. Rosenauer, A., Krause, F. F., Müller, K., Schowalter, M., and Mehrtens, T.: Conventional transmission electron microscopy imaging beyond the diffraction and information limits. Physical review letters, 113(9):096101, 2014.

215. Kondo, Y., Ito, T., and Harada, Y.: New electron diffraction techniques using electronic hollow-cone illumination. Japanese Journal of Applied Physics, 23(3A):L178, 1984.

216. Kevan, S. D. and Gaylord, R. H.: High-resolution photoemission study of the electronic structure of the noble-metal (111) surfaces. Physical Review B, 36(11):5809, 1987.

217. Bürgi, L., Petersen, L., Brune, H., and Kern, K.: Noble metal surface states: deviations from parabolic dispersion. Surface science, 447(1):L157–L161, 2000.

218. Hörmandinger, G.: Imaging of the cu(111) surface state in scanning tunneling microscopy. Phys. Rev. B, 49:13897–13905, May 1994.

219. Miranda, R., Daiser, S., Wandelt, K., and Ertl, G.: Thermodynamics of xenon adsorption on pd (s)[8 (100)×(110)]: from steps to multilayers. Surface science, 131(1):61–91, 1983.

220. Salmerón, M., Ferrer, S., Jazzar, M., and Somorjai, G. A.: Photoelectron-spectroscopy study of the electronic structure of au and ag overlayers on pt(100), pt(111), and pt(997) surfaces. Phys. Rev. B, 28:6758–6765, Dec 1983.

221. Methfessel, M., Hennig, D., and Scheffler, M.: Trends of the surface relaxations, surface energies, and work functions of the 4 *d* transition metals. Phys. Rev. B, 46:4816–4829, Aug 1992.

222. S.V.Murav'ev, O.A.Mal'shakova, Golant, K. M., Denisov, A. N., Mashinsky, V. M., and Sazhin, O. D.: Action of the 216-nm fifth harmonic of a nd:yap laser on photosensitive germanosilicate glass films. Quantum Electronics, 33(11):953, 2003.

223. Lang, N. and Kohn, W.: Theory of metal surfaces: work function. Physical Review B, 3(4):1215, 1971.

224. Jézéquel, G. and Pollini, I.: Experimental band structure of lead. Phys. Rev. B, 41:1327–1339, Jan 1990.

225. Smrčka, L.: Energy band structure of aluminium by the augmented plane wave method. Czechoslovak Journal of Physics B, 20(3):291–300, 1970.

226. Baysinger, G.: CRC Handbook of Chemistry and Physics. Doctoral dissertation, National Institute of Standards and Technology, 2015.

227. Wang, X. J., Babzien, M., Malone, R., and Wu, Z.: Mg cathode and its thermal emittance. In Proc. EPAC, 2000.

228. Marzari, N., Vanderbilt, D., De Vita, A., and Payne, M. C.: Thermal contraction and disordering of the al(110) surface. Physical Review Letters, 82(16):3296–3299, April 1999.

229. Singal, C. M. and Das, T. P.: Electronic structure of ferromagnetic hcp cobalt. i. band properties. Physical Review B, 16(11):5068–5092, December 1977.

230. Loucks, T. L. and Cutler, P. H.: Band structure and fermi surface of beryllium. Physical Review, 133(3A):A819–A829, February 1964.

231. Stark, R. W. and Falicov, L. M.: Band structure and fermi surface of zinc and cadmium. Physical Review Letters, 19(14):795–798, October 1967.

232. Batallan, F., Rosenman, I., and Sommers, C. B.: Band structure and fermi surface of hcp ferromagnetic cobalt. Physical Review B, 11(1):545–557, January 1975.

233. Gotsis, H., Papaconstantopoulos, D., and Mehl, M.: Tight-binding calculations of the band structure and total energies of the various phases of magnesium. Physical Review B, 65(13):134101, 2002.

234. Mattheiss, L. F.: Band structure and fermi surface for rhenium. Physical Review, 151(2):450–464, November 1966.

235. Altmann, S. L. and Bradley, C. J.: The band structure of hexagonal close-packed metals II. sc, ti, y and zr. Proceedings of the Physical Society, 92(3):764, November 1967.

236. Chatterjee, P.: Electronic, superconducting, and optical properties of technetium from its augmented-plane-wave band structure. Physical Review B, 27(8):4722–4728, April 1983.

237. Ishizawa, Y. and Datars, W. R.: de haasvan alphen effect in thallium. Physical Review B, 2(10):3875–3882, November 1970.

238. Holtham, P. M., Jan, J.-P., and Skriver, H. L.: Bandstructure of thallium by the LMTO method. Journal of Physics F: Metal Physics, 7(4):635, April 1977.

239. Deegan, R. A.: Structure dependence of d bands in transition metals. Physical Review, 171(3):659–664, July 1968.

240. Pettifor, D. G.: Theory of energy bands and related properties of 4d transition metals. i. band parameters and their volume dependence. Journal of Physics F: Metal Physics, 7(4):613, April 1977.

241. Singh-Miller, N. E. and Marzari, N.: Surface energies, work functions, and surface relaxations of low-index metallic surfaces from first principles. Physical Review B, 80(23):235407, 2009.

242. Chen, S.: Anomalous relaxations of (0001) and (1010) surfaces in hcp metals. Surface science, 264(1):L162–L168, 1992.

243. Green, M.: Solid state surface science, volume 1. M. Dekker, 1969.

244. Green, A. K. and Bauer, E.: Work function and purity of the beryllium (0001) surface. Surface Science, 74(3):676–681, June 1978.

245. Chulkov, E. V., Silkin, V. M., and Shirykalov, E. N.: Surface electronic structure of be(0001) and mg(0001). Surface Science, 188(12):287–300, September 1987.

246. Sobczak, E., P. O. N. and Karlsson., K.: Photoemission of cd (0001) using synchrotron radiation. ACTA PHYSICA POLONICA, SERIES A:337–337, 1992.

247. Lahtinen, J., Vaari, J., and Kauraala, K.: Adsorption and structure dependent desorption of CO on co(0001). Surface Science, 418(3):502–510, December 1998.

248. Lang, N. D. and Kohn, W.: Theory of metal surfaces: Work function. Physical Review B, 3(4):1215–1223, February 1971.

249. Kawano, H.: Effective work functions for ionic and electronic emissions from mono- and polycrystalline surfaces. Progress in Surface Science, 83(12):1–165, February 2008.

250. Himpsel, F. J., Christmann, K., Heimann, P., Eastman, D. E., and Feibelman, P. J.: Adsorbate band dispersions for c on ru(0001). Surface Science, 115(3):L159–L164, March 1982.

251. Hanson, D. M., Stockbauer, R., and Madey, T. E.: Photon-stimulated desorption and other spectroscopic studies of the interaction of oxygen with a titanium (001) surface. Phys. Rev. B, 24:5513–5521, Nov 1981.

252. Yamamoto, M., Chan, C. T., and Ho, K. M.: First-principles calculations of the surface relaxation and electronic structure of zr(0001). Physical Review B, 50(11):7932–7939, September 1994.

253. Fomenko, V. S.: Work function of yttrium and lanthanide single crystals. Powder Metallurgy and Metal Ceramics, 33(1-2):85–90, January 1995.

254. Methfessel, M., Hennig, D., and Scheffler, M.: Trends of the surface relaxations, surface energies, and work functions of the 4d transition metals. Physical Review B, 46(8):4816–4829, August 1992.

255. Morikawa, Y., Ishii, H., and Seki, K.: Theoretical study of n-alkane adsorption on metal surfaces. Physical Review B, 69(4):041403, January 2004.

256. Klein, R.: A field emission study of carbon monoxide on hcp metals rhenium and ruthenium. Surface Science, 20(1):1–17, March 1970.

257. Sahni, V., Perdew, J. P., and Gruenebaum, J.: Variational calculations of low-index crystal face-dependent surface energies and work functions of simple metals. Physical Review B, 23(12):6512–6523, June 1981.

258. Jerner, R. C. and Magee, C. B.: Effect of surface oxidation on the thermionic work function of beryllium. Oxidation of Metals, 2(1):1–9, March 1970.

259. Wilson, R. G.: Vacuum thermionic work functions of polycrystalline be, ti, cr, fe, ni, cu, pt, and type 304 stainless steel. Journal of Applied Physics, 37(6):2261–2267, May 1966.

260. Kocks, U. F., Tomé, C. N., and Wenk, H.-R.: Texture and anisotropy: preferred orientations in polycrystals and their effect on materials properties. 2000.

261. Kimball, J., Stark, R., and Mueller, F.: The fermi surface of magnesium iii: local and nonlocal pseudopotential band structure models for magnesium. Physical Review, 162(3):600, 1967.

262. Papaconstantopoulos, D. A.: Handbook of the band structure of elemental solids. Springer, 1986.

263. Tripp, J. H., Everett, P. M., Gordon, W. L., and Stark, R. W.: Fermi surface of beryllium and its pressure dependence. Phys. Rev., 180:669–678, Apr 1969.

264. Feibelman, P. J. and Hamann, D.: Surface states of sc (0001) and ti (0001). Solid State Commun., 31(6):413–417, 1979.

265. Blyth, R. I. R., Andrews, P. T., and Barrett, S. D.: The unoccupied states of a rare earth metal: Y(0001). J. Phys. Condens. Matter, 3(16):2827, April 1991.

266. Chulkov, E., Silkin, V., and Shirykalov, E.: Surface electronic structure of be (0001) and mg (0001). Surface Science, 188(1):287–300, 1987.

267. Karlsson, U. O., Hansson, G., Persson, P., and Flodström, S.: Surface electronic structure of mg (0001). Physical Review B, 26(4):1852, 1982.

268. Choy, T., Naset, J., Chen, J., Hershfield, S., and Stanton, C.: A database of fermi surface in virtual reality modeling language (vrml). Bull. Am. Phys. Soc., 45(1):L36–42, 2000.

269. Svane, A., Christensen, N. E., Cardona, M., Chantis, A. N., van Schilfgaarde, M., and Kotani, T.: Quasiparticle self-consistent GW calculations for PbS, PbSe, and PbTe: Band structure and pressure coefficients. Physical Review B, 81(24), June 2010.

270. Rabii, S.: Investigation of energy-band structures and electronic properties of pbs and pbse. Physical Review, 167(3):801, 1968.

271. Wu, H. F., Zhang, H. J., Lu, Y. H., Si, J. X., Li, H. Y., Bao, S. N., Wu, H. Z., and He, P.: AgPbTe(111) interface behavior studied by photoemission spectroscopy. Applied Physics Letters, 92(12):122112, 2008.

272. Dimmock, J. O. and Wright, G. B.: Band edge structure of PbS, PbSe, and PbTe. Physical Review, 135(3A):A821, 1964.

273. Heremans, J. P., Jovovic, V., Toberer, E. S., Saramat, A., Kurosaki, K., Charoenphakdee, A., Yamanaka, S., and Snyder, G. J.: Enhancement of thermoelectric efficiency in pbte by distortion of the electronic density of states. Science, 321(5888):554–557, 2008.

274. Snyder, G. J. and Toberer, E. S.: Complex thermoelectric materials. Nature materials, 7(2):105–114, 2008.

275. Dughaish, Z.: Lead telluride as a thermoelectric material for thermoelectric power generation. Physica B: Condensed Matter, 322(1):205–223, 2002.

276. Jin, X., Yamamoto, N., Nakagawa, Y., Mano, A., Kato, T., Tanioku, M., Ujihara, T., Takeda, Y., Okumi, S., Yamamoto, M., et al.: Super-high brightness and high-spin-polarization photocathode. Applied physics express, 1(4):045002, 2008.

277. Shields, A. J.: Semiconductor quantum light sources. Nature photonics, 1(4):215–223, 2007.

278. Montgomery, E. J.: Characterization of quantum efficiency and robustness of cesium-based photocathodes. 2010.

279. Day, R. H.: Photoelectric quantum efficiencies and filter window absorption coefficients from 20 eV to 10 KeV. Journal of Applied Physics, 52(11):6965, 1981.

280. Granados, D., García, J. M., Ben, T., and Molina, S. I.: Vertical order in stacked layers of self-assembled in (ga) as quantum rings on gaas (001). Applied Physics Letters, 86(7):071918, 2005.

281. Ruvimov, S., Werner, P., Scheerschmidt, K., Gösele, U., Heydenreich, J., Richter, U., Ledentsov, N., Grundmann, M., Bimberg, D., Ustinov, V., et al.: Structural characterization of (in, ga) as quantum dots in a gaas matrix. Physical Review B, 51(20):14766, 1995.

282. Heitz, R., Kalburge, A., Xie, Q., Grundmann, M., Chen, P., Hoffmann, A., Madhukar, A., and Bimberg, D.: Excited states and energy relaxation in stacked inas/gaas quantum dots. Physical Review B, 57(15):9050, 1998.

283. Schreiber, S., Michelato, P., Monaco, L., and Sertore, D.: On the photocathodes used at the ttf photoinjector. In Particle Accelerator Conference, 2003. PAC 2003. Proceedings of the, volume 3, pages 2071–2073. IEEE, 2003.

284. Aspnes, D. E. and Studna, A. A.: Dielectric functions and optical parameters of si, ge, gap, gaas, gasb, inp, inas, and insb from 1.5 to 6.0 ev. Phys. Rev. B, 27:985–1009, Jan 1983.

285. Chelikowsky, J. R. and Cohen, M. L.: Nonlocal pseudopotential calculations for the electronic structure of eleven diamond and zinc-blende semiconductors. Phys. Rev. B, 14:556–582, Jul 1976.

286. Chelikowsky, J. R. and Cohen, M. L.: Erratum: Nonlocal pseudopotential calculations for the electronic structure of eleven diamond and zinc-blende semiconductors. Phys. Rev. B, 30:4828–4828, Oct 1984.

287. Sootsman, J., Chung, D., and Kanatzidis, M.: New and old concepts in thermoelectric materials. Angewandte Chemie International Edition, 48(46):8616–8639, 2009.

288. Sootsman, J., Kong, H., Uher, C., D'Angelo, J., Wu, C.-I., Hogan, T., Caillat, T., and Kanatzidis, M.: Large enhancements in the thermoelectric power factor of bulk pbte at high temperature by synergistic nanostructuring. Angewandte Chemie International Edition, 47(45):8618–8622, 2008.

289. Snyder, G. J. and Toberer, E. S.: Complex thermoelectric materials. Nature Materials, 7(2):105–114, February 2008.

290. Logothetis, E., Holloway, H., Varga, A., and Wilkes, E.: Infrared detection by schottky barriers in epitaxial pbte. Applied Physics Letters, 19(9):318–320, 1971.

291. Rogalski, A.: Infrared detectors. CRC Press, 2010.

292. Wang, H., Pei, Y., LaLonde, A. D., and Snyder, G. J.: Heavily doped p-type pbse with high thermoelectric performance: An alternative for pbte. Advanced Materials, 23(11):1366–1370, 2011.

293. Yamamoto, N., Nakanishi, T., Mano, A., Nakagawa, Y., Okumi, S., Yamamoto, M., Konomi, T., Jin, X., Ujihara, T., Takeda, Y., et al.: High brightness and high polarization electron source using transmission photocathode with gaas-gaasp superlattice layers. Journal of Applied Physics, 103(6):064905, 2008.

294. Németh, K., Harkay, K. C., van Veenendaal, M., Spentzouris, L., White, M., Attenkofer, K., and Srajer, G.: High-brightness photocathodes through ultrathin surface layers on metals. Physical review letters, 104(4):046801, 2010.

295. Li, T., Rickman, B. L., and Schroeder, W. A.: Density functional theory analysis of hexagonal close-packed elemental metal photocathodes. Phys. Rev. ST Accel. Beams, 18:073401, Jul 2015.

296. Skelton, J. M., Parker, S. C., Togo, A., Tanaka, I., and Walsh, A.: Thermal physics of the lead chalcogenides pbs, pbse, and pbte from first principles. Phys. Rev. B, 89:205203, May 2014.

297. Dimmock, J. and Wright, G.: Band edge structure of pbs, pbse, and pbte. Phys. Rev., 135:A821–A830, Aug 1964.

298. Dalven, R.: Introduction to applied solid state physics: topics in the applications of semiconductors, superconductors, ferromagnetism, and the nonlinear optical properties of solids. Plenum Press New York, 1990.

299. I. Weinberg, J. C.: Nuovo cimento. 24, 1962.

300. Stiles, P., Burstein, E., and Langenberg, D.: Observations of de haas-van alphen oscillations in p-type pbte. Phys. Rev. Lett., 6:667–669, Jun 1961.

301. Aspnes, D. and Cardona, M.: Electro-optic measurements of pbs, pbse, and pbte. Phys. Rev., 173:714–728, Sep 1968.

302. Cardona, M. and Greenaway, D. L.: Optical properties and band structure of group iv-vi and group v materials. Physical Review, 133(6A):A1685, 1964.

303. Stiles, P., Burstein, E., and Langenberg, D.: de haas-van alphen effect in p-type pbte and n-type pbs. Journal of Applied Physics, 32(10):2174–2178, 1961.

304. Hoang, K.: Atomic and electronic structures of novel ternary and quaternary narrow band-gap semiconductors. ProQuest, 2007.

305. Mattsson, A.: Designing meaningful density functional theory calculations in materials science. In APS Shock Compression of Condensed Matter Meeting Abstracts, volume 1, page 5001, 2005.

306. Hood, R. Q., Chou, M., Williamson, A., Rajagopal, G., Needs, R., and Foulkes, W.: Quantum monte carlo investigation of exchange and correlation in silicon. Physical review letters, 78(17):3350, 1997.

307. Hood, R. Q., Chou, M., Williamson, A., Rajagopal, G., and Needs, R.: Exchange and correlation in silicon. Physical Review B, 57(15):8972, 1998.

308. Madelung, O., Rössler, U., and Schulz, M.: Semiconductors: Group iv elements, iv–iv and iii–iv compounds, landolt-börnstein, new series, group iii, vol. 41, pt. a. ASpringer-Verlag, Berlin, 2005.

309. Dornhaus, R., Nimtz, G., and Schlicht, B.: Narrow-gap semiconductors. Springer, 1983.

310. Strehlow, W. H. and Cook, E. L.: Compilation of energy band gaps in elemental and binary compound semiconductors and insulators. Journal of Physical and Chemical Reference Data, 2(1), 1973.

311. Frank, N., Springholz, G., and Bauer, G.: Imaging of misfit dislocation formation in strained layer heteroepitaxy by ultrahigh vacuum scanning tunneling microscopy. Physical review letters, 73(16):2236, 1994.

312. Khokhlov, D.: Lead chalcogenides: physics and applications. CRC Press, 2002.

313. Berger, J. A., Greco, M. J., and Schroeder, W. A.: High-power, femtosecond, thermal-lens-shaped yb: Kgw oscillator. Optics express, 16(12):8629–8640, 2008.

314. Knapp, R.: Photoelectric properties of lead sulfide in the near and vacuum ultraviolet. Phys. Rev., 132:1891–1897, Dec 1963.

315. Pattantyus-Abraham G A Kramer J I, Barkhouse R A, W. X. K. G. D. R. L. L. R. I. N. K. M. G. M. and E, S. H.: . ACS Nano, 4:337, 2010.

316. Nill, K., Calawa, A., Harman, T., and Walpole, J.: Laser emission from metal-semiconductor barriers on pbte and pb0. 8sn0. 2te. Applied Physics Letters, 16(10):375–377, 1970.

317. Bi, G., Zhao, F., Ma, J., Mukherjee, S., Li, D., and Shi, Z.: Modeling of the potential profile for the annealed polycrystalline PbSe film. PIERS Online, 5(1):61–64, 2009.

318. Saliba, S. D., Putkunz, C. T., Sheludko, D. V., McCulloch, A. J., Nugent, K. A., and Scholten, R. E.: Spatial coherence of electron bunches extracted from an arbitrarily shaped cold atom electron source. Opt. Express, 20(4):3967–3974, Feb 2012.

319. Maxson, J., Bazarov, I., Wan, W., Padmore, H., and Coleman-Smith, C.: Fundamental photoemission brightness limit from disorder induced heating. New Journal of Physics, 15(10):103024, 2013.

320. Zhang, H. and Davison, W.: Performance characteristics of diffusion gradients in thin films for the in situ measurement of trace metals in aqueous solution. Analytical chemistry, 67(19):3391–3400, 1995.

321. Mahan, G.: Theory of photoemission in simple metals. Physical Review B, 2(11):4334, 1970.

322. Haynes, W.: Crc handbook of chemistry and physics, 95th edition. 2014.

323. Chelvayohan, M. and Mee, C. H. B.: Work function measurements on (110), (100) and (111) surfaces of silver. Journal of Physics C: Solid State Physics, 15(10):2305, April 1982.

324. Levinson, H. J., Greuter, F., and Plummer, E. W.: Experimental band structure of aluminum. Physical Review B, 27(2):727–747, January 1983.

325. Johansen, G.: The electronic structure of barium by the RAPW method. Solid State Communications, 7(10):731–734, May 1969.

326. Kennedy, T. A. and Seidel, G.: Azbel'-kaner cyclotron resonance and magnetic surface levels in beryllium. Physical Review B, 6(10):3706–3713, November 1972.

327. Ast, C. R. and Höchst, H.: Two-dimensional band structure and self-energy of bi (111) near the γ point. Physical Review B, 66(12):125103, 2002.

328. Gonze, X., Michenaud, J.-P., and Vigneron, J.-P.: First-principles study of as, sb, and bi electronic properties. Physical Review B, 41(17):11827–11836, June 1990.

329. Shoenberg, D.: The de haas-van alphen effect. Philosophical Transactions of the Royal Society of London. Series A, Mathematical and Physical Sciences, 245(891):1–57, July 1952.

330. Bhargava, R. N.: de haas-van alphen and galvanomagnetic effect in bi and bi-pb alloys. Physical Review, 156(3):785–797, April 1967.

331. Berlincourt, T. G.: de haas-van alphen effect in cadmium. Physical Review, 94(5):1172–1178, June 1954.

332. Rosenman, I. and Batallan, F.: Low-frequency de haas-van alphen effect in cobalt. Physical Review B, 5(4):1340–1347, February 1972.

333. Graebner, J. E. and Marcus, J. A.: de haas-van alphen effect in antiferromagnetic chromium. Physical Review, 175(2):659–673, November 1968.

334. Okumura, K. and Templeton, I. M.: The fermi surface of caesium. Proceedings of the Royal Society of London. Series A, Mathematical and Physical Sciences, 287(1408):89–104, August 1965.

335. Kokko, K., Salo, P., Laihia, R., and Mansikka, K.: First-principles calculations for work function and surface energy of thin lithium films. Surface Science, 348(12):168 – 174, 1996.

336. Brandt, G. B. and Rayne, J. A.: Low-field de haas-van alphen effect in indium. Physical Review, 132(4):1512–1516, November 1963.

337. Hrnfeldt, S., Hammarstrm, ., Carrander, K., and Bjrck, G.: The de haas-van alphen effect and the fermi surface in iridium. Journal of Physics and Chemistry of Solids, 32(4):753–760, 1971.

338. D. Shoenberg, C. J. G.: in progress in low temperature physics. Vol.2:226–265, North-Holland, Amsterdam, 1957.

339. Dobson, K. and Myers, A.: Effective mass measurements and electron velocities in molybdenum. Solid State Communications, 35(1):27–29, July 1980.

340. Tsui, D. C. and Stark, R. W.: de haas-van alphen effect in ferromagnetic nickel. Physical Review Letters, 17(16):871–875, October 1966.

341. Startsev, V. E., Coleridge, P. T., Templeton, I. M., Fawcett, E., Muir, C., and Perz, J. M.: Conduction electrong-factors in ruthenium and osmium from de haas-van alphen measurements. Journal of Low Temperature Physics, 55(1-2):175–188, April 1984.

342. Ogawa, K., Aoki, H., and Nakatani, I.: de haas-van alphen oscillation for the symmetry direction [011] in leadorigin of the long beat and the shape of the third zone electron arm. Journal of Physics and Chemistry of Solids, 40(6):469–475, 1979.

343. Vuillemin, J. J.: De haas-van alphen effect and fermi surface in palladium. Physical Review, 144(2):396–405, April 1966.

344. Windmiller, L. R. and Ketterson, J. B.: de haas-van alphen effect and fermi surface in pt. Physical Review Letters, 20(7):324–326, February 1968.

345. Martin, B. D., Zych, D. A., and Heer, C. V.: Atomic heats of cesium, rubidium, and lithium between 0.35 and 2k. Physical Review, 135(3A):A671–A679, August 1964.

346. Joseph, A. S. and Thorsen, A. C.: de haasvan alphen effect and fermi surface in rhenium. Physical Review, 133(6A):A1546–A1552, March 1964.

347. Carrander, K., Dronjak, M., and Hrnfeldt, S. P.: De haas-van alphen effect in rhodium. Journal of Physics and Chemistry of Solids, 38(3):289–296, 1977.

348. Schirber, J. E., Switendick, A. C., and Schmidt, F. A.: de haas-van alphen effect in sc metal. Physical Review B, 27(10):6475–6477, May 1983.

349. Green, M. A.: Intrinsic concentration, effective densities of states, and effective mass in silicon. Journal of Applied Physics, 67(6):2944–2954, March 1990.

350. Dexter, R. N., Zeiger, H. J., and Lax, B.: Cyclotron resonance experiments in silicon and germanium. Physical Review, 104(3):637–644, November 1956.

351. Croft, G. T., Love, W. F., and Nix, F. C.: De haas-van alphen effect in tin and tin-antimony alloys. Physical Review, 95(6):1403–1408, September 1954.

352. HALLORAN, M.: Experimental study of the fermi surfaces of niobium and tantalum.

353. Haanappel, E. G.: De haasvan alphen effect in heavy fermions, high tc superconductors, and quasicrystals. Physica B: Condensed Matter, 246247:78–82, May 1998.

354. Parker, R. D. and Halloran, M. H.: Experimental study of the fermi surface of vanadium. Physical Review B, 9(10):4130–4137, May 1974.

355. Priestley, M. G.: Pulsed-field de haas-van alphen effect in thallium. Physical Review, 148(2):580–585, August 1966.

356. Girvan, R. F., Gold, A. V., and Phillips, R. A.: The de haas-van alphen effect and the fermi surface of tungsten. Journal of Physics and Chemistry of Solids, 29(9):1485–1502, September 1968.

357. Mattocks, P. G. and Young, R. C.: de haas-van alphen effect and fermi surface of yttrium. Journal of Physics F: Metal Physics, 8(7):1417, July 1978.

358. Everett, P. M.: de haas-van alphen studies in zirconium to 92 kG. Physical Review B, 20(4):1419–1425, August 1979.

359. Loucks, T. L. and Cutler, P.: Band structure and fermi surface of beryllium. Physical Review, 133(3A):A819, 1964.

360. Kimball, J. C., Stark, R. W., and Mueller, F. M.: The fermi surface of magnesium iii: Local and nonlocal pseudopotential band structure models for magnesium. Phys. Rev., 162:600–608, Oct 1967.

361. Falicov, L. M.: The band structure and fermi surface of magnesium. Philosophical Transactions of the Royal Society of London. Series A, Mathematical and Physical Sciences, 255(1051):55–83, 1962.

362. Ketterson, J. and Stark, R.: Fermi surface of magnesium. i. magnetoacoustic attenuation. Physical Review, 156(3):748, 1967.

363. Stark, R.: Fermi surface of magnesium. ii: The de haasvan alphen effect. Physical Review, 162(3):589, 1967.

364. Watts, B.: The fermi surface of beryllium. Physics Letters, 3(6):284–285, 1963.

365. Stewart, A., Shand, J., Donaghy, J., and Kusmiss, J.: Fermi surface of beryllium by positron annihilation. Physical Review, 128(1):118, 1962.

366. Skriver, H. L. and Rosengaard, N.: Surface energy and work function of elemental metals. Physical Review B, 46(11):7157, 1992.

367. Simmons, J.: Richardson-schottky effect in solids. Physical Review Letters, 15(25):967, 1965.

368. Valfells, ., Feldman, D. W., Virgo, M., OShea, P. G., and Lau, Y. Y.: Effects of pulse-length and emitter area on virtual cathode formation in electron guns. Physics of Plasmas (1994-present), 9(5), 2002.

369. Bazarov, I. V., Dunham, B. M., and Sinclair, C. K.: Maximum achievable beam brightness from photoinjectors. Physical review letters, 102(10):104801, 2009.

370. Berntsen, M. H., Gtberg, O., and Tjernberg, O.: An experimental setup for high resolution 10.5 ev laser-based angle-resolved photoelectron spectroscopy using a time-of-flight electron analyzer. Review of Scientific Instruments, 82(9):–, 2011.

371. Parker, R. D. and Halloran, M. H.: Experimental study of the fermi surface of vanadium. Phys. Rev. B, 9:4130–4137, May 1974.

372. Ashcroft, N. W. and Mermin, N. D.: Solid state physics (holt, rinehart and winston, new york, 1976). There is no corresponding record for this reference, 2005.

373. Ashcroft, N.: Electron-ion pseudopotentials in metals. Physics Letters, 23(1):48 – 50, 1966.

374. Levinson, H. J., Greuter, F., and Plummer, E. W.: Experimental band structure of aluminum. Phys. Rev. B, 27:727–747, Jan 1983.

375. Larson, C. O. and Gordon, W. L.: Low-field de haas¯van alphen study of the fermi surface of aluminum. Phys. Rev., 156:703–715, Apr 1967.

376. Ashcroft, N.: The fermi surface of aluminium. Philosophical Magazine, 8(96):2055–2083, 1963.

377. Harrison, W. A.: Fermi surface in aluminum. Phys. Rev., 116:555–561, Nov 1959.

378. Fredriksson, H. and Åkerlind, U.: Physics of functional materials. John Wiley & Sons, 2008.

379. Noda, Y., Masumoto, K., Ohba, S., Saito, Y., Toriumi, K., Iwata, Y., and Shibuya, I.: Temperature dependence of atomic thermal parameters of lead chalcogenides, PbS, PbSe and PbTe. Acta Crystallographica Section C, 43(8):1443–1445, Aug 1987.

380. Cohen, M. L. and Bergstresser, T. K.: Band structures and pseudopotential form factors for fourteen semiconductors of the diamond and zinc-blende structures. Phys. Rev., 141:789–796, Jan 1966.

381. Farr, M. K., Traylor, J. G., and Sinha, S. K.: Lattice dynamics of gasb. Phys. Rev. B, 11:1587–1594, Feb 1975.

382. Ikuno, Y. and Kusakabe, K.: A determination method of the work function using the slab model with a first-principles electronic structure calculation. e-Journal of Surface Science and Nanotechnology, 6:103–106, 2008.

383. Cardona, M. and Ley, L.: Photoemission in solids i. Photoemission in Solids I: General Principles, 1, 1978.

384. Yamamoto, N., Yamamoto, M., Kuwahara, M., Sakai, R., Morino, T., Tamagaki, K., Mano, A., Utsu, A., Okumi, S., Nakanishi, T., et al.: Thermal emittance measure-

ments for electron beams produced from bulk and superlattice negative electron affinity photocathodes. Journal of Applied Physics, 102(2):024904, 2007.

385. Roberts, J. P., Taylor, A. J., Lee, P. H. Y., and Gibson, R. B.: High-irradiance 248-nm laser system. Opt. Lett., 13(9):734–736, Sep 1988.

386. Fall, C.: Ab initio study of the work functions of elemental metal crystals. EPFL, 1999.

387. Kajita, S., Nakayama, T., and Yamauchi, J.: Density functional calculation of work function using charged slab systems. Journal of Physics: Conference Series, 29:120–123, January 2006.

388. Weiser, K.: Doping of pbte with group-iii elements: An ionic lattice approach. Phys. Rev. B, 23:2741–2751, Mar 1981.

389. Courths, R., Wern, H., Hau, U., Cord, B., Bachelier, V., and Hufner, S.: Band structure of cu, ag and au: location of direct transitions on the line using angle-resolved photoelectron spectroscopy (ARUPS). Journal of Physics F: Metal Physics, 14(6):1559, June 1984.

390. Overhof, H. and Rössler, U.: Electronic structure of pbs, pbse, and pbte. physica status solidi (b), 37(2):691–698, 1970.

391. Conklin, J., Johnson, L., and Pratt, G.: Energy bands in pbte. Phys. Rev., 137:A1282–A1294, Feb 1965.

392. Herman, F., Kortum, R. L., Ortenburger, I. B., et al.: Relativistic band structure of gete, snte, pbte, pbse, and pbs. Le Journal de Physique Colloques, 29(C4):C4–62, 1968.

393. Tung, Y. and Cohen, M.: Relativistic band structure and electronic properties of snte, gete, and pbte. Phys. Rev., 180:823–826, Apr 1969.

394. Lin, P. J. and Kleinman, L.: Energy bands of pbte, pbse, and pbs. Physical Review, 142(2):478, 1966.

395. Cardona, M., Langer, D. W., Shevchik, N. J., and Tejeda, J.: Photoelectric properties of the lead chalcogenides. physica status solidi (b), 58(1):127–137, 1973.

396. Hummer, K., Grüneis, A., and Kresse, G.: Structural and electronic properties of lead chalcogenides from first principles. Phys. Rev. B, 75:195211, May 2007.

397. Hogan, M. J., Assmann, R., Decker, F.-J., Iverson, R., Raimondi, P., Rokni, S., Siemann, R. H., Walz, D., Whittum, D., Blue, B., Clayton, C. E., Dodd, E., Hemker, R., Joshi, C., Marsh, K. A., Mori, W. B., Wang, S., Katsouleas, T., Lee, S., Muggli, P., Catravas, P., Chattopadhyay, S., Esarey, E., and Leemans, W. P.: E-157: A 1.4-m-long plasma wake field acceleration experiment using a 30 gev electron beam from the stanford linear accelerator center linac. Physics of Plasmas (1994-present), 7(5), 2000.

398. Sebetci, A., Güvenç, Z. B., and Kökten, H.: Thermodynamics of small platinum clusters. Computational materials science, 35(3):192–197, 2006.

399. Jones, F. and Wood, K.: The melting point of thin aluminium films. British journal of applied physics, 15(2):185, 1964.

400. Mathematical modeling of laser induced heating and melting in solids. 33.

401. Graves, W., DiMauro, L., Heese, R., Johnson, E., Rose, J., Rudati, J., Shaftan, T., and Sheehy, B.: Measurement of thermal emittance for a copper photocathode. In Particle Accelerator Conference, 2001. PAC 2001. Proceedings of the 2001, volume 3, pages 2227–2229 vol.3, 2001.

402. Piróth, A. and Sólyom, J.: Fundamentals of the Physics of Solids: Volume II: Electronic Properties, volume 2. Springer, 2008.

403. Goldmann, A.: Tc (technetium) (z = 43). goldmann, a. (ed.). SpringerMaterials - The Landolt-Brnstein Database.

404. Vergs, J. A. and Louis, E.: Electron states on the (111) surface of copper. Solid State Communications, 22(10):663–666, June 1977.

405. Fermi surfaces of cr, mo, and w by the augmented-plane-wave method. 139.

406. Fomenko, V.: Work function of yttrium and lanthanide single crystals. Powder Metallurgy and Metal Ceramics, 33(1-2):85–90, 1995.

407. Lakh, K. and Stasyuk, Z.: Surface electron–adsorption properties of potassium films on the(1010) surface of rhenium. Sov. Phys. Solid State,, 20(7):1149–1150, 1978.

408. Huang, Z. and Kim, K.-J.: Review of x-ray free-electron laser theory. Phys. Rev. ST Accel. Beams, 10:034801, Mar 2007.

409. SrinivasanRao, T., Fischer, J., and Tsang, T.: Photoemission studies on metals using picosecond ultraviolet laser pulses. Journal of Applied Physics, 69(5), 1991.

410. Krakow, W. and Howland, L. A.: A method for producing hollow cone illumination electronically in the conventional transmission microscope. Ultramicroscopy, 2(0):53 – 67, 19761977.

411. Hanssen, K. and Trepte, L.: Influence of voltage and current fluctuations and of a finite energy width of electrons on contrast and resolution in electron microscopy. Optik, 32(6):519, 1971.

412. Rössler, U.: Znte: lattice parameters. In New Data and Updates for several Semiconductors with Chalcopyrite Structure, for several II-VI Compounds and diluted magnetic IV-VI Compounds, pages 250–252. Springer, 2013.

413. Graner, G. and Kuchitsu, K.: Landolt-Börnstein: Numerical Data and Functional Relationships in Science and Technology. Molecules and radicals. Structure data of free polyatonic molecules. Molecules containing three or four carbon atoms, volume 25. Springer, 2001.

414. Donohue, J.: Structures of the Elements. John Wiley and Sons, Inc., New York, 1974.

415. Mehl, M. J. and Papaconstantopoulos, D. A.: Applications of a tight-binding total-energy method for transition and noble metals: Elastic constants, vacancies, and surfaces of monatomic metals. Phys. Rev. B, 54:4519–4530, Aug 1996.

416. Featherston, F. H. and Neighbours, J. R.: Elastic constants of tantalum, tungsten, and molybdenum. Phys. Rev., 130:1324–1333, May 1963.

417. Mattheiss, L. F.: Electronic structure of niobium and tantalum. Phys. Rev. B, 1:373–380, Jan 1970.

418. Kiejna, A.: Surface atomic structure and energetics of tantalum. Surface science, 598(1):276–284, 2005.

419. Brener, N., Fuster, G., Callaway, J., Fry, J., and Zhao, Y. Z.: Magnetic structure of bcc and fcc manganese. Journal of Applied Physics, 63(8):4057–4059, 1988.

420. Swank, R. K.: Surface properties of ii-vi compounds. Phys. Rev., 153:844–849, Jan 1967.

421. Zakharov, O., Rubio, A., Blase, X., Cohen, M. L., and Louie, S. G.: Quasiparticle band structures of six ii-vi compounds: Zns, znse, znte, cds, cdse, and cdte. Phys. Rev. B, 50:10780–10787, Oct 1994.

422. Garrity, K. F., Bennett, J. W., Rabe, K. M., and Vanderbilt, D.: Pseudopotentials for high-throughput {DFT} calculations. Computational Materials Science, 81(0):446 – 452, 2014.

423. Aresti, A., Garbato, L., and Rucci, A.: Some cohesive energy features of tetrahedral semiconductors. Journal of Physics and Chemistry of Solids, 45(3):361 – 365, 1984.

424. Verma, A., Sarkar, B., and Jindal, V.: Cohesive energy of zincblende (aiiibv and aiibvi) structured solids. Pramana, 74(5):851–855, 2010.

425. Goldfinger, P. and Jeunehomme, M.: Mass spectrometric and knudsen-cell vaporization studies of group 2b-6b compounds. Transactions of the Faraday Society, 59:2851–2867, 1963.

426. Zhang, S., Wei, S.-H., and Zunger, A.: Intrinsic n-type versus p-type doping asymmetry and the defect physics of zno. Physical Review B, 63(7):075205, 2001.

427. [pseudo] we used the pseudopotentials cd.pbe-mt_fhi.upf, te.pbe-mt_fhi.upf and zn.pbe-mt_fhi.upf from $http://www.quantum-espresso.org$.

428. Mattheiss, L. F.: Fermi surface in tungsten. Phys. Rev., 139:A1893–A1904, Sep 1965.

429. Dobson, K. and Myers, A.: Effective mass measurements and electron velocities in molybdenum. Solid State Communications, 35(1):27 – 29, 1980.

430. EVENSON, W. E., FLEMING, G. S., and LIU, S. H.: Generalized susceptibilities and magnetic properties of some bcc transition metals. Phys. Rev., 178:930–931, Feb 1969.

431. Halloran, M. H., Condon, J. H., Graebner, J. E., Kunzier, J. E., and Hsu, F. S. L.: Experimental study of the fermi surfaces of niobium and tantalum. Phys. Rev. B, 1:366–372, Jan 1970.

432. Kresse, G. and Furthmüller, J.: Comp mater sci 1996, 6, 15. CrossRef, CAS, Web of Science® Times Cited, 6104, 1996.

433. Nordheim, L.: . Ann. Phys., 9(5):607–640, 1931. cited By (since 1996)128.

434. Bostanjoglo, O. and Liedtke, R.: Tracing fast phase transitions by electron microscopy. physica status solidi (a), 60(2):451–455, 1980.

435. Dmer, H. and Bostanjoglo, O.: High-speed transmission electron microscope. Review of Scientific Instruments, 74(10), 2003.

436. Lobastov, V. A., Srinivasan, R., and Zewail, A. H.: Four-dimensional ultrafast electron microscopy. Proceedings of the National Academy of Sciences of the United States of America, 102(20):7069–7073, 2005.

437. Armstrong, M. R., Reed, B. W., Torralva, B. R., and Browning, N. D.: Prospects for electron imaging with ultrafast time resolution. Appl. Phys. Lett., 90(11), 2007.

438. Németh, K., Harkay, K. C., van Veenendaal, M., Spentzouris, L., White, M., Attenkofer, K., and Srajer, G.: High-brightness photocathodes through ultrathin surface layers on metals. Phys. Rev. Lett., 104:046801, Jan 2010.

439. Perdew, J. P. and Zunger, A.: Self-interaction correction to density-functional approximations for many-electron systems. Phys. Rev. B, 23:5048–5079, May 1981.

440. Mattheiss, L. F.: Energy bands for the iron transition series. Phys. Rev., 134:A970–A973, May 1964.

441. Holstein, T., Norton, R. E., and Pincus, P.: de haas-van alphen effect and the specific heat of an electron gas. Phys. Rev. B, 8:2649–2656, Sep 1973.

442. RESONANCE, C.: Cyclotron resonance and de haas-van alphen oscillations of an interacting electron gas. Physical Review, 123(4), 1961.

443. Surma, M., Lebech, J., and Smark, K.: Cyclotron effective masses and fermi velocities for the ellipsoidal hole surfaces in molybdenum. Solid State Communications, 17(11):1359–1362, December 1975.

444. Surma, M., Lebech, J., and Saermark, K.: Cyclotron resonance observation on the electron lenses of molybdenum fermi surface. Solid State Communications, 20(5):493–495, November 1976.

445. Leaver, G. and Myers, A.: De haas-van alphen measurements in molybdenum. Philosophical Magazine, 19(159):465–475, 1969.

446. Hoekstra, J. A. and Stanford, J. L.: Determination of the fermi surface of molybdenum using the de haasvan alphen effect. Physical Review B, 8(4):1416–1429, August 1973.

447. Fawcett, E. and Reed, W. A.: High-field magnetoresistance of molybdenum and tungsten. Physical Review, 134(3A):A723–A727, May 1964.

448. Pickett, W. E. and Allen, P. B.: Optical properties of nb and mo calculated from augmented-plane-wave band structures. Physical Review B, 11(10):3599–3603, May 1975.

449. Gasparov, V. A. and Harutunian, M. H.: Precision investigations of the fermi surface of molybdenum. physica status solidi (b), 93(1):403414, 1979.

450. Cleveland, J. R. and Stanford, J. L.: Radio-frequency size effect and the fermi surface of molybdenum. Physical Review B, 4(2):311–319, July 1971.

451. Jones, C. K., Klemens, P. G., and Rayne, J. A.: Temperature dependence of ultrasonic attenuation in fused quartz up to 1 kMc/s. Physics Letters, 8(1):31–32, January 1964.

452. Jani, A. R., Tripathi, G. S., Brener, N. E., and Callaway, J.: Band structure and related properties of molybdenum. Physical Review B, 40(3):1593–1602, July 1989.

453. Iverson, R. J. and Hodges, L.: Molybdenum: Band structure, fermi surface, and spin-orbit interaction. Physical Review B, 8(4):1429–1432, August 1973.

454. Peloi, M., Ferrini, G., Banfi, G., Secondi, G., and Parmigiani, F.: Non-linear photoemission from polycrystalline molybdenum irradiated by 790 nm150fs laser pulses. Solid state communications, 118(7):339344, 2001.

455. Sosa, E. D.: The electron emission characteristics of aluminum, molybdenum and carbon nanotubes studied by field emission and photoemission. Doctoral dissertation, University of North Texas, 2002.

456. Davis, J. R.: Heat-resistant materials. ASM International, 1997.

457. Berge, S., Gartland, P. O., and Slagsvold, B. J.: Photoelectric work function of a molybdenum single crystal for the (100), (110), (111), (112), (114), and (332) faces. Surface Science, 43(1):275–292, May 1974.

458. Knizhnik, A. A., Iskandarova, I. M., Bagaturyants, A. A., Potapkin, B. V., and Fonseca, L. R. C.: Impact of oxygen on the work functions of mo in vacuum and on ZrO2. Journal of Applied Physics, 97(6):064911, March 2005.

459. Berger, J. A. and Schroeder, W. A.: Semianalytic model of electron pulse propagation: Magnetic lenses and rf pulse compression cavities. Journal of Applied Physics, 108(12):124905, 2010.

460. Zunger, A., Kerker, G. P., and Cohen, M. L.: Calculation of the electronic properties of mo in a first-principles nonlocal-pseudopotential approach. Physical Review B, 20(2), July 1979.

461. Bacalis, N. C., Blathras, K., Thomaides, P., and Papaconstantopoulos, D. A.: Various approximations made in augmented-plane-wave calculations. Physical Review B, 32(8):4849–4856, October 1985.

462. Monkhorst, H. J. and Pack, J. D.: Special points for brillouin-zone integrations. Physical Review B, 13(12):5188–5192, June 1976.

463. Surma, M.: Cyclotron resonance in molybdenum by transmission and identification of carriers on the molybdenum fermi surface. Journal of Magnetism and Magnetic Materials, 11(13):56–58, April 1979.

464. Michalik, A. M. and Sipe, J. E.: Analytic model of electron pulse propagation in ultrafast electron diffraction experiments. Journal of Applied Physics, 99(5):054908, 2006.

465. Li, W. and Li, D. Y.: On the correlation between surface roughness and work function in copper. The Journal of Chemical Physics, 122(6):064708, February 2005.

466. Hckstdt, C., Schmidt, S., Hfner, S., Forster, F., Reinert, F., and Springborg, M.: Work function studies of rare-gas/noble metal adsorption systems using a kelvin probe. Physical Review B, 73(7):075409, February 2006.

467. Hckstdt, C., Schmidt, S., Hfner, S., Forster, F., Reinert, F., and Springborg, M.: Work function studies of rare-gas/noble metal adsorption systems using a kelvin probe. Physical Review B, 73(7):075409, February 2006.

468. Price, D. L., Cooper, B. R., and Wills, J. M.: Effect of carbon vacancies on carbide work functions. Physical Review B, 48(20):15311–15315, November 1993.

469. Skriver, H. L. and Rosengaard, N. M.: Surface energy and work function of elemental metals. Phys. Rev. B, 46:7157–7168, Sep 1992.

470. Liu, Z., Sun, Y., Pianetta, P., and Pease, R. F. W.: Narrow cone emission from negative electron affinity photocathodes. Journal of Vacuum Science & Technology B: Microelectronics and Nanometer Structures, 23(6):2758, 2005.

471. Reinert, F.: Spinorbit interaction in the photoemission spectra of noble metal surface states. Journal of Physics: Condensed Matter, 15(5):S693, 2003.

472. Smoluchowski, R.: Anisotropy of the electronic work function of metals. Physical Review, 60(9):661, 1941.

473. Kulis, P., Butikova, J., Polyakov, B., Marcins, G., Pervenecka, J., Pudzs, K., and Tale, I.: Work function of colloidal semiconducting nanocrystals measured by kelvin probe. IOP Conference Series: Materials Science and Engineering, 38:012048, August 2012.

474. Lee, H. Y., Kang, Y. S., Choi, B. C., Tabata, H., Jeong, J., and Kawai, T.: Photoelectric properties by interface effect of organic/inorganic (cupc/pbte) multilayer prepared by pulsed laser deposition and thermal evaporation. J. Korean Phys. Soc., 34:64–68, 1999.

475. Nill, K. W.: LASER EMISSION FROM METAL-SEMICONDUCTOR BARRIERS ON PbTe AND pb0.8sn0.2te. Applied Physics Letters, 16(10):375, 1970.

476. Graham, R. and Yu, D.: High carrier mobility in single ultrathin colloidal lead selenide nanowire field effect transistors. Nano Letters, 12(8):4360–4365, August 2012.

477. McLane, G. and Zemel, J.: Surface interaction of h and {O2} on thin pbse epitaxic films. Thin Solid Films, 7(34):229 – 246, 1971.

478. Hussain, A. and Rahman, A.: Synthesis and electrical characteristics of al/(p)PbS schottky barrier junction. Materials Science in Semiconductor Processing, 16(6):1918–1924, December 2013.

479. Calixto-Rodriguez, M., García, H. M., Nair, M., and Nair, P.: Antimony chalcogenide/lead selenide thin film solar cell with 2.5% conversion efficiency prepared by chemical deposition. ECS Journal of Solid State Science and Technology, 2(4):Q69–Q73, 2013.

480. Spicer, W. E. and Lapeyre, G. J.: Photoemission investigation of the band structure of PbTe. Physical Review, 139(2A):A565, 1965.

481. Glen, Y., Alanyalolu, M., Ejderha, K., Nuholu, ., and Turut, A.: Electrical and optical characteristics of au/PbS/n-6hSiC structures prepared by electrodeposition of PbS thin film on n-type 6hSiC substrate. Journal of Alloys and Compounds, 509(6):3155–3159, February 2011.

482. Joseph, A. S. and Thorsen, A. C.: Low-field de haas-van alphen effect in copper. Physical Review, 134(4A):A979–A980, May 1964.

483. D'Arcy, R. J. and Surplice, N. A.: Work function of titanium films. Surface Science, 36(2):783–788, May 1973.

484. Qian, H. J., Murphy, J. B., Shen, Y., Tang, C. X., and Wang, X. J.: Surface photoemission in a high-brightness electron beam radio frequency gun. Applied Physics Letters, 97(25):253504, December 2010.

485. Hussermann, U. and Simak, S. I.: Origin of the c/a variation in hexagonal close-packed divalent metals. Physical Review B, 64(24):245114, December 2001.

486. Gotsis, H., Papaconstantopoulos, D., and Mehl, M.: Tight-binding calculations of the band structure and total energies of the various phases of magnesium. Physical Review B, 65(13):134101, 2002.

487. Engstrom, R.: Rca photomultiplier handbook (pmt-62). Lancaster, PA: RCA Electroptics and Devices, 1980.

488. Davis, S.: Effect of surface roughness on particle size predictions from photoemission results. J. Catal., 122(2):240 – 246, 1990.

489. Silkin, V., Balasubramanian, T., Chulkov, E., Rubio, A., and Echenique, P.: Surface-state hole decay mechanisms: The be(0001) surface. Physical Review B, 64(8), August 2001.

490. Nicolay, G., Reinert, F., Hüfner, S., and Blaha, P.: Spin-orbit splitting of the l-gap surface state on au (111) and ag (111). Phys. Rev. B, 65(3):033407, 2001.

491. Kim, M., Hwang, D. J., Jeon, H., Hiromatsu, K., and Grigoropoulos, C. P.: Single cell detection using a glass-based optofluidic device fabricated by femtosecond laser pulses. Lab on a Chip, 9(2):311–318, 2009.

VITA

NAME:	Tuo Li
EDUCATION:	M.S. of Stat., University of Illinois at Chicago, 2013, M.S. of Appl. Math., University of Illinois at Chicago, 2012 M.S. of Phys., University of Illinois at Chicago, 2011
SELECTED PUBLICATIONS:	Li, T., Rickman, B. L., Schroeder, W. A.: Density Functional Theory Analysis of Hexagonal Close-Packed Elemental Metal Photocathodes. Phys. Rev. ST Accel. Beams, 18.073401, 2015. Li, T., Rickman, B. L., Schroeder, W. A.: Emission Properties of Group VIb Elemental Photocathodes. J. Appl. Phys., 134901., 2008. Berger, J. A., Rickman, B. L., Li, T., Nicholls, A. W., and Schroeder, W. A.: Excited-state thermionic emission in III-antimonides: Low emittance ultrafast photocathodes. Appl. Phys. Lett., 101(19):194103, 2012.